A dual assembly multileaf collimator for radiotherapy

Peter Brian Greer, M.Sc (Dist.), M.A.C.P.S.E.M.

Supervisor: Assoc. Prof. T. van Doorn

Department of Physics and Mathematical Physics
Adelaide University

A thesis submitted in fulfilment of the requirements for the degree of Doctor of Philosophy, October, 2000

Table of contents

Figures

Chapter 2

Chapter 3

Chapter 4

Chapter 5

Chapter 6

Chapter 7

Chapter 8

Tables

Abstract

Medical physics seeks to provide methods to improve radiation therapy for cancer treatment. A multileaf collimator (MLC) for radiation therapy has been designed that splits each leaf bank into two vertically displaced assemblies or levels with each level consisting of alternate leaves and leaf spaces. The leaves in the upper level shield the spaces in the lower level. Each level can shift laterally, in the direction perpendicular to leaf motion by one leaf width. Following lateral movement of one level, the leaves align with the other level and radiation is transmitted through the collimator as multiple slit fields in a grid pattern. This transmission can be used to form an image of the external anatomy and would enable rapid double-exposure portal images to be acquired during the treatment.

The radiation profiles transmitted for image formation through the collimator design were investigated to examine their dependence on the collimator design features. The slit or leaf width was found to have the major influence on the transmitted profiles. As the slit width decreases the profiles become broader than the geometric slit projection resulting in a modulated image of the external anatomy, rather than a sampled or 'grid' image. The shielding of this design was found to be adequate provided the leaf faces of the adjacent vertically displaced leaves are at least aligned, therefore an overlap or tongue and groove is not required.

To examine the image quality of the modulated images, an algorithm to calculate the modulation transfer function (MTF) from an edge object image was developed. The effect of the algorithm on the measured MTF was investigated. To examine whether the spatial resolution of the image due to the source (geometric unsharpness) varies for the regions under the slits and under the leaves MTF measurements were made. The regions under the leaves were found to show poorer spatial resolution due to the more peripheral (extra-focal) source view. Image processing techniques were developed to remove the modulation from the images, including spatial domain and frequency domain methods. Finally, a prototype dual assembly multileaf collimator was constructed and the imaging and shielding properties were investigated.

Declaration

This work contains no material that has been accepted for the award of any other degree or diploma in any university or tertiary institution and, to the best of my knowledge and belief, contains no material previously published or written by another person, except where due reference has been made in the text.

I give consent for this thesis, when deposited in the University Library, being available for loan and photocopying

Signed

Date: 31 May 2001

Acknowledgements

I would like to acknowledge the support of the Department of Medical Physics and the Department of Radiation Oncology of the Royal Adelaide Hospital. Foremostly my supervisor Tim van Doorn for his guidance and patience. Also Mr Shane Hein for his design input and equipment manufacture and Mr Peter Blias for his equipment manufacture. Thank you to all the other staff for their support and their hospitality during my time in Adelaide.

Thanks to my roomates, Guilin Liu, Jeremy Booth and Kurt Byas for their help and tolerance of strong smells, and to Kurt for his superb help whenever needed.

To my wife Jane, thank you for your love, support and sacrifice over the past few years, and thank you to my daughters Madeleine and Genevieve, for just being there.

Publications and presentations associated with this research

Publications

- Greer PB and van Doorn T, Evaluation of an algorithm for the assessment of the MTF using an edge method, *Med. Phys.*, **27,** 2048-2059, 2000.
- Greer PB and van Doorn T, A design for a dual assembly multileaf collimator, *Med. Phys.*, **27,** 2242-2255, 2000.

Conference Presentations

- Greer PB and van Doorn T, A collimation design for double-exposure portal imaging, 41st Annual Meeting of the AAPM, Nashville, USA, July, 1999.
- Greer PB and van Doorn T, The transfer function of an MTF calculation algorithm, 41st Annual Meeting of the AAPM, Nashville, USA, July, 1999.
- Greer PB and van Doorn T, A collimation design for dynamic double-exposure portal imaging, ACPSEM Annual Conference, Hobart, Australia, 1998.
- Greer PB and van Doorn T, A Windows based program for modulation transfer function measurements from edge-object images, ACPSEM Annual Conference, Hobart, Australia, 1998.
- van Doorn T, Greer PB, Liu G and Schirmer M, A comparative study of the imaging characteristics of five portal imaging receptors, ESTRO, Edinburgh, Scotland, 1998.

Other Presentations

- Greer PB and van Doorn T, A multileaf collimator with fast portal imaging capability, Presented at the Vancouver Cancer Centre, Vancouver, Canada, March, 2000.
- Greer PB and van Doorn T, A collimation design for double-exposure portal imaging, ACPSEM (SA Branch) Postgraduate paper night, October, 1999 (Awarded best paper).

1. Introduction

1.1. Radiation Therapy

Radiotherapy or radiation therapy is the treatment of cancer with radiation. The cancer cell clumps or tumours are often sensitive to radiation, the effect of which is to damage the cell's DNA and prevent further cell division. The tumour presents the target in the body for the radiotherapy treatment, the aim is to deliver a prescribed dose of radiation to the tumour while minimising the dose to the surrounding normal tissues.

Radiotherapy machines produce beams of ionising radiation that can be aimed at the patient's tumour. The radiation usually consists of high or medium energy x-rays (photons) or high energy electrons, although other ionising particles are also used. Dose is imparted to the tissue along the path of the radiation through the body. Beams are delivered from several directions and combine at the tumour to increase the tumour dose relative to normal tissue.

1.2. Multileaf collimators

To minimise the dose to the normal tissues the radiation beam is shaped to conform or nearly conform to the cross-sectional shape of the tumour for the beam direction. Radiotherapy treatment machines incorporate beam shaping devices or collimators to achieve this. The most recently developed collimators consist of multiple leaves, each leaf blocking a portion of the beam and are referred to as multileaf collimators (MLCs). The leaves are used to form an aperture shape for the beam and attenuate the radiation outside of the aperture. Limitations of the current MLC design include high inter-leaf transmission. A tongue and groove design of abutting leaves is employed to reduce this. The tongue and groove however can result in regions of underdose in intensity modulated treatments for sequentially irradiated contiguous areas. When defining angled field edges the stepped pattern of the leaves results in stair-stepping of the isodoses and a larger effective penumbra than for alloy blocks. To reduce the stair-stepping the treatment field can be delivered in segments. The treatment couch and patient are moved a fraction of the leaf width in the direction orthogonal to leaf motion, and the leaves repositioned to the field border between each segment.

1.3. Imaging to verify beam placement

When the treatment is delivered, the accuracy of the beam localisation or placement must be confirmed to ensure that the tumour is fully treated and the normal tissue irradiation limited. This is done by acquiring images with the high energy radiation beam. These images show the treatment beam location relative to bony anatomical structures. They are generally acquired as a composite image of the treatment beam and a larger area image to clearly show the location of the beam relative to the anatomy, referred to as double-exposure images. The collimation must be retracted before the larger area image is acquired. The time to retract the collimation for double-exposure imaging lengthens the treatment time and the images can not be acquired during the treatment delivery.

1.4. Aims of this study

This thesis proposes and investigates a multileaf collimation design that addresses some of the limitations of conventional MLCs as well as providing a means to acquire double-exposure portal images rapidly. In the design, adjacent MLC leaves are vertically displaced so that the MLC consists of two vertically displaced levels or assemblies, each consisting of alternate MLC leaves and leaf width spaces. This allows a small overlap of adjacent leaves to reduce inter-leaf transmission. By minimising this overlap the underdose region in intensity modulated therapy can be reduced, or possibly eliminated.

The assemblies can also shift laterally by up to a leaf width. By shifting of the leaf assemblies by a fraction of a leaf width and repositioning to the field aperture the effective leaf width can be reduced by MLC movement, rather than treatment couch movement. This lateral movement capability also facilitates rapid acquisition of double exposure portal images. By a lateral shift of one leaf assembly by a leaf width to align with the other leaf assembly, radiation is transmitted through the MLC in a grid pattern of slit fields. By this mechanism the larger area image of the double exposure image could be acquired much more rapidly than at present and image acquisition could be performed during the treatment delivery.

The aims of this thesis are to investigate the properties of such an MLC design. In particular the formation of images by the multiple slit field irradiation with the MLC leaf assemblies aligned is of interest. To investigate how the radiation intensity distribution transmitted through the grid of aligned leaves depends on the design characteristics of the MLC, as well as the image quality of the images formed in this manner. Whether image processing can be effective at reconstructing such images to form images similar to open field images. A further aim of the project is to construct a prototype of the MLC and investigate the properties of this prototype.

1.5. Outline of thesis

The main investigations in this thesis are presented in Chapters 4 through to 8. Chapters 2 and 3 present background information and theory to provide understanding of the physics that is applied in the principal investigations in later chapters.

Chapter 2 introduces multileaf collimators. The chapter begins with a discussion of radiotherapy beam production and collimation as well as the main dosimetric properties of radiotherapy beams. The current design of MLCs as well as their dosimetric effects, the verification of MLC performance, and use for intensity modulated radiotherapy treatment is discussed.

Chapter 3 presents an overview of imaging at megavoltage energies. The chapter begins with a discussion of the physics of image formation with emphasis on megavoltage energies. Specific detectors that have been developed for megavoltage imaging are then introduced. This is followed by an introduction to the enhancement of digital images. Finally the chapter discusses utilisation of portal images for treatment verification including the quantitative measurement of beam placement, and correction strategies to reduce errors in beam placement

In Chapter 4 an algorithm for modulation transfer function (MTF) measurement from edge-object images is described and the accuracy of the algorithm is evaluated. The algorithm was developed for image quality assessment of the images produced by the multileaf collimator design. The major novel aspect of this work is investigation of the effect of error in edge angle determination on MTF measurement and derivation of an expression to quantify this error.

The radiation intensity distribution transmitted through the MLC when the MLC leaf levels are aligned to form a grid of multiple slit fields is investigated in Chapter 5. How the distribution depends on the design characteristics of the collimator is determined. The efficacy of shielding when adjacent MLC leaves are vertically displaced is also studied. This research contributes an understanding of the properties of megavoltage radiation transmission through a grid of collimated shielding leaves of varying dimensions and placement. A theoretical model that explains the main features of the transmission is developed.

Acquiring megavoltage images through a grid of aligned MLC leaves is a novel area of research and the subject of the investigations in Chapter 6. A theory of image formation through the grid of aligned leaves is developed. The image quality in the image regions under the slits and under the leaves is compared to open field imaging via MTF measurement. The variation in image quality with design parameters of the MLC is investigated.

Chapter 7 investigates image processing methods to remove the modulation pattern from images formed with the MLC leaf assemblies aligned. Both spatial domain and Fourier domain methods are investigated. This research shows how image processing can be applied to these type of images and determines the efficacy and limitations of the applied techniques.

Finally, Chapter 8 investigates the properties of a prototype dual assembly MLC for radiotherapy. Imaging with the leaf assemblies aligned, shielding and field edge defining properties are examined along with lateral shifting of the MLC leaves to reduce stair-stepping of the isodoses at the field borders. This work investigates the practical implementation of this multileaf collimator design in radiotherapy.

The research work outlined in these chapters has resulted in the aims of the thesis being achieved. The properties of the MLC design for radiotherapy are described by these investigations, in particular the formation of images by the multiple slit field irradiation with the MLC leaf assemblies aligned. The leaf width of the MLC was found to have the greatest influence on image formation, smaller leaf widths being optimal for image quality. The shielding of the design is effective provided adjacent leaves are aligned. Image processing can effectively remove the modulation from images formed through the MLC for smaller leaf widths. A dual assembly MLC was constructed and its properties for radiotherapy treatment determined.

2. Multileaf Collimators

2.1. Introduction

To minimise the volume of normal tissue irradiated to high doses, the radiotherapy treatment field cross-sectional shape or beam aperture can be matched to the cross-sectional projection of the target volume in the patient. Multileaf collimators are now widely used for this purpose. This chapter introduces radiotherapy beam production and collimation and the main dosimetric properties of radiotherapy beams. The current design of multileaf collimators, their dosimetric effects, commissioning for treatment and use for intensity modulated radiation therapy (IMRT) are then discussed.

2.2. Radiotherapy Beam Collimation

2.2.1. Beam production

High energy x-ray beams for radiotherapy are generally produced by medical linear accelerators. The main components of a medical linear accelerator are shown in Figure 2-1. The high voltage power supply (pulsed modulator) energises a microwave power source. The pulsed microwaves are injected into the waveguide to accelerate electrons that are injected into the end of the waveguide synchronised with the pulses of microwave power. These electrons are accelerated to near light speed by the microwaves and when they reach the end of the waveguide, strike a target to produce x-rays. The target can be retracted for electron beam therapy. For horizontal waveguides bending magnets are used to direct the electron beam exiting the waveguide vertically downward. The treatment head of the accelerator contains filters for producing uniform intensity (flattened) beams as well as collimators to produce the desired field shape. It also contains devices for the monitoring of the amount of radiation being delivered.

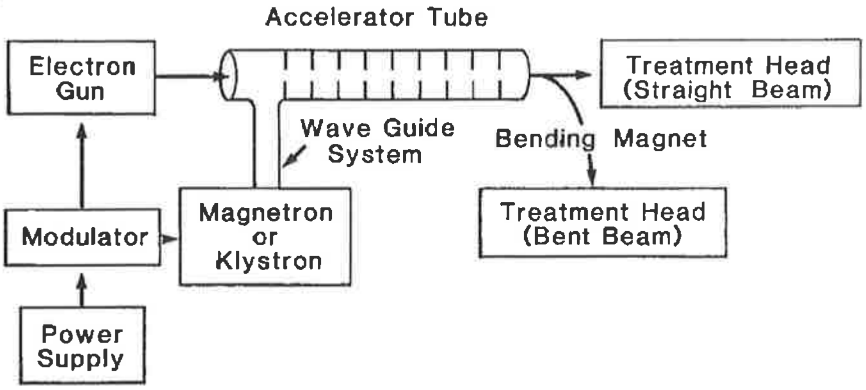

Figure 2-1 Block diagram of a typical medical linear accelerator (from Khan, 1994).

2.2.2. Beam Collimation

The treatment head contains the components to produce, flatten, collimate and monitor the treatment beam before it reaches the patient. These comprise the x-ray target where the x-rays are produced, the flattening filter, collimators, beam output and symmetry monitors (Figure 2-2). Surrounding the head is a large amount of lead shielding (~ 3 tonnes) to prevent leakage of radiation. Immediately below the target lies the circular cross-section conical primary collimator which limits the radiation aperture entering the accelerator head.

2.2.2.1. Flattening filter

The x-ray beam produced by the target is strongly forward peaked. To obtain a uniform intensity beam, a conically shaped filter is used to attenuate the beam in the centre. This is usually composed of tungsten or steel or a lead/steel combination. The placement of the filter in the radiation beam is critical to achieve symmetric radiation beams. The flattening filter becomes a source of scattered photons incident on the patient and is referred to as the extra-focal source.

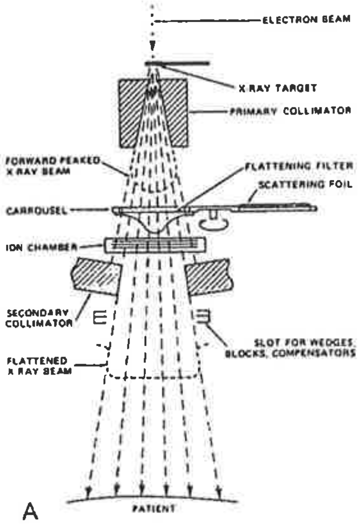

Figure 2-2 Main components of the treatment head of a medical linear accelerator (from Khan, 1994).

2.2.2.2. Beam Monitoring Chambers (BMC)

The photon beam is then incident on the BMC. These are large flat transmission-type ionisation chambers which measure the dose-rate, integrated dose and beam symmetry. The incident photons ionise the gas (oxygen enriched air) inside the chamber. A large bias voltage of 300 to 1000 V is applied across the chamber which results in an ionisation current. This current is proportional to the ionisation, or dose deposited in the chamber, and hence records the output of the beam. They are sealed from the outside air so that pressure and temperature do not influence their response. The dose-rate measured by the ionisation chamber is fed-back to the accelerator to ensure uniform dose-rate is delivered. This can be used to vary the pulse length or to ‘drop’ pulses. The integrated dose measured by the ion chamber is used to determine that the required dose has been delivered. The units of dose recorded are referred to as monitor units (MU); one MU corresponding to a preset dose measured by the chamber. These are calibrated so that 1 MU results in a known dose at a depth (usually 10 cm) in water. The symmetry difference signals are used to control the bending magnets steering coils. Because of the importance of the BMC there are always two completely independent chambers measuring the dose delivered. These are both interlocked to turn the beam off once the desired number of monitor units have been delivered. If one fails the other will interrupt the beam. There is a further safety feature which turns the beam off after a preset time, which is slightly longer than the time required to deliver the prescribed MU’s.

2.2.2.3. Secondary collimators

These collimators comprise two orthogonal jaw systems which can form an aperture from zero to 40 cm projected at 100 cm below the target, forming two sides of a rectangular field. The orthogonal jaw system forms the other two sides of the field. The jaws move in an arc so that the edge is always projected toward the source. Any rectangular field shape up to 40×40 cm square (at 100 cm) can be set. The jaws are made of tungsten or lead alloy and are 7-8 cm thick. The radiation transmission through such a jaw is ~ 0.5%. Jaw systems that allow each jaw to move independently can produce asymmetric fields, fields that are not symmetric about the central axis of the beam. They can also move some distance over the central axis. This capability is extremely useful in some treatment setups. For example when one of the jaws is brought to align along the central axis, this edge of the field has no divergence through the patient, which makes matching it to another field easier. The jaws on newer accelerators can also move during the treatment to create the effect of a wedge (dynamic wedge).

2.2.2.4. Tertiary Blocking

To produce an arbitrary beam aperture, custom-made lead-alloy blocks can be positioned below the collimator jaws. These are generally 7 cm thickness, and due to the lower density have a greater transmission than the secondary collimators at ~ 5%. These blocks are labour intensive to manufacture, a polystyrene mould is produced for the block using a divergent cutting device, and the low melting point alloy poured into the mould. They are also potentially harmful due to lead and cadmium components and the potential for injury due to dropped blocks or strains when lifting. The treatment of patients with many fields becomes inefficient due to the large number of blocks that must be manufactured as well as the treatment setup time.

2.2.2.5. Multileaf Collimator

To overcome many of the problems with lead-alloy block shielding, multileaf collimators (MLCs) were developed and have become a standard feature of new linear accelerators for radiation therapy. They consist of two banks of 40-60 opposing leaves or shields, each leaf under individual motor control. The leaves are positioned to form the field or aperture shape of the treatment beam (Figure 2-3). Each leaf blocks a portion of the radiation beam.

The hazards involved with lead-alloy blocks are eliminated. Shielding preparation time and storage space is reduced. As the positioning of the leaves is under computer control, the field apertures can be set remotely from outside the treatment room. Thus treatment times can be reduced, and treatment with larger numbers of fields becomes feasible. The treatment aperture shape can also be easily modified if necessary without having to manufacture new blocks. More recently, MLCs have been utilised to produce intensity modulated radiation therapy.

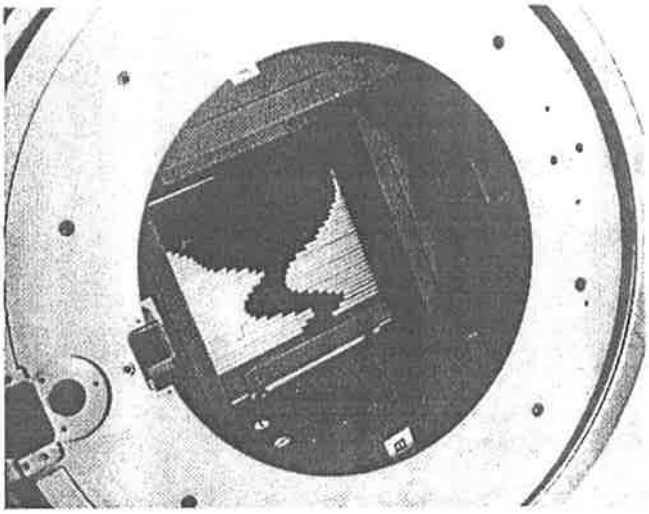

Figure 2-3 Picture of the Phillips (Elektra) MLC. From PMS Company literature.

2.2.2.6. Light field

Between the BMC and the secondary collimators is a light source and a 45 degree mirror, which is retracted from position before the beam is turned on. This is designed to project light down through the secondary collimators as though the source of light was the x-ray target and the light shows the x-ray beam. This assists the radiation therapists setting up the patient by displaying the field shape and location on the patients skin. Just below the collimation sits a thin plate that projects the central axis of the radiation beam when the light field is illuminated. The projection shows the therapist the centre of the radiation beam (beam axis) which is aligned to markers on the patients skin or immobilisation device. An optical distance indicator is provided to assist with patient setup. This is situated on the underside of the treatment head and projects the distance from the source down along the central axis of the beam.

2.2.3. Dosimetric properties of radiotherapy beams

2.2.3.1. Percentage Depth Dose

The features of the deposition of energy in the patient due to the treatment beam can be described by several relative dose parameters. The percentage depth dose is the dose variation with depth of the beam normalised to 100% at the depth of maximum dose. Figure 2-4 shows depth dose curves for various beam energies. These are usually measured along the central axis of the beam but can also be measured at off-axis points. The percentage depth dose varies with position in the beam due to the thickness of the flattening filter altering the incident intensity and energy of the beam. Increasing the field size of the beam increases the percentage depth dose as the contribution of scattered radiation increases. This increase in scattered dose is greater at larger depths than at the depth of maximum dose, therefore the percentage depth dose increases with field size.

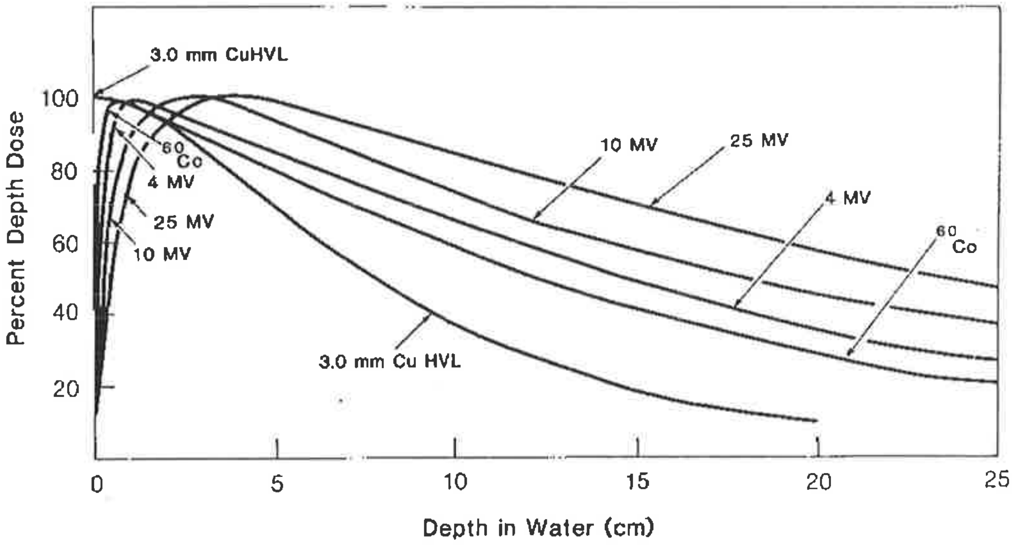

Figure 2-4 Percentage depth dose curves for differing incident energy of the x-ray beam (from Khan, 1994).

2.2.3.2. Beam Penumbra

The dose profile transverse to the beam direction at a particular depth in the medium can be recorded. This is usually normalised to 100% at the central axis of the beam. At the edges of the treatment field defined by the collimators, the dose falls off gradually due to the finite source size (geometric penumbra), and lateral electron scatter within the medium. This region of the beam is known as the penumbra region. Figure 2-5 illustrates the cause of the geometric penumbra due to the reduction in the amount of source that can irradiate the points as the point becomes more lateral. The penumbral width can be quantified by the distance between two of the relative dose levels. Commonly used are the 20-80% penumbral width and the 10-90% width although other combinations can be used. For a fixed distance the penumbra becomes greater if the collimators are closer to the source due to the increasing magnification.

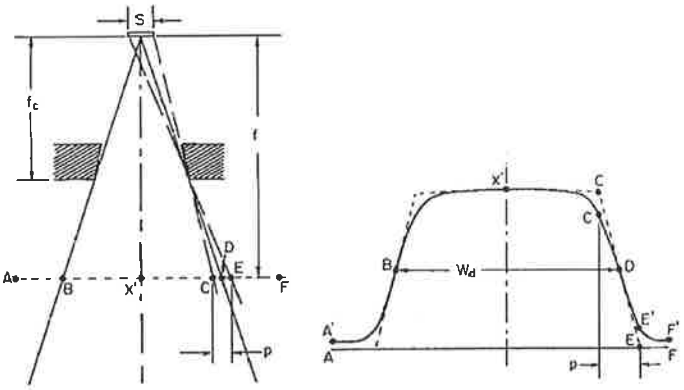

Figure 2-5 Dose profile illustrating the penumbral width of the beam (from Johns and Cunningham, 1983).

2.2.3.3. *Output Factor*

The setting of the collimation affects the absolute value of the dose delivered to a point in the patient. This is due to two main factors, change in the incident number of photons, and change in the amount of scatter in the phantom. The field of view of the flattening filter (extra-focal source) changes with collimator position. Reducing the size of the secondary collimator opening will reduce the view of the extra-focal source and therefore reduce the incident intensity. This change in intensity with field size can be measured in air and is referred to as the Output Factor or Head/Collimator Scatter Factor and is a function of the secondary collimator setting. The tertiary blocking does not generally alter the dose in air as this blocking is placed far enough from the source, that the entire extra-focal source is seen from the dosimetry point. However as the field size incident on the patient reduces, the amount of scattered radiation to the dosimetric point from the surrounding tissue will also reduce. This variation with field size is known as Phantom Scatter Factor, and is a function of the tertiary blocked field size. This is difficult to measure as it would require measurement of the dose change in phantom for many field sizes set by tertiary blocking. An easier approach is to measure the variation of dose in phantom with varying secondary collimator setting and divide this with the measured output variation in air (Khan, 1994). This yields the change in dose purely due to the changing scatter conditions.

2.3. Design of Multileaf Collimators

2.3.1. Leaf Design

An illustration of the MLC leaf design is shown in Figure 2-6. The leaves are made of tungsten or other dense material. The width of the leaf determines the resolution of the field shape and is usually specified as the width projected to the treatment isocentre distance of 100 cm from the source. Generally the leaves project to 0.5-2 cm width. To produce a maximum field size of 40×40 cm with 1 cm width leaves, each opposing leaf bank contains 40 leaves. Some designs incorporate smaller width leaves in the central region.

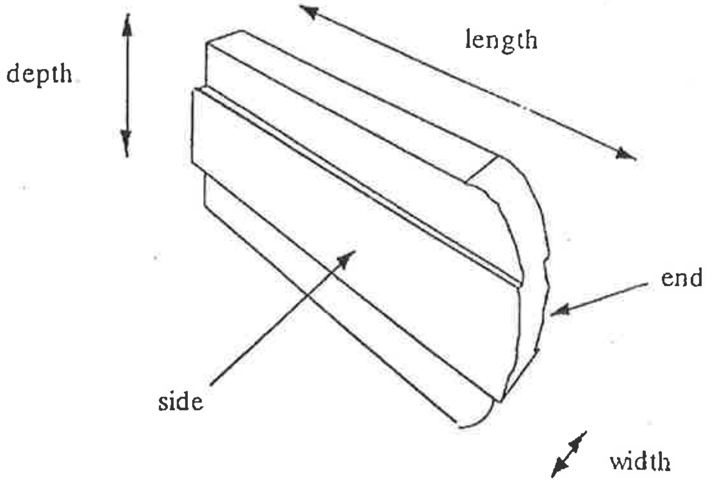

Figure 2-6 MLC leaf design illustrating the leaf terminology. Figure from Boyer *et al.* (1992a)

The thickness of the leaf determines the attenuation of the radiation. Leaf thicknesses of 5-7.5 cm are standard. The leaf sides are divergent to the source to minimise penumbra. The leaf ends are curved for the case when the leaves move in one horizontal plane (single-focussed) to maintain a constant penumbra with leaf position. The curvature is designed so that the radius of curvature is the maximum for which the chords defining the 20% transmission ray intersect the bottom corner of the leaf when fully withdrawn and the top corner of the leaf when fully across the central axis. When the leaves move in an arc about the source the leaf end is straight as it always is divergent to the source (double-focussed).

The leaves employ a tongue and groove design to abut adjacent leaves. The tongue in one leaf inserts into the groove in the adjacent leaf to prevent a direct transmission path for the radiation between the leaves. The tongue and groove design can affect the delivered dose distribution for IMRT. When two contiguous areas are sequentially irradiated with slit fields using an MLC, there is an underdose region where the fields abut due to the tongue and groove. This is illustrated in Figure 2-7.

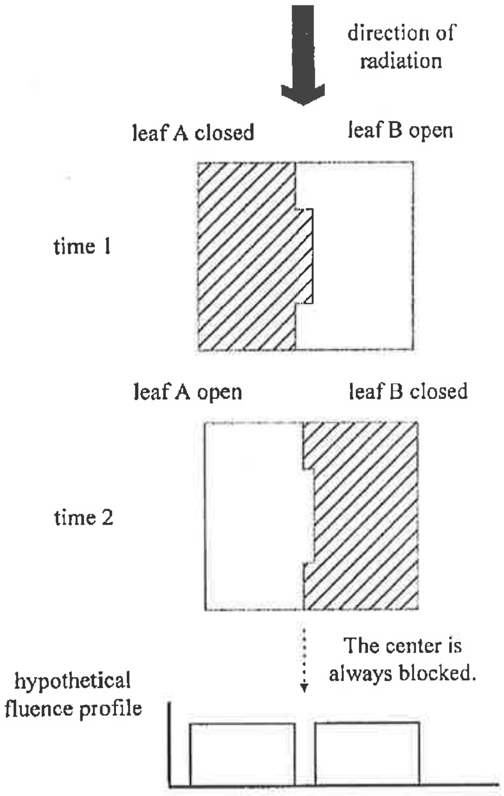

Figure 2-7 Potential underdosage due to the tongue and groove design when contiguous area are sequentially irradiated. (from Balog *et al.*, 1999).

Balog *et al.* (1999) have studied this effect for a tomotherapy intensity modulating vane collimator. They found that the while some of the underdose is due to penumbral blurring of each slit field, the tongue and groove is the predominant effect. In intensity modulated treatment where the fields are split into multiple adjacent slit fields the tongue and groove design could therefore lead to regions of underdose. The leaves can also travel over the central axis to form asymmetric fields. This overtravel varies from 10-16 cm between the three main commercially available MLCs. The leaf positions are verified electronically or by optical means.

2.3.2. Collimator Geometry

The position of the MLC in the treatment head of the linear acclerator varies for the three major linear accelerator manufacturers Varian, Siemens and Elekta. The Varian MLC is a tertiary collimator positioned below the secondary collimator jaws whereas the Elekta replaces the upper collimator jaw and the Siemens replaces the lower collimator jaw. To reduce the dose penetration through the MLC leaves in the Varian implementation the secondary collimator jaws are used as backup and are positioned at the borders of the rectangle that encloses the irregular field shape. The Elekta implementation has a thin backup collimator that moves in the same direction as the leaf movement so that this collimator and the orthogonal secondary jaw are positioned to the enclosing rectangle. The placement close to the source means that the leaf length can be shorter to traverse the field width, and the MLC is compact, however the leaf widths are smaller and therefore the manufacturing and movement tolerances must be smaller.

Placement further from the source increases the necessary bulk of the MLC as the leaf width and lengths are longer. To reduce the bulk of the collimator the Varian design incorporates two carriages for the leaves. The leaves project from the carriage into the field up to 14.5 cm. The carriage moves in and out of the field moving the entire leaf bank to achieve the full range of movement. This design limits the difference in extension of two adjacent leaves to 14.5 cm, however the limited extension of leaves from the carriage results in a more closely defined trajectory of the leaf. This means that adjacent but opposing leaves can pass each other (interdigitate). This has benefit for intensity modulated treatment techniques.

2.3.3. Field shape configuration

To produce the leaf settings, the treatment aperture can be digitised at a digitising tablet arrangement. The aperture is digitised from the field shape drawn by the clinician on the simulator film. The leaf settings are then automatically generated. These settings are transferred to the treatment machine console, and can be automatically set for the patients treatment. Alternatively the latest generation of treatment planning computers can produce the MLC leaf settings from the cross-sectional target shape for the field.

2.4. Dosimetric Properties of Multileaf Collimators

2.4.1. Rectangular field penumbra

Boyer *et al.* (1992a) compared the penumbra of fields formed with the secondary collimator jaws with the penumbra of the same field sizes when the fields were formed with the Varian MLC. When the field edge was formed with the MLC leaf sides the penumbra was similar to the upper collimator jaws. The penumbra when the field edge was formed with the curved leaf ends was 1-2 mm wider than the penumbra for the upper jaw. There was a small variation in the leaf end penumbra with leaf position. Galvin *et al.* (1993a) compared the penumbra of fields formed with alloy blocks to that of fields formed with the Varian MLC. The leaf side penumbra was virtually identical for both the tongue and groove sides of the leaves. There was only a small change in leaf end penumbra with leaf position and the penumbral profiles were similar to the alloy block profiles for both leaf ends and sides. Jordan and Williams (1994) measured penumbra for the Elekta MLC and found that the curved leaf end 20%-80% penumbral width varied by only 1 mm over the full range of leaf movement. The MLC penumbra was compared to the secondary collimator penumbra from an accelerator without the MLC. The differences in penumbral widths were within 1 mm. Similarly Huq *et al.* (1995) found no significant variation in penumbra with leaf position.

2.4.2. Angled edge penumbra

When the MLC defines an angled edge the stair-stepped dose pattern due to the finite width of the leaves becomes important. The stair-stepping pattern or undulation of the resulting isodoses (lines of constant dose) is most pronounced for MLCs positioned further from the source. This is due to the sharper penumbra (reduced blurring due to the source size) at smaller magnifications of the collimator. Boyer *et al.* (1992a) compared some corner blocked fields defined by MLC with the same fields defined by alloy blocking. The stair-stepping was most pronounced for the 50% isodose line and tended to "wash out" for the 80% and 20% contours. Isodose patterns were measured for the penumbra region for 45° and 15° angled edges defined by MLC (Galvin *et al.*, 1993a). For the 45° angle the

50% isodose was stepped however the 90% and 20% isodoses were virtually straight (Figure 2-8).

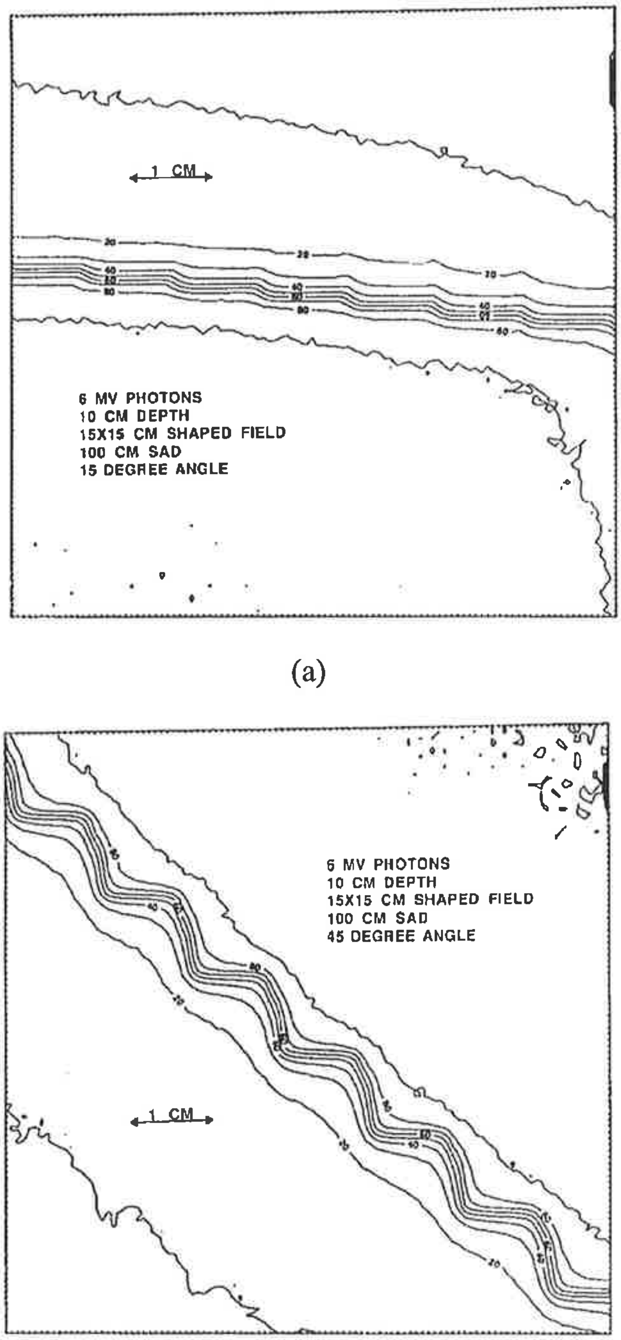

(a)

(b)

Figure 2-8 Measured isodoses for angled field edges defined by MLC for (a) 15° and (b) 45° angles. From Galvin *et al.* (1993a).

LoSasso *et al.* (1993) defined an "effective penumbra" as the distance between the tangents to two stepped isodose lines when the field edge is defined by MLC. They found for a 45° edge at d_{max} and 10 cm depths that the 20%-80% effective penumbra was 3-5 mm larger than for an alloy block. For the 10%-90% width this reduced to 2 mm. They produced treatment plans for 6 field conformal prostate treatment with MLC and alloy blocking. They found that the stair-stepping was moderated by the addition of multiple fields and that the stepping shifted to higher isodose levels. When setup variation was added by convolving the planned dose distribution with a Gaussian function the stepping was removed.

Frazier *et al.* (1993) compared irregular field penumbra of MLC and alloy blocked fields with and without incorporation of setup variation. The dose distributions at the dose prescription depth were recorded with film for head and neck, lung and pelvic fields. Previously measured setup variation was incorporated by convolution of the measured dose distributions with the setup variation. The 20%-80% effective penumbra was only slightly larger (average 1 mm) for the MLC than the alloy blocks with setup variation incorporated. The change in the penumbra due to the setup variation was twice as large as the change in penumbra due to the MLC.

More recently Galvin *et al.* (1998) utilised film within a phantom to measure isodoses for a single field, two parallel-opposed fields, and a four orthogonal field box treatment. In all cases one of the field edges was angled at 45° defined by MLC and an alloy block. Setup variation was also simulated by discrete movements of the phantom with dose delivered at each setup position. They found that the 20%-80% effective penumbra was wider than for an alloy block for the single field treatment. Adding the additional field made no difference. Adding the two lateral fields shifted the stair-stepping pattern to higher isodose levels. Incorporating setup variation largely removed the differences between the MLC field edge penumbra and the alloy block penumbra by affecting the block edge penumbra more than the MLC edge (Figure 2-9).

In summary, stair-stepping of the field edge isodoses is present for single MLC fields, with the stepping most pronounced for the 50% isodose. The effective penumbra is wider than that for alloy blocks. Addition of multiple fields tends to shift the stepping to higher isodose levels but may not remove it. The incorporation of setup variation removes any difference between the MLC and alloy block penumbra.

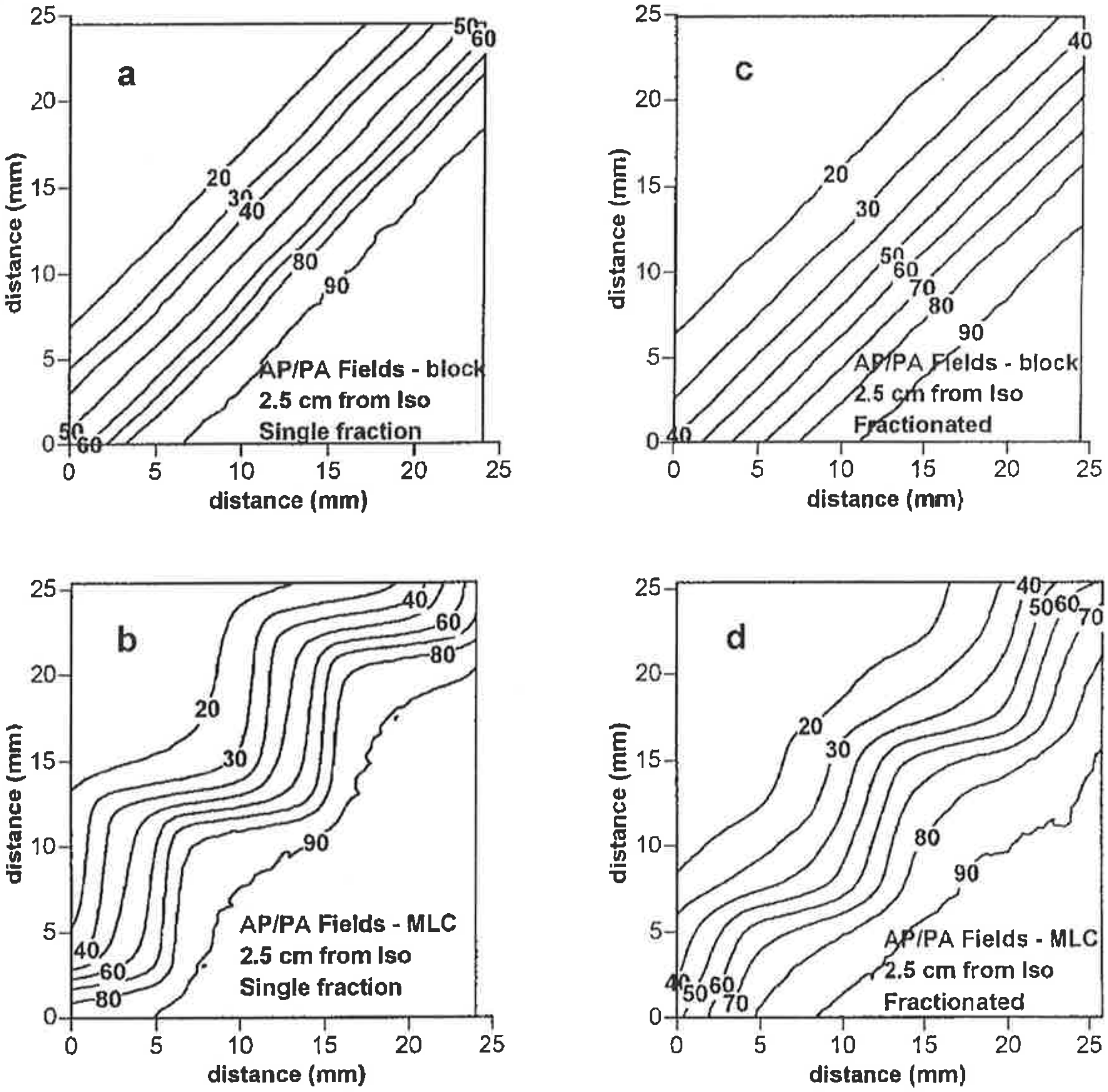

Figure 2-9 Comparison of angled edge penumbra for an alloy block and MLC with and without incorporation of setup variation; (a) alloy block single field, (b) MLC single field, (c) alloy block with setup variation and (d) MLC with setup variation. Figure from Galvin *et al.* (1998).

The distance of the MLC from the source, i.e. the magnification of the MLC to the patient plane has a large influence on the penumbra. Closer to the source more blurring occurs of the stair-step pattern due to the source size. The Elekta MLC replaces the upper collimator jaw therefore has a reduced stair-stepping of the penumbra than the Varian which is below the lower collimator jaw, much closer to the patient.

2.4.3. Methods to reduce dose undulation

An obvious way to reduce the stair-stepped dose undulation is to reduce the width of the leaves. Recently an MLC with 5 mm leaf width over the central 20 cm of the field has been introduced. Another method proposed by Galvin *et al.* (1996) delivers a portion of the treatment field dose with the leaves positioned to the field edge. The table is then shifted by a small amount (e.g. half a leaf width) in the direction orthogonal to the direction of leaf motion, and the leaves repositioned to the field edge. A further portion of the field dose is then delivered. Figure 2-10 illustrates this method for a field delivered with two positions of the MLC leaves. For a single field this technique was found to remove the stair-stepping pattern, however the penumbral width was not reduced and was wider than for an alloy block. The effective penumbra was the same as the MLC edge without any table shifting. Svatos *et al.* (1999) however found that with a half leaf shift the effective penumbra was reduced from that of a single MLC edge. A potential problem with this method is that if the penumbra is not reduced for a single field by the table movement, incorporating setup variation may result in a penumbra wider than that of an alloy block. This technique has recently been implemented by a linear accelerator manufacturer.

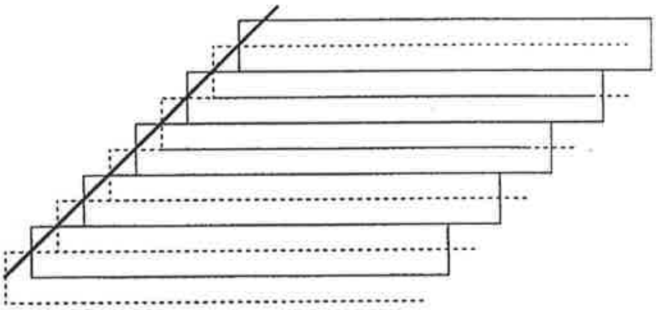

Figure 2-10 Leaf-positioning technique to reduce MLC dose undulation. One position of the MLC is shown as the solid leaves, and the second position laterally shifted by half a leaf width is shown as the dashed MLC leaves. Figure from Galvin *et al.* (1996).

2.4.4. Radiation transmission through MLC

The radiation transmission through the MLC leaves undulates due to the increased transmission at the junctions of adjacent leaves (interleaf transmission) as shown in Figure 2-11. The transmission has been measured to be approximately 1-2% minimum under the leaves (of an open 10×10 cm field dose) rising to 3-4% under the leaf junctions (Galvin *et al.*, 1993a; Jordan and Williams, 1994; Huq *et al.*, 1995). It has also been measured as low as 1.1-1.4% (Das *et al.*, 1998). These values are generally lower than the transmission through alloy blocks of 4-5% but higher than the transmission through the secondary collimators (< 1%). At the junctioning of opposing leaves the transmission can be very high due to the curved end design of the single focussed MLCs. To overcome this problem the leaves are junctioned underneath the secondary collimators. The secondary collimators or backup collimator are usually positioned at the enclosing rectangle of the irregular field shape.

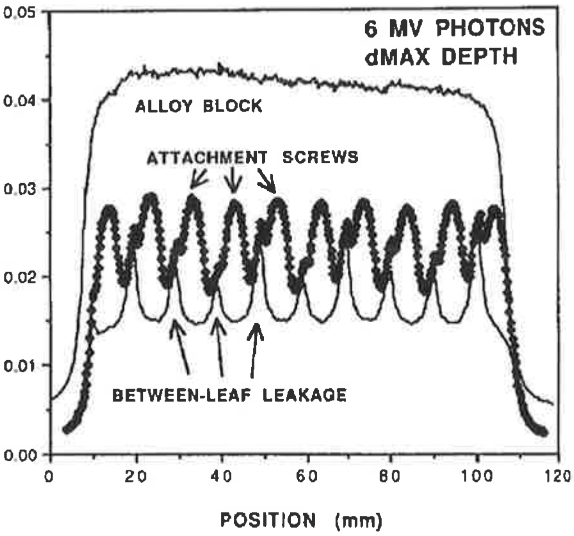

Figure 2-11 Measured MLC transmission profile compared to an alloy block for 6 MV x-rays. The profile clearly shows the peaks of transmission due to interleaf leakage. From Galvin *et al.* (1993a).

2.4.5. Percentage depth dose and output factors

No significant changes in percentage depth dose have been observed when the MLC is used to define the beam aperture rather than the secondary collimator jaws (Boyer *et al.*, 1992; Jordan and Williams, 1994; Huq *et al.*, 1995). The change in dose with field size (output factor) has been found to be similar when the MLC defines the field aperture to the secondary collimator output factors (Jordan and Williams, 1994; Huq *et al.*, 1995). It was also noted that the collimator exchange effect for rectangular fields (differing output for the same field dimensions depending on whether the upper or lower collimators define the long edge of the field) was removed when the MLC was used as it resides in a single plane (Jordan and Williams, 1994).

Boyer *et al.* (1992) found that for the Varian MLC the variation in output when a significantly (50%) blocked field was shaped with the MLC was predicted well when the secondary collimator setting was used to determine the variation in the output in air with field size (collimator scatter factor) and the MLC equivalent square field size was used to determine the variation in output in phantom (phantom scatter factor). This is similar to the effect of tertiary lead-alloy blocking. It implies that since the Varian MLC is at a large distance from the source, that the MLC when blocking does not significantly occlude the extra-focal source and thus affect the output in air.

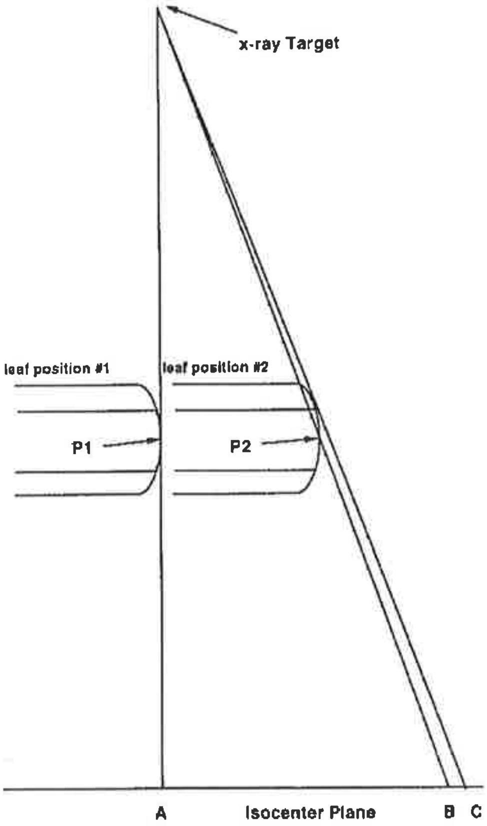

Figure 2-12 Coincidence of light field and radiation field with MLC. The projection of the light field (C) does not remain coincident with the edge of the radiation field (B) as the leaf travels across the field (from Galvin, 1993a).

2.4.6. Light and radiation field coincidence

A consequence of the curvature of the leaf ends in the single focussed design is a mismatch of light field aperture and radiation field aperture size. The light field is defined by the tangent to the leaf end whereas the radiation field border is defined by the 50% transmission chord through the curved end of the leaf (Figure 2-12). If the leaves were set to a 10×10 cm aperture according to the light field then the radiation field would not be 10×10 cm. Software correction is therefore used to position the leaf ends so that the 50% radiation border corresponds to the field size set. A problem also occurs when the field aperture is defined by the sides of the leaves due to the tongue and groove, although this is a small effect. For the double-focussed design the light field and radiation field should be coincident.

2.4.7. Optimal orientation of leaves

When an arbitrary irregular target shape is to be treated by the MLC leaves, the leaves should be orientated to achieve the best possible conformation to the aperture. Brahme (1988) determined that the direction of motion of the leaves should be in the direction in which the target presents its smallest cross-section. This means that the leaves should be aligned to minimize the opening of the collimator from the fully closed position.

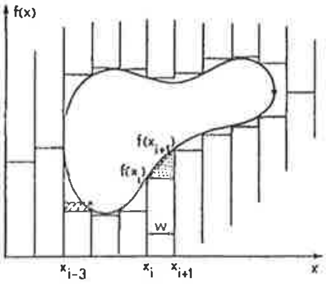

Figure 2-13 Optimal orientation of MLC leaves. Diagram showing how the stepped MLC is fitted to the continuous aperture shape to minimise the collimator opening (from Brahme, 1988).

2.4.8. Setting leaf ends to target cross-section

When alloy blocking is used to define an irregular aperture shape the edge of the block corresponds approximately to the 50% isodose line. Due to the stair-step nature of the MLC isodose, the 50% isodose will pass into and out of the aperture border depending on the position of the leaf ends. If the MLC leaves are positioned so that they just touch the border, then the 50% isodose will oscillate generally outside the border but with increased dose then outside the target volume. If the leaves are positioned so that the entire leaf end is just within the border then the 50% isodose will generally oscillate within the aperture, reducing the volume treated but sparing a greater volume of normal tissue. Alternatively to compromise between providing adequate coverage of the target and minimising dose outside the target, the leaves can be set to intersect the aperture border half way along the leaf end.

Zhu *et al.* (1992) found that for a 45° angle of the field border to the MLC leaves that the 50% isodose was sinusoidal with amplitude less than the amplitude of the sawtooth projection of the leaves by approximately 1 mm. Therefore the leaves could be positioned to ensure that the 50% contour undulated up to the field border. LoSasso *et al.* (1993) proposed setting the leaf so that the area of the target cross-section blocked by the leaf is equal to the area of extra irradiation outside the target (Figure 2-14). This is referred to as the cross-bound mode where the total area irradiated is the same as that for an alloy block defining the field contour. This method is now widely used. Alternatively Webb (1993a) calculated the margin necessary to add to the PTV when defining the field edge with a MLC by varying the margin between the PTV border and a 45° MLC edge and computing the TCP. It was found that a 7 mm margin gave the same TCP as defining the edge with an alloy block, although this did not account for normal tissue effects. Ultimately the setting of the leaves may depend on clinical factors such as proximity to normal tissue structures, and in some cases automated methods may be unsuitable.

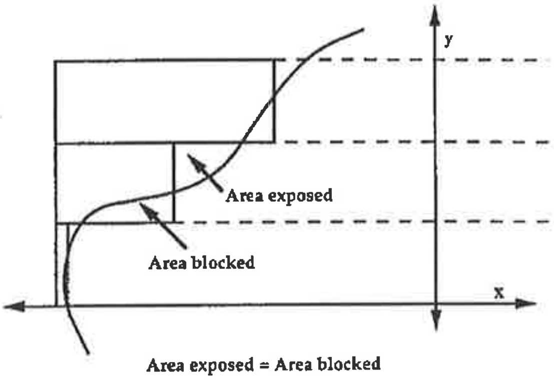

Figure 2-14 Cross-bound mode for leaf positioning to field borders. The area blocked by the leaf inside the aperture boundary is equal to the area left exposed outside the aperture (from Mohan, 1995).

2.5. Acceptance Testing and Commissioning

2.5.1. Mechanical acceptance and commissioning tests

The leaf positioning accuracy is verified by setting known positions of the MLC over the entire range of movement and confirming that the light field size at isocentre matches the MLC setting. The MLC leaves are usually all set to the same position. The leaf travel speed, the distance that the leaves travel over the central axis (overtravel) and if applicable the interdigitation capability are verified. Similarly the maximum leaf span range, the difference between the most extended and the most retracted position should be measured as this is important if opposing leaves are to be abutted under the secondary jaws. The reproducibility of leaf positioning is measured by forming the same leaf positions at different times and ensuring these are consistent. The isocentricity of the treatment machine should also be checked if an MLC is fitted to ensure that the extra weight of the MLC does not increase the size of the mechanical isocentre.

2.5.2. Leaf positioning with collimator rotation

To ensure that the x-ray beam defined by the MLC leaves has small variation in position due to collimator rotation, a slit field is formed with the MLC leaves. A radiation image of the field is recorded on a film for several collimator angles through the entire range of motion (usually every 45°). Lines are drawn along the centres of these slit fields and the intersection of the lines shows the variation in field position with collimator angle. If the MLC leaves are not aligned either side of the axis of collimator rotation then variation will be apparent.

A different approach used by Galvin (1999) is to define a half-beam or centre blocked field where one leaf bank is positioned at the zero position. Film is placed at the isocentre distance with appropriate buildup. The film is exposed and then the collimator rotated through 180 degrees and the exposure repeated. The film is scanned and dose homogeneity across the abutment region demonstrates correct calibration of the leaf position whereas a low density region means the leaf is positioned too far into the field. This test is repeated for the opposing leaf bank.

2.5.3. Leaf positioning with gantry rotation

To measure the variation in the x-ray beam position due to gantry rotation a similar test is performed. The x-ray film is positioned perpendicular to the machine axis of rotation and a slit field is formed with the MLC parallel to the axis of rotation. The short dimension of the field passes through the film forming an image. These images are formed at gantry angles every 45 degrees and should intersect within a circle of small (~ 1.0 mm) radius. Similarly Galvin (1999) uses a centre blocked field to perform this test exposing the film on end and then rotating the gantry by 180 degrees and repeating the exposure.

2.5.4. Coincidence of light field and x-ray field

The coincidence of the light field and the x-ray field is verified. This is done by setting a known MLC field size such as 10×10 cm and marking the estimated light field border (50%) on a film placed at isocentre. The film is then irradiated with this field size and the radiation field border estimated. The light field border and radiation field border are compared to ensure that the difference is within the allowed tolerance. This is done for all x-ray energies of the accelerator.

A measurement of the isodose line that corresponds to the leaf and light field setting can be performed (Klein *et al.,* 1995). This test consists of two exposures on a film placed at isocentre distance. In the first exposure the leaves from one carriage are brought to the desired position (i.e. the A leaves brought to the zero position). The opposing B leaves are retracted to a position to give a 10 cm field size. For the second half of the exposure the positions of the leaves are reversed, i.e. the B leaves are brought to the zero position and the A leaves retracted to give a 10 cm field abutting the previous. The dose profile across the junction is found and normalised to the 5 cm off-axis position. The maximum or minimum isodose level found at the zero position is used to determine the dose value for each leaf bank corresponding to the zero position. For example a 120% value implies a 60% isodose value for each leaf bank at the zero position. This test is repeated for the junctioning positions over the entire range of the leaf travel. The values are likely to be higher than 50% as the tip of the leaf end defines the light field and leaf position whereas the 50% isodose line will be through a certain thickness of the leaf. Similarly the tests can be performed for the leaf sides, where the effect of the tongue and groove will modify the isodose line from the light field projection location.

2.5.5. Leaf transmission

The transmission through the leaves is specified as the transmission dose reading under the leaves divided by the dose reading in the centre of an open 10×10 cm field expressed as a percentage. A measurement of this transmission can be made with an ion chamber or by film dosimetry. A typical ion chamber technique involves placing the chamber at the isocentre distance (100 cm) at the centre of a 10×10 cm field formed with the secondary collimator jaws with the MLC fully retracted. Several ion chamber readings are acquired at this point for a fixed number of monitor units and averaged to yield the open field (100%) transmission reference. The MLC leaves are then driven so that they fully extend over the region that was previously the open field area with the secondary jaws remaining in the previous position. A film is exposed with a large number of monitor units to record the transmission through the MLC leaves. This film identifies by the region of highest optical density the peak transmission location. The ion chamber is then placed at this location and several readings acquired for the same number of monitor units used above. The averaged reading divided by the reference reading multiplied by 100 gives the transmission which must be less than the specified tolerance. The test must be repeated for the opposing bank of leaves.

To perform the same test with film the reference 100% transmission is acquired in the same conditions as above but with film placed at isocentre distance exposed to the monitor unit setting. The MLC leaves are then extended across as above and a new film placed underneath. This film is exposed to a much larger number of monitor units. Both films are scanned with a densitometer to determine the relative optical densities. The optical density at the centre of the reference field is taken as 100% level while the peak density is found for the MLC transmission film. By use of the film dose to optical density conversion curve the relative dose to the films can be determined. As the relative dose delivered is known the transmission can be calculated to ensure that it is within tolerance. Galvin (1999) recommends repeating this test at the four cardinal gantry angles to ensure that any shift of leaves due to gravity is detected.

2.5.6. Penumbra

To quantify the penumbra, beam profiles are measured at appropriate depth (e.g. 10 cm) in a water phantom with a small detector. Film placed in solid water could be used provided the accuracy of the film profiles has been verified by comparison with other ion chamber measurement (Galvin *et al.*, 1993a). This can be done for different field sizes and positions of the MLC field edge across its range of travel. The penumbra for the field edge defined by the MLC leaf ends and the leaf sides is compared. The 80% to 20% penumbra should not vary by a large amount (e.g. less than 2 mm) for different positions of the leaves.

The stepped field edge penumbra when the MLC defines a 45° field edge can be measured with film, and a densitometer with a small spot size. In general though the literature information (for the same manufacturer) on these field edge distributions is utilised due to the lack of sufficient resolution densitometers in many radiation therapy departments.

2.5.7. Dosimetric parameters

When introducing a MLC for clinical field shaping the monitor unit calculation when a MLC is used must be verified. The monitor unit calculation for sample MLC field shapes should be verified by measurement with an ion chamber in water phantom. The Varian MLC, placed as a tertiary collimator below the secondary jaws has been found to influence the dose similarly to alloy blocks (Boyer *et al.*, 1992; Klein *et al.*, 1993). The phantom scatter factor depends on the MLC field shape whereas the collimator scatter factor depends on the secondary jaw setting. The monitor unit calculations incorporating the MLC in this manner can be verified for representative field shapes. For the Elekta design both the phantom scatter and collimator scatter factors have been found to depend on the MLC setting (Palta *et al.*, 1996) and again the accuracy of the monitor units calculated with this approach for MLC field settings must be verified.

2.5.8. Interlocks and file transfer

All safety interlocks associated with the MLC must be tested for correct operation. These interlocks ensure that when the MLC is defining the field shape that the backup secondary jaws are in the correct position to minimise leakage. Also the interlocks ensure that a leaf is not inserted into the treatment field when the leaves should be retracted. The faithful transfer, storage and formation by the MLC leaves of an MLC shape entered at the shaper station or derived from a treatment planning system must be verified. The tests performed for the commissioning of the MLC must be done at regular intervals to ensure that the MLC continues to operate safely and within the accepted tolerances.

2.6. MLCs and intensity modulated radiation therapy

2.6.1. IMRT

Intensity modulated radiation therapy is currently a topic of much interest in radiation therapy. Presently most treatments are given where the beam is either of relatively uniform intensity or has a wedged intensity profile in one direction, produced by physical wedges or movement of the secondary collimators during the treatment delivery (dynamic wedge). These constraints on the incident beam intensity profile place constraints on the dose distribution that can be delivered to the target region and also the sparing of normal tissues. The ability to produce arbitrary incident beam intensity profiles gives more degrees of freedom and the ability to produce arbitrarily shaped dose distributions in the patient.

The traditional treatment planning approach is to place beams from various directions with or without wedges and then modify beam directions, beam weights and wedging to achieve an "acceptable" distribution. With IMRT the flexibilty of being able to produce complex incident intensity patterns means that the planning process can begin with dose distribution criteria such as minimum dose to tumour and maximum allowed dose to normal tissues. The number of beams and directions are first defined. The planning software then iteratively searches for the incident intensity patterns that will produce a dose distribution that achieves these criteria. The complex intensity profiles can be produced with MLCs and the two methods to produce them are discussed here.

2.6.2. Static segmented method

This method also known as the "step and shoot" method divides each treatment field into subfields of different shape (Galvin *et al.*, 1993b). Each subfield or segment is formed with the MLC and some fraction of the total field dose is delivered with this field shape. The doses to the segments combine to produce the overall intensity pattern for the field (Figure 2-15). Advantages of this method are that it is straightforward to verify, portal images of the segments can be summed to verify that the overall intensity pattern delivered was as intended. These images can also verify that the fields were in the correct anatomical location. The method requires only a simple accelerator control system and it is easy to resume interrupted treatments. The disadvantage of this method is that it is relatively inefficient as complex patterns can require many segments per field. The number of segments is equal to the number of desired intensity levels in the pattern. This can result in 15-20 minute treatment times.

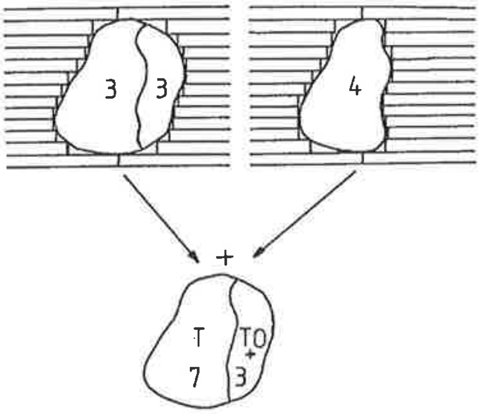

Figure 2-15 Static-segmented method for producing IMRT fields. The addition of the two field shapes gives the net intensity pattern. From Webb (1993b).

2.6.3. Dynamic sliding window method

Producing arbitrary intensity distributions by dynamic movement of a multileaf collimator was first proposed by Kallman *et al.* (1988). In their method a small element of the beam was formed with the multileaf collimator and this element was moved over the entire treatment field. Convery and Rosenbloom (1991) proposed using the secondary collimator jaws to form a slit field that swept across the treatment field. By varying the width of the field aperture by controlling the speed of each jaw, arbitrary one-dimensional beam profiles could be produced. The dose received at a point in the patient depends on how long the aperture was above the point. Methods incorporating these two ideas were then developed (Bortfeld *et al.*, 1994; Spirou and Chui, 1994) where each leaf pair form an elemental slit field of variable width that moves across the field (Figure 2-16). As each leaf pair can create a different one-dimensional profile in the direction of leaf movement, a two-dimensional profile can be created by using all the leaf pairs swept across the field (Figure 2-17).

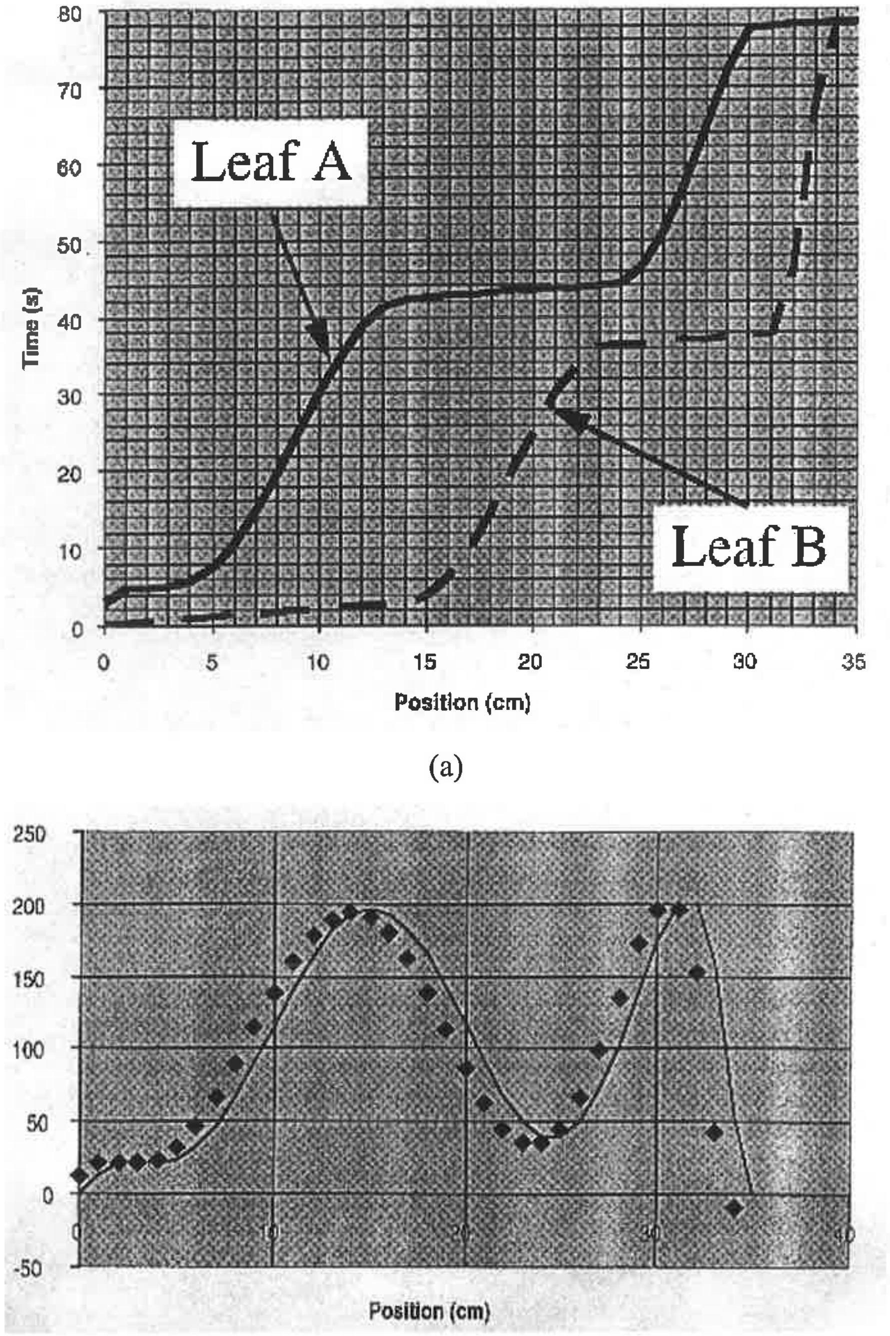

(a)

(b)

Figure 2-16 Dynamic sliding window technique for IMRT. Illustration of how the sweeping leaves across the field is used to produce a particular dose at a point in the phantom; (a) shows the position with time of a moving leaf pair and (b) shows the intensity profile with position resulting from this movement. From Mohan (1995).

This method results in faster beam delivery than the static segmented method, and more complex dose distributions can be delivered. The intensities are smoothly varying compared to the discrete intensity levels of the static method. Disadvantages are that the beams are more difficult to verify due to the movement of the leaves during the irradiation, and it is more difficult to recover from an interruption. Leaf edge effects such as penumbral blurring and the effect of the tongue and groove also become important when contiguous areas are irradiated sequentially.

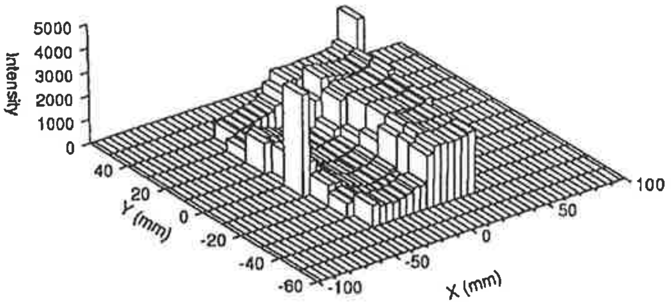

Figure 2-17 An intensity map produced by dynamic MLC movement. From Ling *et al.* (1996)

2.6.4. MLC tests for IMRT

The use of MLC for IMRT delivery results in tighter tolerances on the leaf positioning, leaf speed, interleaf transmission and through leaf leakage. The dynamic method requires that leaf speed is accurately controlled. Tolerances in positioning of less than 0.5 mm may be required for IMRT treatments. Thus for dynamic dose delivery the leaf speed control must be verified. The leaf positioning accuracy and isocentricity (variation with collimator and gantry rotation) must be measured but with tolerances reduced.

3. Megavoltage Imaging

3.1. Introduction

Portal imaging refers to imaging of the radiotherapy treatment to verify the geometric (and potentially dosimetric) accuracy of the treatment. Images are acquired that show the geometric placement of the treatment field relative to bony anatomical landmarks. The image is compared to a reference image showing the intended beam placement. Errors or field displacements can then be determined either by quantitative measurement or visual assessment. If the portal images are in digital form then they can also be processed to improve quality. This chapter begins with a discussion of the physics of image formation with emphasis on imaging at megavoltage energies. The specific detectors developed for megavoltage imaging are then introduced. This is followed by an introduction to the enhancement of digital images. Finally the chapter discusses utilisation of portal images for treatment verification including the quantitative measurement of beam placement, and correction strategies to reduce errors in beam placement.

3.2. Theory of image formation

3.2.1. Imaging system and image formation

The radiographic image is formed by the interaction of a distribution of x-ray photons with a detector. These are either primary photons that are transmitted through the patient without interacting or secondary photons that result from an interaction within the patient. The secondary photons are deflected from their initial direction and carry little useful imaging information. The primary photons give a measure of the probability of the photons passing through the patient without interacting. This probability depends on the sum of the x-ray attenuation property of the tissue along the path of the photon. The image is therefore a projection of the x-ray attenuation property along the photon path.

The components of a basic imaging system are shown in Figure 3-1. The photons from the x-ray producing device enter the patient and are either transmitted without interaction, absorbed or scattered. The primary photons recorded by the detector form the image and the scattered photons create a background signal that degrades contrast and reduces signal-to-noise ratio.

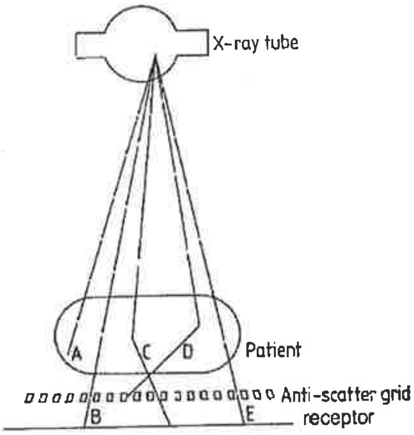

Figure 3-1 Basic components of an imaging system. A is an absorbed photon, B and E are photons that pass through the patient without interacting, C and D are scattered photons. Photon D has been absorbed by an anti-scatter grid. From Webb (1988).

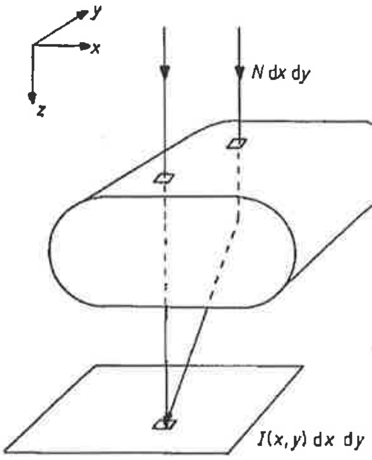

Figure 3-2 Simple model of the formation of the radiographic image showing both a primary and a secondary photon (from Webb, 1988).

A simple mathematical model of the imaging process can be developed. Considering an x-ray beam parallel to the *z*-axis of energy *E*, with the image recorded at the *xy* plane (Figure 3-2). The detector is considered to be linear, and the image is the distribution of absorbed energy. If the intensity of the photons incident on the patient is *N* photons per unit area, and *I(x,y)*d*x*d*y* is the energy absorbed in area d*x*d*y* of the detector, then

$$I(x,y) = N\varepsilon(E,0)E\exp\left(-\int\mu(x,y,z)\mathrm{d}z\right) + \int\varepsilon(E_s,\vartheta)E_s S(x,y,E_s,\Omega)\mathrm{d}\Omega\mathrm{d}E_s \qquad (3.1)$$

where the first term represents the primary transmission and the second term describes the scatter contribution. The line integral is over all tissues along the path of the primary photons reaching the point (x,y) and $\mu(x,y,z)$ is the linear attenuation coefficient. The scatter distribution function S is defined so that $S(x,y,E,\Omega)\mathrm{d}E\mathrm{d}\Omega\,\mathrm{d}x\mathrm{d}y$ gives the number of scattered photons of energy range $E + \mathrm{d}E$ and solid angle range $\Omega + \mathrm{d}\Omega$ that are incident on the area d*x*d*y* of the detector. The energy absorption efficiency ε of the detector is a function of photon energy and incident angle. The scatter contribution can be simplified by considering the value at the centre of the image. In general this function is slowly varying and will be maximal at the centre of the image.

$$I(x,y) = N\varepsilon(E,0)E\exp\left(-\int\mu(x,y,z)\mathrm{d}z\right) + \bar{S}\bar{\varepsilon}(E)E \qquad (3.2)$$

where

$$\bar{S} = \int S(0,0,E_s,\Omega)\mathrm{d}\Omega\mathrm{d}E_s \tag{3.3}$$

and

$$\bar{\varepsilon}(E)E = \int \varepsilon(E_s,\vartheta)E_s S(0,0,E_s,\Omega)\mathrm{d}\Omega\mathrm{d}E_s / \bar{S} \tag{3.4}$$

If the ratio F of the scattered radiation to the primary radiation is known then Equation 3.2 can be expressed

$$I(x,y) = N\varepsilon(E,0)E\exp\left(-\int \mu(x,y,z)\mathrm{d}z\right)(1+F) \tag{3.5}$$

3.2.2. Contrast and signal-to-noise ratio

3.2.2.1. Contrast

Subject contrast is the difference in attenuation between an anatomical object imbedded in a medium and the background. This results in a difference in the number of x-ray quanta reaching the detector behind the object compared to the background. The linear attenuation coefficients of bone and soft-tissue (water) vary with incident photon energy. Photoelectric absorption is the dominant interaction for energies up to 50 keV, and from 60 to 90 keV both Compton and Photoelectric are important. From 200 keV to 2 MeV only Compton scattering is present (Johns and Cunningham, 1983). The energy of photons produced by medical linear accelerators is largely in the Compton scattering range. The mass attenuation coefficients (linear coefficients divided by the mass) taken from Johns and Cunningham (1983) for bone and water with photon energy are shown in Figure 3-3. The attenuation is high for the bone at the low energies due to photoelectric absorption. This is strongly dependent on atomic number, and hence bone absorbs much more strongly than tissue (water) due to the difference in atomic number. However as the energy increases, the predominant interaction process becomes Compton scattering which is largely independent of atomic number, and dependent on electron density. Thus the attenuation difference between bone and tissue becomes small and is less than the attenuation difference between air and tissue where there is a greater density difference.

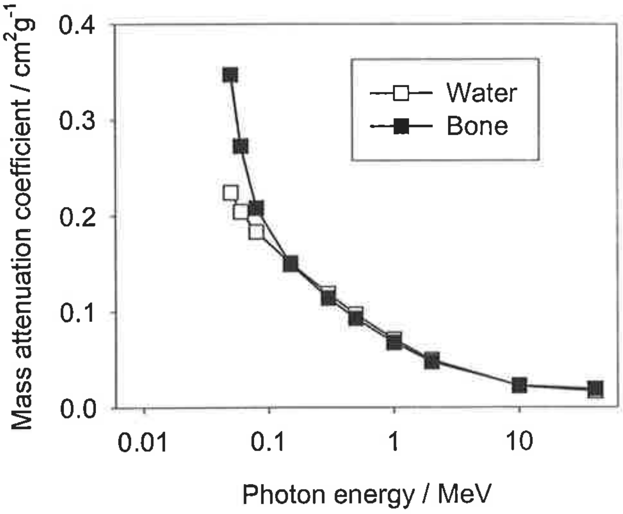

Figure 3-3 Mass attenuation coefficients of water and bone as a function of photon energy.

A simplified analysis of the image formation process has been developed by Motz and Danos (1978) where the detectability of a small anatomic structure embedded within a homogeneous body is determined. The model restricts the estimation of signal-to-noise ratio (SNR) to primary subject contrast, statistical noise and scatter. Considering a homogeneous medium of thickness L and linear attenuation coefficient μ. On average $n = n_T$ x-ray quanta are detected as image background of which a fraction $F = n_S/n_T$ have been scattered (scatter fraction).

Embedded within the medium there is a structure of thickness L_x and attenuation coefficient μ_x such that n' total quanta are detected behind the anatomical object. If on average n are detected as the background then the subject contrast (ratio of the signal difference between the anatomical structure and the background, to the mean carrier signal) can be expressed as

$$C = 2|n - n'|/(n + n') \tag{3.6}$$

This can be rewritten as (Motz and Danos, 1978)

$$C = \frac{2(1 - e^{-\Delta})}{1 + e^{-\Delta} + 2F/(1-F)} \tag{3.7}$$

where $\Delta = L_x(\mu_x - \mu)$ represents the attenuation difference between the anatomic structure and the background. Subject contrast therefore increases as this attenuation difference Δ increases, or if the scatter fraction F decreases.

Due to the small difference in attenuation coefficient between bone and soft tissue, subject contrast is very low at megavoltage photon energies, 10-20 times less than at diagnostic energies. For a 1 cm thick bone structure within a 20 cm thick water medium the subject contrast decreases from 18.5% at 50 keV to 1.4% at 2 MeV (Boyer *et al.*, 1992b). This is illustrated in Figure 3-4 where the contrast C for a 1 cm bone structure and a 1 cm air cavity in a 20 cm thick water phantom is plotted as a function of monoenergetic incident photon energy. This contrast was calculated using Equation 3.7 from tabulated attenuation coefficients for bone, air and water as a function of energy (Johns and Cunningham, 1983).

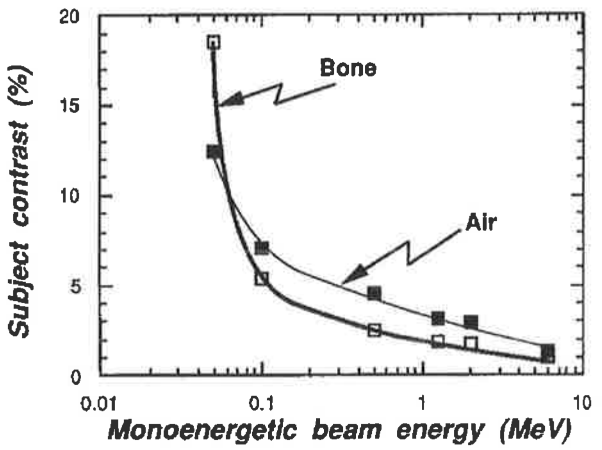

Figure 3-4 Subject contrast as a function of monoenergetic beam energy for a 1 cm bone structure and a 1 cm air cavity embedded in a 20 cm thick water phantom (from Boyer *et al.*, 1992b).

3.2.2.2. Noise

There are two major contributions to the noise in the image. Statistical fluctuations in the number of x-ray photons detected per unit area is known as quantum noise. Fluctuations in the signal will also occur due to the properties of the x-ray detection system. This latter noise is a function of spatial frequency and can be expressed in terms of the Wiener spectrum or noise power spectrum (NPS(f)) function. The mean-square departure of a signal from its average value is the variance, and the analysis of these fluctuations into spatial frequency components gives NPS(f). An important quantity that is closely related to image information content is the SNR. This can be expressed as the ratio of the signal difference between the structure and the background to the statistical noise associated with detection of the quanta.

$$SNR = |(n - n')| / \sqrt{n + n'} \tag{3.8}$$

Motz and Danos (1978) have shown that this can be written as

$$SNR = \left[A\Phi\eta e^{-\mu L}\left(1 + e^{-\Delta} + \frac{2F}{1-F}\right)\right]^{\frac{1}{2}} \cdot \frac{C}{2} \tag{3.9}$$

where A is the area of the anatomical object, Φ is the photon fluence incident on the phantom, and η is the x-ray quantum efficiency of the detector. The SNR will therefore improve as the size of the structure increases, the subject contrast C increases and the number of x-ray quanta utilised for image formation increases.

Much larger numbers of x-ray quanta reach the detector in megavoltage imaging due to the much higher doses given, the penetrating power of the radiation and the lack of any grids to attenuate the transmitted radiation. Potentially this greater number of quanta could partly offset the low subject contrast in terms of SNR. This is illustrated in Figure 3-5. The SNR is calculated from Equation 3.9 for the 1 cm object in the 20 cm phantom, assuming a dose of 0.05 cGy for the low energy image, and a 10 cGy dose for the high energy image. The result shows that an increase in dose (quanta) can compensate for the lower subject contrast, and the object should be equally detectable at 50 keV or 1.25 MeV. This model does not account for loss of spatial resolution or detector noise.

This implies that megavoltage imaging systems should be efficient at detecting photons, and should add as little noise as possible. Other desirable aspects are linearity with dose, or at least a well-defined relationship, and minimal spatial distortion of the image.

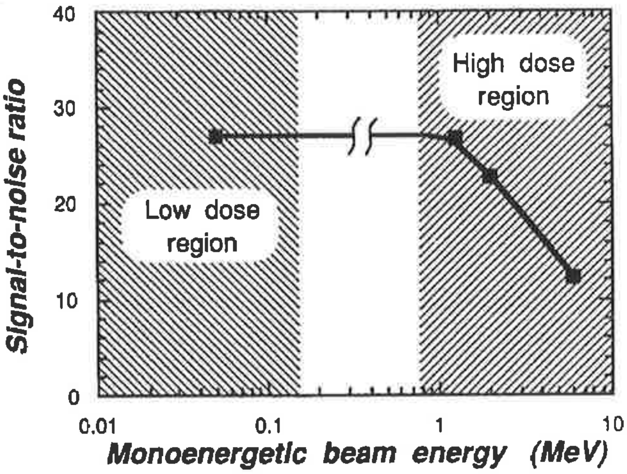

Figure 3-5 SNR for a 1 cm bony object embedded in a 20 cm thick water medium for exposures typical of diagnostic radiology (low dose region, 0.05 cGy) and radiation therapy (high dose region, 10 cGy). From Boyer *et al.* 1992b.

The signal-to-noise properties of an imaging system can be determined by the detective quantum efficiency (DQE). This gives the SNR^2 transfer characteristics of the imaging system as a function of spatial frequency and is defined as

$$\mathrm{DQE}(f) = \left[\mathrm{SNR}_{\mathrm{out}}(f)/\mathrm{SNR}_{\mathrm{in}}(f)\right]^2 \tag{3.10}$$

This can be rewritten in terms of the NPS and the modulation transfer function (MTF). The MTF is defined in Section 3.2.3.2.

$$\mathrm{DQE}(f) = K^2\,\mathrm{MTF}^2(f)/\Phi\,\mathrm{NPS}(f) \tag{3.11}$$

where K is a constant that takes into account the response of the imaging system to radiation exposure.

3.2.2.3. Scattered radiation

The physical characteristics of x-rays scattered by the patient and reaching the imaging detector as well as their effect on portal imaging quality have been investigated for megavoltage (0.1-20 MeV) x-ray beams by Jaffray *et al.*, (1994). Monte Carlo (MC) simulations were used along with measurements to check the MC validity. The aim was to determine the scatter and primary fluences reaching the detector for different geometries and incident energy spectra. The electron component reaching the detector was not investigated. The MC calculations modelled the source as a point source.

With a geometry of 30×30 cm field, 0 cm air gap, and a 17 cm PMMA slab, the variation of scatter fraction with energy of the monoenergetic incident beam was studied on the central axis of the beam, normalised to the incident fluence with no slab. The primary transmitted fluence increases from a few percent at 100 keV to 72% at 20 MeV. The scatter fluence first increases rapidly from 100 to 700 keV, then drops slightly then slowly increases. The scatter fraction declines rapidly from 100 keV to 5 MeV and then is relatively flat. The change in scatter fraction from 0.5 to 10 MeV (energies of interest for radiation therapy) is more affected by the increase in the primary signal than change in the scatter signal. The energy of the scatter fluence was found to be much lower than the primary for megavoltage energies.

The effect of medium thickness, field size and air-gap between the medium and detector were studied by MC modelling with clinical spectra of 6 and 24 MV beams. The effect of medium thickness was investigated for PMMA slabs with a 30 cm air gap and 30 × 30 cm field size. With increasing slab thickness the scatter fluence changed little, however the primary reduced and hence the scatter fraction increased. The scatter fraction increased from about 0.1 for both energies for 5 cm thickness to 0.4 for 6 MV and 0.3 for 24 MV at 20 cm thickness. The scatter fraction is less for the higher energy as the primary is less attenuated. Variation with field size was studied for a 30 cm air gap and a 17 cm thick PMMA slab. The primary fluence was independent of field size (modelled independent of output factor), while the scatter fraction increased from near zero for a 5×5 cm field to 0.2 for a 30×30 cm field. The primary transmissions for this geometry were about 0.3 for 6 MV and 0.5 for 24 MV. The scatter fluences were very similar for the 6 and 24 MV energies.

The effect of air gap was studied with a 30×30 cm field size and 17 cm PMMA. Changing the air gap from 0 to 60 cm reduces the scatter fraction from 0.6 to 0.2 for 6 MV and from 0.5 to 0.2 for 24 MV. The scatter fluence falls faster than the inverse square falloff of primary. Figure 3-6 illustrates how the air gap reduces the scattered component of the beam (scatter-to-primary ratio). The scattered radiation falls off with distance more rapidly than the primary radiation due to the angle of scatter.

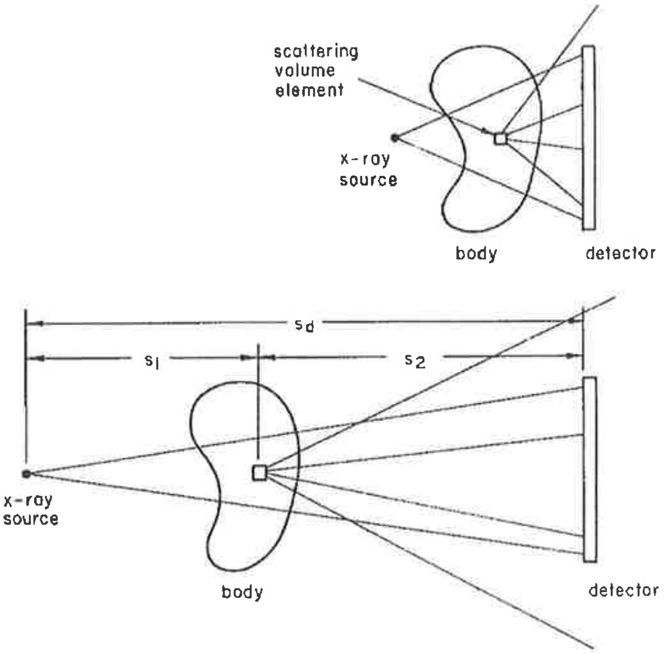

Figure 3-6 Reduction of scatter component with increasing air-gap, (from Barrett and Swindell, 1981).

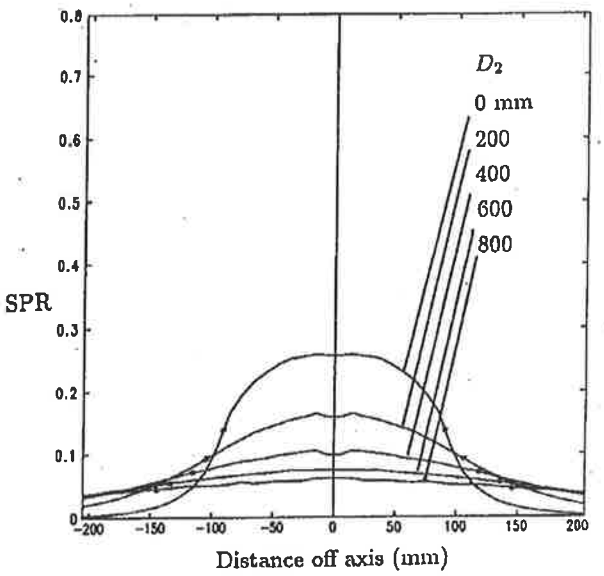

Figure 3-7 Distribution of scatter at the detector plane for varying air gap, from Swindell *et al.* (1991).

Swindell *et al.* (1991) have calculated the scatter to primary ratio at the detector plane by Monte Carlo modelling. This was modelled considering a 25 cm thick water slab at 100 cm from the source, a 15 cm diameter field of 2 MeV energy photons, and varying air-gap to the detector. The results are shown in Figure 3-7, the scatter falls off with distance from the central axis and the profile becomes flatter with increasing air-gap.

At megavoltage energies the scatter spectrum is of considerably lower energy than the primary. Because different detectors have different energy responses, the same primary and scatter spectra arriving at the detector will result in different signal scatter fractions. Detectors with thick ~1 mm lead plates on the entrance face minimise the scatter signal, by preferentially filtering the low energy scatter fluence. These low energy scatter are also filtered by the air gap so the scatter signal reduces with air gap. For fixed display contrast (e.g. film) the scatter signal fraction results in a loss of contrast, equal to the scatter fraction. For 0.8 mm Pb/Kodak AA film the scatter can result in 25-50% contrast loss. For quantum noise-limited systems the noise introduced by the added scatter fluence will reduce the differential SNR by 10-20% for typical imaging geometries.

Scattered radiation may be therefore minimised by reducing the area of the incident beam, increasing the air-gap between the scattering medium and the detector. A grid placed in front of the detector will also reduce the scattered radiation. These are widely employed at diagnostic radiology energies but have not been used at megavoltage energies where the grid would be thick and therefore extremely heavy to attenuate the radiation. The grid will produce a pattern on the image, however this can be eliminated by moving the grid during the exposure. An alternative method that reduces the area of the irradiation combined with collimation is the scanning slit assembly method (Pasche, 1903). The slit placed before the patient defines a narrow fan beam of x-rays, while the slit before the detector rejects most of the scattered radiation. The two slits scan across to form a complete image, and move together so as to remain in line with the source and each other. Multiple slit assemblies have also been developed (Jaffe and Webster, 1975) to reduce the imaging time.

3.2.3. Linear Systems Theory for imaging systems

3.2.3.1. Point Spread Function (Impulse Response)

The linear systems theory presented here is a summary of that presented in Chapter 2 of Barrett and Swindell (1981). Imaging systems can be considered as a linear system where the input is the x-ray attenuation property of the object being imaged and the output the x-ray flux at the detector or the output of the detector. A linear system receives a stimulus $w_{in}(u)$ where u is an independent variable such as spatial position, and produces an output $w_{out}(u)$. If the input $w_{in}^{(1)}(u)$ produces output $w_{out}^{(1)}(u)$ and a different input $w_{in}^{(2)}(u)$ produces output $w_{out}^{(2)}(u)$ the linearity means that if the input was $w_{in} = w_{in}^{(1)}(u) + w_{in}^{(2)}(u)$ then the output would be $w_{out} = w_{out}^{(1)}(u) + w_{out}^{(2)}(u)$. This linearity is an approximation for imaging systems, nevertheless the linear model is an important tool for understanding the behaviour of these systems.

In an imaging system an object point contributes to the response at many image points. The output for a linear system for an arbitrary object can then be written as a linear superposition of the outputs for the values of w_{in} for all values of u.

$$w_{out}(u) = \int_{-\infty}^{\infty} p(u;u')w_{in}(u')du' \tag{3.12}$$

Supposing that the input stimulus is the delta function $\delta(u-u_0)$ and the output for this input is $w_{out}^{\delta}(u)$ then

$$w_{out}^{\delta}(u) = \int_{-\infty}^{\infty} p(u;u')\delta(u-u_0)du' \tag{3.13}$$

becomes

$$w_{out}^{\delta}(u) = p(u;u_0) \tag{3.14}$$

The function $p(u;u_0)$ is thus the response of the system measured at point u when the stimulus is the unit impulse applied at point u_0. The output $p(u;u_0)$ is referred to as the impulse response of the system, or when the system is an imaging system it is known as the point spread function (PSF), and u becomes a two-dimensional position vector $\mathbf{r}$. For example for a simple camera where a planar object is imaged at unit magnification onto a planar film then $p(\mathbf{r};\mathbf{r}_0)$ is the light distribution at point **r** in the image plane resulting from a point source of light at point $\mathbf{r}_0$.

The system is said to be shift-invariant if the shape of the blurred image of a point is independent of the location of the point. A general input-output relation for a linear shift invariant imaging system can be written

$$w_{out}(u) = \int_{-\infty}^{\infty} p(u-u')w_{in}(u')du' \tag{3.15}$$

This is a convolution integral. If u is the two-dimensional position vector **r** we have

$$w_{out}(\mathbf{r}) = \int_{\infty} p(\mathbf{r}-\mathbf{r}')w_{in}(\mathbf{r}')d^2r' \tag{3.16}$$

$$= p(\mathbf{r}) ** w_{in}(\mathbf{r}) \tag{3.17}$$

where $p(\mathbf{r})$ is the shift-invariant PSF, and ** refers to two-dimensional convolution. In Cartesian coordinates this becomes

$$w_{out}(x,y) = \int_{-\infty}^{\infty} dx' \int_{-\infty}^{\infty} dy' p(x-x', y-y')w_{in}(x',y') \tag{3.18}$$

$$= p(x,y) ** w_{in}(x,y) \tag{3.19}$$

3.2.3.2. Modulation Transfer Function (System Transfer Function)

An arbitrary input to the system can be resolved into a linear superposition of complex exponential functions. If the input to the system is a complex exponential function $\exp(2\pi i\kappa u)$ where i is the square root of -1 it can be shown that

$$w^e_{out}(u) = const \cdot w^e_{in}(u) \tag{3.20}$$

The output of the system to a complex exponential input is simply the input multiplied by a constant factor. The constant is called the *transfer function* of the system. By defining a Fourier transform of $w_{in}(u)$ as

$$W_{in}(\kappa) = \int_{-\infty}^{\infty} \exp(-2\pi i \kappa u) w_{in}(u) du \tag{3.21}$$

The inverse Fourier transform is

$$w_{in}(u) = \int_{-\infty}^{\infty} \exp(2\pi i \kappa u) W_{in}(\kappa) d\kappa \tag{3.22}$$

The arbitrary input is then resolved into a linear superposition of complex exponential functions. For the arbitrary input each exponential term in the superposition will pass through the system independently. The output is a superposition of terms each with weighting factors $W_{in}(\kappa)$. This leads to

$$W_{out}(\kappa) = W_{in}(\kappa) P(\kappa) \tag{3.23}$$

where $W_{out}(\kappa)$ is the Fourier transform of the output, $P(\kappa)$ is the Fourier transform of the impulse response, and is known as the *system transfer function.* A particular Fourier component, one term in the superposition is transferred through the system unchanged in functional form but multiplied by the factor $P(\kappa)$. If the input modulation of the signal is defined as

$$M_{in} = \frac{w_{in}^{\max} - w_{in}^{\min}}{w_{in}^{\max} + w_{in}^{\min}} \tag{3.24}$$

The ratio of the input modulation to the output modulation is given by

$$M_{out}/M_{in} = \frac{|P(\kappa)|}{P(0)} \tag{3.25}$$

This ratio of the output modulation to the input modulation is called the *modulation transfer function*, the zero normalised modulus of the system transfer function.

3.2.3.3. *Line Spread Function*

The response of an imaging system to a point object is given by the PSF. The response of the system to a line object aligned along the *y*-axis, $w_{in}^{line}(x,y) = \delta(x)$, is the line spread function (LSF). This is usually easier to measure. The LSF is the line integral of the PSF

$$l(x) = w_{out}^{line}(x,y) = \int_{-\infty}^{\infty} p(x,y)dy \tag{3.26}$$

It can be shown that the Fourier transform of the LSF is the two-dimensional system transfer function $P(\xi,\eta)$ evaluated on the line $\eta = 0$, i.e. $P(\xi,0)$. Measurement of $l(x)$ at different orientations of the line can be used to determine $P(\xi,\eta)$ along a series of radial lines through the origin of the $\xi-\eta$ plane. If $P(\xi,\eta)$ is radially symmetric then a single measurement of the LSF is sufficient to characterise the system.

3.2.3.4. *Edge Spread Function*

The response to a step-edge object is known as the edge spread function (ESF). It can be shown that for an edge along the *y*-axis

$$w_{in}^{edge}(x,y) = \begin{cases} 1 & x > 0 \\ 0 & x < 0, \end{cases} \tag{3.27}$$

the output is

$$e(x) = w_{out}^{edge}(x,y) = \int_{-\infty}^{x} l(x')dx' \tag{3.28}$$

Hence the ESF is the indefinite integral of the LSF

$$l(x) = \frac{de(x)}{dx} \tag{3.29}$$

The ESF may in many cases be easier to measure than the LSF, and the LSF can be obtained by differentiating the ESF.

3.2.3.5. Sampling

When a continuous image distribution $f(x,y)$ such as a light distribution is incident on a camera the image is sampled, with values obtained at an array of points with coordinates (x_n, y_m) given by $x_n = n\Delta, y_m = m\Delta$, where n and m are positive integers from 0 to N. The finite size of the apertures of the camera detector matrix means that the sampled value at each point is an average over the area ε^2 of the aperture about the point.

$$a_{nm} = \frac{1}{\varepsilon^2} \int_{x_n-\varepsilon/2}^{x_n+\varepsilon/2} dx \int_{y_m-\varepsilon/2}^{y_m+\varepsilon/2} dy \cdot f(x,y) \tag{3.30}$$

The array of sampled values form a sampled function $f_s(x,y)$. To examine the effect of sampling separately from the effect of the sampling aperture size, we consider the sampled function in the limit as $\varepsilon \rightarrow 0$, referring to this function as $f_{s0}(x,y)$ and

$$f_{s0}(x,y) = f(x,y)\Delta^{-2}\mathrm{comb}(x/\Delta)\mathrm{comb}(y/\Delta) \tag{3.31}$$

where

$$\mathrm{comb}(x/\Delta) = \sum_{n=-\infty}^{\infty} \delta(x - n\Delta) \tag{3.32}$$

is an array of delta functions situated spaced at multiples of the sampling interval Δ. The Fourier transform of the sampled function is the convolution of the transform of $f(x,y)$ with the transform of the comb function. Since the Fourier transform of a comb function is also a comb function, this gives the transform of the sampled function as a superposition of replicas of the Fourier transform of the original function $F(\xi,\eta)$:

$$F_{s0}(\xi,\eta) = 1/\Delta^2 \sum_{n=-\infty}^{\infty} \sum_{m=-\infty}^{\infty} F(\xi - n/\Delta, \eta - m/\Delta) \tag{3.33}$$

If the original function is band-limited, the Fourier transform of the function is limited to a finite frequency range with maximum frequencies $\xi_{\max} = \eta_{\max}$. The replicas of $F(\xi,\eta)$ then do not overlap if the sampling interval satisfies

$$1/\Delta \geq 2\xi_{\max} \tag{3.34}$$

The sampling rate or frequency $1/\Delta$ must then be at least twice the maximum frequency of the function being sampled. This frequency is referred to as the *Nyquist* frequency. A single replica of $F(\xi,\eta)$ can then be isolated by a low-pass filtering operation and the original function $f(x,y)$ retrieved by inverse Fourier transforming. If the sampling frequency is less than the Nyquist then the replicas of $F(\xi,\eta)$ overlap and exact reconstruction of $f(x,y)$ is not possible. The reconstruction contains artifacts known as aliasing.

The above discussion isolated the effect of the sampling from the effect of the sampling aperture by considering the limit as $\varepsilon \to 0$. The sampling aperture results in a convolution of $f(x,y)$ with the aperture function. For a rectangular aperture the result is

$$\bar{f}(x,y) \equiv f(x,y) ** \left[\varepsilon^{-2} rect(x/\varepsilon) rect(y/\varepsilon)\right] \tag{3.35}$$

and the sampled values are

$$a_{nm} = \bar{f}(x_n, y_m) \tag{3.36}$$

Provided $f(x,y)$ is band-limited then $\bar{f}(x,y\ )$ must be band-limited and $\bar{f}(x,y\ )$ can be reconstructed if sampling is performed at the Nyquist frequency or greater. In the frequency domain the effect of the aperture is a multiplication by the transform of the aperture

$$\bar{F}(\xi,\eta) = F(\xi,\eta)\text{sinc}(\xi\varepsilon)\text{sinc}(\eta\varepsilon) \tag{3.37}$$

3.2.4. Linear systems model for Spatial Resolution

3.2.4.1. Effect of source on resolution

The general model for image formation presented in Section 3.2.1 assumed a parallel beam of photons. In practice the photons are emitted from a source and hence are diverging through the patient. The source size also influences the spatial resolution of the image. The effect of source size on image formation is discussed here using the linear systems formalism of Barrett and Swindell (1981). The radiographic system is simplified to a source plane $\mathbf{r} = r(x,y)$ that contains the source function $f(\mathbf{r})$, an object plane $\mathbf{r}' = r'(x',y')$ containing the object transmission function $g(\mathbf{r}')$, and the image plane $\mathbf{r}'' = r''(x'',y'')$ where the x-ray photon density $h(\mathbf{r}'')$ is described at a distance (Figure 3-8). The distance from the source plane to the object plane is s_1 and the distance from the object plane to the image plane is s_2. The source $f(\mathbf{r})$ represents the number of photons emitted per unit area of the source per steradian (toward the object). The following expression for image formation can then be derived (Barrett and Swindell, 1981)

$$h(\mathbf{r}'') \approx C \int_{source} d^2r\, f(\mathbf{r})g(\mathbf{r}') \tag{3.38}$$

where

$$C = 1/(s_1 + s_2)^2 \tag{3.39}$$

This is illustrated in Figure 3-8. For an image point at $\mathbf{r}''$ the photon intensity is formed from the contribution of all source points along ray paths through the object with each source point contribution weighted by the transmission of the object along the path.

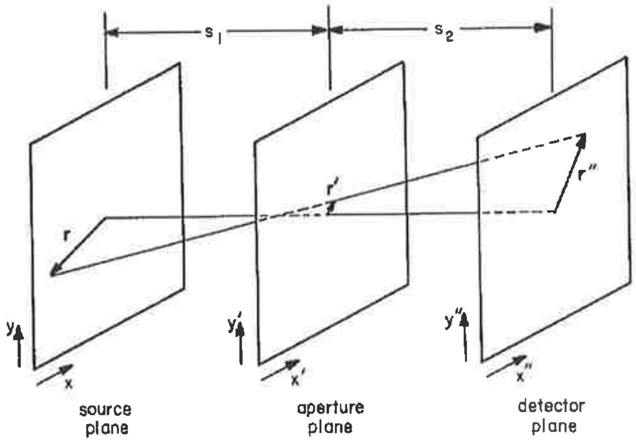

Figure 3-8 Geometry of the model for the formation of the radiographic image, from Barrett and Swindell (1981).

Recognising that the vector $\mathbf{r}'$ can be expressed in terms of $\mathbf{r}$ and $\mathbf{r}''$ gives

$$h(\mathbf{r}'') \approx C \int_{source} d^2r\, f(\mathbf{r}) g(a\mathbf{r}'' + b\mathbf{r}) \tag{3.40}$$

where

$$a = s_1/(s_1 + s_2) \tag{3.41}$$

$$b = s_2/(s_1 + s_2) = 1 - a \tag{3.42}$$

By expressing the equation in terms of the variable $\mathbf{r}_0'' = -b\mathbf{r}/a$, with source and object functions scaled to the image plane

$$\tilde{\tilde{f}}(\mathbf{r}_0'') = f(\mathbf{r}) = f(-a\mathbf{r}_0''/b) \tag{3.43}$$

and

$$\tilde{\tilde{g}}(\mathbf{r}_0'') = g(a\mathbf{r}_0''), \tag{3.44}$$

we then have

$$g(a\mathbf{r}'' + b\mathbf{r}) = g(a\mathbf{r}'' - a\mathbf{r}_0'') = \tilde{g}(\mathbf{r}'' - \mathbf{r}_0'') \tag{3.45}$$

The scaled function $\tilde{f}(\mathbf{r}'')$ is the original source function projected through a point in the object plane to the source plane (pinhole magnification of the source). The function $\tilde{g}(\mathbf{r}'')$ may be considered as the original object function projected from a point in the source plane to the image plane (object magnification). These magnifications can also be expressed in terms of a magnification factor $M = 1/a$, the source is pinhole magnified $(-1/M - 1)\mathbf{r}''$, and the object is magnified $\mathbf{r}''/M$. The image formation can then be written

$$h(\mathbf{r}'') \approx \left(\frac{a}{b}\right)^2 C \int_{\infty} d^2 r_0'' \tilde{\tilde{f}}(\mathbf{r}_0'') \tilde{\tilde{g}}(\mathbf{r}'' - \mathbf{r}_0'') \tag{3.46}$$

$$= (a/b)^2 C\tilde{\tilde{f}}(\mathbf{r}'') ** \tilde{\tilde{g}}(\mathbf{r}'') \tag{3.47}$$

which is a convolution of the source function and the object transmission functions projected to the image plane. This leads to the frequency-domain description by Fourier transformation of the above equation

$$H(\boldsymbol{\rho}'') = (a/b)^2 C\tilde{\tilde{F}}(\boldsymbol{\rho}'')\tilde{\tilde{G}}(\boldsymbol{\rho}'') \tag{3.48}$$

where $\boldsymbol{\rho}''$ is the spatial frequency vector conjugate to $\mathbf{r}''$ in the image plane, and F and G are the Fourier transforms of f and g respectively.

3.2.4.2. Effect of Detector on resolution

The incident x-ray intensity distribution is convolved with the point spread function (PSF) of the detector, $d(\mathbf{r}'')$. This is the response of the detector to a point image, including the blurring introduced by the finite size of the sampling aperture. The detector output is then given by

$$q(\mathbf{r}'') = \eta_x \mathbf{R}_1 h(\mathbf{r}'') ** d(\mathbf{r}'') \tag{3.49}$$

where η_x is the probability of x-ray interactions within the detector and $\mathbf{R}_{\text{I}}$ is a factor describing the conversion of incident photon energy into image signal. The sampling of a digital detector results in an image data set $q(n_x, n_y)$ of N_x, N_y pixels. The sampling of the distribution $q(\mathbf{r}'')$ by the discrete sampling array gives

$$q(n_x, n_y) = q(\mathbf{r}'')\delta(x'' - s''_x n_x, y'' - s''_y n_y) \tag{3.50}$$

where the samples are made on a rectangular grid with intervals of s''_x and s''_y. If the Fourier transform of $d(\mathbf{r}'')$ is $D(\boldsymbol{\rho}'')$ then ignoring the periodicity due to the sampling, the Fourier transform of the detector output is

$$Q(\boldsymbol{\rho}'') = (a/b)^2 C\tilde{\tilde{F}}(\boldsymbol{\rho}'')\tilde{\tilde{G}}(\boldsymbol{\rho}'')D(\boldsymbol{\rho}'') \tag{3.51}$$

The resolution is of interest in the plane of the object, therefore the result is rescaled to the $\mathbf{r}'$ plane.

$$\tilde{q}(\mathbf{r}') = \eta\mathbf{R}_{\text{I}}\left\lfloor C/(ab)^2 \right\rfloor\tilde{f}(\mathbf{r}') ** g(\mathbf{r}') ** \tilde{d}(\mathbf{r}') \tag{3.52}$$

where

$$\tilde{q}(\mathbf{r}') = \tilde{\tilde{q}}(\mathbf{r}''/a) \tag{3.53}$$

$$\tilde{f}(\mathbf{r}') = \tilde{\tilde{f}}(\mathbf{r}''/a) \tag{3.54}$$

$$\tilde{d}(\mathbf{r}') = \tilde{\tilde{d}}(\mathbf{r}''/a) \tag{3.55}$$

The total transfer function $TF(\boldsymbol{\rho}')$ of the imaging system is given by setting $g(\mathbf{r}') = \delta(\mathbf{r}')$. This gives

$$TF(\boldsymbol{\rho}') = \tilde{F}(\boldsymbol{\rho}')\tilde{D}(\boldsymbol{\rho}') \tag{3.56}$$

and the modulation transfer function is obtained by normalising this to the value at zero spatial frequency.

Increasing the magnification increases the effect of the source however it decreases the blurring due to the detector. There will exist an optimal magnification for a digital system which maximises the resolution of the imaging system. This has been found to be 70-100 cm below the patient for an electronic portal imaging device. (Bissonnette *et al.*, 1994). For film which has a narrow detector response, the optimal magnification is just below the patient to minimise the reduction in resolution due to the source.

3.2.4.3. *Effect of scatter on resolution*

Scattered radiation reaching the detector contributes little useful information and reduces contrast and increases quantum noise. The overall PSF $p_{tot}(\mathbf{r})$ of the radiation incident on the detector can be expressed as the sum of the PSF of the primary radiation $p_{pri}(\mathbf{r})$ and the scattered radiation $p_{scat}(\mathbf{r})$, (Barrett and Swindell, 1981). The primary PSF represents the point image formed by photons that have not undergone any interactions in the patient's body or the collimation system of the detector. The scatter PSF consists of photons that have undergone one or more scattering events.

$$p_{tot}(\mathbf{r}) = p_{pri}(\mathbf{r}) + p_{scat}(\mathbf{r}) \tag{3.57}$$

The scatter PSF is generally a broad slowly varying function. Modulation transfer functions are shown in for a model in which both the scatter PSF and primary PSF are Gaussian functions. The effect of the scatter is to reduce the contrast at low and intermediate spatial frequencies.

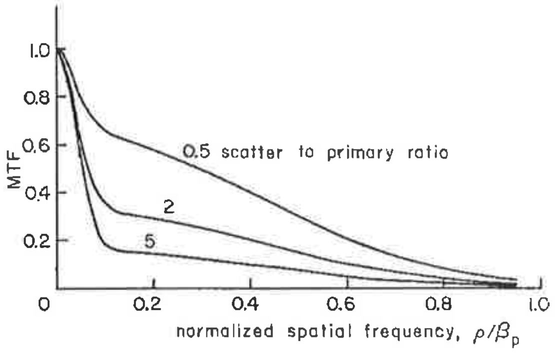

Figure 3-9 Modulation transfer functions incorporating the effect of increasing scatter (from Barrett and Swindell, 1981)

3.3. Megavoltage Image Detectors

Megavoltage images have traditionally been acquired with radiographic film/screen combinations designed specifically for portal imaging. More recently, electronic portal imaging devices have been developed to acquire the megavoltage images. These include scanning linear arrays of diodes (Taborsky *et al.*, 1982) and scintillating crystals (Morton *et al.*, 1991), video-camera based systems (Baily *et al.*, 1980; Leong, 1986; Shalev *et al.*, 1989; Visser *et al.*, 1990; Munro *et al.*, 1990; Wong *et al.*, 1990), matrix ion-chamber systems (Meertens *et al.*, 1985), and flat-panel arrays (Antonuk *et al.*, 1990; Zhao and Rowlands, 1992).

3.3.1. Film/Screen

3.3.1.1. Construction and image formation

The majority of images of radiotherapy treatments are still acquired with film/cassette combinations. These have consisted of a metal plate and film contained within a cassette. Transmitted photons interact in the metal plate producing electrons which expose the film. The cassette ensures good film/screen contact to maximise resolution. The film emulsion consists of silver halide crystals in a gelatin matrix. The emulsion is usually coated on both sides of a film base to improve efficiency. The base is composed of polyester or cellulose acetate (Figure 3-10). The incident radiation neutralises mobile silver ions in the halide grains, forming a latent image. When the film is developed the sensitised grains are converted to metallic silver, and the unsensitised grains removed.

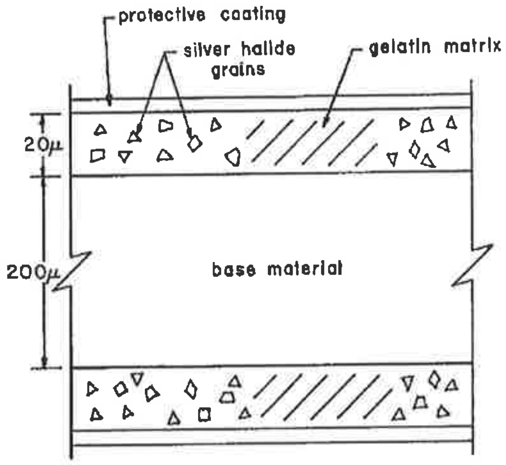

Figure 3-10 Cross-section of radiographic film (from Barrett and Swindell, 1981).

Increasing film contrast has been achieved by the use of a fluorescent screen and light sensitive film, to improve the SNR (Sephton *et al.,* 1989). Although widely used in diagnostic radiology, fluorescent screen and film combinations have only recently been used at megavoltage energies. Sephton *et al.* (1989) developed a metal plate/fluorescent screen combined with a light-sensitive film and demonstrated improved contrast over existing systems. This technique has been implemented in a commercial system with a 1 mm copper front screen used with front and rear gandolinium oxysulphide fluorescent screens (Haus *et al.*, 1997).

The improved contrast of fluorescent screen detectors is due to several factors. Several light event exposures are required to form a latent image in the film. Further exposure results in greater increases in density to produce higher contrast. In the direct electron exposure case the energy deposited by one exposure event is sufficiently high to make one or more grains developable. The film used with the fluorescent screen has a more uniform grain size. Because sensitivity to light is proportional to grain size, a narrow distribution of grain sizes will be exposed with a narrower range of exposure. This will increase contrast relative to film that has a wider grain size distribution. Incorporation of metal ion doping further increases contrast by narrowing the distribution of light sensitivities.

3.3.1.2. Characteristic (H-D) Curve

The opacity that results from irradiation and development of the film then has a transmittance to light

$$T = I/I_0 = \exp(-D) \tag{3.58}$$

where I is the irradiance transmitted by the film for incident irradiance I_0. The optical density (D) of the film is

$$D = -\log(T) \tag{3.59}$$

The characteristic curve or H-D curve of the film gives the response or OD of the film to incident differences in the x-ray quanta (subject contrast).

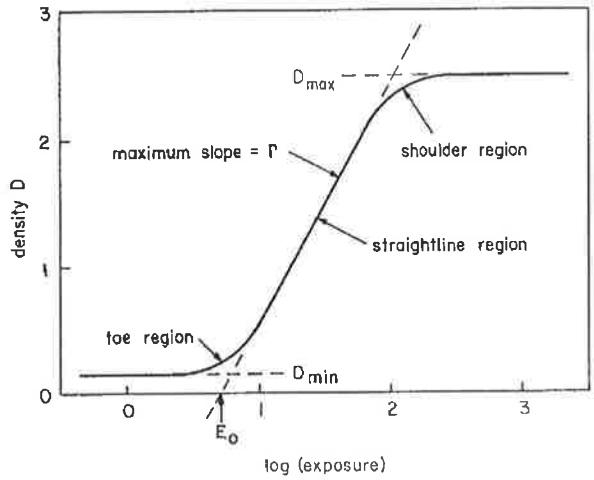

Figure 3-11 Idealised film characteristic curve for a typical film emulsion.

3.3.1.3. Resolution

The resolution of the film/screen is due to lateral spread of the electrons or light photons in the metal screen. The screen reduces resolution as the electrons can scatter more laterally however if it is not thick enough, obliquely scattered electrons from the patient will not be absorbed and degrade image quality. Hence high density plates are required and copper of about 1 mm thickness is usually employed for megavoltage screens. Rear metal screens are sometimes used to backscatter electrons onto the film. This reduces the dose required to form an image (increases the *speed* of the system). This backscattering backward and forward between the front and rear plates results in a loss of resolution, although this is not significant when double-emulsion films are used. The rear screen significantly increases the weight of the cassette so more commonly a low Z rear screen is used which minimises backscatter.

The resolution of a metal screen/film combination can be quantified by the modulation transfer function. Munro *et al.* (1987a) measured the MTF of metal plate/film combinations. Tungsten blocks were used to form a 25 μm slit. They found that the LSFs and MTFs were dominated by electron spread in the detectors. The MTF(*f*) declined (i.e. less passing of spatial frequencies) with 1) energy of the beam; 2) decreased density of plate; 3) fluorescent screen interposed between metal plate and film; 4) increasing thickness of the fluorescent screens; and, 5) if a rear metal plate is used. The first effect can be explained by the electrons having greater energy and hence travelling further to give greater electron spread. Similarly for 2) for the same thickness an increased density will lower the range of the electrons.

Scattered photons in the metal plate contribute mainly to the broad low magnitude tails in the LSFs. This causes a drop in the MTF at low spatial frequencies. The MTFs results were consistent with high spatial resolution, greater than a diagnostic energy MTF values at high spatial frequencies. Therefore the lack of resolution in megavoltage imaging is not due to the film/screen system but other factors.

3.3.1.4. Noise

There are several sources of noise in a film/screen detector. These are

1. Statistical fluctuations in the number of incident photons (quantum noise)
2. Fluctuations in the energy absorbed per interacting photon
3. Spatial fluctuations in the screen absorption associated with inhomogeneities in the phosphor coating (structure mottle), and in the number of light fluorescent photons emitted per unit energy absorbed. This applies to fluorescent screen systems.
4. Fluctuations in the number of silver halide grains per unit area of the film emulsion (film granularity).

Film granularity has been found to be 50-90% of the total noise with the remainder x-ray quantum noise (Munro *et al.* 1987b). The NPS(*f*) is dominated by the film noise (mottle due to film granularity), not by the quantum noise (Munro *et al.*; 1987a). Thus the possibility to improve the SNR(f) of megavoltage images comes from reducing the noise contribution from the detectors rather than improving the signal transfer (MTF) of the detectors.

3.3.2. Video-camera based detectors

Video-camera electronic portal imaging devices (VEPIDs) consist of a metal plate with the underside coated with a fluorescent phosphor screen to produce visible photons. A 45 degree mirror deflects some of the light onto a video-camera. The major potential advantage of VEPIDs is that the detector subtends the entire area of the irradiated screen. Images can also be acquired rapidly, at up to 30 frames per second. However a major limitation to the design is that only a very small fraction of the light is captured by the lens (0.01-0.1%) and focussed onto the camera (Munro *et al.*; 1990). The light is highly scattered in the phosphor and so emerges at all directions with equal probability. This poor light collection efficiency means that the noise generated in the camera may be large compared to the small signal measured. Therefore the development of these devices has concentrated on improving light collection efficiency by increasing the output of the phosphor, increasing the aperture of the lens and increasing the detection efficiency of the camera. The noise in the camera has also been minimised by using CCD cameras and cooling the camera electronics. When cooled the CCD cameras are extremely low noise devices.

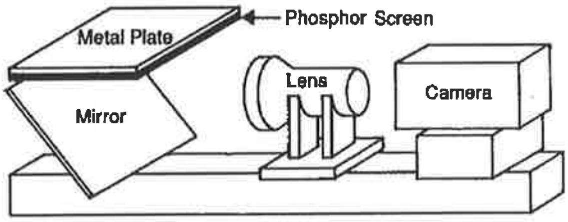

Figure 3-12 Components of a video-camera based EPID (from Boyer *et al.*, 1990).

3.3.2.1. Screen/Phosphor

Munro *et al.* (1990) examined the performance of a video-camera based portal imaging system. They measured the overall MTF of the fluoroscopic imaging system and the MTF of the metal plate/phosphor was measured using film. Thus the contribution to the reduction in spatial resolution from the optical chain/camera/frame-grabber could be deduced. Five thicknesses of phosphor from 50 to 400 mg/cm^2 were tested and the MTFs were found to decline with increasing phosphor thickness. The MTFs for the system as a whole were significantly lower than for the detector alone. They were also dependent on the orientation of the slit to the raster scan direction, and were lower when parallel to the scan.

For the NPS they compared illuminating the video camera using an incandescent source in place of the phosphor (camera noise only), with illuminating the camera with light from x-rays impinging on the detector (quantum noise). They were found to give identical NPS hence other noise is dominant. They suggest that this is not due to the camera but to light quanta noise due to the poor optical efficiency of the optical chain. Therefore increasing the light collection efficiency by phosphor thickness, lens aperture increase, larger camera, light amplification could result in a six-fold increase in light detected per x-ray quanta.

Wowk and Shalev (1993) developed a grooved phosphor screen to improve the light output from the screen. This improves the low spatial frequency DQE at the expense of high frequency resolution. The low frequency is of more interest in portal imaging. Light photons in the phosphor have approximately 1 mm (500 mg/cm^2 phosphor) scatter path lengths (for a 10 μm scatter length) before absorption. Thus increasing the phosphor thickness beyond this will not improve light output as the photons from deeper layers are absorbed. To allow photons from deeper layers to escape implies the idea of grooves or pyramidial holes where the photons can escape by internal reflection. This also results in highly forward directed light output. With grooves where no point is more than half a millimetre from a groove most of the light will escape to a groove. Pyramidial screens do not suffer from reduced spatial resolution in the direction of the grooves. Forward light output was found to be almost ten times that of flat phosphor screens. The resultant image depends on the position of the groove pattern relative to the object being imaged.

Wowk *et al.* (1994) varied the thickness of the phosphor layer and also the metal plate to examine the dependence of light output and resolution on phosphor thickness and metal plate thickness. Phosphor thicknesses from 100 to 1000 mg/cm^2 were placed on brass plates from 1 to 5 mm thick. Light output was measured with a light spotometer, and modulation transfer functions were measured with a high magnification video technique.

Light output was found to increase approximately linearly with phosphor thickness up to 500 mg/cm^2, reaching a plateau at 1000 mg/cm^2. Spatial resolution decreased exponentially with phosphor thickness up to 750 mg/cm^2, where a minimum was reached. From the results, and assuming that most of the noise is generated by light photon statistics, an expression for the DQE(*f*) as a function of phosphor thickness was developed. It was found that a 1000 mg/cm^2 thick phosphor was optimal for spatial frequencies below 0.15 mm^{-1}. The optimal thickness decreases for higher spatial frequencies. The metal plate thickness was found to have a smaller effect on system performance, with 2 mm brass optimal for a dual energy linear accelerator. Bissonnette *et al.* (1997) calculated the optimal phosphor thickness by determining the DQE(*f*) of a video-camera based system and using this to determine indices of displayed and perceived image quality for two types of object: a pelvis object and a point-like object. Eight phosphor thicknesses from 67 to 947 mg/cm^2 were tested. The maximal indices of image quality were obtained for screen thicknesses between 358 and 947 mg/cm^2. The results showed that the optimal thickness depended on the imaging task, with the higher indices for pelvic structures obtained with thicker screens than for a point object. This is because the information is concentrated at lower spatial frequencies where degradation with thicker screens is modest. However, overall there were only modest improvements in quality for phosphor screens thicker than 350-400 mg/cm^2.

However there are problems with these increasing phosphor or plate thickness. As well as the degradation in spatial resolution with phosphor thickness, thicker phosphor screens currently introduce blemishes into the image. These could be corrected for, but the imaging systems suffer from slop as the gantry rotates meaning the camera is not always focussed onto the same area of the phosphor making corrections for fixed spatial artifacts difficult.

Bissonnette and Munro (1996) evaluated a 12 mm thick glass scintillator detector for portal imaging. The high density glass was doped (3%) with phosphor (Gd_2O_2S:Tb) and was transparent to the light emitted from the x-ray interactions. They compared it to the light output from a standard 1 mm copper (Cu) plate with 1 mm phosphor layer detector. At the exit face the light output from the glass was 82% of the Cu plate. At the video camera the output was half that of the Cu due to the refraction of the light at the glass/air interface. The spatial resolution of the two were similar however the resolution of the glass was not independent of the incident photon angle like the copper. Due to the limited light output and variable spatial resolution they concluded that the glass scintillator was not suitable for portal imaging.

3.3.2.2. *Optical chain*

The optical chain (mirror/lens) has poor efficiency. The efficiency of the lens can be expressed (Boyer *et al.*, 1992)

$$\varepsilon_{lens} = k\left\lfloor \tau M^2/(1+M)^2 f^2 \right\rfloor \tag{3.60}$$

where τ is the lens transmission factor (generally $\tau \approx 0.9$); M is the lens magnification factor, defined as the size of the virtual image on the video-camera divided by the size of the image on the x-ray detector ($M \leq 1$); k is the factor equal to 1/16 assuming that the light emitted from a point on the phosphor is emitted isotropically into 4π steradians; and f is the *f*-number (focal length/diameter of the lens). The efficiency increases as the inverse square of the *f*-number. Increasing the size of the camera or light sensor will increase M, improve the efficiency of the optical system and hence improve the DQE.

Large aperture lenses would increase light collection efficiency, however these suffer from spherical aberrations (light rays incident at the edge of the lens do not focus to the same point as those incident at the centre of the lens). Large aperture lenses also suffer from vignetting which results in images that are brighter at the centre of the lens. They also cause barrel distortion which causes straight lines to appear as curves. This is undesirable for portal imaging where the image may yield a geometrically inaccurate patient position.

3.3.2.3. *Cameras*

The use of CCD-based cameras has been found to result in improvement in image quality, particularly when the cameras are cooled to reduce electronic noise in the camera (Jaffray *et al.*, 1996). To determine the physical quantities governing image quality Althof *et al.* (1996) developed a model describing the signal and noise propagation through a CCD camera based fluoroscopic EPID. They developed equations to describe the electron fluence produced by the CCD chips and the subsequent gray level starting from a dose absorbed at d_{max} in a water phantom at isocentre. Similarly a description of the various components of noise was developed, quantum noise, dark current noise, read-out noise, and analog-digital conversion noise. From the signal to noise calculation and a threshold of signal 5 times the noise, the dose required to view a particular contrast object can be found. They validated their model by comparison with images taken of a contrast phantom. They found 4 MU images sufficient to view 4-10 mm water equivalent thickness (1-2 cm large diameter bony structures). They found that camera read-out noise is the largest contributor to noise. They calculated for a cooled 512×512 pixel CCD camera with negligible read-out noise and high quantum efficiency that the imager would be quantum noise limited (low spatial resolution) at clinical imaging doses of 1-4 MU. Cameras with 2048×2048 pixels are now available which should improve spatial resolution.

Another disadvantage of the video-camera based systems is their bulkiness due to the housing for the mirror. This can hamper patient setup, however the design can enable the detector assembly to be retracted. Fibre-optical systems have been developed to couple the camera to the phosphor (Wong *et al.,* 1990), however, these have not been developed commercially.

3.3.3. Matrix-ion chamber device

This commercially available EPID was first developed by Meertens *et al.* (1985) and van Herk and Meertens (1988). The EPID consists of a detector unit with a 256 × 256 array of ionisation chambers, and switching electronics, connected to a control unit. The detector consists of two sets of 256 strip electrodes perpendicular to each other. The electrodes lie on the inner surfaces of two printed circuit boards, separated by a 0.8 mm gap filled with iso-octane. One set of electrodes is connected to a high-voltage supply, and the other connected to sensitive electrometers. At the cross-point of the electodes a small ionisation chamber is formed. There is a 1 mm steel buildup plate in front of the upper board. The liquid is ionised when irradiated. To read out the image, the high-voltage (HV) is switched to each of the high-voltage electrodes in turn and the resulting currents in the 256 signal electrodes measured. Thus the image is scanned one row at a time. As the A/D conversion time is ~ 4 μs, a single row can be read-out in 1 ms. The active area of the matrix is 32.5 × 32.5 cm. The outputs of the electrometers are multiplexed to a single amplifier and digitized in the control unit.

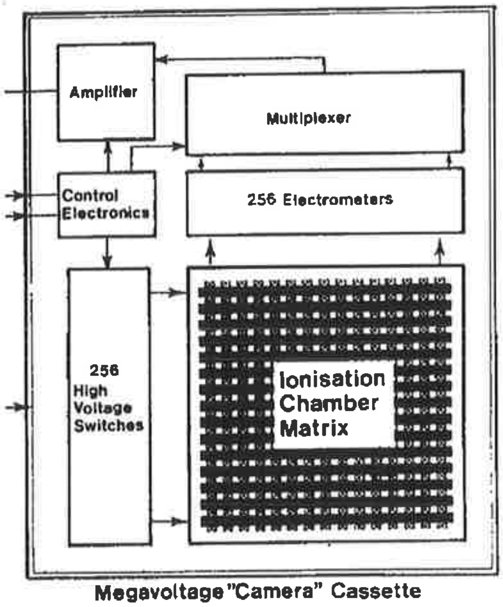

Figure 3-13 Matrix ion chamber EPID (from Boyer *et al.;*1992b)

When the HV is switched to a row, a transient pulse is induced in the electrometers. Thus each row cycle consists of a wait-time for this pulse followed by readout of the 256 electrometers. The HV in the latest model of this detector is 500 V (van Herk *et al.*, 1995). The HV cycle time, based on two cycles of the linear accelerator 360 Hz timing pulse is 5.6 ms, comprising a wait time of 3 ms the remainder signal readout time. Total frame acquisition time is therefore ~ 1.4 s. Signal readout is synchronised with the pulse timing of the accelerator to obtain smooth images without artifacts due to radiation pulse variation. Several frames can be averaged depending on the time available to image, and the dose delivered.

The signal measured by the ion-chambers depends on the rate of formation and rate of recombination of the ion-pairs formed in the liquid layer (van Herk; 1991).

$$\frac{dn(t)}{dt} = N_{in}(t) - \alpha n(t)^2 \tag{3.61}$$

where $n(t)$ is the ion-pair concentration, $N_{in}(t)$ is the formation rate of the ions or ionisation rate, and $\alpha n(t)^2$ is the recombination rate, or loss of ions due to volume recombination. When irradiated, the number of ions formed increases until an equilibrium is reached between ion-pair formation and ion-pair recombination. This equilibrium occurs after ~ 0.5

s of irradiation and forms a latent image in the ion-chamber matrix. Irradiating for longer periods does not increase the size of the signal. The signal measured does not depend greatly on the dose-rate when the HV is applied. At equilibrium the change in the number of ions with time is zero, therefore from

$$N_{in.eq}(t) = \alpha n_{eq}(t)^2 \tag{3.62}$$

and

$$n_{eq}(t) = \sqrt{N_{in,eq}(t) / \alpha} \tag{3.63}$$

The collected charge or signal is proportional to the number of ion-pairs $n(t)$. The number of ions formed $N_{in}(t)$ is proportional to the ionisation rate or dose rate, therefore from Equation 3.63 the signal is proportional to the square-root of the dose-rate.

The major drawback to the scanning design is the quantum utilisation, as only one row of the image is recorded at a time. However, the fact that the signal is due to the integrated charge in the chamber over a 0.5 s period and not due to the amount of charge generated during the time the HV is switched to the row, improves the quantum utilisation of the matrix. The scanning also means the device can not be used to image dynamically changing beam intensity or field size.

Due to varying sensitivity of the ion-chambers, and offsets of the electrometers, regular calibration of the cassette is required. Images (b_{ij}) without radiation are taken to determine the offsets for the chambers (dark-field), and images (f_{ij}) with a flat irradiation (flood-field) acquired for the chamber sensitivities. The corrected image is therefore

$$p_{ij} = \left(p_{ij}^{*} - b_{ij}\right) / \left(f_{ij} - b_{ij}\right) \tag{3.64}$$

where $p*_{ij}$ is the raw uncorrected image. The variation in chamber sensitivities are due to electrode shape differences, electrode surface inhomogeneities, and local thickness of the liquid layer.

A major advantage of this EPID design over the video-based EPIDs is that it is compact. Other advantages are that the images are spatially correct, having no geometric distortions. The EPID detector has no moving parts, reducing the likelihood of mechanical problems. However the cassette contains a large amount of electronics just peripheral to the ionisation chamber matrix, and these are susceptible to radiation damage, either from direct or scattered radiation. This means the cassettes have a limited lifetime.

3.3.4. Scanning linear arrays

Taborsky *et al.,* (1982) have developed a linear array of 255 diodes with a centre-to-centre spacing of 2 mm that scan the image in 2 mm increments using a stepping motor. A 1.1 mm thick lead plate covers the diode array. As the array only covers a small portion of the field the doses required to form an image are large. Spatial resolution was also poor due to the large diode spacing. Morton *et al.,* (1991) produced a linear array of scintillating crystals ($ZnWO_4$), each 5×5×25 mm in size. The crystals are arranged in a double row, 64 crystals per row with each row offset by half the crystal width to reduce the sampling interval. The x-rays interact in the crystal producing visible photons that are detected by photodiodes. As the crystals are optically transparent they can be long (25 mm) and hence the detection efficiency for the x-ray photons is very high at ~50% for 6 MV. The spatial resolution is however low. These type of scanning portal imaging devices are not currently available commercially.

3.3.5. Flat-panel devices

There are two main types of flat-panel solid state imaging devices currently under development for megavoltage imaging. These are amorphous silicon photodiode arrays (Antonuk *et al.,* 1992), and amorphous selenium photoconductor arrays (Zhao and Rowlands, 1992).

3.3.5.1. Amorphous Silicon

These detectors comprise a two-dimensional (2D) integrated circuit matrix of photodiodes and thin-film transistors (TFTs) The circuits are composed of amorphous silicon which is extremely resistant to radiation damage (Antonuk *et al.*, 1990). They act in the same manner as a large area video camera, collecting the emitted light from a phosphor layer, but can be placed in direct contact with the metal plate and phosphor, being only ~ 1 mm thick. The photodiode detects the light and the TFTs control the readout of the signal. The light discharges the diode which has a bias voltage applied. During readout the TFT is made conducting by applying a voltage. The current then flows from the photodiode to an external amplifier. By activating the TFTs one row at a time, with the TFTs in one column connected to a common external amplifier, the signal can be read out one row at a time, until the entire array is recorded, at 10-50 frames per second. About 30% of the visible photons are detected and therefore this overcomes the light collection efficiency problems of the video-camera as well as the bulkiness. The spatial resolution of the array has been found to be determined by the finite pixel size (Yorkston *et al.*, 1994; Munro and Bouius, 1998) with no spreading of the light within the sensor itself, the spread of light is produced by the metal plate/phosphor combination. Munro and Bouius (1998) studied a 96×96 mm area array with pixel size 0.75×0.75 mm, and determined that the array was x-ray quantum noise limited, and that the x-ray noise power is up to 100 times greater than the noise power added by the electronics of the array. They found that the response of the array was linear with dose rate. Disadvantages of the array were variations in dark-current of the pixels, and non-uniform sensitivity. These effects are believed to be due to migration of oxygen or water through the silicon material. This problem should be solved by large-scale manufacturing processes. The arrays also suffer from two problems shared by the matrix ion-chamber device. The readout electronics adjacent to the matrix need to be radiation insensitive, and the readout must be synchronised with the radiation pulsing as the time to readout a frame is much larger than the interval between radiation pulses (~ 3 ms). This means that pulses during the readout would cause artifacts on the images.

3.3.5.2. *Amorphous selenium*

These consist of a layer of amorphous selenium deposited onto a copper or aluminium plate. The metal acts as an electrode and a transparent electrode (indium tin oxide) is deposited on the other side. Before irradiation the selenium layer is charged to create a uniform 10^7 V/m field across the layer. Upon irradiation x-rays interact in the metal plate and the selenium to create electron/hole pairs which migrate under the action of the field. This partially discharges the E field to create a voltage pattern on the readout electrode which is proportional to the incident x-ray fluence. This pattern is stable for a long time period. Currently the image is read out by using a scanning line of electrostatic probes or a scanning laser beam. This readout is slow and involves bulky equipment. Active matrix readout is being developed using a 2D matrix of thin film transistors (Zhao and Rowlands, 1993). These are however constructed from cadmium selenide which is vunerable to radiation damage. The spatial resolution of the selenium flat-panel is extremely high (Que and Rowlands, 1995), and is mainly due to lateral spread of high-energy electrons and beam divergence. The x-ray quantum efficiency of the selenium is expected to be lower than that of the silicon with the current thicknesses of the selenium layers.

3.3.6. Lower energy imaging devices

To overcome the limited contrast of objects at megavoltage energies, and reduce the dose required for open-field exposures, an alternative is to employ a lower x-ray energy for the localisation imaging of the patient. Biggs *et al.* (1985) mounted a kV x-ray tube on the gantry of the linear accelerator, offset from the radiation beam. By rotating the gantry so that the kV tube was in the beam direction, a diagnostic energy image of the patient could be acquired. Similar techniques have been reported (Sephton and Hagekyriakou, 1995) where the kV imager was on a mobile cart. These techniques produce high quality images that can be used to verify patient setup although the images do not directly verify the placement of the beam portal. To overcome this problem Jaffray *et al.* (1995) placed the kV imager at 45 degrees to the central axis but with the same isocentre. Images were acquired by rotating the gantry and imaging along the beam line, then rotating the gantry back and delivering the treatment. During treatment a megavoltage image was acquired with the same detector. The advantage of this is that both images have the same coordinate system and do not have to be registered. However the imaging detector is not fixed to the accelerator and thus only anterior-posterior images were possible. More recently (Jaffray *et al.*, 1999) placed a kV imaging system at 90 degrees to the central axis on an accelerator along with a megavoltage imaging system. The kV system was also capable of cone-beam tomography to visualise soft-tissue structures. Galbraith (1989) proposed, for imaging of the beam that the normal x-ray producing target in the accelerator be replaced with a low atomic number target to produce a greater number of low energy photons and hence increase the contrast.

3.4. Image Processing

Image processing to improve image quality is important for megavoltage imaging where the subject contrast is low, and the spatial resolution of electronic devices may be poor. This section describes general image processing, and processing techniques commonly applied to portal images.

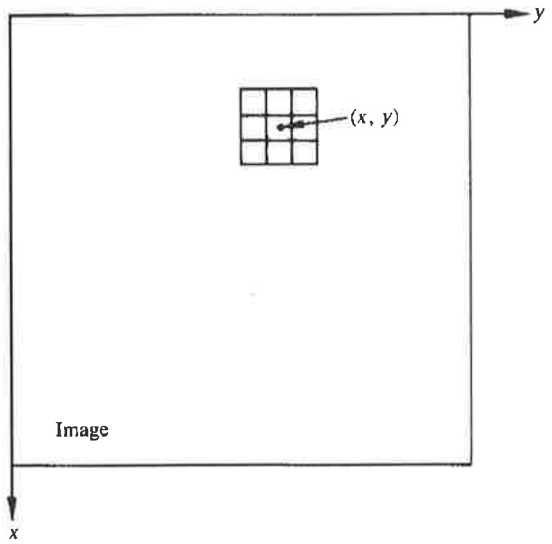

Figure 3-14 A 3 × 3 neighbourhood about a point (*x*,*y*) in an image.

Image processing techniques are generally divided into spatial domain and frequency domain methods. Spatial domain methods operate directly on the pixel values of the image. The spatial domain function can be expressed as (Gonzalez and Woods, 1992)

$$g(x,y) = T[f(x,y)] \tag{3.65}$$

where $f(x,y)$ is the input image, $g(x,y)$ is the processed image, and T is an operator on f. The approach is to use a square or rectangular neighbourhood or sub-image about (*x*,*y*) (Figure 3-14). The operator is defined over the sub-image. The sub-image region is moved from pixel to pixel and the processed pixel value determined by the pixel values in the sub-image and the transformation. When the neighbourhood is 1 × 1, *g* depends only on the value of *f* at (*x*,*y*) and is called a gray-level transformation. Frequency domain methods operate on the Fourier transform of the image. In the linear systems model of image formation, the convolution of the incident image intensity distribution with the detector

PSF is equivalent to multiplication of the incident image transform by the detector transform. Therefore in many cases, image processing can be more effectively applied in the frequency domain.

3.4.1. Point Processing

3.4.1.1. *Background*

For an image *f*(*x*,*y*), point processing techniques modify a pixel value *r* at (*x*,*y*) based only on the intensity of single pixels

$$s = T(r) \tag{3.66}$$

T is called a gray-level transformation or mapping function. This is illustrated in Figure 3-15.

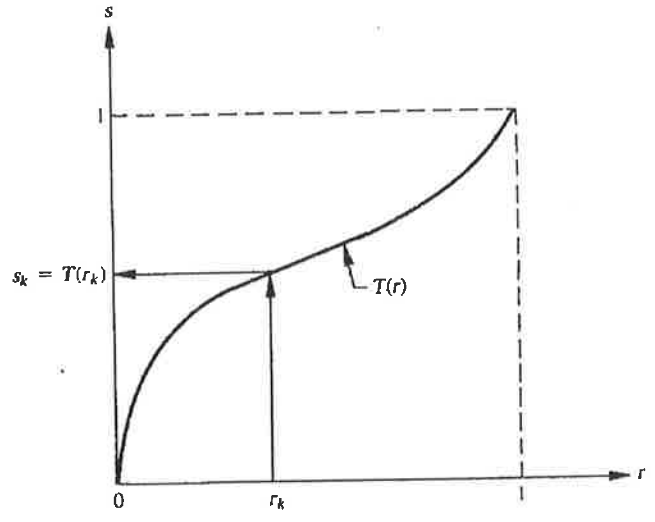

Figure 3-15 Gray level transformation function (from Gonzalez and Woods, 1992).

3.4.1.2. *Image Negatives*

Obtaining the negative of an image is achieved using a transformation which of the form

$$s = -r + (L - 1) \tag{3.67}$$

where *L* is the number of gray levels.

3.4.1.3. Contrast Stretching

Increasing the dynamic range of the gray levels can be achieved by contrast stretching. For example the pixel values can be divided into three regions. The values below r_1 will be compressed, between r_1 and r_2 expanded, and greater than r_2 compressed. A transformation which would achieve this is

$$\begin{cases} r < r_1 & s = m_1 r \\ r_1 \leq r \leq r & s = m_2 r \\ r > r_2 & s = m_1 r \end{cases} \tag{3.68}$$

where $m_1 < 1$ and $m_2 > 1$.

3.4.1.4. Compression of dynamic range

If the image contains too great a dynamic range to display then it is desirable to compress the gray levels to the display range. This can be achieved by a transformation such as

$$s = c\log(1+|r|) \tag{3.69}$$

where c is a scaling constant which could be used to ensure the transformed values fill the display range.

3.4.1.5. Gray-level slicing

Used for highlighting a specific range of gray levels. One approach is to highlight a specific range and reduce all other gray levels to a low constant value. Another is to boost the gray levels of a specific range.

3.4.1.6. Bit-plane slicing

If an image is composed of 8 bit values, then the image can be considered to be composed of 8 1-bit planes, ranging from plane 0 for the least significant bit to plane 7 for the most significant bit. If a bit-plane is displayed then plane 7 contains the most image information and plane 0 the least. The lower bit planes contribute to subtle details in the images. Each bit plane corresponds to the gray levels thresholded, e.g. plane 7 corresponds to image thresholding at level 128, level 6, 64 etc.

3.4.1.7. *Histogram equalisation*

Considering the gray level values r as continuous variables that have been normalised so they lie in the interval from 0 (black) to 1 (white). A transformation $s = T(r)$ will produce a gray level s for every pixel value r in the image. If they are continuous variables the original and transformed gray levels can be characterised by their probability density functions $p_r(r)$ and $p_s(s)$. A transformation is desired that results in the new values having a uniform probability distribution $p_s(s) = 1;\ 0 \le s \le 1$, thus improving the contrast of the image by utilising the full dynamic range. The transformation function

$$s = T(r) = \int_0^r p_r(w)dw \qquad 0 \le r \le 1 \tag{3.70}$$

where w is a dummy variable of integration, achieves this. This is the cumulative distribution function of r (Gonzalez and Woods, 1992).

For the more useful discrete form, the number of pixels n_k with gray level r_k where $k = 1,\ldots L-1$ (L the number of levels) can be used to form a histogram of the probability of occurrence. Each gray level histogram bin value is equal to $p(r_k) = n_k/n$, where n is the total number of pixels in the image. This histogram will in general have a limited range of brightness levels (r_k's). For each brightness gray level r_k it is the purpose to find a new brightness gray level s_k. The technique to obtain a uniform histogram is known as *histogram equalisation*. The number of pixels with this new brightness level will be the same as with the old level. The new level is set to be the cumulative sum of the number of pixels up to the old level, so before the old histogram starts all values of the new level will be zero. The first new brightness gray level will be the value of the height of the histogram at the first old level, and so on. This does not achieve a perfect result but does dramatically improve contrast.

$$s_k = T(r_k) = \sum_{j=0}^{k} \frac{n_j}{n} \tag{3.71}$$

The result of this transformation is not a uniform probability density as in the continuous case. The transformation serves to spread the histogram so that it starts at value 0 and finishes at value 1 (Figure 3-16).

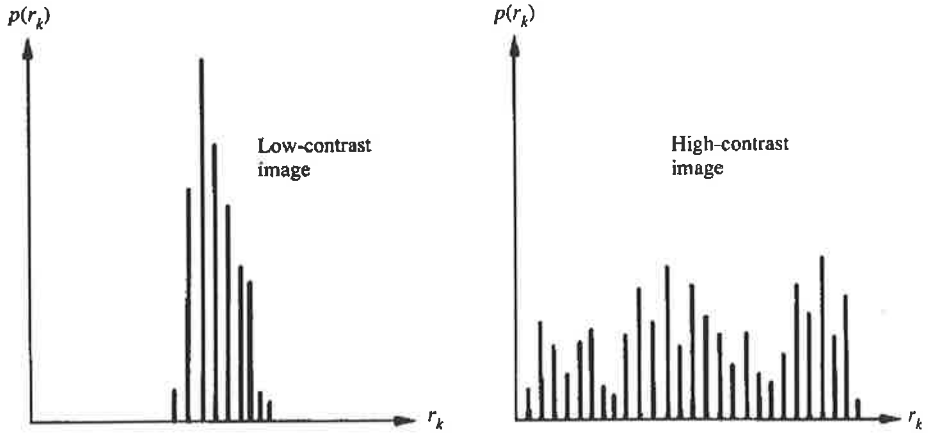

Figure 3-16 Histogram equalisation (from Gonzalez and Woods, 1992).

Global Histogram Equalisation

The purpose of this technique is to equalise the histogram of the whole image. The histogram of pixel brightness values is computed. Most pixels will usually be within a small brightness range. By spreading this range out to cover the entire display range, the difference between different pixel values in the image is increased, i.e. image contrast is increased. The transformation modifies the gray level to a new value, being the cumulative sum of n_k/n up to the k^{th} gray level, i.e. if there are no pixels up to a value, the new gray levels up to that value will all be set to zero, essentially removing that range from the image. The first bin that contains pixels, the gray level of that bin will be set to the number of pixels n_k/n in that bin, and so on. Eventually the last bin that contains pixels will be set to the maximum gray level, and all bins after this which contain no pixels will yield the same cumulative value, and hence be set to the maximum gray level, i.e. removed.

Adaptive Histogram Equalisation (AHE)

AHE and its variations are widely used for enhancement of contrast for the low-contrast images obtained at megavoltage energies. A square or rectangular neighbourhood area is defined, and the centre of this area moved from pixel to pixel. At each location the histogram of the area is computed and the histogram transformation applied. This transformation is used to calculate the new pixel value at the centre of the region (Hummel, 1977).

Contrast limited adaptive histogram equalisation (CLAHE)

When images contain relatively homogeneous regions and have low signal-to-noise ratio (both apply to portal images) the results of AHE can show disturbing increases in noise. To counter this, clipped, or contrast-limited adaptive histogram equalisation (CLAHE) can be performed (Pizer *et al.*, 1986). The contrast enhancement is proportional to the slope of the mapping function. By reducing this slope the contrast enhancement is reduced. Since the derivative of the mapping function (cumulative histogram) is the histogram, then reducing the slope at a brightness level corresponds to reducing the number of pixels at that level, or *clipping* that level. High peaks are generally the result of near-uniform regions, and hence in ordinary AHE this results in a limited range of values mapped to a wide range of values which can over-enhance noise. Enforcing a maximum on the content of the gray level bins limits the amount of contrast enhancement and hence enhancement of noise.

The clipped histogram must be renormalised to retain the same area otherwise a mapping for all pixels in the area does not exist. This can be considered as redistributing the pixel values that are clipped over the whole histogram. This raises the effective clipping level, as the number of pixels at each pixel value increases by a fixed amount, including the pixel values that were clipped.

In general rather than calculate for every pixel, interpolation is used. Moving histogram equalisation (MHE) refers to using linear interpolation rather than bilinear. This is to reduce artifacts obtained with AHE in regions of low contrast. Selective Region (SR) histogram equalisation routines first find the contour of the radiation field edge, and selectively apply contrast enhancement inside this region, thus avoiding the effect of the background levels outside the field in any enhancements.

Size of contextual region

The size of the contextual region for AHE can be set to 1/64th of the area of the image for most medical images. This corresponds to 64×64 for a 512×512 image. As the image may only occupy half the area of the pixel matrix, then 32×32 would also be appropriate. If the region is too small the contrast becomes too sensitive to local variations and hence image noise.

Adaptive Histogram Clip

This approach (Gluhchev and Shalev, 1995) segments the image into three regions, background, field edge, and field pixels, and applies AHE with different clip levels in each region. Obviously contrast enhancement is not necessary outside the field region. The edge is enhanced but not as much as the field to preserve the edge. The field area can be assigned a suitable clip level.

Histogram specification

Particular histogram shapes that highlight certain gray-level ranges can be specified. If $p_r(r)$ and $p_z(z)$ are the initial and desired probability distributions, the image is initially histogram equalised (Equation 3.70). If the desired image with probability density $p_z(z)$ was known then this too could be histogram equalised

$$v = G(z) = \int_0^z p_z(w)dw \tag{3.72}$$

The probability distributions of v and s are both uniform and hence identical, thus v can be replaced with s

$$s = G(s) = \int_0^z p_z(w)dw \tag{3.73}$$

Thus the levels $z = G^{-1}(s)$ would have the desired probability function. Thus the steps are

1) Equalise the levels of the original image
2) Specify the desired density function and obtain $G(z)$
3) Apply the inverse transformation $z = G^{-1}(s)$, to the levels obtained in step 1

In the discrete case the function G^{-1} need not be found analytically, as a mapping for each pixel value can be stored.

3.4.1.8. Local statistically based enhancement

The local enhancement can be based on other properties of the neighbourhood pixel values such as the mean and standard deviation, where the mean is a measure of average brightness, and the standard deviation a measure of contrast. A typical example is

$$g(x,y) = A(x,y) \cdot [f(x,y) - m(x,y)] + m(x,y) \qquad (3.74)$$

where

$$A(x,y) = k \frac{M}{\sigma(x,y)} \qquad 0 < k < 1 \qquad (3.75)$$

In this transformation the pixel at (x,y) is modified according to the values A, m and σ which depend on the predefined neighbourhood of (x,y). M is the global mean, m and σ the local mean and standard deviation. The difference between the pixel value at (x,y) and the local mean is multiplied by the gain factor A. This amplifies local variations. The lower the local contrast given by $\sigma(x,y)$, the higher the gain value. Lastly the mean is reinstated to restore the average intensity level in the region. Often a fraction of the mean is added and A is limited between two values to balance large differences in intensity between regions.

3.4.1.9. Image averaging

If a noisy image $g(x,y)$ is formed from a noiseless image $f(x,y)$ by adding noise $n(x,y)$

$$g(x,y) = f(x,y) + n(x,y) \qquad (3.76)$$

By adding a set of such noisy images $g_i(x,y)$ the noise can be reduced and the result converges to $f(x,y)$. If M images are averaged then the expectation value of $g(x,y)$ is

$$E\{\overline{g}(x,y) = f(x,y) \qquad (3.77)$$

and the variance of $g(x,y)$ is

$$\sigma^2_{\bar{g}(x,y)} = \frac{1}{\sqrt{M}} \sigma^2_{n(x,y)} \tag{3.78}$$

The noise level of the result is the noise level of the initial images divided by the square root of the number of averages.

3.4.2. Spatial Filtering

3.4.2.1. Background

The use of spatial masks in the spatial domain is called spatial filtering. The most simple implementation is to sum the products between the mask coefficients and the intensities of the pixels under the mask. The mask is centred at a pixel at (*x*,*y*) and the pixel value there replaced with the summation. Partial neighbourhoods are used for pixels near the edge. (Figure 3-17) shows a general 3 × 3 mask.

w_1	w_2	w_3
w_4	w_5	w_6
w_7	w_8	w_9

Figure 3-17 Spatial mask filter with arbitrary coefficients or weights.

Denoting the gray levels of the pixels under the mask as z_1, z_2, …, z_9 the response of a linear mask is

$$R = w_1 z_1 + w_2 z_2 + \cdots + w_9 z_9 \tag{3.79}$$

If the centre of the mask is located at (*x*,*y*) the gray level of the pixel located at (*x*,*y*) is replaced by *R*. A new image is created using the values of *R* so that modified pixels are not used for the processing of other pixels.

3.4.2.2. Lowpass filtering (smoothing)

Smoothing filters are used to achieve noise reduction and image blurring. All coefficients must be positive. A mask based on a rectangular or square-wave function is simple averaging, whereas a mask based on a Gaussian shape is weighted averaging. An example of a simple averaging mask filter is 1/9 ×

1	1	1
1	1	1
1	1	1

Figure 3-18 Spatial lowpass filter.

3.4.2.3. Median filtering

To achieve noise reduction without blurring, median filtering replaces the pixel value with the median value of the neighbourhood. This is effective when the noise pattern consists of strong, spikelike components, and edge sharpness is to be preserved. If a pixel has a high value, then this will be the first value in the sorted list of pixel values. As the central value is chosen from this list as the median, then this strong value is effectively ignored, whereas it would be incorporated in averaging.

3.4.2.4. Highpass filtering

Highpass filtering is useful to increase the sharpness of the image, and highlight edges. The highpass filter should have positive coefficients near its centre and negative at its periphery. An example of a 3×3 highpass mask is 1/9 ×

-1	-1	-1
-1	8	-1
-1	-1	-1

Figure 3-19 Basic highpass spatial mask filter.

When the mask is over an area of constant or slowly varying gray level the result is zero or very small, i.e. the highpass filter reduces the zero-frequency term (frequency space) to zero. The average gray level of the image is then reduced to zero and the contrast reduced significantly, thus high boost filtering generally achieves better overall results. With an average value of zero some values must be negative and so these must be scaled and/or clipped so that gray levels of the final result span the range [0, L-1].

3.4.2.5. *High boost filtering*

A highpass image can be considered as *Highpass = Original–Lowpass*. When the original image is amplified by *A; High-boost = A×Original–Lowpass*, a high-boost or high-frequency-emphasis filter results. This can be rewritten *High-boost = (A–1)×Original+Highpass*. When $A > 1$, part of the original is added to the highpass result partially restoring the low frequency components. The relative amount of edge enhancement of the image thus depends on A. Subtracting a blurred image (*Lowpass*) from an original is called unsharp masking. For a 3×3 mask, the original image multiplied by (A-1) results in a central value of A-1 surrounded by zeros. When this is added to the highpass mask (Figure 3-19) this results in a central value of $1/9\times 8+(A-1)$ $=-1/9+A$ $=1/9(9A-1)$. Thus the high-boost mask can be implemented with a central value of $w=9A-1$, with $A \geq 1$, as 1/9 ×

-1	-1	-1
-1	*9A-1*	-1
-1	-1	-1

Figure 3-20 High-boost mask

3.4.2.6. *Derivative filters*

As averaging blurs, the opposite, differentiation sharpens an image. The gradient of the image function $f(x,y)$ is given by

$$\nabla f = \begin{bmatrix} \frac{\partial f}{\partial x} \\ \frac{\partial f}{\partial y} \end{bmatrix} \tag{3.80}$$

The magnitude of this is

$$\nabla f = mag(\nabla f) = \left[\left(\frac{\partial f}{\partial x} \right)^2 + \left(\frac{\partial f}{\partial y} \right)^2 \right] \tag{3.81}$$

This is used as the basis of differentiation processing. Various mask methods are used to approximate the gradient at a particular pixel. The Prewitt operators estimate the gradient in the *x*-direction (↓) by the difference between the third row and the first row values

-1	-1	-1
0	0	0
1	1	1

Figure 3-21 Prewitt Operator for *x*-direction

and the gradient in the *y*-direction (→) by the difference between the third and the first column values

-1	0	1
-1	0	1
-1	0	1

Figure 3-22 Prewitt Operator for *y*-direction

to obtain the magnitude of the gradient. Other approaches are also used e.g. Sobel

-1	-2	-1
0	0	0
1	2	1

-1	0	1
-2	0	2
-1	0	1

Figure 3-23 Sobel Operators for the *x* and *y*-directions.

3.4.3. Enhancement In The Frequency Domain

3.4.3.1. Lowpass filtering

Filtering is achieved in the frequency domain by multiplying the Fourier transform of the image by a filter, then inverse Fourier transforming to yield the filtered image. The filtering can be represented by

$$G(u,v) = H(u,v)F(u,v) \tag{3.82}$$

where $F(u,v)$ is the Fourier transform of the image and $H(u,v)$ is the filter. The ideal lowpass filter is a step function, of value 1 up to the cutoff frequency of the filter D_0 and zero thereafter

$$H(u,v) = \begin{cases} 1 & \text{if } D(u,v) \le D_0 \\ 0 & \text{if } D(u,v) > D_0 \end{cases} \tag{3.83}$$

where

$$D(u,v) = (u^2 + v^2)^{1/2} \tag{3.84}$$

is the distance from the point (u,v) to the origin. This corresponds to convolving with a $\sin(x)/x$ shape function in the spatial domain.

$$g(x,y) = h(x,y) * f(x,y) \tag{3.85}$$

Provided the filter affects the real and imaginary parts of $F(u,v)$ in exactly the same manner, the filter does not alter the phase of the transform and is referred to as a *zero phase shift filter.*

The cutoff frequency can be set according to the total signal power P_T enclosed by the filter

$$P_T = \sum_{u=0}^{N-1}\sum_{v=0}^{N-1} P(u,v) \tag{3.86}$$

where $P(u,v)$ is the squared magnitude of $F(u,v)$

$$P(u,v) = |F(u,v)|^2 = R(u,v)^2 + I(u,v)^2 \tag{3.87}$$

If the power within a circle of radius r is found by summing the power at each point within the circle

$$P_r = \sum_{u=0}\sum_{v=0} P(u,v) \tag{3.88}$$

then the percent of the power enclosed by this circle is given by

$$\beta = 100\, P_r / P_T \tag{3.89}$$

Decreasing the width of the filter is equivalent to a convolving with a broader $\sin(x)/x$ function and vice versa. The radii of the rings are inversely proportional to D_0. Ringing artifacts in the image can occur with ideal filters due to the $\sin(x)/x$ shape.

3.4.3.2. Highpass filtering

The ideal highpass filter in the frequency domain is the opposite of the lowpass filter blocking frequencies below D_0 and passing those above. Similarly to the spatial domain, a pure highpass filter lowers image contrast making different but smooth levels in the image appear the same, so a constant can be added to preserve the low frequency components at a lower level than the high frequencies (high frequency emphasis). Histogram equalisation is often then performed.

3.4.4. Image Restoration

3.4.4.1. Degradation model (algebraic)

Restoring an image involves recovering a degraded image, whereas the previously discussed enhancement procedures manipulate the image to take advantage of human interpretation. Restoration techniques are oriented toward modelling or identifying the degradation, and applying the inverse process to restore the original image. A linear systems model of the imaging process with degradation is (Webb, 1998)

$$g(x,y) = H\left[f(x,y)\right] + \eta(x,y) \tag{3.90}$$

where H represents the system response and $\eta(x,y)$ represents the additive noise or degradation. The resulting image $g(x,y)$ is given by the convolution of $h(x,y)$ with $f(x,y)$ with the degradation then added to the result

$$g(x,y) = \int_{-\infty}^{\infty}\int f(\alpha,\beta)h(x-\alpha,y-\beta)d\alpha d\beta + \eta(x,y) \tag{3.91}$$

where H is position invariant.

To illustrate this convolution in a discrete matrix representation the 1-D case is first considered. Suppose $f(x)$ and $h(x)$ are sampled uniformly to give arrays of length A and B. In this case x (↓) is discrete in the range 0, 1, 2, …, A - 1, for $f(x)$, and 0, 1, 2, …, B-1 for $h(x)$. The discrete convolution can be formed by assuming that the sampled functions are periodic, with a period M. M is chosen so that there is no overlap $M \geq A + B - 1$, and the functions are extended with zeros to M length. If $f_e(x)$ and $h_e(x)$ represent the extended functions then the convolution is (ignoring noise)

$$g_e(x) = \sum_{m=0}^{M-1} f_e(m)h_e(x-m) \tag{3.92}$$

for $x = 0, 1, 2, \ldots, M-1$. Using matrix notation this can be expressed in the form

$$\mathbf{g} = \mathbf{Hf} \tag{3.93}$$

where

$$\mathbf{f} = \begin{bmatrix} f_e(0) \\ f_e(1) \\ \vdots \\ f_e(M-1) \end{bmatrix} \tag{3.94}$$

and similarly **g**, while **H** is an $M \times M$ matrix. For the 2-dimensional case

$$g_e(x,y) = \sum_{m=0}^{M-1}\sum_{n=0}^{N-1} f_e(m,n)h_e(x-m, y-n) + \eta_e(x,y) \tag{3.95}$$

If **f**, **g**, and **n** represent $M \times N$ vectors formed by stacking the rows (y-values) of the $M \times N$ functions $f_e(x,y)$, $g_e(x,y)$ and $\eta_e(x,y)$. Therefore, in matrix form

$$\mathbf{g} = \mathbf{Hf} + \mathbf{n} \tag{3.96}$$

H is of dimension $MN \times MN$.

3.4.4.2. *Algebraic restoration*

Unconstrained restoration involves finding an estimate of **f**, denoted by $\hat{\mathbf{f}}$, that minimises a criterion of perfomance, i.e. find an $\hat{\mathbf{f}}$ such that

$$\|\mathbf{n}\|^2 = \|\mathbf{g} - \mathbf{H}\hat{\mathbf{f}}\|^2 \tag{3.97}$$

is mimimum. Solving this yields

$$\hat{\mathbf{f}} = \mathbf{H}^{-1}\mathbf{g} \tag{3.98}$$

Constrained restoration uses the method of Lagrange multipliers, minimising

$$\|\mathbf{Q}\hat{\mathbf{f}}\|^2 + \alpha\left(\|\mathbf{g} - \mathbf{H}\hat{\mathbf{f}}\|^2 - \|\mathbf{n}\|^2\right) \tag{3.99}$$

where **Q** is a linear operator. The solution to this is

$$\hat{\mathbf{f}} = (\mathbf{H}^{\mathrm{T}}\mathbf{H} + 1/\alpha\, \mathbf{Q}^{\mathrm{T}}\mathbf{Q})^{-1}\mathbf{H}^{\mathrm{T}}\mathbf{g} \tag{3.100}$$

3.4.4.3. Inverse filtering

The algebraic representation can be rewritten as

$$\hat{F}(u,v) = \frac{G(u,v)}{H(u,v)} \tag{3.101}$$

$H(u,v)$ is considered a filter function that multiplies $F(u,v)$ to produce the transform of the degraded image. Obviously zeros in $H(u,v)$ should be avoided in the calculation. In the presence of noise, the above equation with

$$G(u,v) = H(u,v)F(u,v) + N(u,v) \tag{3.102}$$

yields

$$\hat{F}(u,v) = F(u,v) + \frac{N(u,v)}{H(u,v)} \tag{3.103}$$

This shows that for small values of $H(u,v)$ the second term could dominate the result. In practice $H(u,v)$ drops off rapidly in the frequency plane whereas $N(u,v)$ falls off more slowly. Thus by limiting the restoration to values of frequency close to the origin, small values of $H(u,v)$ are avoided.

3.4.4.4. *Least mean square (Wiener) filter*

The least squares filter is an approach that minimises (in a statistical sense) the mean squared error between $f(x,y)$ and its restoration $\hat{f}(x,y)$

$$\hat{F}(u,v) = \frac{G(u,v)}{H(u,v)} \frac{|H(u,v)|^2}{|H(u,v)|^2 + \gamma\left[S_\eta(u,v)/S_f(u,v)\right]} \tag{3.104}$$

where $M = N$ and $S_f(u,v)$ is the power spectrum or spectral density of $f_e(x,y)$ so the ratio is the noise-to-signal power density ratio. The noise power density $S_n(u,v)$ and the signal power density can be estimated with the help of the suitably normed squared moduli of the Fourier transform of a noise image and a portal image. When these are unknown the above equation is often approximated by using a constant *K* to replace the ratio.

3.4.4.5. *Interactive restoration*

If a 2-D sinusoidal interference pattern (coherent noise) is superimposed on an image

$$\eta(x,y) = A\sin(u_0 x + v_0 y) \tag{3.105}$$

The Fourier transform of this noise is

$$N(u,v) = \frac{-jA}{2}\left[\delta\left(u - {}^{u_0}\!/_{2\pi}, v - {}^{v_0}\!/_{2\pi}\right) - \delta\left(u + {}^{u_0}\!/_{2\pi}, v + {}^{v_0}\!/_{2\pi}\right)\right] \tag{3.106}$$

i.e a pair of impulse functions of strength $-A/2$ and $A/2$ located at coordinates $(u_0/2\pi, v_0/2\pi)$ and $(-u_0/2\pi, -v_0/2\pi)$, containing only imaginary components. The Fourier transform of the signal with this noise added is given by

$$G(u,v) = F(u,v) + N(u,v) \tag{3.107}$$

If the magnitude of $G(u,v)$ is displayed then if A is large enough the two impulses of $N(u,v)$ appear as bright dots and can be interactively eliminated by placing bandpass filters around them. Similarly if $\eta(x,y)$ and hence $N(u,v)$ is known then it can be simply subtracted.

3.5. Clinical applications of portal imaging

3.5.1. Types of images

The images acquired for treatment field position verification are predominantly double-exposure portal images. These images comprise an exposure formed with the collimated treatment field, followed by a larger "overflash" or open-field image to clearly show the treatment field location relative to bony anatomical structures (Figure 3-24). Image acquisition is slow due to the retraction of the collimation to acquire the overflash image. The images can also only be acquired before or after the treatment due to this collimation retraction and hence may be unrepresentative of the treated position. Electronic portal imaging devices (EPIDs) acquire double-exposure images in a similar manner. An image is acquired of the treatment field. The field edge is determined from this image, the collimation is retracted, and a larger image acquired. The field edge of the treatment field is then superimposed on the larger image to give the double-exposure image.

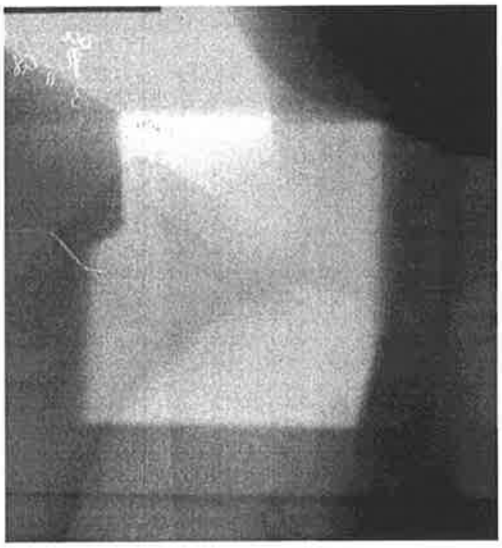

Figure 3-24 Example of a double-exposure portal image

Images can also be taken during the treatment with the treatment field only. These have not gained widespread acceptance for visual field placement verification, however they have been utilised with registration algorithms to quantitatively determine field placement. This is only possible if the images show sufficient anatomical structures, and for small fields this is problematic.

3.5.2. Determination of field placement

3.5.2.1. Visual inspection

The purpose of acquiring a megavoltage image of the radiotherapy treatment is to determine the field placement, either ensuring that it is correct or determining the error so that correction can be performed. The megavoltage image is compared to a reference image, either a kilovoltage image acquired in the treatment simulator or a digitally reconstructed radiograph (DRR) produced by the treatment planning system. The reference image shows the intended treatment field location relative to the bony anatomy. Most commonly the megavoltage image is visually compared to the reference image. Herman *et al.* (1994) studied the accuracy of visual inspection of field placement by comparison with the measured displacement. They found that 14% of images that were passed as having less than 5 mm error had 5-10 mm errors and 4% had errors over 10 mm. Perera *et al.* (1999) similarly examined the accuracy of visual inspection. They concluded that human observers can detect large placement errors but have difficulty identifying field placement errors when the errors are around 5 mm or smaller. There was also great variability in the results from different observers.

3.5.2.2. Image Registration

A more objective method of determining the field placement error or setup error is image registration, where the treatment image is registered to the reference image and the displacement measured. Registration algorithms require that both the reference image and portal image are in digital form. Both simulator and port films can be digitised however electronic portal images are more conveniently employed. A variety of approaches have been taken to the registration of the reference image and the portal image. The algorithms require that the reference image and portal images are placed in a common reference frame, as they may be acquired with different magnifications. The location of the treatment field boundary on an electronic portal image matrix may also vary from day to day due to mechanical slop, and this makes an absolute frame of reference difficult to obtain. A common reference frame can be achieved by registering the manually determined field outline on the reference image to the field border extracted automatically from the megavoltage image. All registration algorithms require knowledge of the pixel dimension at isocentre so that any measured field displacement can be reported as a distance at the isocentre plane.

Field edge detection

Verification of the field shape during treatment is of obvious importance not only to detect gross errors, but as a precursor to image registration methods which rely on determination of the field edge. Bijhold *et al.* (1991a) have developed a method of detecting the field edge in electronic portal images by finding the maximum gradient of radiation intensity in the penumbra of the field. This method was found to accurately determine the field edge when compared with in-phantom measurements. The accuracy was limited by the pixel size of the images.

Fiducial Point Registration

In this method of registration common anatomical points are interactively marked on the reference and portal images (Meertens *et al.* 1990). The coordinates of the points marked on the reference image are then transformed by translation, rotation and scaling until they best match the coordinates of the points on the portal image. The best fit is determined by minimising the sum of the squares of the distances between the corresponding points. The accuracy of this method is determined by how accurately the identical anatomical landmarks are marked. The accuracy has also been found to depend on the spacing of the points but not the number of points (McParland, 1993). To account for the fact that one or more points may be incorrectly marked, Gluhchev and Shalev (1993) have developed a method that evaluates the accuracy of point placement and also deletes unreliable points. The algorithm determines a 'guilt parameter' for each point pair to determine whether these should be deleted.

Template Matching

A variety of techniques have been developed to register the two images based on overlay of the two images. In the most widely used implementation a line drawing or template of the reference image anatomy is overlaid onto the portal image (Bijhold *et al.*, 1991b). The digital line drawing or templates of the field edge and bony structures is created interactively using the digitised reference film. The radiation field edge is detected automatically on the portal image and a digital line graph constructed. The reference image field line is aligned to the portal image field line. When these are aligned, the position of the reference image anatomical template relative to the anatomy of the portal image can be seen. The reference field template is then moved (manually or automatically) until the bony structure line drawing overlies the bony structures in the portal image. The transformation from field edge match to anatomical match gives the setup error. Assuming the field edges at treatment were correct then this gives the setup error independently of the position of the portal imaging device. The method is limited to an accuracy of about 2 mm with out-of-plane rotations less than 2 degrees and translations less than 10 mm.

Chamfer Matching

Chamfer matching (Gilhuijs and van Herk, 1993a) is a powerful algorithm for automatic image registration. Again a reference image template is used. Features in the portal image are automatically extracted using edge detection. A 'cost function' image is then generated from this image yielding an image where the pixel value increases with distance from the extracted feature forming 'valleys' corresponding to the features. The optimum position of the template is found so that it 'falls' into the valleys. Chamfer matching is applied to the field edges in the portal and reference images as well as to the anatomical outlines. The average accuracy was found to be 1.8 mm. Gilhuijs *et al.* (1993b) have evaluated this automatic algorithm clinically for prostate treatments, and the success rate was 96% for large AP pelvic views. A similar method based on the matching of line segments (Balter *et al.*, 1992) was also developed where the template is drawn on the portal image using contours and matched using chamfer matching. However this was too time consuming for clinical use. To improve the accuracy of chamfer matching the mid-line location of various structures was identified and the portal image segmented (Fritsch *et al.*, 1995). This gave more robust segmentation than edge detection methods.

Three dimensional methods

Methods based on a 2-D projection image have limited accuracy and are vulnerable to out-of-plane rotations (Hanley *et al.*, 1995). An approach utilising DRRs to perform 3D registration has been developed (Gilhuijs *et al.*, 1996). Fast computation of a DRR (~1 s) is performed from the CT data set which can be rotated and translated to produce a DRR which corresponds to the portal image. A template of the portal image anatomy and field edge can be drawn or produced automatically, overlaid onto the DRR and the CT set manually adjusted, and a DRR produced until the template matches. Alternatively a more sensitive approach can be used where the DRR and portal image are rapidly alternately displayed, and a "shifting" and "rocking" motion are perceived between the structures in the two images when there are translational and rotational differences respectively. The rotation and translation of the CT data set to produce the matching DRR gives the patient position for the treatment. The DRRs are produced from bony structures pre-segmented from the CT data to speed up the DRR production. Using a laboratory study where portal images with known offsets and rotations were produced from a patient's CT data set they found a mean error of less than 1 mm and 1 degree with about 0.5 mm per degree standard deviation using this method. It required a trained operator 10 minutes on average to perform the 3D analysis, with 45 iterations on average.

Gilhuijs *et al.* (1995) have automated the 3D matching technique by adjusting the position and orientation of the CT data in order to maximise the distance through bone in the CT data along lines between the focus of the irradiation unit and bony structures in the portal images. These bony ridges are automatically delineated (or manually) by first enhancing the ridges, then covering them with a large number of isolated dots. The image coordinates of the dots indicate the location of the bony ridges. The cost function is the negated average of the path lengths through bone of a CT orientation along the lines connecting the focus with the dots indicating the bony ridges in the portal images. This is minimised by the downhill simplex minimisation starting from the planned setup. Fail rate was about 3%, accuracy was about 1 mm and 1°. It was found to be robust for imperfections in the bony ridge delineation.

Other methods that cross-correlate the portal image with the reference image have been developed. However these have the drawback that the grey-scale in the two images must be similar. Therefore the technique can only register the portal image with another portal image.

3.5.3. Correction of patient position

The measurement of patient position with registration algorithms has led to statistically based strategies to determine from the measurements whether a systematic error in positioning is present and hence correct the patient position.

3.5.3.1. Field Placement Errors

Field placement errors for a particular patient can be considered to have systematic and random components. If the field placements are measured each day for a patient's course of treatment the systematic or simulator-to-treatment error is given by the mean displacement for the patient. The random or treatment-to-treatment errors describe the day-to-day fluctuations about this mean position. This is illustrated in the Figure 3-25.

3.5.3.2. Intra-fraction corrections

It is possible to measure the patient position at the start of every daily treatment (fraction) and correct the position (intra-fraction correction). This method aims to remove both random and systematic components of the field placement errors. Ezz *et al.* (1992) examined this and found that patient positioning was improved, however visual inspection was used to determine the positioning of the patient. De Neve *et al.* (1993) similarly visually compared a portal image acquired at the start of the treatment with a reference image, and corrected the patient position by remote movement of the couch from outside the room. They found that adjustments were performed on 55% of fields and that treatment times were increased on average by 46%.

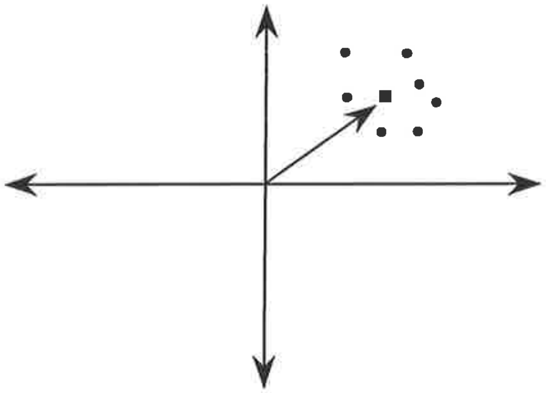

Figure 3-25 Systematic and random errors in field placement. The mean position is the systematic error and the random errors are fluctuations about this mean.

Gildersleve *et al.* (1994) acquired images at the start of daily treatments and applied a registration technique similar in principle to template matching, where the reference and portal images were alternately displayed at a frequency of 6 Hz (Evans *et al.*, 1992). Discrepancies in anatomical position between the reference and portal images are then perceived by the eye as rapid movement. They compared the results to a group of patients that did not have the on-line adjustments. They found that the mean error was reduced from 5 mm to 2 mm, and the number of fields with ≥ 5 mm errors reduced from 69% to 7%. However the treatment times were increased by 1-2 minutes for each irradiated field. Van den Heuvel *et al.* (1995) performed image registration to measure and correct patient positioning before each treatment. They found that both systematic and random positioning errors can be reduced to the order of 1 mm, however the mean increase in treatment time was 37%, largely due to the repositioning of the patient. Luchka and Shalev (1996) reported the treatment of an obese patient with megavoltage simulation and intra-treatment corrections. With the interventions only 2% of the displacements were more than 10 mm compared to 10% without interventions. As random variation is generally small for the non-obese population of patients, and intra-treatment corrections expensive in time, obese patients or patients with poor reproducibility may become the focus of intra-fraction treatment corrections.

3.5.3.3. Inter-fraction corrections (correction strategies)

These strategies often referred to as off-line, involve acquisition of portal images to correct systematic errors in patient position, the random displacements are not corrected. The correction strategy attempts to determine on the basis of only a few images, whether a systematic error is present, and the magnitude. The difficulty is that any measurement of patient position will include both the systematic error and the random displacement for that days treatment. The most primitive form of this strategy is the traditional port film approach where films are acquired on the first day of treatment and the film visually compared to the reference film. If a field placement error is seen, the film is usually repeated to ensure that the error is still present, i.e. a systematic error, and the patient position is then shifted to remove the estimated error. When patient position is determined more accurately by image registration, statistically based correction strategies can be used to determine and correct these systematic errors.

Due to the presence of random motion of the patient, the measurement made of patient position only yields an estimate of the true mean position of the patient over the entire course. Elementary sampling statistics applies to this situation. Considering one displacement direction, after a number of measurements n, the mean value of field placement $\bar{d}_n$ is found and this is a sample mean from a population (the daily treatment placements for the patient). The true mean Δ can only be determined with total confidence by measurement of the patient's position at every fraction. If many samples of size n were taken, the distribution of sample means ($\bar{d}_n$'s) found would itself have mean Δ (the mean position or systematic error) and standard deviation $\sigma_p/\sqrt{n}$ (standard error of the mean; SE) where σ_p is the standard deviation of the displacements for all the treatment fractions. A finite population correction should also be included, as the number of fractions is generally small.

If only n measurements have been made for the patient then σ_p is unknown. If random motion for all patients is the same ($\sigma_p = \sigma$) then σ measured from a population of patients can be used. This then enables a 95% confidence interval for the true mean position of the patient to be found from the sampled mean position as

$$\bar{d}_n \pm 1.96\sigma/\sqrt{n} \tag{3.108}$$

The finite population correction should also be included, giving

$$\bar{d}_n \pm 1.96\sigma/\sqrt{n} \cdot \sqrt{1-n/N} \tag{3.109}$$

where N is the total number of fractions. This confidence interval will include the patient's true mean positon Δ on 95% of occasions. It decreases in size as the number of measurements n increases. If the random movement is not the same for all patients then the standard deviation of the sample of n measurements S is used as an estimate of σ_p. The confidence interval for the true mean postion is then larger (due to the greater uncertainty in σ_p) and constructed from the t-distribution

$$\bar{d}_n \pm t_{n-1}(0.025)S/\sqrt{n} \cdot \sqrt{1-n/N} \tag{3.110}$$

From the measured patient positions a 95% confidence interval for the true mean position is produced. If this confidence interval does not include the 0 or reference image position then a systematic error is present (at the 95% confidence level) and the patient position should be corrected.

Bijhold *et al.* (1992) developed a correction strategy based on the above, although varying confidence regions were used as the number of measurements increased. They placed the confidence interval about the origin (0,0) point and then if the measured mean position falls outside of the confidence interval, a systematic error is present. They investigated confidence intervals based on both 2D displacement vectors and 3D displacement vectors. They found that the random variations σ_p were equal for most patients at around 2 mm (1 SD).

Denham *et al.* (1993) also implemented a similar approach, however no assumptions were made of the random variation for a particular patient. They showed that the two-dimensional 95% confidence interval ellipse for the systematic error is often tilted on its axis and changes little after 8-10 measurements. Systematic errors are detected when the ellipse does not include the origin, therefore the systematic error is significantly different from zero (95% confidence level). The centre-of-gravity of the ellipse would then be taken as the systematic error estimate. They also quantified the random variation as the 95% confidence ellipse for the measured field placements, or in other words the bivariate normal ellipse.

Bel *et al.* (1993) use a similar approach except one dimensionally, and assumed that the random variation of the patient σ_p is equal to the population mean variation σ. The aim of the strategy is to make a decision as fast as possible, and as few decisions as possible. They use $\alpha/\sqrt{n}$ ($\alpha = f\sigma$) as the confidence limit or action level for identifying a systematic error, where f is a variable. They measure for $n = 1,2,..n_{max}$ thus the final value of $\bar{d}_n$ (the estimate of systematic error) that will be detected is $\alpha/\sqrt{n_{max}}$. They found $f = 2$ and $n_{max} = 2$ gave good results. This is approximately a 95% confidence interval, and only two measurements performed if the first measurement or the average of the first and second are within the confidence interval. The size of the confidence interval for the systematic error is reset if a correction is made i.e. $n = 1$ after a correction. Large systematic errors ($\Delta > 2\sigma$) will be effectively corrected. When random errors are greater than or equal to the systematic error unnecessary corrections will be made, i.e the random error will be corrected.

To improve the above technique in cases where the random error is greater than or equal to the systematic error Pouliot and Lirette (1996) have introduced a factor of maximum likelihood FML factor in the above formalism. The action level is again given by $\propto/\sqrt{n}$ ($\propto = f\sigma$), however the correction made is FML$\bar{d}_n$. FML is the estimated fraction of the average deviation measured due to the systematic error. This is estimated from the maximum likelihood of the two distributions as $\Sigma^2 / (\Sigma^2 + \sigma^2)$. The product of FML and $\bar{d}_n$ represents the maximum likelihood estimation of the systematic displacement at the n_{th} fraction. They also found $f = 2$, and $n = 2$ measurements gave best results.

4. Evaluation of an algorithm for the assessment of the MTF using an edge method

4.1. Introduction

In this chapter an algorithm developed to measure modulation transfer functions from edge object images is described. The algorithm is applied in Chapter 6 to the measurement of MTF for images acquired through the grid of MLC leaves. The accuracy of the algorithm for MTF measurement is evaluated.

The modulation transfer function (MTF) of a radiographic system can be obtained through the analysis of the image of a knife-edge object (Tatian, 1965; Barakat, 1965; Jones, 1965). The MTF is expressed as the zero frequency normalised modulus of the Fourier Transform of the line spread function (LSF) determined by differentiation of the edge spread function (ESF).

To determine the presampling MTF, the edge is angled to the sampling matrix to obtain oversampled edge function profiles (Judy, 1976; Fujita *et al.*, 1992). A typical analysis algorithm then determines the edge angle relative to the sampling matrix, and to improve the signal to noise ratio (SNR), multiple profiles are registered by shifting each profile according to the determined angle. The averaged ESF is then differentiated to obtain the LSF, but this process decreases the SNR of the data. Thus smoothing and folding (Droege, 1979a; le Heron and Poletti, 1988) of the LSF are applied to further reduce noise.

Ideally the edge-object produces a perfect step-edge intensity input to the imaging system. In practice the finite thickness of the edge, the source size, and the resulting contrast and SNR will degrade the input from this ideal, affecting the measured MTF.

Each stage of the MTF calculation process will also affect the accuracy of the calculated MTF. The frequency response of the algorithm is the product of the inherent transfer functions of the angle of the sampling aperture, profile registration, differentiation, smoothing and folding. The transfer function of each component of the algorithm must therefore be quantified to ensure the accuracy of the calculated MTF. Analyses of the transfer functions for the above processes have been previously reported (Droege, 1979a; Villafana, 1975a; Steckner *et al.*, 1993; Wowk *et al.*, 1994; Cunningham and Fenster, 1987). In this work, we derive the transfer function of profile registration accounting for error in the determined edge angle, and incorporate the results of this and the previous analyses into an examination of the transfer function of the MTF algorithm.

When multiple profiles are sampled from an angled edge or slit image, the profiles are shifted with respect to each other due to the angle. To register these profiles one approach has been to find the edge location in each profile by centre-of-gravity analysis of the differential of the profile (Steckner *et al.*, 1993). To improve the accuracy of the profile alignment the edge angle has also been utilised (Reichenbach *et al.*, 1991). Methods to determine the edge angle have included linear least squares fit to individual edge locations found from inverse polynomial fitting to the edge profiles (Bentzen, 1983) and Hough transformation (Samei and Flynn, 1998).

When the profiles are aligned they can only be registered to the sample point nearest to the required shift, resulting in misalignment errors. The effect of these errors on the calculated MTF at the system cutoff frequency has been determined (Steckner *et al.*, 1993). A transfer function of registration has been derived that utilises the misalignment errors that result after each profile is aligned to the nearest sample point (Wowk *et al.*, 1994). An analytical expression has also been derived that applies when the profiles are first grouped together and the profiles in a group shifted by the same amount (Droege 1979a). This latter method of alignment however increases the misalignment errors as each profile is not optimally registered.

These transfer function analyses, however, do not account for error in the determination of the edge angle. This chapter derives the transfer function of profile registration incorporating error in the determined angle. The effect of the error in edge angle on the calculated MTF is determined. An error in the angle will also introduce an error into the frequency axis of the MTF, as the discrete spatial frequency interval is calculated from the sampling interval, in turn derived from the edge angle.

To facilitate the transfer function analyses, a Windows-based MTF calculation program has been developed. The effect of the transfer function of each component of the algorithm on the measured MTF is examined. The MTF algorithm is then applied to a perfect step-edge input image to verify the overall transfer function description. Finally the algorithm is applied to determine an experimental MTF, by the measurement of the MTF of a CCD-camera film scanner.

4.2. Description of the MTF calculation algorithm

Data input to the program is in the form of a digital image of an edge object with the edge at a small angle to the horizontal axis of the image sampling matrix. An edge region for profile sampling is then interactively selected.

4.2.1. Profile sampling

Figure 4-1 illustrates that sampling directly in the *y*-direction across the edge would result in a sampling interval equal to the sampling pitch p_y. For digital systems that undersample (Dobbins, 1995) the MTF calculated from this would be aliased. However, sample points that are adjacent in the *x*-direction are displaced from each other with respect to the edge by an amount Δ (Figure 4-1)

$$\Delta = \tan(\vartheta) p_x = p_y / a \tag{4.1}$$

where θ is the angle of the edge to the horizontal x-axis, p_x and p_y are the image sampling pitches in the x and y directions. The parameter a refers to the edge angle or slope, being the number of sample points across that each row is displaced from the previous due to the edge angle. In this work this form of the angle is referred to as the edge slope to differentiate it from the usual definition of angle measured in radians or degrees. Assuming uniformity of the edge along its length, these adjacent points along the row of the image form an oversampled edge function profile with sampling interval Δ (Judy, 1979). Thus sampling in this manner results in measurement of the presampled MTF.

Multiple oversampled profiles are obtained along the rows of the image according to the edge region selected. As shown in Figure 4-1 W is the pixel aperture width across the edge, and H is the pixel aperture length. In this diagram these are equal to the sampling pitches although this is not necessarily the case.

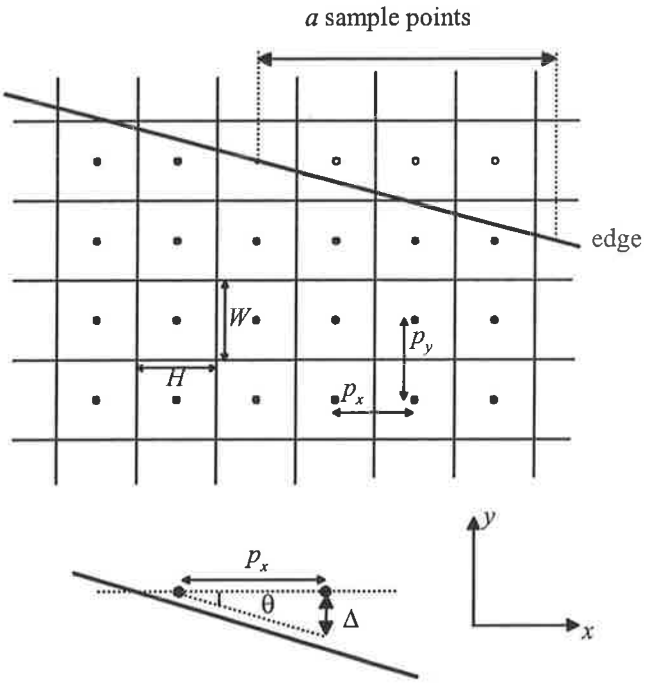

Figure 4-1 Sampling method utilising an angled or sloped edge to obtain oversampled profiles across the edge.

4.2.2. Edge angle determination

The slope of the edge relative to the sampling matrix is determined through a two-stage process. The edge location (x-coordinate) in each row profile is determined to sub-sample point accuracy by a least squares fit of an inverse polynomial (approximation to the integral of a Gaussian) to each profile (Bentzen, 1983)

$$E(x) = C_1 \cdot P\left(\frac{x-m}{\sigma}\right) + C_2 \tag{4.2}$$

where the inverse polynomial is

$$P(x) = 1 - \tfrac{1}{2}\left(\sum_{i=0}^{4} a_i x^i\right)^{-4} \tag{4.3}$$

and

$$a_0 = 1,\ a_1 = 0.196854,\ a_2 = 0.115194,\ a_3 = 0.000344,\ a_4 = 0.019527. \tag{4.4}$$

For negative values of x the relation

$$P(-x) = 1 - P(x) \tag{4.5}$$

is employed. The four fitted parameters are C_1 and C_2 that define the low side of the edge value and the edge contrast, m the mean x-position and σ the standard deviation. The value of m after fitting yields the edge location. The edge slope relative to the axis of the sampling matrix is then determined from a linear least squares fit to the distribution of edge locations against profile (row) number. The edge slope is determined in terms of the parameter a (Figure 4-1), the number of sample points each row profile is displaced from the previous relative to the edge.

4.2.3. Profile Registration

The multiple oversampled row profiles are registered together to give an average ESF with improved SNR. The row profiles are sampled from a common starting coordinate and the offset of each profile from the previous is a sample points. Note that although registration is to the nearest pixel in the row profile, the registration is actually to the nearest sampling interval Δ, as the profiles are oversampled. To align the k^{th} profile to the first ($k = 0$) profile the desired shift is ka sample intervals, where $k = 0,.., N-1$, N the number of profiles. In practice a will be a non-integer value and therefore the profile is shifted by the nearest whole number of sample intervals to the desired shift.

4.2.4. Smoothing

As the differentiation process reduces the SNR (Cunningham and Fenster, 1987), smoothing of the ESF is employed. The ESF profile is smoothed by convolving with a spatial mask, replacing each sample value by the mean of n neighbouring samples, centred on the sample, where n is an odd number and $\text{ESF}_s(x_j)$ is the j^{th} value of the smoothed ESF.

$$\text{ESF}_s(x_j) = \frac{1}{n} \sum_{i=j-(n-1)/2}^{j+(n-1)/2} \text{ESF}(x_i) \tag{4.6}$$

4.2.5. Differentiation

The differential of the ESF to provide the LSF is obtained by the finite-element difference method.

$$\text{LSF}(x_j) = \text{ESF}_s(x_{j+1}) - \text{ESF}_s(x_j) \tag{4.7}$$

where $\text{LSF}(x_j)$ is the j^{th} value of the LSF and $\text{ESF}_s(x_j)$, $\text{ESF}_s(x_{j+1})$ are adjacent values of the ESF.

4.2.6. Folding

To further improve the SNR, the LSF is folded about a central sample point (Droege, 1979a). For accurate folding, the central point of reflection of the LSF is found by fitting the inverse polynomial to the (lower noise) ESF to determine the centre of the ESF. The LSF centre location is then the value of the ESF centre location minus half a sampling interval (to account for the phase shift introduced by the differentiation process). This is then rounded up/down to the nearest sample point.

The MTF is then calculated as the modulus of the discrete Fourier transform of the LSF with the discrete spatial frequency interval, Δf, determined from the sampling interval, and the number of sample points M in the LSF.

$$\Delta f = {}^{1}\!/_{M\Delta} \tag{4.8}$$

4.3. Derivation of transfer function of profile registration

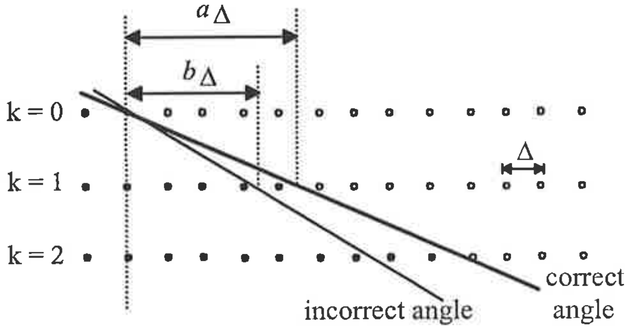

Figure 4-2 Misalignment error of profiles offset by an edge slope where an incorrect slope is used to align the profiles.

Registration of multiple row profiles oversampled from an angled edge image is illustrated in Figure 4-2. Each profile is offset from the previous by a sample intervals (a non-integer), where a is the edge slope. With zero error in the edge slope, the k^{th} profile would be aligned to the first profile by shifting to the nearest sample point to the shift ka. The residual misalignment error δ_k for each profile (within ±0.5 sample intervals) will result in an average ESF given by the general expression

$$\overline{\mathrm{ESF}}(x) = \frac{1}{N}\sum_{k=0}^{N-1} \mathrm{ESF}(x - c_k), \tag{4.9}$$

where

$$c_k = \delta_k \Delta \tag{4.10}$$

and N is the number of profiles averaged, ESF(x) is the unregistered ESF, and c_k is the misalignment for the k^{th} profile. The modulus of the Fourier transform of the above equation is (Wowk *et al.*, 1993):

$$\mathrm{MTF}_{reg}(f) = \left| \frac{1}{N} \sum_{k=0}^{N-1} \exp(-j\omega\, c_k) \right| \tag{4.11}$$

where $\omega = 2\pi f$. Wowk *et al.* (1993) derived this equation to calculate the registration transfer function by finding c_k for each profile after determining the edge slope. Droege (1979a) utilised a grouping scheme for the profiles, first dividing the profiles into K groups of profiles and shifting each group as a whole. An analytical form for the registration transfer function for the misalignment errors for this shifting procedure was developed.

These transfer functions assume that the slope is accurately determined. However, some error in the edge slope will always occur and the effect of this when registering profiles is considered here. The error in the edge slope will result in the profiles being shifted by the nearest whole number of sampling intervals to the shift kb, where b is the incorrect edge slope (Figure 4-2). The misalignment for the k^{th} profile can then be expressed as:

$$c_k = k\nu\Delta + \delta_k \Delta \tag{4.12}$$

where

$$\nu = |a - b| \tag{4.13}$$

is the edge slope error. In this case the distribution of δ_k depends on the value of b and is not the same as for zero error in the edge slope. By assuming a large number of profiles N so that the distribution of δ_k's is approximately uniform, Equation 4.9 can be expressed:

$$\overline{\mathrm{ESF}}(x) \approx \frac{1}{N}\sum_{k=0}^{N-1}\mathrm{ESF}(x - kv\Delta) * rect(x/\Delta) \qquad (4.14)$$

where $rect(x / \Delta)$ is the rectangular function, and is equal to 1 for $-0.5\Delta \le x \le 0.5\Delta$ and 0 elsewhere. The * symbol represents convolution. Fourier transforming, and taking the modulus of the above equation gives:

$$\mathrm{MTF}_{\mathrm{reg}}(f) \approx \left|\frac{1}{N}\sum_{k=0}^{N-1}\exp(-j\omega kv\Delta)\right| \cdot \frac{\sin(\pi f\Delta)}{\pi f\Delta} \qquad (4.15)$$

As the modulus of expressions of the form $\sum_{k=0}^{N-1}\exp(-j\omega kT)$ is given by $\sin(N\omega T/2)/\sin(\omega T/2)$ (Blackman and Tukey, 1958) the above equation therefore becomes:

$$\mathrm{MTF}_{\mathrm{reg}}(f) \approx \frac{\sin(N\pi fv\Delta)}{N\sin(\pi fv\Delta)} \cdot \frac{\sin(\pi f\Delta)}{\pi f\Delta} \qquad (4.16)$$

The first term describes the registration transfer due to the error in the edge slope and the second term describes the transfer due to registering to the nearest sampling point.

4.4. Theoretical transfer function of the algorithm

The transfer function of the algorithm can be expressed as a multiplication of the transfer function of each stage of the algorithm:

$$\mathrm{MTF}_{\mathrm{algorithm}}(f) = \mathrm{MTF}_{\mathrm{aper}}(f)\mathrm{MTF}_{\mathrm{reg}}(f)\mathrm{MTF}_{\mathrm{smooth}}(f)\mathrm{MTF}_{\mathrm{diff}}(f)\mathrm{MTF}_{\mathrm{fold}}(f) \qquad (4.17)$$

where

$\mathrm{MTF}_{\mathrm{aper}}$ is the transfer function for the sampling aperture and the angle of this aperture to the edge,

$\mathrm{MTF}_{\mathrm{reg}}$ is the transfer function for registration of multiple ESFs to reduce noise using the detected edge slope,

$\mathrm{MTF}_{\mathrm{smooth}}$ is the transfer function for smoothing of the ESF,

$\mathrm{MTF}_{\mathrm{diff}}$ is the transfer function for differentiation of the ESF to obtain the LSF,

$\mathrm{MTF}_{\mathrm{fold}}$ is the transfer function for folding of the LSF,

f is the spatial frequency.

and

$$\mathrm{MTF}_{\mathrm{calc}}(f) = \mathrm{MTF}_{\mathrm{system}}(f)\mathrm{MTF}_{\mathrm{algorithm}}(f) \tag{4.18}$$

The measured MTF (assuming an ideal step-edge input to the system) is the product of the MTF of the system and the MTF of the algorithm. In the case of digital imaging systems, the sampling aperture is part of the overall performance of the digital system and is not considered as an algorithm effect, however it is discussed here to demonstrate the effect of the angle of a square or rectangular aperture to the edge. The transfer functions of each of the above are defined below.

4.4.1. Sampling aperture

The MTF of a rectangular sampling aperture of width W perpendicular to an edge ($\theta = 0$) is given by Villafana (1975b):

$$\mathrm{MTF}_{\mathrm{aper}}(f) = \frac{\sin(\pi f W)}{\pi f W} \tag{4.19}$$

A rectangular sampling aperture angled to an edge is illustrated in Figure 4-3. The effect of the angle of the aperture is most easily understood by considering the aperture scanned continuously across the edge (Villafana, 1975a). When an aperture is scanned over an edge perfectly aligned to the aperture, there is linear increase in the area of the aperture overlap with the edge resulting in a ramp ESF. However when the aperture is angled, the overlap with the edge in the top and bottom regions shown in Figure 4-3 increases non-linearly, curving the top and bottom portions of the ramp (Villafana, 1975a). This curvature increases with increasing angle of the aperture, resulting in the transfer function variation with angle.

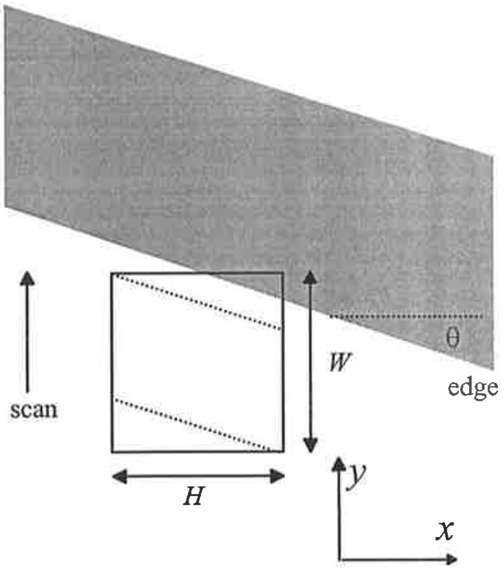

Figure 4-3 Cause of the variation in transfer function of the aperture with angle of the aperture to the edge.

The MTF of an angled aperture has been derived by Droege (1979a).

$$\mathrm{MTF}_{\mathrm{aper}}(f) = \frac{\sin(\pi f W \cos\vartheta)}{\pi f W \cos\vartheta} \frac{\sin(\pi f H \sin\vartheta)}{\pi f H \sin\vartheta} \tag{4.20}$$

A different expression for the MTF of an angled aperture has also been derived by Villafana (1979a) where, the first term describes the transfer of a sampling aperture perfectly aligned with an edge, and the second term describes the transfer due to the angle of the aperture to the edge. The relative accuracy of these two derivations is detailed in Section 4.5.

$$\mathrm{MTF}_{\mathrm{aper}}(f) = \frac{\sin(\pi f W)}{\pi f W} \cdot \frac{\sin(2\pi f H \sin(\vartheta/2))}{2\pi f H \sin(\vartheta/2)} \tag{4.21}$$

4.4.2. Profile Registration

When N edge profiles are registered using a determined edge slope with an error of v sample intervals in the slope, the transfer function is (from the previous Section):

$$\mathrm{MTF}_{\mathrm{reg}}(f) \approx \frac{\sin(N\pi f v\Delta)}{N\sin(\pi f v\Delta)} \cdot \frac{\sin(\pi f\Delta)}{\pi f\Delta} \tag{4.22}$$

4.4.3. Differentiation

The transfer function for finite-element differentiation (Equation 4.7) has been derived by Cunningham and Fenster (1987).

$$\mathrm{MTF}_{\mathrm{diff}}(f) = \frac{\sin(\pi f \Delta)}{\pi f \Delta} \tag{4.23}$$

4.4.4. Smoothing

The transfer function of the smoothing procedure is given by Droege (1979a):

$$\mathrm{MTF}_{\mathrm{smooth}}(f) = \frac{\sin(n\pi f \Delta)}{n\sin(\pi f \Delta)} \tag{4.24}$$

4.4.5. Folding of the LSF

If the points in the LSF either side of the sample point closest to the true centre of the LSF are averaged, an error in the MTF is introduced due to the distance between the true centre and the closest sampling point. The MTF of folding derived by Droege (1979a), modified to express the folding error in terms of sample intervals is:

$$\mathrm{MTF}_{\mathrm{fold}}(f) = \frac{\sin(4\pi f \lambda \Delta)}{2\sin(2\pi f \lambda \Delta)} \tag{4.25}$$

where λ is the displacement of the central sample point from the true centre of the LSF in sample intervals.

4.4.6. Frequency axis scaling

When a sloped edge is used to produce an oversampled edge function with sampling interval Δ, an error in the determined edge slope will introduce an error into the determined sampling interval Δ' (Equation 4.1). The fractional error in the sampling interval is from Equation s 4.1 and 4.8.

$$\varepsilon = {}^{\Delta'}\!/_{\Delta} = {}^{a}\!/_{b} = {}^{\Delta f}\!/_{\Delta f'} \tag{4.26}$$

This introduces a scaling error into the frequency axis of the calculated MTF. The displayed MTF is therefore

$$\mathrm{MTF}_{\mathrm{calc}}(f') = \mathrm{MTF}_{\mathrm{calc}}\left(\frac{f}{\varepsilon}\right) \tag{4.27}$$

where $\mathrm{MTF}_{\mathrm{calc}}(f')$ is the MTF with the sampling interval error and $\mathrm{MTF}_{\mathrm{calc}}(f)$ the MTF without this error.

4.5. Transfer function evaluation

In this section the derived transfer functions for each stage of the algorithm are compared against the known response of a modelled imaging system and the effect of each stage of the algorithm on the measured MTF is evaluated.

To verify the theoretical algorithm MTF expressions, LSFs were produced, simulating the sampling of an analytical LSF distribution. The LSF rather than ESF was used to avoid the transfer function of differentiation. The analytical function sampled to form the LSF was the sinc function.

$$\mathrm{sinc}(y) = \frac{\sin(2\pi Sy)}{2\pi Sy} \tag{4.28}$$

This function has the MTF equal to 1 up to a frequency of S mm^{-1} and then zero at higher frequencies. This function was used to represent a system with perfect frequency transfer up to the cutoff frequency of $f_c = S$ mm^{-1}, defined as the maximum frequency reproducible without aliasing when sampled at a frequency of $f_s = 2f_c$. This form of system MTF enables degradation of this MTF due to the sampling aperture transfer function and other algorithm process transfer functions to be easily seen.

4.5.1. Sampling Aperture

To examine the effect of the angled sampling aperture, LSF profiles sampled from the above distribution with an aperture at arbitrary angle were simulated. The cutoff frequency of the sinc MTF was set to S = 10 mm^{-1}. The profiles were sampled at the minimum frequency of $f_s = 2S$ or 0.05 mm sampling interval. An aperture of size W = 0.1 mm, and H = 0.1 mm was chosen so that the first zero crossing of the (perfectly aligned) aperture MTF was equal to S. The resulting MTF should then be equal to the aperture MTF up to the frequency S. Each sample value was obtained by integrating the sinc function along the y-direction with the y-integration limits varying as a function of the x-coordinate according to the angle and dimensions of the aperture (Figure 4-4). The spacing of each x-coordinate was 0.001 mm. To obtain the full LSF profile the centre position of the aperture was shifted in the y-direction relative to the sinc by the sampling interval. In this manner a LSF profile from sampling the sinc with an aperture at any angle could be produced. The modelled sample LSF was Fourier transformed to obtain the MTF, and the result compared to Equations 4.20 and 4.21 for the transfer function of the angled aperture. Angles of the aperture to the x-axis were studied over the range of θ = 2.4° up to θ = 45.0°.

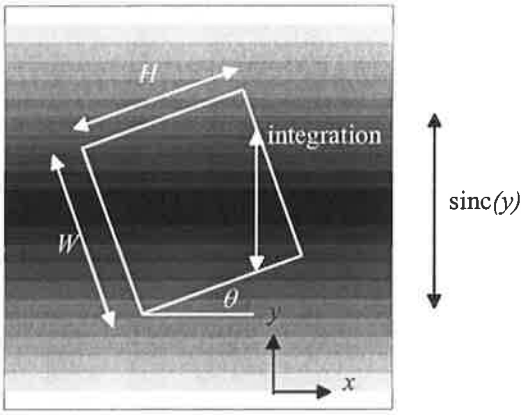

Figure 4-4 Method to obtain a simulated sampled profile from a sinc function distribution with an angled aperture.

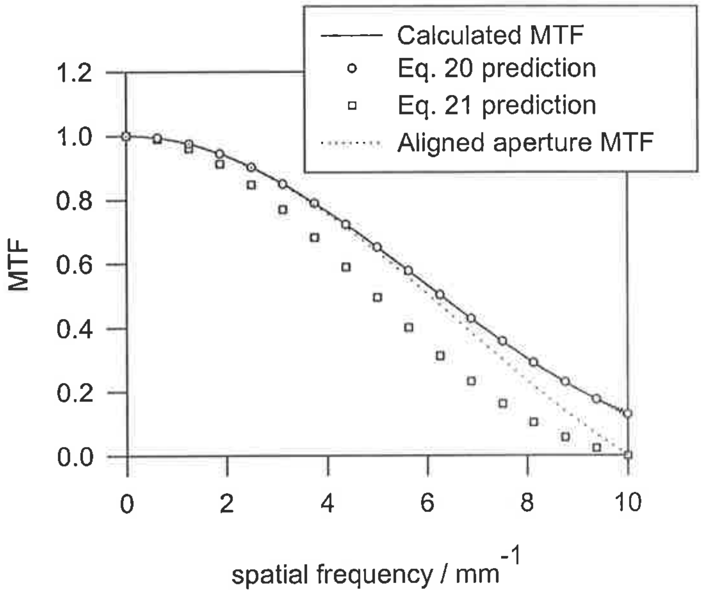

Figure 4-5 Angled aperture MTF from the sampled LSF compared to the theoretical transfer function equations for an angle of θ = 45°, the largest possible. Also shown is the aperture transfer for a perfectly aligned aperture (θ = 0°). Equation 4.20 **accurately predicts the aperture MTF while Equation** 4.21 **underestimates it.**

Figure 4-5 shows the MTF from the sampled LSF compared to the theoretical transfer functions for the aperture of width $W = 0.1$ mm and length $H = 0.1$ mm, at an angle of θ = 45°, the largest possible. Also shown is the aperture transfer function for a perfectly aligned aperture ($\theta = 0°$). Equation 4.20 accurately predicts the angled aperture MTF while Equation 4.21 underestimates it. For all angles studied, Equation 4.20 had excellent agreement with the calculated MTF. Equation 4.21 was found to have increasing error with increasing angle.

The modification of the aperture MTF due to the angle of the aperture is demonstrated in Figure 4-6 for a square $W = 0.1$ mm, $H = 0.1$ mm aperture, and a rectangular aperture with $W = 0.1$ mm and $H = 0.2$ mm. The value of Equation 4.20, at the first zero-crossing frequency of the perfectly aligned aperture (10 mm^{-1}) is shown with varying angle of the aperture. The angle of the square aperture increases the transfer function value relative to a perfectly aligned aperture. The figure shows that for angles of less than 10 degrees, the transfer function value is increased by less than 0.01 in both cases, and therefore the angle will have minimal impact on the measured MTF. These results are independent of aperture size W, as at the first zero-crossing frequency, f is equal to $1/W$ in Equation 4.20.

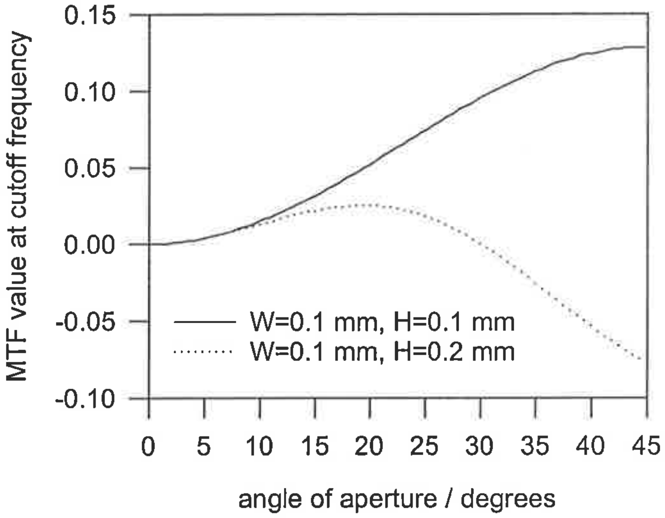

Figure 4-6 Effect of angle of the aperture on the aperture MTF at the cutoff frequency. Values of Eq. 20 are shown for a square $W = H = 0.1$ mm aperture, and a $W = 0.1$ mm, $H = 0.2$ mm, rectangular aperture. The transfer value is increased due to the angle by less than 0.01 for angles below 10 degrees.

4.5.2. Profile Registration

To verify that the derived Equation 4.16 accurately describes the transfer function of registration, multiple LSF profiles were sampled from the sinc function (S = 10 mm^{-1}), each profile shifted relative to the previous, simulating profiles sampled along the rows of an angled slit image. A zero-width aperture was used to eliminate the transfer function of the sampling aperture. The offset of each profile (edge slope) was an arbitrary a = 8.3 sample intervals. The profiles were oversampled at a sampling frequency $f_s = 1/\Delta = 8f_c$ (4 times oversampling). Note that f_c here retains its definition as the maximum frequency reproducible without aliasing when sampling at $f_s = 2f_c$. It refers to a system cutoff frequency f_c = 10 mm^{-1}, rather than a maximum frequency reproducible without aliasing at the measurement oversampling frequency. Fifty profiles were sampled in this manner and then registered to the nearest sample point to the offset ka, representing perfect edge slope determination (b = 8.3). The MTF was then calculated by Fourier transformation of the registered LSF and compared to Equation 4.16. Similarly, the 50 profiles were registered but with a ν = 0.08 sample interval error in the edge slope (b = 8.22). This corresponds to a 0.07° error in the 7° edge angle θ (1% angle error). The MTF was again calculated from the registered LSF by Fourier transformation.

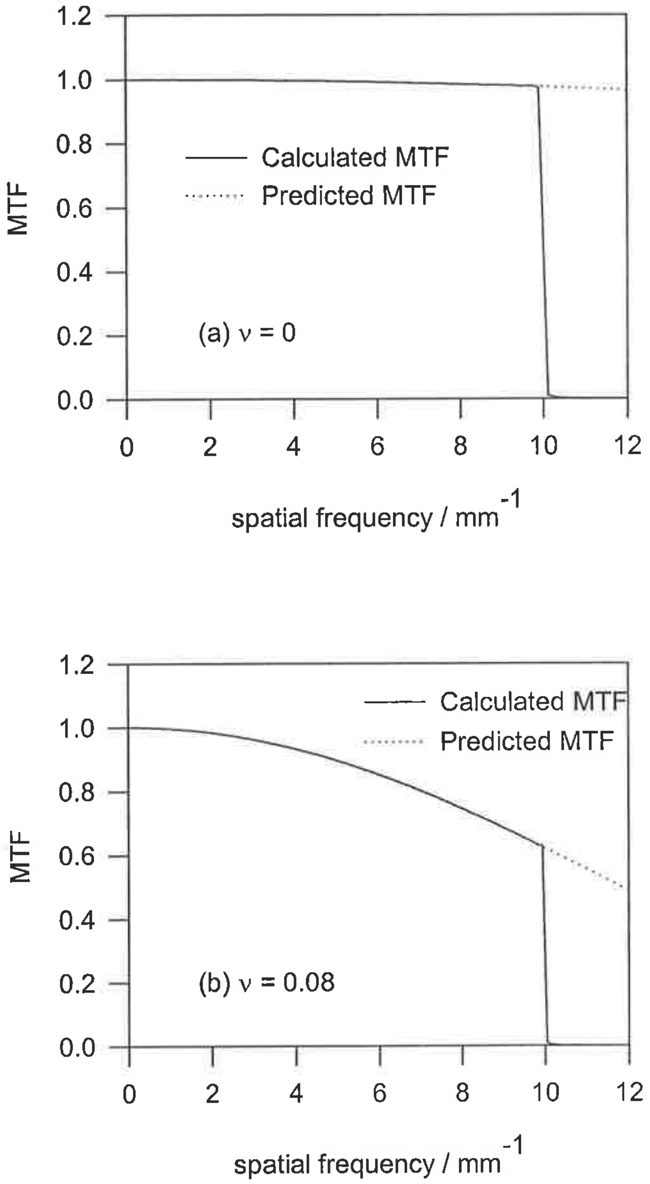

Figure 4-7 Registration MTF resulting from 50 LSF profiles, (a) due to registration to the nearest sampling point, and (b) with a 0.08 sample interval error in the edge slope (1%). The sampling frequency was 8 times the system cutoff frequency of 10 mm^{-1}.

Figure 4-7(a) shows the MTF resulting from the registration to the nearest sample point ($\nu = 0$). There is a small but apparent effect on the sinc MTF due to the registration errors that are within ±0.5 sample intervals in this case, (Equation 4.16 becomes undefined for $\nu = 0$, however in the limit as ν tends to zero, the first term tends to 1). The relatively small effect of these registration errors (MTF = 0.974 at f_c) is due to the oversampling at $f_s = 8f_c$, as this reduces Δ and hence the effect of the registration. Figure 4-7(b) shows the MTF resulting from the profiles registered with the $v = 0.08$ sample interval error in the edge slope. The effect of this edge slope error is large, with a 36% error in the MTF at f_c due to the edge slope error. The large effect of the error in the edge slope is due to the increase in the misalignment error c_k with profile number (Equation 4.12), a small error in the edge slope compounds to produce large misalignments. The registration MTF is therefore very sensitive to the value of v. In this case the maximum misalignment is 4 sample intervals. Equation 4.16 predicts the resulting transfer function due to the registration errors in both cases.

The accuracy of the edge slope determination algorithm was investigated to determine the size of the edge slope errors, and hence the magnitude of the registration MTF. Initially, the accuracy of the edge location determination in the individual profiles from the inverse polynomial fitting was found. Gaussian noise with a standard deviation of 2% of the edge contrast was added to edge profiles to represent a low SNR (Steckner, 1993). The inverse polynomial was fitted to the profiles to obtain the edge locations. The edge locations were determined to within ±0.2 sample intervals; mean = 0.000, standard deviation (SD) = 0.08, 250 trials. The noise was increased to 5% to represent an extremely noisy image. The locations were then determined to within ±0.65 sample intervals (SD = 0.2, 250 trials). The distributions of the individual edge location errors were found to be Gaussian in shape.

To find the edge slope determination accuracy, the linear least squares line fit was performed to $N = 25$ individual edge locations, each edge location representing one row profile from an edge at arbitrary edge slope of $a = 8$, or $\theta = 7.1°$. The 25 locations were initially assigned values of ka according to the edge slope, and then errors in these locations were added by sampling from Gaussian distributions with SD = 0.08 (2% noise level), and SD = 0.2 sample intervals (5% noise level) respectively. The linear least squares fit was then applied to the edge locations to determine the edge slope. The distribution of errors in the edge slope were recorded. For the 2% noise level, the edge slope was determined within ±0.009 sample intervals (SD = 0.002, 1000 trials). For the 5% noise the slope was determined within ±0.02 sample intervals (SD = 0.006, 1000 trials). An error of $v = \pm 0.02$ corresponds to an error of ±0.02° in an edge angle of $\theta = 7.1°$ (0.25% error), or an error of ±0.23° in an edge angle of 26.7° (0.9% error). The actual slope of the edge was found to have no effect on the values of v when the slope was varied with $a = 8$

to 24 ($\theta = 7.1°$ to $1.8°$). Therefore for a particular system, decreasing the edge slope will reduce the effect of edge slope error when registering profiles, as the sampling interval Δ will decrease (oversampling increases), provided the same N is maintained.

The number of edge locations was varied to determine the relationship between the length of the edge used for the slope determination and the slope estimate. The edge slope error was determined for values of N from 10 to 100. The error was found to decrease approximately exponentially with increasing N. For example, for values of N of 12, 25 and 50 for the 2% noise level the resulting errors ν were within ±0.025, 0.009 and 0.003 sample intervals, with SD's of 0.007, 0.002 and 0.0008 respectively. The MTF of registration is a function of $N\nu$ for fixed Δ (Equation 4.16). If all the profiles used to determine the edge angle are registered then as N increases linearly, the value of ν decreases more rapidly (exponentially). Therefore utilising more row edge profiles (length of edge) will reduce $N\nu$ and the effect of profile registration. Alternatively a greater number of row profiles could be used for the edge slope determination than the number of profiles registered. This will reduce ν without increasing N. Provided $N\nu$ is less than or equal to 1, the effect of the edge slope error will be similar or less than the effect of registration to the nearest sample point (Equation 4.16).

Figure 4-8 illustrates that with the edge slope accuracy of this algorithm, the effect of the edge slope error on the MTF is small, provided the edge profiles are oversampled. The figure shows the value of Equation 4.16 for the MTF of registering $N = 25$ profiles with a slope error of $\nu = 0.02$ sample intervals, oversampling at $f_s = 8f_c$. This error ν corresponds to an error of 0.02° in an edge angle of $\theta = 7.1°$ ($a = 8$). The MTF is only slightly modified from the MTF that would result from zero error in the edge slope. The value of the component of the MTF due to the edge slope error is 0.994, compared with 0.974 for the nearest sample point component. The edge slope and therefore the shift of each profile, is determined sufficiently accurately that the registration error c_k is largely comprised of the error due to registering to the nearest sample point (Equation 4.12). However the same edge slope error will have a greater effect if the profiles are not oversampled. Sampled at $f_s = 2f_c$ the same error produces a 10% error in the MTF at f_c when 25 profiles are registered, and a 36% error at f_c when 50 profiles are registered. This maximum slope error of $\nu = 0.02$ (0.02° in an edge angle of $\theta = 7.1°$) for up to 5% noise levels, means that provided an edge slope is employed that results in oversampling at $f_s = 8f_c$ (4 times oversampling), and the number of profiles registered is $N \leq 50$, the MTF error at $f = f_c$ due to edge slope error will be less than 2.5%. In practice the error will be less than this as the edge slope error will be less than 0.02. Note that the component of the registration MTF due to nearest sample point registration results in a further error of 2.6% at this oversampling rate.

The accuracy of the edge determination does however depend on the algorithm employed. This algorithm finds the edge location for each profile to sub-sample point accuracy. If the edge locations were determined by thresholding the image, the individual edge location errors will be distributed between 0 to 1 sample intervals, assuming perfect thresholding. To compare the accuracy in this case to the sub-sample point method, errors in the edge locations were sampled from a uniform distribution of width 1 sample interval. The linear fit was then made to these locations. For $N = 25$ the results for v were within ± 0.03 sample intervals, (1000 trials). The errors are much greater than that found for the 2% noise level with sub-sample point edge detection, although similar to the 5% noise level.

The registration MTF when the profiles are registered using the shift determined from the edge angle was compared to the MTF when the profiles are registered using the individual edge locations. Twenty five individual edge location errors were sampled from a Gaussian distribution a SD of 0.2 sample intervals representing the 5% noise level. The residual misalignment of each profile was then found by aligning each profile to the nearest sample point. The MTF of registration was calculated with Equation 4.11. The edge slope was then determined from the edge locations and the residual misalignments calculated when the shifts were determined by the edge angle. Again the MTF or registration was determined and compared to the MTF when the individual locations were used. This was repeated 100 times and the mean MTF in both cases calculated and compared. The MTF when the line fit was used to calculate the offset of each profile was a maximum of 20% higher than the MTF when the individual locations are used. When this was repeated for the 2% noise level the MTFs were similar. These results suggest that the edge slope gives more accurate registration than the individual locations when the edge locations are determined to sub-sample point accuracy.

The measured MTF can be corrected for the component of the registration errors due to registering to the nearest sample point. This can be done by utilising the second term in Equation 4.16 that describes the effect of these errors. Obviously the error in the edge slope is generally unknown and the calculated MTF can not be corrected for this component of the registration transfer function. However if the edge slope errors are small the residual error in the MTF due to these errors is small. For example in the above case of the 0.02 sample interval error in the slope, sampling at $f_s = 8f_c$, correction for only the component due to nearest sample point registration errors leaves a residual error in the final MTF of only 0.6% at the cutoff frequency.

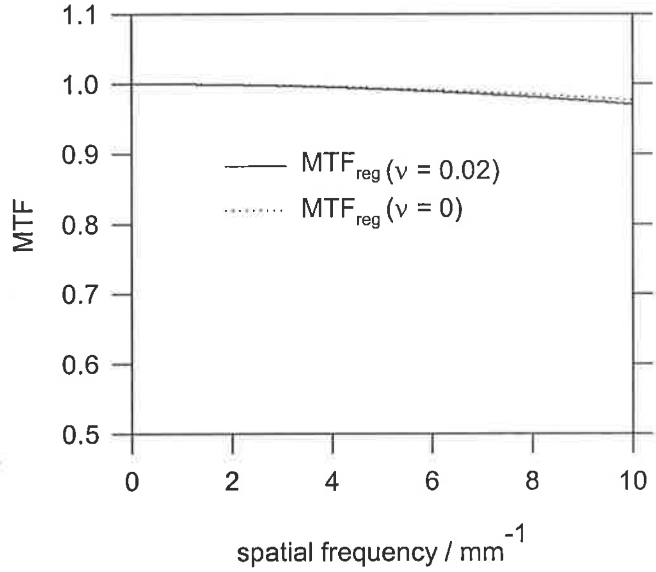

Figure 4-8 MTF of registration of 25 profiles, sampled at 8 times the system cutoff frequency, with and without a 0.02 sample interval error in the edge slope. The effect of the error in the slope is small, the predominant effect being registration to the sample point nearest the offset of the profile. The error of 0.02 pixels was the maximum found with this edge slope determination algorithm up to a 5% noise level.

4.5.3. Smoothing, Differentiation, and Folding

The transfer functions for the smoothing and folding processes were verified in the same manner, by calculation of the MTF from a LSF sampled with zero width aperture from the sinc distribution after the individual process had been applied. These MTFs were compared to the theoretical expressions. In all cases there was good agreement. Verification of the transfer of differentiation has been previously reported (Cunningham and Fenster, 1987).

Smoothing of the edge profile is employed to increase the SNR as a low SNR increases the uncertainty in the MTF determination.

Figure 4-9 illustrates from Equation 4.24 the variation of the MTF of smoothing at the system cutoff frequency f_c with the oversampling frequency f_s relative to f_c. This shows the effect of oversampling the profiles on the smoothing MTF. It is seen that high profile oversampling frequencies are required to give a small effect. The measured MTF is not corrected for the effect of smoothing, as this would reintroduce the noise suppressed by the smoothing procedure (Droege, 1979a). Therefore, it is important to ensure that the profile oversampling frequency is sufficient to avoid large errors in the MTF. For example, to limit the error in the calculated MTF at f_c due to smoothing to less than 5%, when employing a $n = 3$ smoothing mask, the profile sampling frequency would have to be at least $16f_c$, or 8 times oversampling. The effect of the smoothing is the same for a real system with blur as for an ideal system.

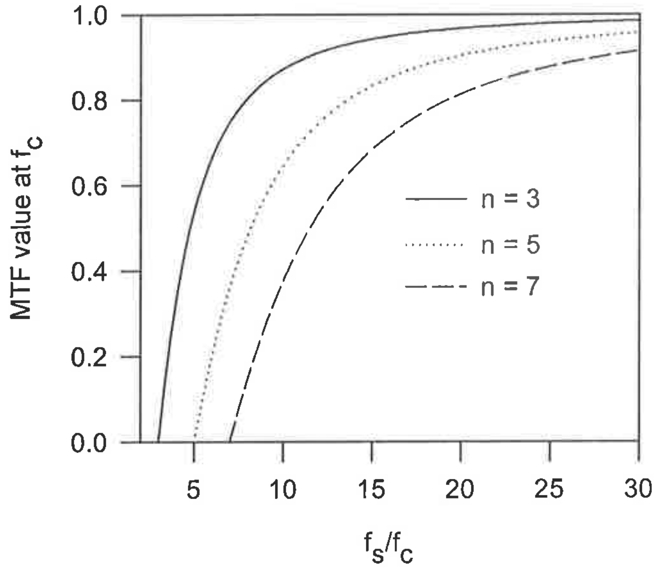

Figure 4-9 MTF of smoothing at the system cutoff frequency as a function of the oversampling frequency relative to the cutoff frequency.

The transfer function of differentiation has the same magnitude effect as that shown in Figure 4-7(a) for the same profile oversampling frequency $f_s = 8f_c$, (2.6% error in the MTF). It reduces in effect as the sampling frequency increases. However, sampling at $f_s = 2f_c$, the differentiation MTF is similar to that shown in Figure 4-7(b) giving an error in the

MTF of 36%. In all cases, the calculated MTF can be corrected for differentiation by dividing by Equation 4.23.

Provided the centre of the LSF is determined precisely then the maximum folding error λ is half a sampling interval. The measured MTF is corrected for the folding procedure by dividing by Equation 4.25, after determination of the centre of the LSF, and hence λ. Errors in the MTF will however be introduced if the centre of the LSF is not determined accurately. The previous analysis of the accuracy of edge location determination shows that the centre location is determined sufficiently accurately by the algorithm, particularly as the noise level in the registered ESF will be low following profile registration.

4.5.4. Frequency axis scaling

Figure 4-10 shows the effect on an MTF of an error in the sampling interval and hence frequency axis due to edge slope error. This is shown for an arbitrary MTF of a sampling aperture of width 0.1 mm. The aperture MTF with the correct frequency axis is shown along with the same MTF but with a 1% and a 5% error in the edge slope and hence frequency axis ($\varepsilon = 0.01$, and 0.05). The impact on the measured MTF due to a 1% edge slope error is small. Thus for the edge slope accuracy determination of this algorithm, this will not be an important effect on the calculated MTF or on the corrections applied for algorithm effects (as these are functions of Δ).

4.6. MTF measurement and transfer function for a simulated image

In this section the accuracy of MTF calculation by the algorithm is verified by applying the algorithm to a test image with known MTF. The effect of the transfer function of the algorithm on the calculated MTF was also investigated. A noiseless knife-edge test image was created with an arbitrary edge slope of $a = 8.3$ ($\theta = 6.9°$) to the horizontal axis, and a 0.2 mm square sampling aperture was assumed. The sampling pitch of the image was in this case made equal to the aperture width. This image was input to the program and the MTF calculated by the program using the procedure outlined in Section 4.2 This digital knife-edge image has an MTF equal to that of the 0.2 mm sampling aperture, a sinc function with a first zero-crossing frequency of 5 mm^{-1}. The MTF measured by the algorithm should therefore be equal to this MTF, but will be modified by the algorithm effects of registration, differentiation, smoothing and folding.

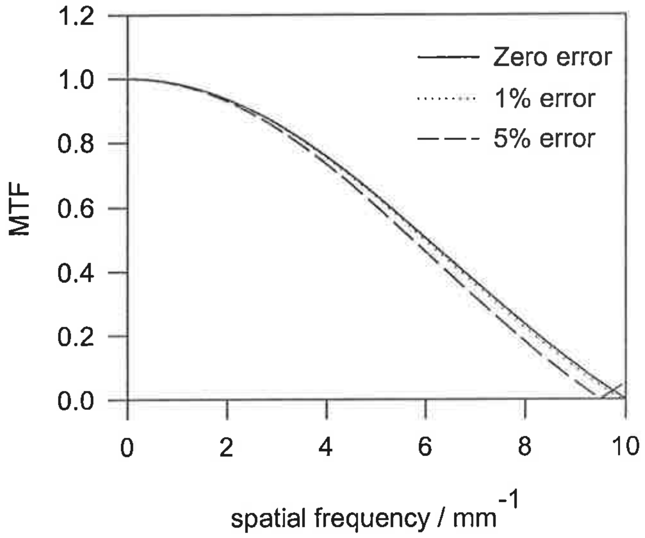

Figure 4-10 Frequency axis scaling. The effect of a 1% and 5% error in the determined edge slope on the MTF due to the incorrect calculation of the sampling interval. The 1% error is small. Thus for the edge slope determination accuracy of this algorithm, this is not an important effect.

Twenty-five row profiles with a sampling interval of 0.2/8.3 = 0.024 mm were sampled from the image. These profiles are oversampled due to the angled edge at a frequency of 8.3 times the first zero-crossing frequency of the image MTF, considering this zero-crossing frequency as the system cutoff frequency. The edge slope was determined, and the profiles registered together by shifting to the sample point nearest the offset due to the edge slope. As the edge slope is determined perfectly for a noiseless image, an edge slope error of 0.02 sample intervals was artificially introduced before registration. The registered ESF was then smoothed by replacing each value by the average of three adjacent sample points (n = 3), differentiated to obtain the LSF, and the LSF was folded about the central sample point. The folding error (distance from the true LSF centre to the closest sample point) was λ = 0.39 sample intervals. Finally, the MTF was calculated by Fourier transformation of the folded LSF.

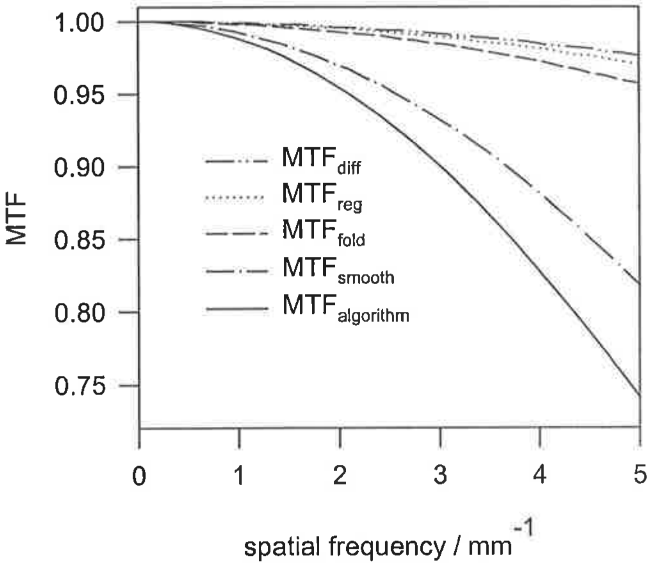

Figure 4-11 Transfer function of the algorithm for the MTF measurement. The differentiation, registration and folding are similar in magnitude while the smoothing has a much larger effect.

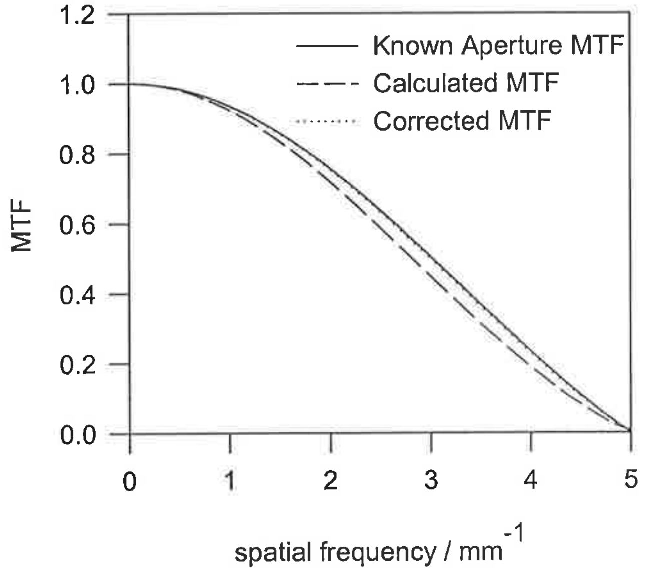

Figure 4-12 Measured MTF for the test image compared to the known sinc MTF of the image, with and without correction for the MTF of the algorithm. When the effect of the algorithm is removed there is good agreement between the MTFs.

Figure 4-11 shows the components of the transfer function of the algorithm for the above measurement and the resultant MTF of the algorithm. Note the reduced *y*-axis. The differentiation and registration are similar, the folding somewhat greater, while the smoothing is a much larger effect. Figure 4-12 shows the calculated MTF compared to the known sinc MTF of the image. The calculated MTF is smaller than the sinc MTF, approximately 0.9 of the sinc MTF value at the 50% MTF level ($f \sim 3$ mm^{-1}), and 0.83 of the sinc MTF at the 20% MTF level ($f \sim 4$ mm^{-1}). Figure 4-12 also shows the calculated MTF after correction for the MTF of the algorithm. Good agreement is then seen. The smoothing procedure would not usually be corrected for in this manner, however this was done to verify that the MTF of the algorithm described the error in the calculated MTF. To reduce the effect of the algorithm, a shallower edge slope (increased a) could be employed to increase the oversampling.

4.7. MTF measurement for an experimental edge image.

The MTF calculation program was applied to the measurement of the MTF of a Vidar VXR-12 CCD-camera film scanner (Vidar Systems Corporation, 460 Spring Park Place, Herndon, VA). The MTF of digital film scanners have been measured by utilising a thin line input to obtain the LSF directly (Yin *et al.*, 1990). To measure the MTF using the edge method, the knife-edge object to be scanned was created by utilising the edge of a sheet of white paper, overlaid onto a sheet of overhead transparency film. This provided a step-edge in optical density on a background density level (to prevent saturation of the scanned values). This edge was scanned with a small angle to the horizontal axis of the scanner with 0.085 mm (300 dots per inch) sampling pitch. A total scanned area of 91 mm across and 22 mm down was saved to file. The pixel values were converted to optical density via cubic spline interpolation of a lookup table of optical density to Vidar pixel value.

The MTF was calculated as described in Section 4.2. The edge slope was determined as a = 12.77 pixels (4.5°) by the algorithm. This slope was utilised to average 50 row profiles oversampled along the edge with sampling interval of 0.085/12.77 = 0.006 mm. The average profile was differentiated to obtain the LSF. The LSF was Fourier transformed to obtain the MTF.

To compare the measured MTF to that obtained with the line method, the MTF was also measured with this technique. A 100 mm long line of width 0.021 mm was drawn on another clear transparency sheet with a Datapoducts Typhoon 1200 dots per inch printer.

This line was again scanned with a small angle to horizontal at 0.085 mm sampling pitch. The Vidar pixel values were converted to optical density as above. The MTF was obtained by Fourier transformation of the average LSF after registering 50 profiles. The edge slope was determined as $a = 5.5$ (10.3°) in this case by centre-of-gravity determination of the centre of each LSF profile (Steckner *et al.*, 1993). No smoothing or folding of the LSF was employed.

The resulting MTFs are shown in Figure 4-13. Reasonable agreement is seen between the two MTFs, although the result from the edge method has a drop at low frequencies. The agreement at higher frequencies is excellent. A rectangular sampling aperture is assumed for the scanner and the MTFs represent the MTF of the scanner and hence the scanning aperture width in the vertical direction. To measure the MTF in the horizontal scanning direction the edge angle would be placed at a small angle to vertical, and the edge function profiles sampled along the column direction.

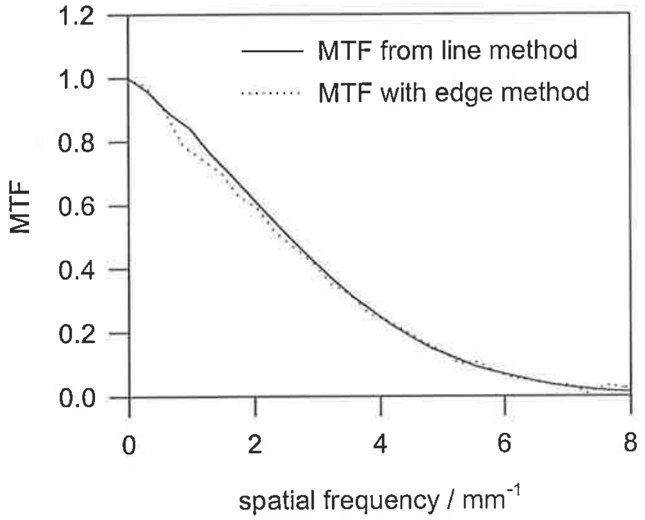

Figure 4-13 MTF of the Vidar film digitiser, measured with the angled edge algorithm, and compared to the traditional line method. There is reasonable agreement between the two although the edge results show a slight low frequency drop. There is good agreement at higher spatial frequencies.

4.8. Discussion

The method of sampling where oversampled edge function profiles are obtained by sampling successive points in the direction most parallel to the edge (Judy, 1979) as shown in Figure 4-1 is a well established technique for digital presampling MTF calculation. Profiles from a two-dimensional (2-D) edge region are sampled and registered together to form a 1-D profile with improved SNR. The profile is obtained with even sample spacing, and the degree of oversampling can be varied according to need by modification of the edge angle. A disadvantage to this approach is that with small edge angles the profile must extend for a large distance along the edge to obtain a sufficient length profile. This relies on edge uniformity across the image.

Methods based on the same principle, but obtaining sample points over a smaller length of the edge have been proposed. Fujita *et al.* (1992) sampled successive profiles in the direction perpendicular to the edge. Each profile is displaced slightly from the previous with respect to the edge due to the edge slope. When the slope is exactly an integer number of pixels, these profiles can then be 'meshed' to form a uniformly spaced profile with reduced sample interval. However an edge slope of exactly an integer number of pixels is difficult to achieve in practice. To avoid this constraint a meshed profile when the edge angle is arbitrary can be formed. The determined edge angle is used to place each profile relative to the previous in the meshed 1-D profile (Reichenbach *et al.*, 1991; Samei and Flynn, 1998). This generally results in non-uniform spacing of the data so the data are then resampled or binned. The bin width then becomes the sub-pixel sampling interval making the sampling interval independent of edge angle. This method has also been referred to as reprojection of the 2-D data set using the edge angle (Samei, 1998). As all of these methods rely on the principle of an angled edge to obtain an oversampled edge profile, they should in principle, produce the same results for presampled MTF measurement.

The verification of the sampling aperture transfer function performed here showed that the method of Droege (1979a) (Equation 4.20) accurately models the transfer function of an angled sampling aperture. The method of Villafana (1975a) was found to become increasingly inaccurate as the edge angle increased. No verifications of these derivations were previously reported. The method of Villafana was derived for the case of a scanning microdensitometer aperture slightly misaligned from an edge or slit. In this case the angle is small and the errors in the transfer function may be unimportant. However in the case of an angled edge or slit for digital presampling MTF measurement, the angle of the aperture can be large, and the method of Droege accurately describes the transfer function. The angle of a rectangular aperture to the edge was found to increase the transfer function values relative to a perfectly aligned aperture. Provided the angle of the aperture was less than 10 degrees, the increase of the aperture MTF value at the cutoff frequency of the aperture was found to be less than 0.01, and will therefore have only a small impact on the measured MTF. The analysis of aperture transfer function was performed here to determine the effect of the angle of a rectangular aperture to the edge on the calculated MTF. For a radially symmetric aperture such as for a laser film scanner, the angle of the edge to the aperture would have no effect on the transfer function of the aperture. As the aperture MTF is part of the system response, the effect of edge angle in this case does not need to be considered as an algorithm effect.

Previous derivations for the MTF of profile registration have accounted for profile misalignment due to the fact that profiles can only be registered to the nearest sampling point (Droege, 1979a, Steckner *et al.*, 1993; Wowk *et al.*, 1994). Samei and Flynn (1998) determined the effect of edge angle error in their projection method. This was done by explicitly calculating the MTF from a knife-edge test image for defined errors in the angle. The results were specific to the edge angle, bin width, and the sinc MTF of the image that were employed. A generalised analytical expression for the effect of the angle error on calculated MTFs was not developed.

In this work, the effect of the error in the edge angle was found to be large for relatively small errors in the edge angle, as seen in Figure 4-7(b). However, the accuracy of the edge slope determination algorithm employed here resulted in the effect of the edge angle error being small compared to the effect of profile registration to the nearest sample point, when 25 profiles were registered with 4 times oversampling. The effect of registration was found to reduce with increased number of profiles (length of edge) utilised for the edge slope determination, as the edge slope errors decrease approximately exponentially. The edge slope errors v were found to be independent of the slope, meaning for a particular system, and fixed N, reducing the edge slope will reduce the registration effect by increasing the oversampling.

The results highlight that edge angle determination algorithms should be tested for accuracy with edges of known angle and SNR. Methods of edge detection have included centre-of-gravity determination of the centre of LSF profiles obtained by differentiating ESF profiles (Steckner *et al.*, 1993). This method reduces the SNR in the profile by differentiation. Thresholding to detect the edge has been employed (Samei and Flynn, 1998), however this does not obtain the edge location to sub-sample point accuracy and will result in larger registration errors. To determine the edge angle Samei and Flynn (1998) applied a gradient operation to the thresholded image to obtain a line image, and then utilised the Hough transform to obtain the angle. This process was not sufficiently accurate in determining the angle and a further MTF maximisation algorithm was required. The edge angle determination method of Bentzen (1983) employed here was found to be accurate and relatively insensitive to noise making this a robust technique.

If curvature of the edge is present this is readily seen from the linear fit to the individual edge locations. Ideally, in this case the profile sampling and edge slope determination should be restricted to a short length of the edge. Slight curvature of the edge will result in a slowly varying rather than fixed sampling interval for the edge function profiles. Similarly the curvature would result in a slowly varying offset of each profile from the previous, although this could be accounted for by shifting each profile according to the individual edge locations rather than the linear line fit.

The effect of the smoothing mask on the MTF was found to be large, and this demonstrates that reduction of noise by this type of spatial mask filter should be used with caution, and only with high sampling frequencies relative to the cutoff frequency. A correction to the MTF should not be applied for the smoothing procedure as this re-introduces the noise suppressed by the smoothing, the smoothing mask is inherently a frequency filter. Other smoothing masks that have been applied to sampled ESF data have included a Gaussian weighted moving polynomial fit (Samei and Flynn, 1998). To determine the effect of the smoothing on the MTF of a noisy knife-edge image, MTFs were calculated by varying the parameters of the polynomial. These results were again specific to the sampling pitch of the image, the bin width, and the sinc MTF of the image. Use of polynomial fitting rather than an equally weighted smoothing mask may reduce the frequency filtering for a similar noise reduction level. However the effect of the smoothing on the calculated MTF is not then defined by a simple analytical equation.

A commonly used alternative to the differential operator employed here is to obtain each LSF value by the expression $\mathrm{LSF}(x_j) = 1/2\Delta\left(\mathrm{ESF}(x_{j+1}) - \mathrm{ESF}\ (x_{j-1})\right)$. In this case the derivation method of Cunningham and Fenster (1987) can also be used to determine the MTF of the differentiation process, and the MTF is a sinc function as in Equation 4.23, but with Δ replaced by 2Δ. The effect on the calculated MTF of the differentiation process is then greater in this case, but can also easily be corrected for.

To determine the centre of the LSF for folding, the algorithm outlined here used the ESF for determination of the centre due to the higher SNR of the edge profile. The accuracy was found to be sufficient so that the maximum folding error λ will be generally half the sampling interval. The folding error λ is easily found and the MTF corrected for this. The folding will however introduce further, unrecognised error into the MTF if the true centre of the LSF is not determined accurately as the nearest sample point to the true centre may then not be used for the folding procedure. Droege (1979a) fitted a symmetric function to the LSF to determine the true centre of the LSF however the accuracy of this method was not stated. Folding is a technique usually applied for noise reduction with symmetric LSF's. In the case where system blur is anisotropic, resulting in a non-symmetric LSF, folding of the LSF would result in an an averaging of the system blur.

The scaling of the discrete frequency axis due to an error in the determined edge angle identified here applies to the display of the calculated MTF. The scaling did not alter the displayed MTF significantly for errors in the edge angle of less than 1%. Thus with the edge determination accuracy of this algorithm the error in the frequency axis is not an important effect.

The measurement of MTF with a knife-edge image of known MTF was used to verify the algorithm calculation of MTF and the overall description of the MTF of the algorithm. After correction of the measured MTF by the theoretical algorithm MTF, good agreement was obtained with the known MTF of the image. The MTF calculated by the algorithm for the film scanner was in reasonable agreement with that obtained with the line technique. The reason for the low frequency difference is unknown, however Cunningham and Reid

(1992) have demonstrated that the edge method is superior to the slit method in assessing low frequency MTF, and therefore this reduction in MTF may be present for this system.

4.9. Conclusion

The transfer function of an MTF algorithm has been analysed, incorporating the effects of angle of the sampling aperture to the edge, registration of multiple profiles using the determined edge angle, differentiation, smoothing and folding. A derivation for the effect of error in the determined edge angle when registering profiles was developed. The edge angle error can modify the calculated MTF significantly. For example a a 0.07 degree error in a 7 degree edge angle produces a 36% error in the MTF at the system cutoff frequency $f = f_c$ when profiles are oversampled at a frequency $f_s = 8f_c$ (f_c is defined as the maximum frequency reproducible without aliasing when sampling at the limiting Nyquist frequency $f_s = 2f_c$). The results emphasise the importance of quantifying the effect of the algorithm on the calculated MTF, and in particular the accuracy of edge angle determination. The algorithm and the description of the algorithm transfer function have been incorporated into a Windows-based program for MTF calculation.

5. A design for a dual assembly multileaf collimator

5.1. Introduction

Multileaf collimators (MLCs) are now widely used to produce irregularly shaped beam apertures in radiotherapy (Brahme, 1987; Galvin *et al.*, 1992; Boyer *et al.*, 1992; Galvin *et al.*, 1993a; Jordan and Williams, 1994; Huq *et al.*, 1995; LoSasso *et al.*, 1993). As seen in Chapter 1 they have a number of advantages over custom made alloy blocks. They save time compared to alloy block fabrication, are non-toxic, and treatment times are reduced as multiple fields can be set without entering the treatment room. This efficiency has led to therapy techniques with larger numbers of beams. MLCs are also currently being utilized for intensity modulated radiation therapy (Kallman *et al.*, 1988; Convery and Rosenbloom, 1992; Galvin *et al.*, 1993b; Bortfeld *et al.*, 1994; Spirou and Chui, 1994; Ling *et al.*, 1996).

Limitations of the MLC include inter-leaf transmission between adjacent leaves. This is of particular concern for intensity modulated radiation therapy where irradiation times are long. A tongue and groove design of abutting leaves is employed to reduce inter-leaf transmission, however this is still higher than the intra-leaf transmission (Galvin *et al.*, 1993a; Jordan and Williams, 1994). The tongue and groove design can also result in regions of underdose in intensity modulated treatments (Balog *et al.*, 1999). When defining angled field edges the stepped pattern of the leaves results in a larger effective penumbra than for alloy blocks (Galvin *et al.*, 1998). A method to reduce the effective leaf width by segmenting the field, moving the couch a fraction of the leaf width in the direction orthogonal to leaf motion, and repositioning of the leaves has been proposed (Galvin *et al.*, 1996; Steinberg, 1999).

Treatment verification by imaging of the field placement relative to the patient anatomy is an important part of the radiation therapy process. The double-exposure port film superimposes a treatment portal image onto a larger "overflash" image of the patient anatomy. Recently electronic portal imaging devices (EPIDs) have also been utilized to provide these images. Single-exposure images of just the treatment portal can be acquired during the treatment however these images have not gained wide acceptance for verification. The double-exposure imaging process however is slow due to retraction of collimation to provide the overflash image. They can not be acquired during the treatment and therefore may not be representative of the treatment position. In this work an MLC design is proposed and investigated that facilitates rapid acquisition of double-exposure treatment verification images, as well a reduction in inter-leaf transmission. The design also enables implementation of the method to reduce the effective leaf width by multileaf collimator rather than couch movement.

Swerdloff *et al.* (1994) in their patent for a tomotherapy fan-beam intensity modulating collimator proposed splitting the vanes of the collimator into two vertically displaced levels, with each level consisting of alternate vanes and vane-width spaces. The upper level of vanes shields the spaces in the lower level. This was proposed to eliminate friction between adjacent vanes in the rapid movement of these in and out of the fan beam aperture, and enable overlap of adjacent vanes to reduce inter-leaf transmission. However this design has not been implemented in the prototype tomotherapy collimator.

The MLC design proposed here separates each bank of a standard MLC into two vertically displaced assemblies or levels, each level consisting of a grid of alternate leaves and leaf-width spaces. The leaves in the upper level shield the spaces in the lower level. Each complete level is also capable of lateral movement up to a leaf width. By such a movement of one level the two grids of leaves would be aligned. Radiation would then be transmitted through the interleaf spaces as multiple slit fields in a grid pattern. This radiation transmission could be utilized to image the patient anatomy external to the treatment field, and the image could be acquired during the treatment. Cone-beam CT could potentially be performed provided sufficient beam directions were used to deliver the treatment. With current MLC leaf speeds of 1.5 cm s^{-1} (at isocenter), retraction of a leaf from the central axis to fully retracted, followed by repositioning to the central axis requires ~ 30 s. Assuming a similar speed for lateral movement of the levels in this design, the time for the movement required for image acquisition would be ~ 1-3 s depending on leaf width. Further time saving may be possible by integrating the imaging process during the treatment delivery and thus removing operator "dial-up" time.

The lateral movement capability also enables the effective leaf width to be reduced by movement of the MLC rather than the treatment couch. Each MLC level would be moved by a fraction of the leaf width and the leaves repositioned to the field border. The vertical displacement of adjacent leaves would also allow overlap of the leaves to reduce inter-leaf transmission. However the collimator would require greater space in the accelerator head due to the vertical displacement of leaves. Note that the collimator proposed here is not a tomotherapy collimator, but a modification to the traditional cone-beam radiotherapy MLC design and could not be used for tomotherapy beam delivery.

In this work this proposed MLC design is investigated in terms of the imaging and shielding capability. Radiation profiles that would result from the multiple slit-field irradiation for imaging are examined to see how they would vary with design characteristics of the collimator. Slit field profiles with varying slit width, collimation thickness, source-collimation distance and source-detector distance are measured and generated by analytical modeling. The effect of the vertical displacement of adjacent leaves on the efficacy of shielding with this design is investigated.

5.2. Proposed Collimation Design and Imaging Procedure

The collimation design is illustrated in Figure 5-1a viewing the MLC leaves end on. All leaf edges are divergent to the source as in the standard single-focussed MLC design. To maintain divergence to the source when the level is moved to the imaging position (Figure 5-1b), the level moves laterally in an arc about the source. Following this movement the external anatomy is irradiated with a grid pattern of multiple slit fields (single-movement image).

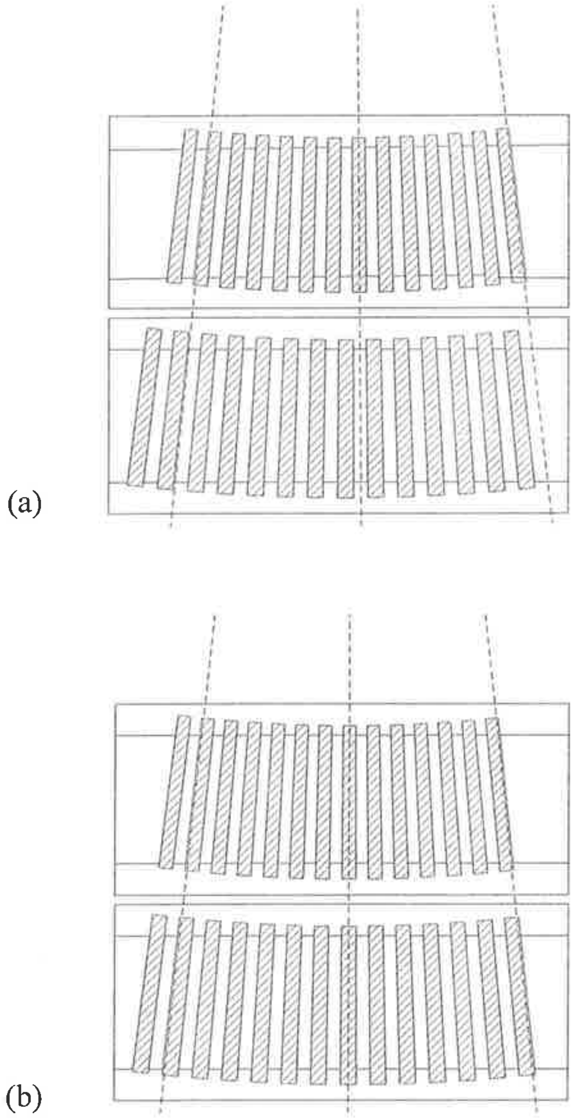

Figure 5-1 (a) Schematic diagram illustrating the multileaf collimator design in shielding position. Each bank of MLC leaves (viewed end on) is split into two vertically displaced levels, with each level consisting of every second leaf. The leaves in the upper level shield the leaf width spaces or slits in the lower level; (b) The multileaf collimator design in imaging position. One of the levels is moved laterally by a leaf width so that the leaves align with the other level. Radiation is then transmitted through the collimator as multiple slit fields.

If possible the full external anatomy image could be reconstructed from this partial irradiation image. Alternatively, a second movement of the collimator could be made, first returning to the shielding position in Figure 5-1(a) then moving the other level of leaves one leaf width in the opposite direction to the previous movement. This grid pattern irradiation would then "fill the gaps" in the first image (double-movement image). Dual size collimator leaves would not be possible as each leaf size would require a different lateral shift to align the leaves.

For acquisition of *port films* the collimation design could be utilized after the treatment delivery. This process is illustrated in Figure 5-2. The treatment field exposure would be first acquired Figure 5-2(a) and then the collimator would be moved from the shielding position to the imaging position and a second exposure acquired Figure 5-2(b). A second movement of the collimator would then be made to image the remaining external anatomy Figure 5-2(c). An example of the total irradiation pattern that would result for the irregular field shape is shown in Figure 5-2(d). The irradiation pattern is more complex than a traditional double-exposure image. This is due to the modification of the treatment field aperture when a level of leaves moves laterally by a leaf width. In the resultant irradiation pattern, the majority of the treatment field receives three exposures, and the remaining regions of the field aperture receive two exposures. The anatomy external to the field only receives the one exposure. Thus the treatment field is still delineated from the external anatomy however there are now three levels of density. The total dose to the external anatomy to acquire such an image would be the same as currently given.

For acquisition of *electronic portal images* the imaging procedure, potentially carried out during the treatment, would be as follows. The treatment field outline would be detected by the EPID during the treatment irradiation prior to the overflash image acquisition. One level of the collimator would then be moved acquiring an image of both the treatment field and the external anatomy. The full image would then either be reconstructed from this by image processing or the other collimator level moved to image the remaining anatomy. The treatment field border would then be overlaid onto this image. If image frames were continuously acquired during the collimator movement some frames would contain a gradient due to this movement. Either these frames would be discarded or the gradient removed by image processing.

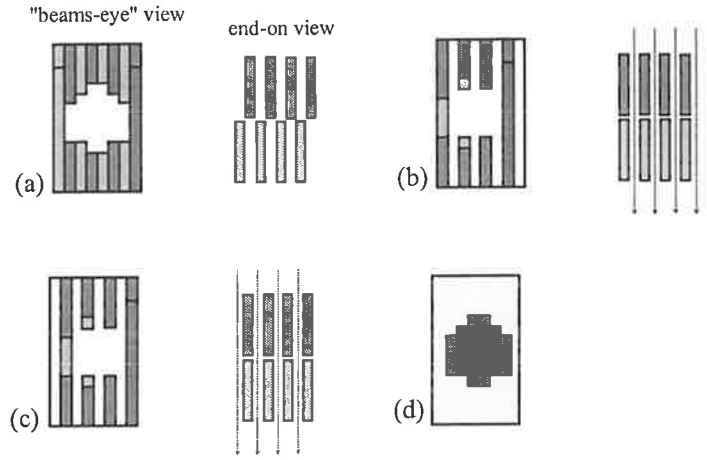

Figure 5-2 Illustration of acquisition of a double-exposure port film with the collimator design. Three exposures are made, the treatment port only, and two multiple slit field exposures formed by movement of the collimator to the two adjacent imaging positions. The resultant exposure pattern contains three levels, the external anatomy receives one exposure, the majority of the treatment field three, and some regions of the treatment field two exposures.

5.3. Methods and Materials of Collimator Characterization

5.3.1. Relative dose determination

The dosimetry in this work was performed with Kodak x-omat film (Kodak Corp., Rochester, NY, USA) digitised with a Vidar VXR-12 film scanner (Vidar Systems Corporation, Herndon, VA, USA). The linearity of the optical density (OD) of the film with dose was therefore measured. It was also necessary to calibrate the Vidar scanner pixel values to optical density and ensure the reproduciblity of this calibration.

5.3.1.1. Film Linearity

The x-omat film was placed in a Kodak cassette at 100 cm from the source of a Siemens KD2 linear accelerator (Siemens Medical Systems Inc., Concord, CA, USA) with a 10 × 10 cm field size. Samples of the film were exposed to varying integrated dose by varying the monitor unit (MU) setting of the accelerator from 20 to 100 MU's in steps of 20 MU at 6 MV. Similar exposures were made for 23 MV with 10 and 30 MU settings also included. The films were processed and the resulting optical densities at the centre of the field measured with an optical densitometer (X-Rite 301X, Grandville, MI, USA). The inherent background density of the film was found from an unexposed and processed film, and subtracted from the results to give the OD due to the irradiation. The resulting characteristic curve of the film is shown in Figure 5-3. The film is reasonably linear over small ranges of the incident dose. The following measurements were therefore performed with OD's up to 1 as the response is quite linear from 0 to 1.

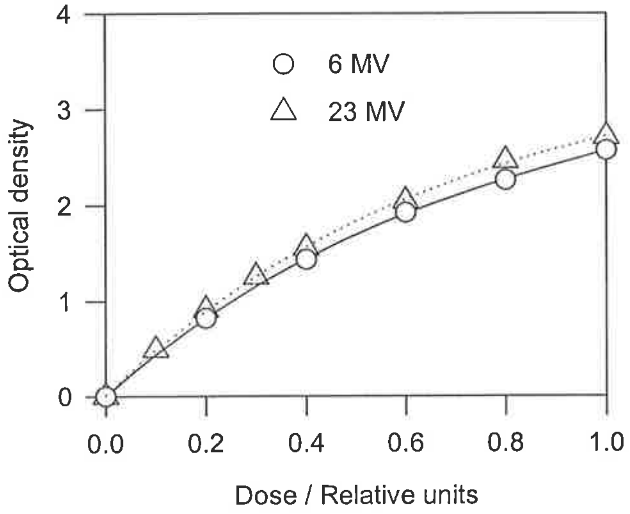

Figure 5-3 Linearity of the x-omat film to dose. The film was exposed to varying monitor unit settings, and the resulting optical densities measured.

5.3.1.2. Vidar pixel values to optical density

Having verified that the optical density of the film will be linear with dose, it is important to ensure that when the films are scanned the pixel values obtained can be accurately converted to the optical density and hence relative dose. The Vidar scanner is a 12-bit CCD camera based film digitiser. A broad light beam from a horizontally aligned fluorescent lamp is attenuated as it passes through the scrolling film. Two sets of shutters then collimate the beam. The vertical direction has fixed collimation while the horizontal shutter width can be adjusted to the film width by the operator. The light is reflected by a mirror and focussed by a lens on to the linear CCD array. The array has 300 dots per inch (dpi) sampling interval (0.083 mm), and can also scan with 150, 75 and 60 dpi by combining the signal from adjacent detector elements. A 12-bit analogue to digital converter then digitises the camera signal and the signal is then transferred to a host PC by a SCSI interface. Built-in conversion tables can be applied to translate the data. The "lin" table simply multiplies the data by a constant, while the "OD" table transforms the pixel values logarithmically. This conversion however is not conversion to absolute OD, and therefore were not used in this study.

Mersseman and De Wagter (1998) have investigated the properties of this scanner including stability, linearity, noise, and effects of aberrant light scatter. They found that the warm-up of the fluorescent lamp following power-on causes a drift in pixel value for ~ 20 minutes. The measured "OD" conversion was found to be linear with known actual OD. The noise analysis showed that OD's below 2.0 should be used. They found that when two adjacent areas had widely different OD (0 and "non-transparent") light scatter from the transparent area can affect the OD of the adjacent area. This is minimised by careful collimation.

The pixel value to OD conversion was found by scanning a film with known optical densities to obtain the pixel values that correspond to these OD's. A calibrated optical density sheet was used (Wellhofer Dosimetrie, Schwarzenbruck, Germany). This was factory calibrated with a Macbeth TD 504 densitometer. The sheet has 17 optical density levels ranging from 0.06 to 3.19. This was scanned and the Vidiscan software provided by Wellhofer automatically determines the locations of each density step and finds the pixel value in each region. The accuracy of this determination was verified by manually determining the pixel values. The scanning was repeated several times to determine the mean pixel value and the uncertainty in each pixel value. A cubic-spline fit was then made to the OD vs pixel value curve to provide a look-up table to convert Vidar pixel value to optical density. This is shown in Figure 5-4. The conversion can be seen to be approximately logarithmic up to an OD of 2. The uncertainty in the OD values obtained by this conversion were estimated to be within 2% (1 SD) by calculating the spline fit and hence OD for each set of pixel values. The calibration was repeated at regular intervals but the pixel values for the OD steps varied by less than 3% from the original values.

5.3.2. Individual slit-field profiles

In this section the radiation profiles transmitted by the collimator to image the external anatomy are investigated to see how these would vary with the collimator design. As the irradiation consists of multiple slit fields, individual slit field profiles were studied. The characteristics of these slit field profiles were investigated with regard to slit width, source-collimator distance (SCD), source-detector distance (SDD) and collimation thickness (Figure 5-5). Both measurement and analytical modelling were employed.

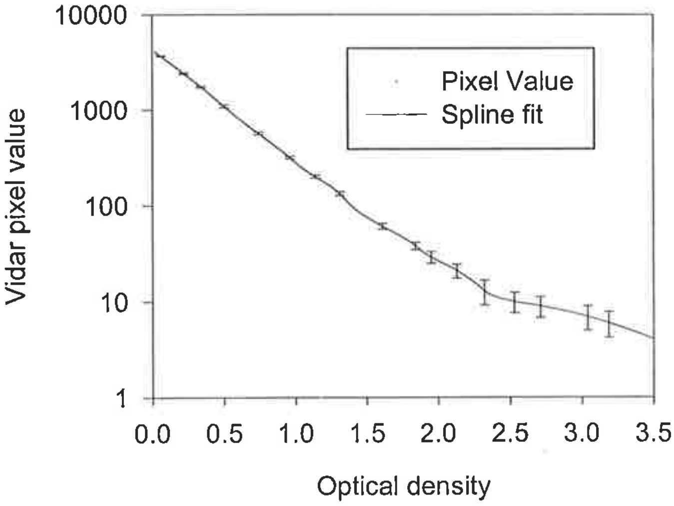

Figure 5-4 Vidar pixel value to optical density conversion. The pixel values were obtained from scanning a calibrated optical density sheet. A cubic spline fit is used to determine the optical density for a particular pixel value.

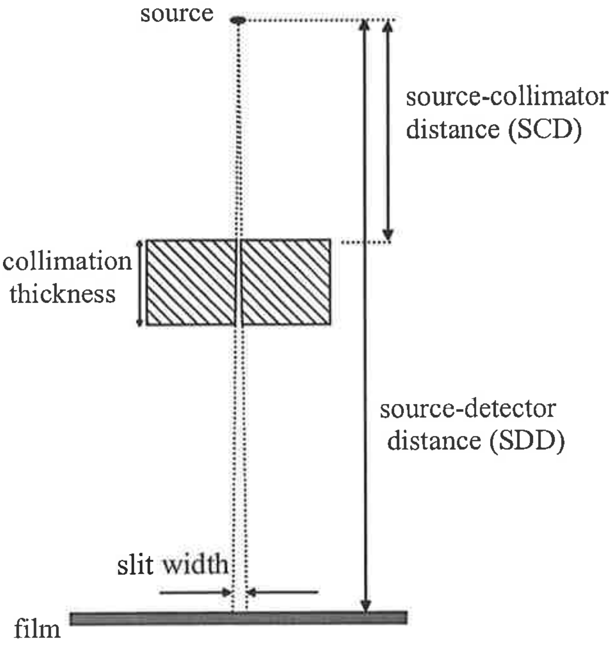

Figure 5-5 Experimental arrangement for measurement of individual slit field profiles.

5.3.2.1. Measurement

Slit width

To examine the effect of the slit width on the profiles, slit-fields were formed by the 7.5 cm thick lower tungsten collimator jaws of a Siemens KD2 accelerator with a SCD of 30.0 cm. The physical slit width of the collimator was measured with calipers to verify the field width setting. These were within 0.2 mm of the nominal slit width settings. Profiles for slit widths of 2, 5, 10, and 20 mm (projected to isocenter) were recorded. The slit was set to 20 cm long at isocenter by the orthogonal (upper) set of jaws. Both 6 MV and 23 MV energies were employed.

The transmitted slit patterns were recorded with Kodak xomat-v film placed at 100 cm from the source and digitized with the Vidar VXR-12 film scanner at 0.17 mm resolution. Conversion of digitized values to optical density was via cubic-spline interpolation of the lookup table produced from the calibrated optical density sheet. Twenty monitor unit (MU) exposures were used to maintain the optical density values in the linear portion of the curve. The inherent background density of the film obtained from an unirradiated processed film was subtracted from the optical density values. The results were obtained by averaging profiles across a central 20 mm region of the slit field irradiation distributions. To provide quantitative summary data on the resulting profiles the full width at half maximum (FWHM), full width at tenth maximum (FWTM) and the peak value of the profiles were measured.

Collimation thickness

To vary the collimation thickness, slit fields of 5, 10 and 20 mm width at isocenter were formed with lead alloy blocks of thickness 5, 7.5 and 10 cm. The blocks were positioned at the shadow tray level of the accelerator with a distance from the source to the distal surfaces of the blocks of 56 cm. The blocks were 5 cm in width and 10 cm in length forming slit fields approximately 18 cm in length at the isocenter. The field size of the secondary collimator jaws was set to 15 × 15 cm so that the field was completely encompassed by the blocked area. The blocks were positioned on a perspex insert of thickness 1 cm. Although this insert will attenuate the beam slightly this uniform attenuation will be constant for these relative intensity measurements. The film was again placed at 100 cm from the source and the profiles obtained as described above.

Source-collimator distance

To examine the effect of the position of the collimator from the source on the transmitted profiles, slit profiles of width 5, 10 and 20 mm were recorded as for the lower jaw profiles but with the slit defined by the upper collimator jaws. These were compared to the slit profiles recorded for the lower jaw and the 7.5 cm thick lead alloy blocks, giving profiles at three SCDs of 22.5, 30.0 and 48.5 cm.

Source-detector distance

The profiles for the lower jaw were also measured by varying the film distance to three SDDs of 68, 100 and 130 cm. The monitor units delivered were scaled according to the inverse square law to achieve the same optical densities at each distance.

5.3.2.2. *Analytical Modelling*

An analytical model to predict transmitted slit profiles was developed to explain trends in the experimental results, and to model increasing the collimation thickness at the level of the collimator jaws. To model the transmitted profiles the relative intensity at a point at the detector plane was found by integrating over the area of a one-dimensional source "seen" through the slit from the irradiation point (Figure 5-6). A two-component source model was developed. To model the focal source an exponential function was utilized. The extra-focal radiation was modeled as a Gaussian function. The tungsten collimators were assumed to be perfectly attenuating, no partial transmission was included. The width of the focal and extra-focal sources, and their relative magnitudes were varied until a reasonable fit to the experimentally measured profiles was obtained. The resulting focal source had a FWHM of 0.7 mm, similar to that experimentally determined (Jaffray *et al.*, 1993). The extra focal source standard deviation was 9 mm. The relative magnitude (area under the distribution) of the extra focal component was 13% of the focal source magnitude.

The effect of increasing the collimation thickness was modeled at the position of the secondary jaws. The measurements for the change in collimation thickness were only possible at a relatively large distance from the source. As several manufacturers place their MLCs at or near the position of the secondary collimators it is important to ensure that these results would still be valid for collimators closer to the source. The collimated slit thickness that would result when two levels of leaves 5-7 cm thick are aligned would also increase the thickness of the slit to 10 to 14 cm.

Modeled profiles were produced for collimation thickness of 7.5 cm and 14.0 cm. The distance from the source to the proximal surface of the collimated slit was kept constant at 30.0 cm. Slit widths of 2, 5, 10 and 20 mm at isocenter were modelled, and the detector plane was 100 cm from the source.

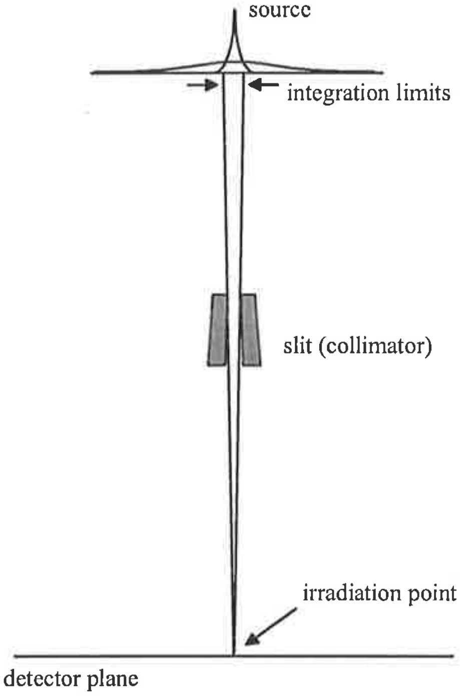

Figure 5-6 Analytical model for prediction of slit field profiles.

5.3.3. Multiple slit profiles and images

If single or double-movement images were acquired with this collimator design the transmitted profiles would be comprised of a combination of multiple individual slit field profiles. The impact of the variation in the individual slit field profiles on the full transmitted profiles was investigated. The full transmitted profiles were obtained both by forming composite profiles from the individual slit field results and by measurement. The composite profiles were obtained by addition of identical profiles with the centers of the profiles separated by twice the slit width for a single-movement profile and one slit width for a double-movement. Before the addition the background level was subtracted from the profile and then added to the final composite profile.

The validity of these composite profiles in representing the profile that would be transmitted by the collimator design was examined. The individual slit fields as measured in Section 5.3.2 are formed with the full collimation thickness extending several centimeters laterally from the slit. In the collimation design the collimated slit thickness extends only one leaf width laterally. If there were significant effects due to penetration of radiation through the leaves of the collimator, the profile would change from a composite of the individual profile measurements in Section 5.3.2. The composite profile constructed from the 10 mm slit formed with the lead alloy blocks was therefore compared to a profile measured with an actual grid of 10 mm lead alloy leaves.

The lead alloy grid was constructed utilizing a divergent hot-wire cutter to produce a polystyrene mould of the leaves of the grid. The low melting point alloy was poured in the moulds cut for the leaves. Initially every second leaf was cut and poured to prevent distortion of the mould when poured. Following cooling the remainder of the mould was cut and poured. The grid was constructed with leaves 7.5 cm thick projecting to 10 mm wide at isocenter, with 10 mm wide slits between the leaves. The profile transmitted through this grid was then measured with the grid placed at 56 cm to the base of the grid, and the x-omat v film at 100 cm from the source as for the lead alloy slit measurements.

To obtain measured multiple slit field profiles, multiple individual slit field exposures on film were made. Single-movement profiles were formed for slit widths of 2, 5, 10, and 20 mm by moving the center of the slit field by twice the slit width and irradiating at each position. The upper collimator jaws were used due to their asymmetric movement capability. A double-movement image was similarly formed with a 10 mm slit width by separating the center of each slit field by 10 mm. The complete profiles were recorded on film placed at 130 cm from the source and processed as in Section 5.3.2. The multiple exposures result in a higher transmission and scatter level on the film than would be present for a single exposure through multiple slits, so the extra transmission and scatter level was measured and subtracted from the digitized films.

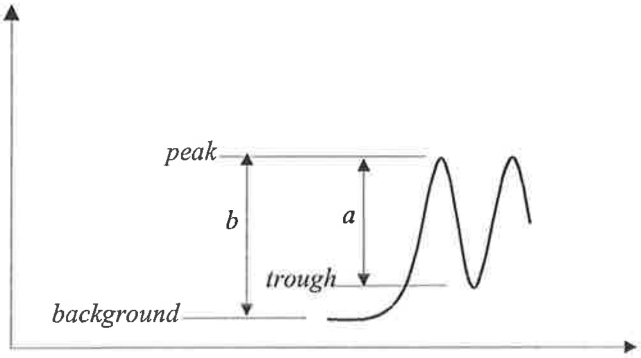

Figure 5-7 Definition of the modulation index (MI). This gives the amount of modulation present in the multiple slit irradiation profile.

The resulting profiles were analyzed by calculating a modulation index (MI). This gives the amount of modulation in the profile and is illustrated in Figure 5-7. A MI index of 1 is full modulation whereas a MI of 0 would be a flat profile with no modulation present.

$$\mathrm{MI} = (peak - trough)/(peak - background) = a/b \tag{5.1}$$

To examine the effect of changes in the transmitted profile on resultant images, multiple slit field exposures of a test object were made. The object was the QC-3F portal imaging phantom (Masthead Imaging Corp., Nanaimo, BC). Only a portion of the phantom was imaged. A megavoltage image of this object acquired with an open-field irradiation is shown in Figure 5-8.

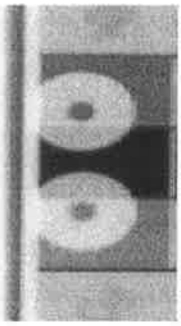

Figure 5-8 Image of the test object acquired with an open field for comparison with the multiple slit irradiation images.

The phantom is 1.9 cm thick. The numbers 3 and 4 visible at the top and bottom of the image are machined into lead to a thickness of 3 and 4 mm respectively. The three rectangular regions between these are of thickness 5 mm lead, 15 mm PVC and 7.5 mm lead respectively. Two brass annular disks of thickness 1.9 cm and diameter 2.2 cm were placed on the phantom for added detail. The phantom was used as an object to form images for visual comparison only, no image quality parameters were measured. For the slit field images the object was placed at isocenter, and the film at 130 cm from the source. Single-movement images were formed using slit widths of 2, 5, 10 and 20 mm with the upper collimator jaws as described above. A double-movement image was formed with a 10 mm slit width.

5.3.4. Shielding transmission

5.3.4.1. Measurement

The MLC design enables the upper leaves to be made slightly wider than the spaces in the lower level that they are shielding. In principle this should reduce the inter-leaf transmission relative to the traditional MLC tongue and groove design, as radiation from a point source would pass through a full thickness of collimation. However, considering the extra-focal source and the finite size of the focal source there is potential for off-axis radiation to pass through the collimator unattenuated (Figure 5-9). The unattenuated transmission will depend on the overlap and the vertical displacement between the two leaf levels. Therefore in this section the efficacy of shielding when adjacent leaves are vertically displaced is investigated both experimentally and by analytical modelling. The significance of the transmission due to the vertical displacement and the amount of overlap necessary to adequately shield is determined.

To investigate experimentally the magnitude of the off-axis radiation transmission, two lead alloy shielding blocks were produced and the surfaces machined flat to a tolerance of better than 0.05 mm. These were placed with one block vertically displaced from the lower block (Figure 5-10). The increase in radiation dose at the detector plane under the upper block relative to under the lower block due to the off-axis transmission was measured. The variation of the increase was studied with overlap of the blocks.

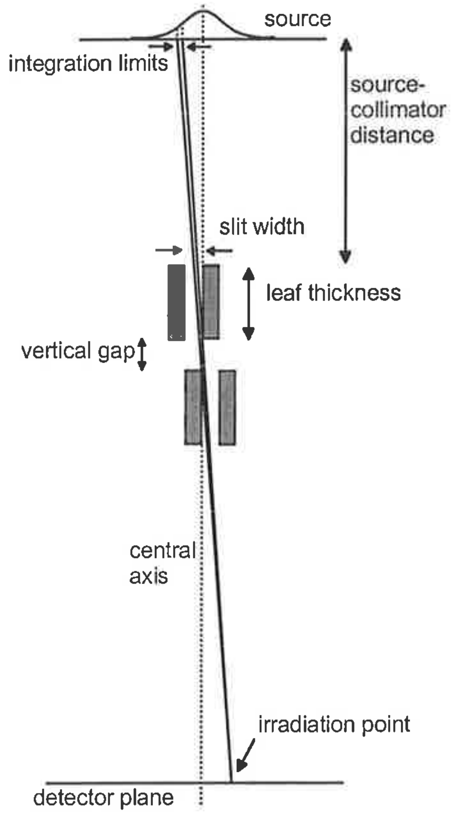

Figure 5-9 Illustration of potential radiation transmission through the collimation design, and the analytical model to predict the transmission profile.

The blocks were positioned at a distance of 55 cm to the proximal surface of the upper block from the source of a Siemens KD2 accelerator. The upper block was placed on a translation stage (Newport UMR8.25, Irvine, CA) enabling it to be moved relative to the lower block by fixed amounts to produce an under or overlap of the blocks. The range of the stage was 25 mm and the centered load capacity 90 kg. The translation stage was placed on polystyrene to place the block at the correct height while providing minimal attenuation of the beam. The whole arrangement was supported on a 13 mm thick perspex section of the couch top of the accelerator. The vertical separation of the two blocks was 5 mm. The alignment to vertical of both block faces was verified with a spirit level to within 0.1 degrees. The lower block was then aligned with the central axis of the beam by exposing a narrow slit field and moving the block until it was in the center of the field. The blocks were 7.5 cm thick in the beam direction, 6 cm in width in the direction of the translation movement, and 12 cm in length along the overlap region. The field size was set to 15 × 10 cm (isocenter) so that there was no field outside the blocked area. X-omat v film was placed at 100 cm from the source with 1 cm of solid water buildup.

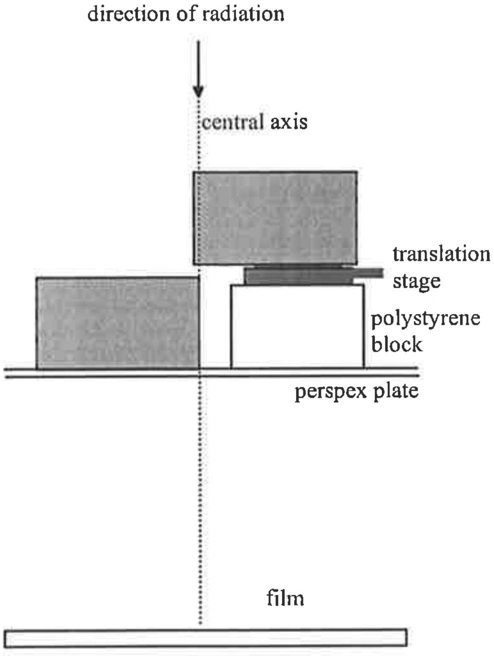

Figure 5-10 Schematic diagram of the experimental arrangement for investigation of off-axis radiation transmission through the collimation design.

The blocks were initially positioned with an horizontal gap of 0.2 mm (± 0.1 mm) and the film irradiated with 200 MU at 6 MV nominal energy. The upper block was then translated in 0.1 mm increments by the translation stage micrometer, up to an overlap of 1.0 mm and the transmission recorded for each upper block position.

The transmission patterns were digitized with the Vidar scanner at 0.17 mm resolution and profiles in the direction of the block movement across the central 2.5 cm of the irradiation pattern were averaged. The pixel values were converted to relative dose as described in Section 5.3.1. The inherent background density of the film obtained from an unirradiated processed film was subtracted from the profiles.

5.3.4.2. Analytical Modelling

Analytical modelling was employed to examine the relative effects of the focal and extra-focal source distributions on this transmission, as well as to see how the collimator design (slit width, leaf thickness, vertical displacement of the two levels, overlap) impacts on the transmission. The model is illustrated in Figure 5-9. The 2-component source distribution was as described earlier. In the model, two blocks define a slit in the upper level, and two blocks define a slit in the lower level. The distance from the source to the proximal surface of the lower blocks was set to 40.0 cm. The block geometry was modeled as initially 7.5 cm thick, with a slit width of 5 mm (at the block plane). The blocks were non-divergent, and the inner face of the lower left block aligned to the central axis. The upper right block position was initially aligned with the lower left block. The profile value at the detector situated at 100 cm from the source was found by integration of the source distribution over the region viewed by a direct unattenuated path through the collimated slits. No partial transmission was modeled. The profiles were divided by the integral over the entire source, representing the transmission values relative to an open field value at the detector point. The slit width, leaf thickness, vertical displacement of the levels, overlap of the levels were varied to examine their impact on the transmission.

5.4. Results

5.4.1. Individual slit-field profiles

5.4.1.1. Measurement

Slit Width

Figure 5-11 shows the slit-field profiles for the four slit widths formed by the lower collimator jaws (SCD = 30.0 cm) for the two nominal beam energies of 6 and 23 MV. These are normalised to the peak dose of the 20 mm profile for 23 MV. The peak values of the profiles decrease for the smaller slit widths. This is consistent with a decrease in the source seen from a detector point with a narrowing slit, reducing the radiation intensity at that point. For smaller slit field widths some reduction in peak dose would also be expected due to the loss of electron scatter. The profiles also become less rectangular in shape as the slit width decreases. The FWHMs in Table 5-1 (all ± 0.2 mm) become broader than the geometric slit width for the 2 mm profile. As the slit width decreases, the effect of the source size and hence penumbral blurring becomes more important. To examine the reproducibility of the measurements, three independent measurements of the 5 mm profile were made. When plotted together there was no discernable difference between the three profiles.

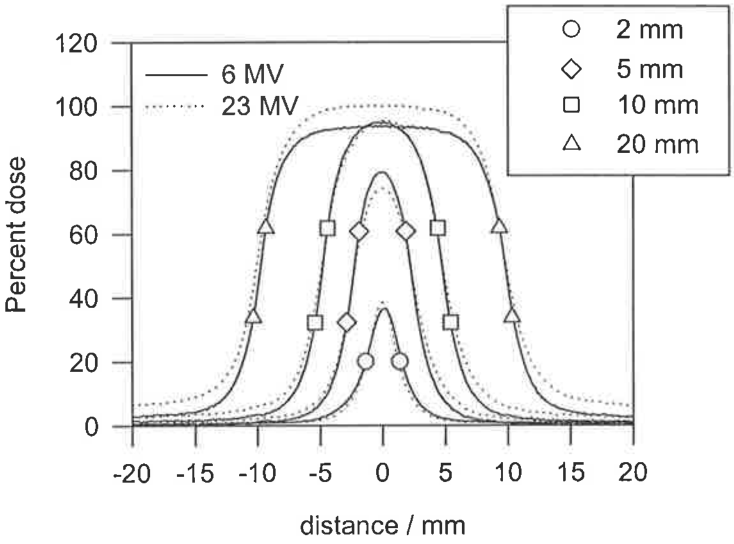

Figure 5-11 Measured slit field profiles with varying slit widths of 2, 5, 10 and 20 mm for both 6 and 23 MV. The slits were formed with the lower tungsten collimator jaws (SCD = 30.0 cm) of a Siemens KD2 accelerator. The results illustrate that as the widths decrease the peak values decrease and the profiles also become less rectangular in shape, the profiles becoming broader than the geometric slit width.

Table 5-1 Summary of the measured widths and peak values of the slit field profile measurements for the lower collimator jaw at the 6 and 23 MV energies. The peak dose values are expressed as a percentage of the 20 mm peaks.

	6 MV			23 MV		
Slit width / mm	FWHM / mm	FWTM / mm	Peak value / %	FWHM / mm	FWTM / mm	Peak value / %
2	3.2	8.1	39	2.7	6.9	38
5	5.1	9.7	84	5.6	11.2	74
10	9.7	14.6	102	9.8	16.3	95
20	19.6	25.1	100	19.8	28.4	100

The 23 MV results were scaled to account for an increased film response of approximately 7% to the higher energy. The 23 MV profiles have higher intensities in the tails of the distributions than the 6 MV profiles, and this is reflected in the broader FWTMs. This could be due to increased penetration through the collimation for the higher energy or higher peripheral source intensities (broader source). The peak value of the 23 MV 20 mm profile is greater than the 6 MV while the peaks are similar for the other slit widths. This is consistent with a broader 23 MV focal source. As the slit width is increased from 10 to 20 mm, the area at the source plane seen increases. The peak value of the 6 MV profile does not change significantly with this increase suggesting that the entire focal source is already

visible with the 10 mm slit width. However if the 23 MV source is broader, the increase in area seen results in an increase in the peak intensity. This increase in source size with energy has been observed experimentally (Jaffray *et al.*, 1993).

Collimation thickness

Figure 5-12 shows profiles for the three collimation thicknesses of 5, 7.5 and 10 cm formed with divergent lead-alloy blocks for the 10 mm slit width. The effect of the change in thickness is largely on the penetration through the collimator. The transmission through the blocks is higher than that through the tungsten for the same thickness. The peak values of the 7.5 and 10 cm profiles are similar suggesting that increasing the collimation thickness has little effect on the central profile region. There is slight narrowing of the 10 cm thick profile relative to the 5 and 7.5 cm collimation thicknesses. Similar results were found for the 5 and 20 mm slit widths. The effect of greater increases in thickness than measured here, at distances closer to the source are investigated with analytical modelling.

Source-collimation distance

The profile results for the three source to collimator distances are shown in Figure 5-13 for the 6 MV, 10 mm width slit profiles. The increased transmission was removed from the lead alloy block profile to facilitate comparison with the tungsten profiles. The results show a reduction in the peaks of the profiles as the slit moves closer to the source. This is consistent with a reduced field of view of the source from a detector point as the slit moves closer to the source. The profiles become more rectangular in shape (reduced penumbra) as the collimated slit moves further from the source due to the decreasing magnification of the source (for a constant source-detector distance).

The quantitative summary data for the upper collimator jaw and the lead alloy block profiles are shown in Table 5-2. These show that there is little change in the FWHMs or FWTMs for the three source-collimation distances, with only a slight decrease in the FWTM with increasing SCD. The main effect of increasing the distance is to reduce the penumbral blurring and to increase slightly the transmitted intensities.

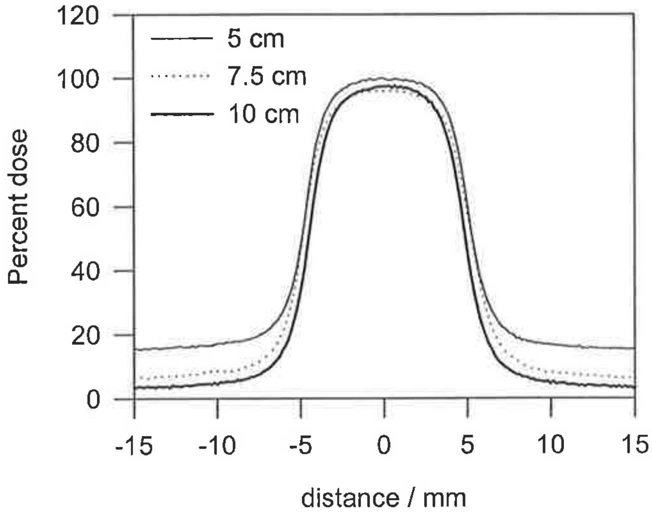

Figure 5-12 Measured slit field profiles for three collimation thicknesses. The slits were formed by lead alloy blocks of thicknesses 5, 7.5 and 10 cm respectively. The blocks were placed on the shadow tray at a distance of 56 cm from the source to the base of the blocks with a slit width of 10 mm. The effect of the change in thickness at this distance from the source was largely on the background level due to increased penetration through the blocks.

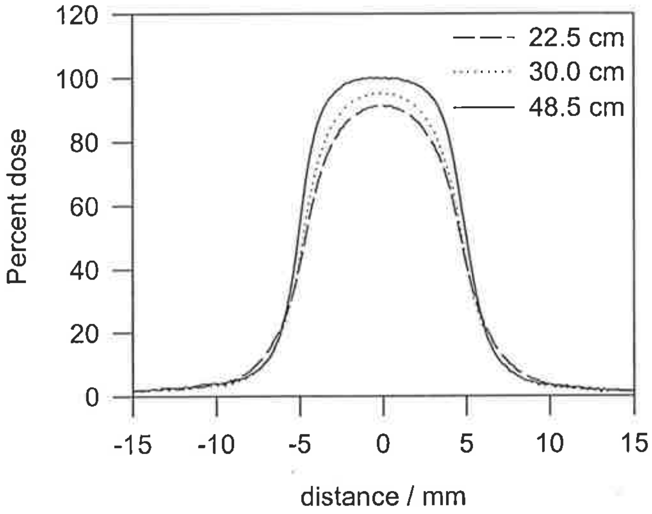

Figure 5-13 Slit field profiles for three source to collimation distances of 22.5 cm, 30.0 and 48.5 cm to the proximal surface of the collimators. The slit width is 10 mm. Moving the collimated slit closer to the source results in a reduction in the intensities of the central regions of the profiles, as the area of the source "seen" through the slit decreases. The profiles become more rectangular with increasing distance from the source.

Table 5-2 Summary of widths and peak values of the 6 MV slit field profile results for two source-collimator distances of 22.5 cm and 48.5 cm. The slit fields were formed with the upper collimator jaws, and lead alloy blocks.

	Upper jaw			Lead alloy block		
Slit width / mm	FWHM / mm	FWTM / mm	Peak value / %	FWHM / mm	FWTM / mm	Peak value / %
5	5.1	10.7	74	5.4	9.3	87
10	9.7	15.6	98	10.2	14.4	92
20	19.5	25.7	100	19.8	24.4	100

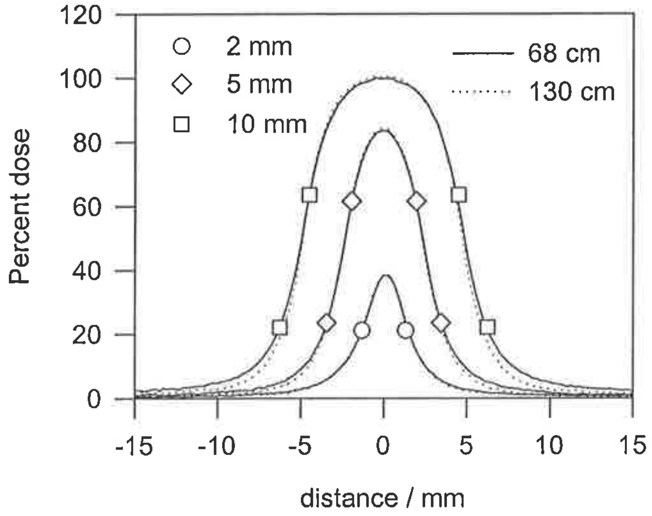

Figure 5-14 Slit field profiles for two collimation to detector distances of 68 cm and 130 cm, with slit widths of 2, 5, and 10 mm. These show that there is little change in the profiles over the range of distances that are likely for the detector placement for imaging.

Source-detector distance

Figure 5-14 illustrates that there is little change in the profile with distance from the collimation. The profile recorded at 68 cm from the source is similar to the profile at 130 cm from the source. The increased width of the profile at 130 cm due to magnification has been removed from the results. The profiles were obtained by scaling the monitor units delivered according to the inverse square difference in dose expected at the two distances. The 100 cm result which was between the two curves has been omitted for clarity. The changes in the profiles are fairly small over this large change in distance of the film from the source..

5.4.1.2. Analytical Modelling

The model was found to qualitatively predict the trends observed in the experimental results, suggesting that the features of the profiles are due to changes in the amount of source seen from each detector point with changes in slit width, source-collimator distance, and collimator thickness. Figure 5-15 shows the model predictions of the upper and lower collimator jaw profiles compared to the experimental results for 6 MV. The model predicts the profile shape, falloff in intensity with decreasing slit width, and the increased penumbra of the upper jaw profiles compared to the lower.

The focal source was found to determine the profile shape in the central regions of the profiles, and to predict the reduction in intensity of the profiles with reducing slit width for the upper and lower collimator jaws, as well as the reduction due to the slit being closer to the source.

The extra-focal source component produces the tails of the distributions and also the reduction of intensity with slit width found for the lead alloy block slits. As these blocks were placed far from the source the entire focal source is seen by the detector points at the center of the profile, and therefore the reduction in intensity may be due to a reduction in the area of extra-focal source seen with reducing slit width. These results show that both focal and extra-focal source components need to be considered to predict the results of the slit profile measurements. The model does not include the effect of electron scatter. For smaller slit field widths some reduction in peak dose at depth would be expected even with a point source due to the loss of electron scatter that would also contribute to the peak dose. However for imaging the primary photon intensity is of most importance and the effect of electron scatter is minimised due to the air-gap and metal screen.

The modeled profiles for increasing the collimation thickness from 7.5 to 14.0 cm at the level of the lower secondary collimator are shown in Figure 5-16 for 2, 5, 10 and 20 mm slit widths. The profiles for the 14.0 cm collimated slit are slightly thinner, although the central regions are similar. For central points at the detector the field of view of the source is determined by the position of the upper corners of the slit, and these are unchanged for the two profiles as the source to proximal surface is the same. However for more peripheral points, the field of view of the source is dependent on the position of the lower corners of the slit, and for the thicker slit, less source is visible, reducing the intensity for these points and thus narrowing the slit profile. This effect increases as the slit width decreases.

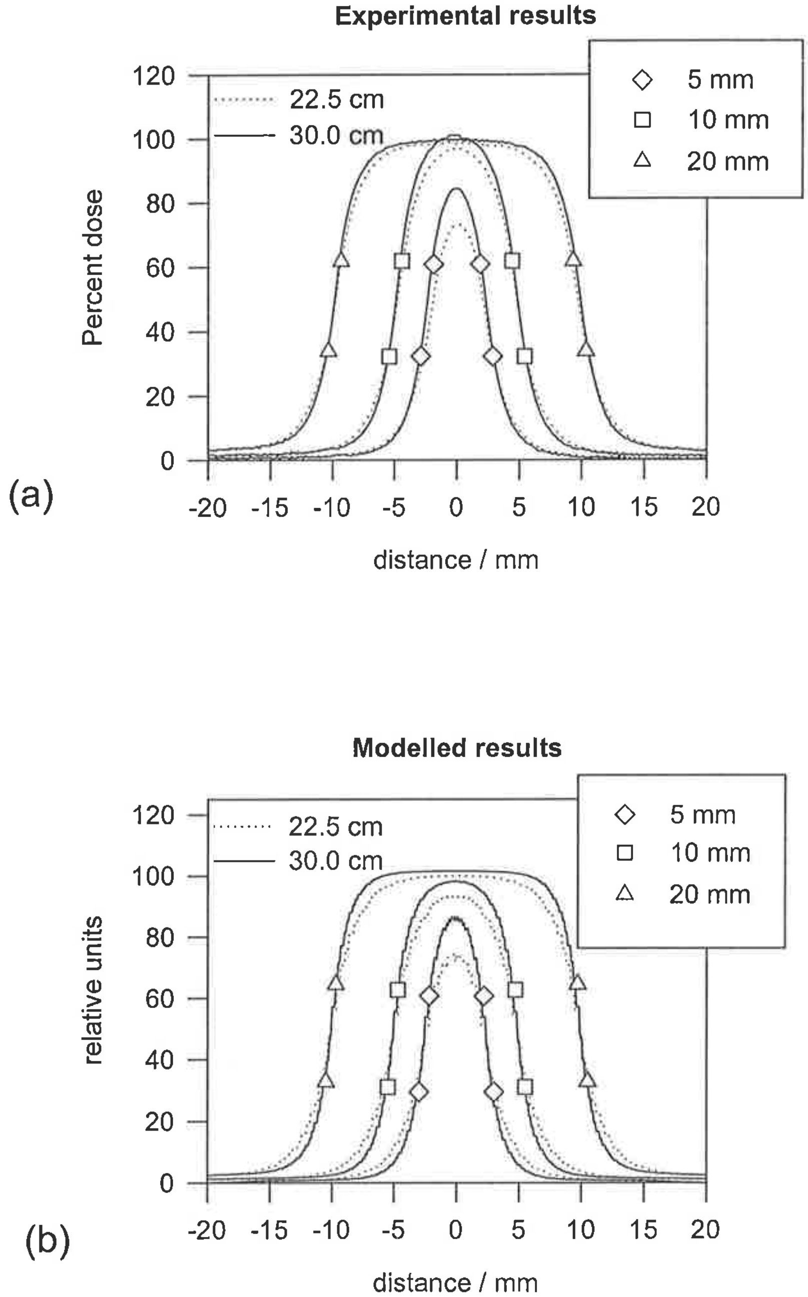

Figure 5-15 Comparison of modeled profile result with experimentally measured results for the slits formed with the upper and lower collimator jaws with 5, 10, and 20 mm widths at 6 MV. The model gives good qualitative prediction of the trends observed in the experimental profiles.

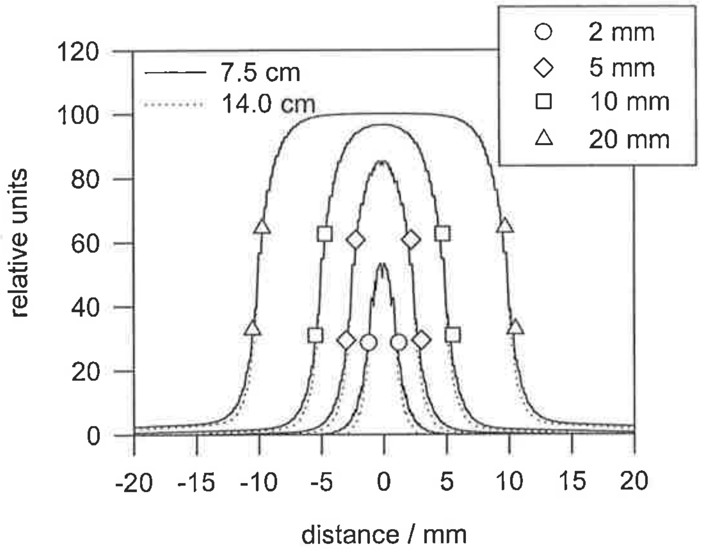

Figure 5-16 Modeled effect of increasing the thickness of the collimated slit from 7.5 to 14 cm, when the slit is positioned at the level of the lower collimator jaws or 30.0 cm to the proximal surface of the collimator from the source. The slit widths shown are 2, 5, 10 and 20 mm. The central region of the profiles are similar however the peripheral regions of the thicker slit have slightly lower intensity, narrowing the profiles. This is because the field of view of the central points remains unchanged by thickening the collimation however the field of view reduces for the peripheral points.

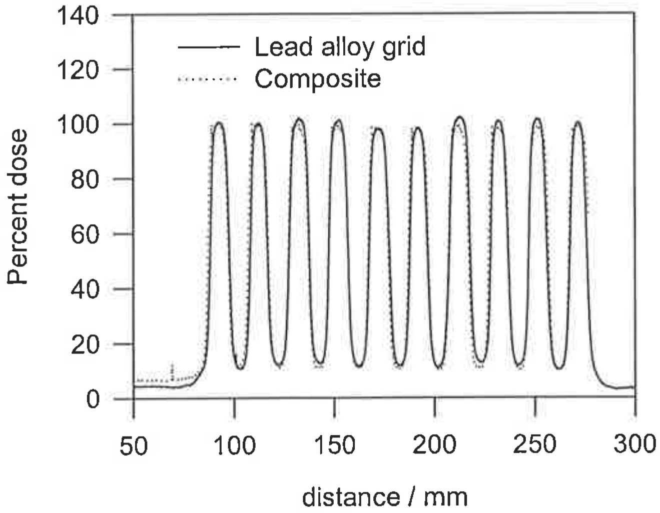

Figure 5-17 Comparison of profile transmitted through a lead alloy grid comprised of multiple leaves projecting 10 mm slits at isocenter with a composite profile constructed from the individual 10 mm slit width profile measurement. The two are very similar suggesting there is no significant effect on the profile due to the smaller lateral extent of the collimation when using a grid of collimated slits.

5.4.2. Multiple slit profiles and images

5.4.2.1. Single Movement

Figure 5-17 shows the comparison of the transmitted profile formed by the lead alloy grid and the composite profile formed from the individual slit profile measurement. The two are in reasonable agreement, validating the procedure used to obtain full multiple slit profiles from an individual slit profile. The slight difference in the background levels is due to the presence of the secondary collimators defining the tail region of the lead alloy grid profile, reducing the intensity.

Figure 5-18 shows the profiles resulting from multiple slit irradiations with the 2, 5, 10 and 20 mm slit widths defined by the upper collimator jaws at 6 MV energy. The results are normalised to the maximum dose of the 10 mm slit width results. The x-axis has been scaled to give the profile at 100 cm from the source. These results show that the overlap increases for the 2 and 5 mm slit widths due to the broadening of the individual profile. The transmitted intensity through the 2 mm slit width is much less than through the 10 mm slit.

The MI's found for the composite multiple slit profiles are given in Table 5-3. The broader individual slit profiles observed in Section 5.4.1 for the 23 MV energy result in greater overlap and hence lower modulation level of the full profile. There is only small change in the overlap with collimation distance from the source. The results are similar for the 10 and 20 mm widths, with almost 100% modulation. The decrease in modulation due to the overlap of profiles occurs for the 5 and particularly the 2 mm slit widths.

Examples of single-movement images obtained with the 2 mm slit width and the 10 mm slit width are shown in Figure 5-19. The slit fields have their long axis in the vertical direction. The monitor units of the 2 mm slit image were increased to give approximately identical peak optical densities for the two images. These images clearly show the effect of the modulation amplitudes of the two profiles. The 2 mm slit width image appears as a full image but with a modulated intensity, whereas the 10 mm slit width appears as a sampled or "grid" image.

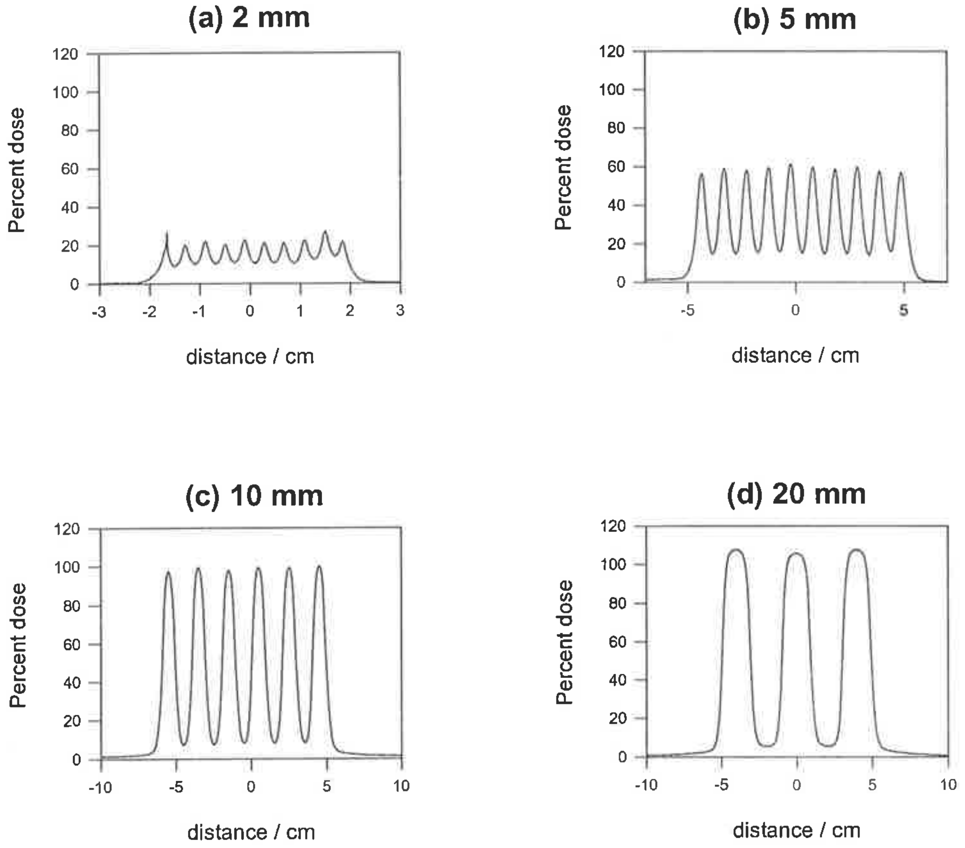

Figure 5-18 Multiple slit irradiation profiles for slit widths of (a) 2 mm, (b) 5 mm, (c) 10 mm and (d) 20 mm. The profiles were formed by the upper collimator jaws. Each slit irradiation was separated by twice the slit width to simulate the single-movement profile that would be transmitted through the collimator to image the external anatomy. The narrower slit width results in smaller modulation of the profile.

Table 5-3 Modulation index results for the composite full transmitted profiles constructed from the individual slit field profile results. The modulation reduces for the 5 mm and 2 mm slit widths.

	6 MV			23 MV		
Slit width / mm	Upper jaw	Lower jaw	Lead alloy blocks	Upper jaw	Lower jaw	Lead alloy blocks
2		0.41			0.48	
5	0.77	0.84	0.82	0.71	0.76	0.77
10	0.95	0.95	0.95	0.90	0.92	0.89
20	0.97	0.96	0.98	0.93	0.89	0.94

5.4.2.2. Double-Movement

Figure 5-20 shows the profile produced from the two 10 mm width slit irradiation with the slits adjacent to each other, the center to center separation equal to the slit width. The slits were formed with the upper collimator jaws of the accelerator. The drop in dose is due to the penumbral blurring of the two slit profiles. The penumbral blurring is large due to the proximity of the collimator to the source (SCD = 22.5 cm). The penumbral blurring would decrease with increasing SCD as can be seen in Figure 5-13.

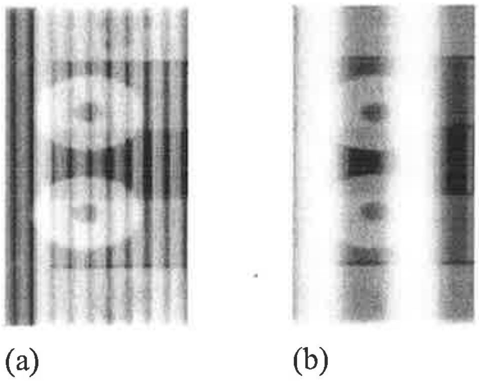

Figure 5-19 Images of a test object acquired by multiple slit irradiations separated by twice the slit width with (a) 2 mm slit width and (b) 10 mm slit width. The slit fields were formed by the upper collimator jaws. The monitor units of the 2 mm slit width were adjusted to give approximately the same optical density on the film as the 10 mm slit width image. The images show the smaller slit width produces a modulated image of the object whereas the larger slit width results in a sampled or grid image. The horizontal stripes are regions of different density in the object.

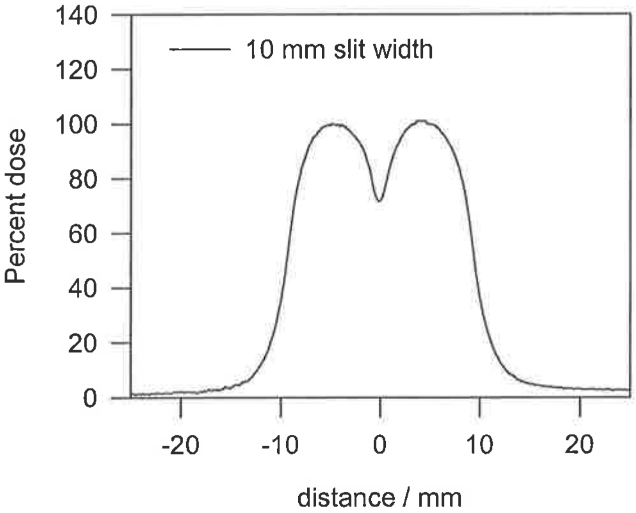

Figure 5-20 Two slit irradiation profiles for a 10 mm slit width. The profiles were formed by the upper collimator jaws (SCD = 22.5 cm). The center to center separation of the profiles was equal to the slit width to simulate a double-movement profile for imaging.

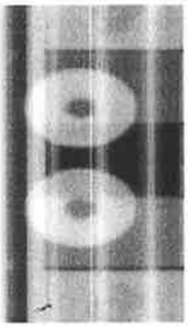

Figure 5-21 Image obtained by multiple slit irradiation of a test object simulating a double-movement image. The slit width was 10 mm, and the center to center separation of the profiles was equal to the slit width.

The image of the test object obtained by multiple 10 mm slit irradiations is shown in Figure 5-21. The slits were formed as above by the upper collimator jaws with the center to center separation of each slit position equal to the slit width. The image clearly shows the object but with a periodic pattern imposed at the frequency of the slit spacing. This is due to the drop in intensity seen in Figure 5-20 due to penumbral blurring of the individual profiles. The results in Section 5.4.1 for the individual profiles showed that these profiles become more rectangular as the collimator distance from the source increases. This will reduce the width of the underdose region due to the reduced penumbra width.

5.4.3. Shielding transmission

5.4.3.1. Measurement

Figure 5-22 shows the relative dose profiles that resulted from the irradiations performed with a 0.1 mm gap between the upper and lower blocks, the blocks aligned, a 0.1 mm overlap and a 1.0 mm overlap. The results are expressed as a percentage of an open field 10 × 10 cm irradiation. The irradiation profile with the gap shows a marked peak due to the direct focal source transmission through the gap. The dose is raised under the upper block relative to the dose under the lower block and falls off with distance from the central axis (zero x-coordinate). The profile under the upper block when the blocks are aligned shows a small peak, then a slight dip in the dose followed by a shallow extended peak, with slightly raised dose compared to the under the lower block. The 0.1 mm overlap of the blocks removes the peak with a slight dip in the dose profile under the region where the thickness is twice that of an individual block. The dose under the upper block is again increased compared to the lower block. Finally, the 1.0 mm overlap of the blocks, removes any increase in the dose under the upper block.

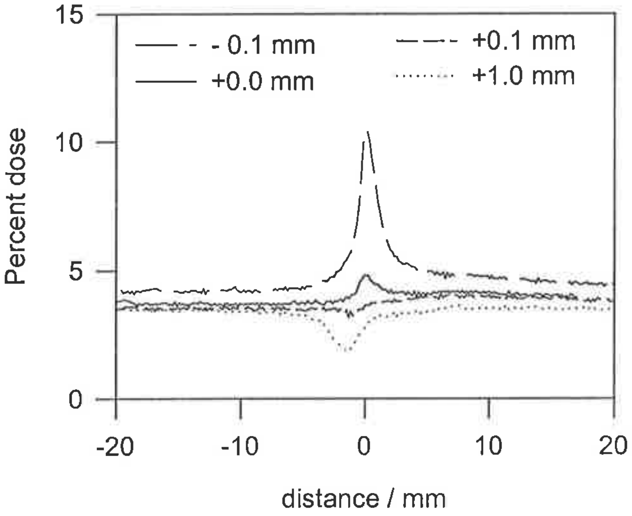

Figure 5-22 Investigation of off-axis radiation transmission. Transmission profiles resulting from a 0.1 mm gap between the upper and lower block, the block faces aligned, a 0.1 mm overlap, and a 1.0 mm overlap. The profiles clearly show that the transmission is raised under the upper block due to this transmission, however with the blocks aligned or small overlap of the blocks this extra transmission is small.

The increased dose seen for the 0.1 mm overlap is small, generally less than 10% of the overall transmission level due to penetration through the blocks. The aligned block exhibits a similar raised level away from the central axis with a peak close to the central axis of approximately 25% increase in dose. There is an increased background transmission level for the 0.1 mm gap compared to the other profiles possibly due to radiation back-scattered to the film. The results show that there is increased transmission due to the off-axis radiation but this is small compared to the level from direct radiation penetration through the blocks provided the blocks are aligned or slightly overlapped.

5.4.3.2. Analytical Modelling

The analytical model result for the transmission profile to the right of the central axis when the upper and lower blocks are perfectly aligned is shown in Figure 5-23. The central axis is the zero *x*-coordinate. Both the focal source and extra-focal source contributions are shown as well as their combined effect. There is a peak close to the central axis due to the focal source, followed by a slight drop in dose and then a shallow gradual peak due to the extra-focal source. This result is qualitatively similar to the experimentally measured profile for the aligned blocks. The modeled result gives a zero value on the central axis directly under the block edges, however the experimental shows a tail off in this region probably due to partially transmitted radiation. The overall magnitude of the transmission is however small, less than 0.4% of the open field value.

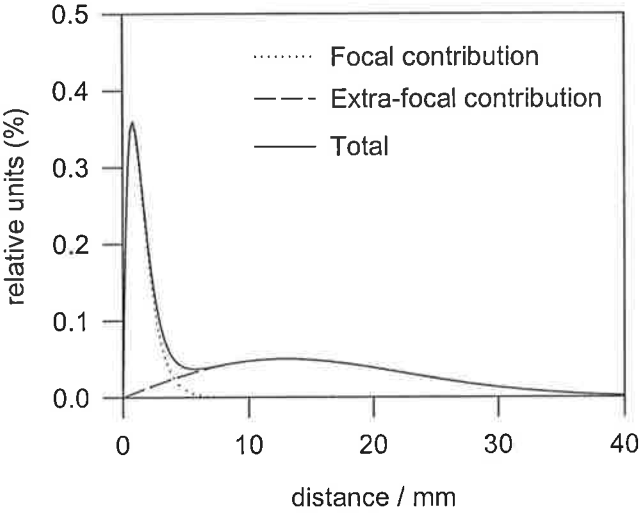

Figure 5-23 Model result for the blocks aligned showing the effect of focal and extra-focal off-axis radiation transmission.

The transmitted profile was investigated varying the slit width, leaf thickness, gap between the two levels, and overlap. The slit width and leaf thickness were found to increase the lateral extent of the transmission for increasing slit width and decreasing leaf thickness, however there was no change in the absolute value of the transmission. This is due to the field of view of a detector point being determined by the position of the bottom corner of the upper right block and the top corner of the lower left block. Increasing the slit width or reducing leaf thickness does not change the positions of these corners. The transmission reduced markedly with increasing overlap of the blocks and decreasing vertical gap between the levels.

5.5. Discussion

The experimental results for the individual slit profile measurements showed that the slit width has a major impact on the transmitted profile, as the slit width decreases the profiles become less rectangular and broader than the geometric projection. The collimation thickness and SDD has only a small effect on the profiles. Increasing the SCD produces more rectangular profiles, the reduction in penumbra due to the reducing magnification of the source, however the overall widths of the profiles are similar. The broadening of the profile for smaller slit widths results in increasing overlap of adjacent profiles when the multiple slit irradiation is considered. This results in a modulated image rather than a sampled or grid image. There is also increased overlap for 23 MV compared to 6 MV. However the transmission through the smaller slit widths is lower due to a reduced field of view at the source plane through the slit. The difference increases as the collimated slit moves closer to the source. This results in increased monitor units necessary to produce an image with the same optical density. The dose to the external anatomy required to acquire an image would not be increased however the dose delivered to the field aperture would increase due to the increased monitor units.

Reconstruction of the external anatomy image from a single-movement image would enable more efficient imaging than a double-movement image. With the modulated image that results from the smaller slit widths the possibility exists for image processing to remove the modulation. These smaller slit widths are therefore the most likely to be amenable to single-movement imaging. However the slit width or leaf width would have to be small. Standard MLCs are now being manufactured with 5 mm widths projected to isocenter and this width or smaller would be required. The image processing aspects are currently being investigated. Smaller leaf widths are also beneficial in reducing the effective penumbra of the MLC when shaping angled field edges.

Reconstruction of single-movement images for the larger slit or leaf widths where the transmitted intensity produces essentially a sampled image would be difficult. The sampling frequency for a 10 mm slit width is 0.05 mm^{-1} which is insufficient to retrieve all spatial frequencies in the image. This suggests that double-movement images would be necessary for these slit widths. For these double-movement images, dose reduction was observed due to penumbral blurring. This was for the idealised case of no overlap between upper and lower leaves. Further dose reduction would occur with overlap of the levels, as each adjacent slit field effectively becomes narrower but with the same spacing.

With the dual assembly design the two vertical levels of leaves would result in different penumbrae for adjacent leaf-defined segments of the field aperture. This is due to the different source to collimator distances, and hence magnifications. Figure 5-13 shows that the penumbra for the upper and lower collimator jaws, with SCD's of 22.5 cm and 30.0 cm are similar, therefore this is unlikely to be important effect. Currently, rectangular fields defined by secondary collimators have different penumbrae in the two orthogonal directions, as do fields with secondary collimation and partial tertiary blocking.

The experimental results for the off-axis radiation transmission due to the vertical displacement of adjacent leaves suggest that this is not an important effect. Alignment of the sides of vertically displaced adjacent leaves or very small overlap of the leaves is sufficient to adequately shield. The off-axis penetration is also minimized by small vertical gap between the levels. This means that in intensity modulated treatment when contiguous areas are sequentially irradiated that the reduction in dose due to the tongue and groove effect is minimised. Reduction in dose will still occur due to penumbral blurring, however this is a smaller effect than the tongue and groove (Balog *et al.*, 1999). In a real collimator some overlap of the levels may be necessary to minimise transmission and for positioning tolerances. Dose reduction for sequentially irradiated contiguous areas will then occur due to the overlap as with the conventional tongue and groove design. For an equivalent overlap the dose reduction may be slightly greater than a tongue and groove as the overlap is a full leaf thickness, however as this work shows, this degree of overlap should not be necessary. Following movement, the re-positioning of the assemblies would have to be accurate, otherwise significant under or over-dosage could occur if either assemblies were in the wrong position.

5.6. Conclusion

A multileaf collimator design is proposed that splits the leaves into two vertically displaced levels, consisting of alternate leaf and leaf-width spaces. Each level can move laterally to align the leaves with the other level, transmitting radiation as multiple slit fields to form an image of the external anatomy. The characteristics of this transmission have been investigated to see how they depend on the collimator design features. The major impact on the transmission was found to be the slit or leaf width. For small widths the individual slit profiles become broader and overlap to produce a modulated transmission profile and hence image. For larger widths the overlap is small and the profile produces a sampled image. The vertical displacement of adjacent leaves produces adequate shielding with alignment or very small overlap of the leaf sides.

6. Image formation with a dual assembly multileaf collimator design: image quality

6.1. Introduction

When imaging with the dual assembly MLC design, the two assemblies or grids of leaves are aligned by movement of one of the assemblies. Radiation is transmitted through the aligned assemblies as multiple slit fields, irradiating the anatomy external to the treatment field. The multiple slit field transmission was found in the previous chapter to result in a modulated radiation intensity distribution incident on the patient and hence detector (Figure 6-1). The other leaf assembly can also be shifted to complete the irradiation of the external anatomy. This is referred to as a double-movement image as both assemblies must be moved and results in an image similar to open field imaging. However, forming the external anatomy image by movement of a single assembly (with the modulated intensity distribution) would be more efficient, require less time, and would also result in a lower dose to the anatomy than movement of both assemblies. It is therefore of interest to determine whether imaging with the modulated intensity distribution is feasible for double-exposure imaging. This chapter therefore investigates the image quality of images formed in this manner and compares this to open field image quality.

The transmitted intensity distribution was found in Chapter 5 to be due to the region of the source that irradiates a point at the image plane. Under the open slits the high intensity is due to the central or focal region of the source distribution. Under the leaves the low intensity is due to the peripheral or extra-focal region of the source distribution. The region of the radiation distribution under the leaves may also have contribution from two adjacent slits, with peripheral source regions on either side of the source distribution irradiating the image points.

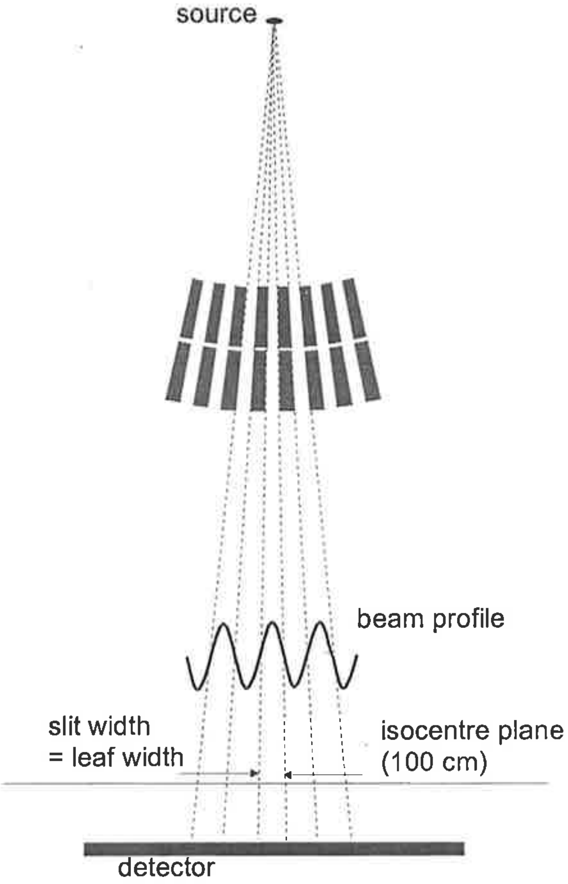

Figure 6-1 Modulated intensity distribution incident on the object produced by the aligned assemblies of the multileaf collimator.

In standard open field portal imaging where the detector is further from the source than the object, the finite size of the source distribution decreases spatial resolution (geometric unsharpness). The source distribution that contributes to an image point and the resulting resolution is constant over the image. However, when imaging the external anatomy with the aligned leaf assemblies of the MLC, the source distribution contributing to an image point depends on the region of the source that irradiates the point through the MLC slits. This source region varies for each image point, therefore the effect of the source distribution on image resolution will vary across the image. Figure 6-2 illustrates this concept. For clarity, only one collimated slit of the grid is drawn with two point objects, one under the slit aperture and one under the centre of the leaf. The blurring of the point object under the slit is due to the focal source region while the blurring of the point object under the leaf is due to the extra-focal source region. The narrow intense focal source would be expected to result in high spatial resolution whereas the broad narrow extra-focal source would result in lower resolution.

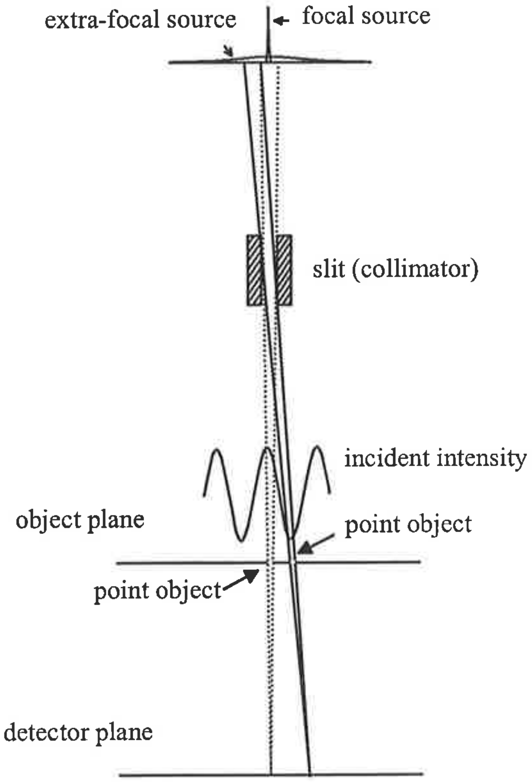

Figure 6-2 Potential difference in spatial resolution for regions of the image under the open slit aperture and under the leaves.

Spatial resolution is also affected by scatter. Increased scatter results in a reduction in low frequency spatial resolution (Barrett and Swindell, 1981). Potentially where the primary intensity is lower under the leaves, the fraction of the signal due to scatter may increase due to scatter from the adjacent high intensity region. If the scatter fluence reaching the detector is relatively spatially uniform then the scatter fluence under the slits and under the leaves will be similar. The lower primary fluence under the leaves will result in an increased scatter fraction. This would manifest as a reduced resolution under the leaves at low spatial frequencies.

Therefore to determine the variation in spatial resolution for images formed with the modulated intensity, MTF measurements were made to compare the spatial resolution in the image regions. The MTFs were determined by imaging an edge object placed at isocentre. The MTF under the centre of the open slit (in the centre of the irradiated slit field) and under the centre of the leaves (centre of the region between the irradiated slit fields) was compared to open field image MTF. The effect of scatter, magnification, leaf width (slit width), leaf spacing, source to collimated grid distance and energy on the MTF was investigated. The contrast-to-noise ratio for the different image regions is also examined.

The chapter begins with a theoretical examination of the effect on spatial resolution of the variation in the source distribution contributing to the image region. The MTF measurement technique with an edge object is then discussed. Finally the MTF measurements to examine the spatial resolution for the images with the collimated grid present are presented.

6.2. Theory

Simplifying the linear imaging model for open field imaging (Chapter 3) to one dimension (Figure 6-3), the image formation (photon density) $h(x'')$ arriving at the image plane is expressed

$$h(x'') = C \int_{source} f(x) g(ax'' + bx) dx \tag{6.1}$$

Where $f(x)$ is the photon intensity emitted toward detector point x'' from the source point at x, and $g(ax'' + bx) = g(x')$ is the transmittance of the object plane at the point x', with

$$a = L_1 / (L_1 + L_2) \tag{6.2}$$

$$b = L_2 / (L_1 + L_2) = 1 - a \tag{6.3}$$

$$C = 1/(L_1 + L_2)^2 \qquad (6.4)$$

For an image point at x'' the photon intensity is formed from the contribution of all source points along ray paths through the object with each source point contribution weighted by the transmission of the object along the path.

This leads to a convolution of the source function and the object transmission functions projected to the image plane

$$h(x'') = (a/b)^2 C\tilde{f}(x'') * \tilde{g}(x'') \qquad (6.5)$$

where

$$\tilde{\tilde{f}}(x'') = f(-ax''/b) = f\left(-\frac{1}{M-1}x''\right) \qquad (6.6)$$

and

$$\tilde{\tilde{g}}(x'') = g(ax'') = g\left(x''/M\right) \qquad (6.7)$$

represent pinhole magnification of the source distribution (magnification factor = $-b/a$) and magnification of the object by projection with magnification given by

$$M = 1/a \qquad (6.8)$$

The reduction in resolution of the image due to the source distribution is the same for all image points, depending only on the source distribution and magnification.

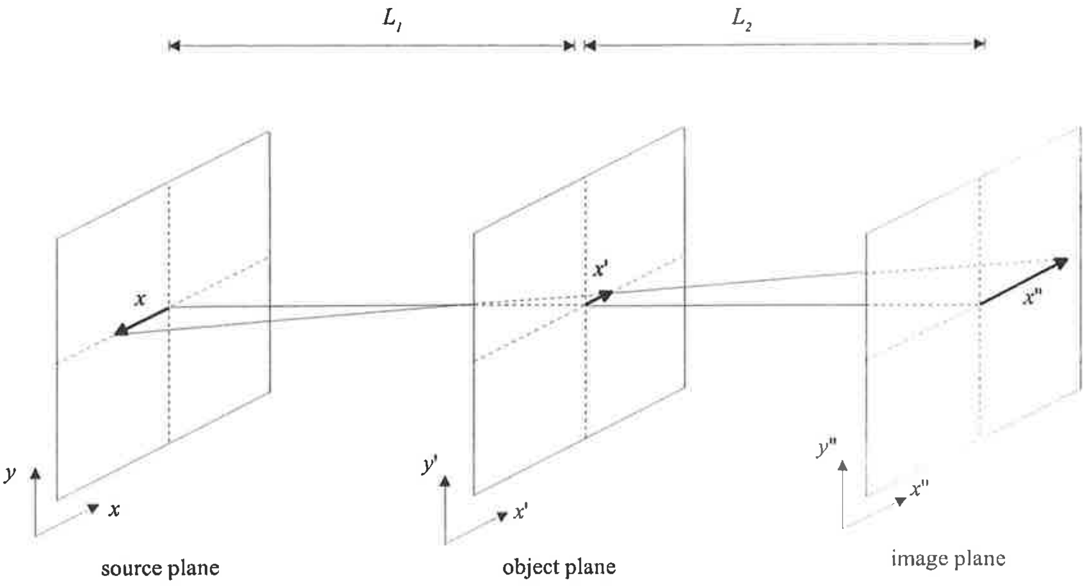

Figure 6-3 The geometry of the model for formation of the radiographic image.

When the aligned MLC grid is present a segment of the source distribution now irradiates the image point, assuming a perfectly attenuating grid. The source intensity is modified by the object transmission along this 'window' of ray paths from the source through the grid to the point. For example for an image point x'' Equation 6.1 for the intensity becomes

$$h(x'') = C \int_{x_a(x'')}^{x_b(x'')} f(x)g(ax'' + bx)dx \tag{6.9}$$

where the integration limits at the source plane are determined by the position of the grid relative to the image point and the source (Figure 6-2). Only source points between these limits contribute to the image formed at the point x''. Image points under the leaves of the grid will also have contribution from the opposite side of the source.

The variation of these limits of the source with image point is complex and depends on the slit width, source to grid distance, source to object distance, and source to detector distance. These limits will repeat periodically due to the periodicity of the grid. For a point directly under the centre of a leaf the inner limit is determined by the position of the bottom corner of the leaf, while the outer limit is determined by the position of the upper corner of the adjacent leaf (Figure 6-2). Representative x-coordinate limits of the source region are shown in Table 6-1 for leaf and slit widths of 2.0, 1.0, 0.5 and 0.2 cm, a source to proximal surface of the grid of 22.5 cm, and source to image distances of 100 and 130 cm. These were calculated from the geometry assuming that the grid is perfectly attenuating and focussed to the centre of the source. The limits are relative to the centre of the source (zero coordinate $x = 0$) at the source plane. For a point directly under the leaf a mirror image region of the source is seen though the adjacent slit with identical limits to those below but on the opposite side of the source. These calculated limits show that as the slit width increases, the source region becomes wider but more peripheral. The increase in distance of the image from the source reduces the limits slightly.

Table 6-1 Limits of the source that contribute to an image point directly under the centre of a leaf at 100 cm and 130 cm from the source. The limits show the *x*-coordinate limits at the source plane of the source region that contributes to the image point.

Slit width (leaf width) at isocentre / mm	Inner limit / mm x_b	Outer limit / mm x_a	Inner limit / mm x_b	Outer limit / mm x_a
	at 100 cm	at 100 cm	at 130 cm	at 130 cm
20	4.3	8.7	3.9	8.1
10	2.1	4.3	2.0	4.1
5	1.1	2.2	1.0	2.0
2	0.4	0.9	0.4	0.8

By considering a small region of the image plane and assuming that each point in this region is irradiated by the same source segment $f_s(x)$ through the grid, the intensity at the image plane for this region can be expressed

$$h(x'') = (a/b)^2 C\tilde{\tilde{f}}_s(x'') * \tilde{\tilde{g}}(x'') \tag{6.10}$$

The spatial resolution of the image point is determined by the source segment distribution contributing to that image point. In practice the image is two-dimensional. However assuming the grid is aligned so that the long axis of the slits are in the y-direction, the view of the source from the image plane is independent of the y-coordinate. The segment of the source that contributes to an image point then becomes a two-dimensional strip of the source with the x-coordinate limits as above. The image for a small region is the two-dimensional convolution (represented by **) of the object transmission function with the two-dimensional source segment.

$$h(x'', y'') = (a/b)^2 C\tilde{\tilde{f}}_s(x'', y'') ** \tilde{\tilde{g}}(x'', y'') \tag{6.11}$$

Therefore in the Fourier domain

$$H(u'', v'') = (a/b)^2 C\,\tilde{\tilde{F}}_s(u'', v'')\tilde{\tilde{G}}(u'', v'') \tag{6.12}$$

where F and G are the Fourier transforms of f and g respectively and u and v are the spatial frequencies corresponding to x and y. The spatial resolution for different regions of the image formed with the modulated intensity is dependent on the source segment. By utilising a delta function object, and considering that the detector response will also affect the image, the transfer function TF is equal to

$$TF(u'', v'') = (a/b)^2 C\,\tilde{\tilde{F}}_s(u'', v'')D(u'', v'') \tag{6.13}$$

where $D(u'', v'')$ is the response of the detector which will be the same for all image regions. Therefore the effect of the source segment on the resolution can be examined by use of an object approximating a delta function transmission (or the integral of) and calculation of the MTF. The measurements are scaled to the object plane to remove the effect of magnification of the object.

$$TF(u', v') = (a/b)^2 C\,\tilde{\tilde{F}}_s\left(u''/M, v''/M\right)D\left(u''/M, v''/M\right) \tag{6.14}$$

An edge object was employed to approximate the delta function object and obtain the ESF and hence MTF. The edge ideally provides a step-edge transmission function. When the detector is placed at magnification the measured intensity profile is then a convolution of the step-edge transmission and the source intensity function, blurring the edge. The edge object is placed under the open slits or under the leaves so that the ESF and MTF reflect the source segment distributions that contribute to these image regions. Increasing source size or magnification will increase the blurring of the edge function due to the source and reduce the MTF.

6.3. Measurement technique

At kilovoltage energies a thin edge is employed for ESF and MTF measurement. However to provide similar attenuation at megavoltage energies, the edge must have a much greater thickness. Morton *et al.* (1991) measured the ESF and hence LSF of their electronic portal imaging system with a 10 cm thick lead edge placed 2 cm above the detector. The effect of edge thickness on the LSF however was not discussed. The effect on the measured MTF of using a thick edge is therefore examined in this section.

The width of the edge transmission profile (ESF) due to the source is increased by the thickness of the edge from the profile that would result from an ideal step-edge transmission (very thin edge). By considering a uniform disk source as shown in Figure 6-4, the width of the ESF can be expressed

$$w' = \left(\frac{gap + t}{SAD - t} \right) d \tag{6.15}$$

where t is the block thickness, SAD is the distance from the source to the distal surface of the edge, gap is the distance from the edge to the detector, and d is the source width. The width of the ESF for a thin edge (w) is given by setting $t = 0$ in the above equation. For a thin edge, $t = 0$ at a magnification of 1 ($gap = 0$) and $SAD = 100$ cm, the width $w = 0$, whereas for a thick edge, $t = 7.5$ cm, the width $w' = 0.15$ mm. As the magnification increases, the percentage difference between w' and w becomes less as seen in the figure. For $t = 0$ and $gap = 40$ cm ($M = 1.4$) the width of the ESF w is 0.8 mm. When the edge has thickness $t = 7.5$ cm, the width is increased to 1.0 mm.

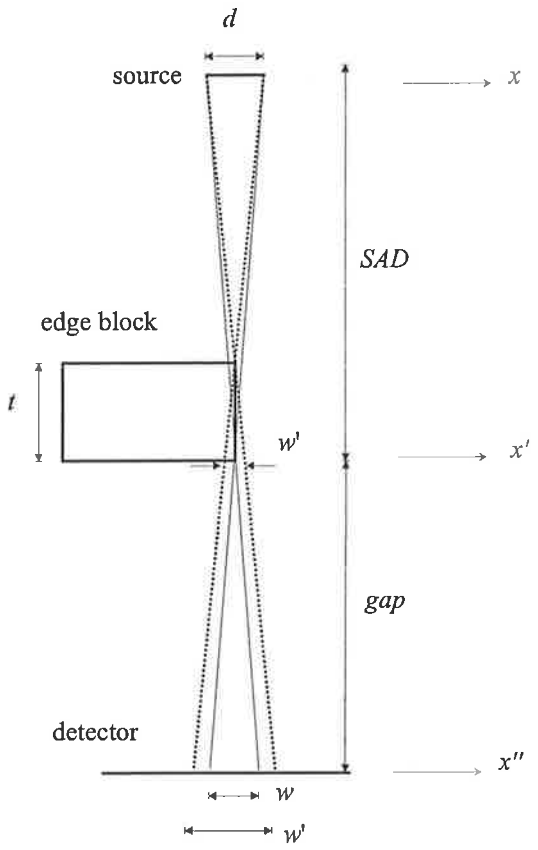

Figure 6-4 Increase in edge function width for a thick edge due to the fact that edge points proximal to the source are at increased magnification.

The thick edge will also influence the shape of the measured ESF profile due to transmission through the block edge. This transmission can be examined by considering a thick edge to be composed of many thin edge elements, each with a transmission T. An edge object comprising three thin edge elements, and a uniform intensity source of width d is shown in Figure 6-5. The detector is placed directly beneath the edge. The incident intensity is I. Each plate attenuates the source to give a transmitted intensity along a raypath of $I \times T$. The intensity at the detector decreases linearly from the point at the detector where the entire source is unattenuated and the intensity is I, to the point where the entire source becomes occluded by the edge, and the intensity is then $I \times T$. However the steepness of the ramp intensity function decreases as the thin edge component becomes further from the detector. For the edge component directly on the detector the transmitted intensity profile is a step-edge function. Considering the transmission profiles for the three plates separately, and the combined transmission profile as the multiplication of individual transmissions, the resultant transmission function is shown in Figure 6-5. The edge profile is asymmetric and distorted from the ramp profile that would be measured for a thin edge at magnifications greater than 1. The use of a thick edge therefore not only results in a broadening of the edge intensity profile but alters the profile shape from that resulting from a thin edge.

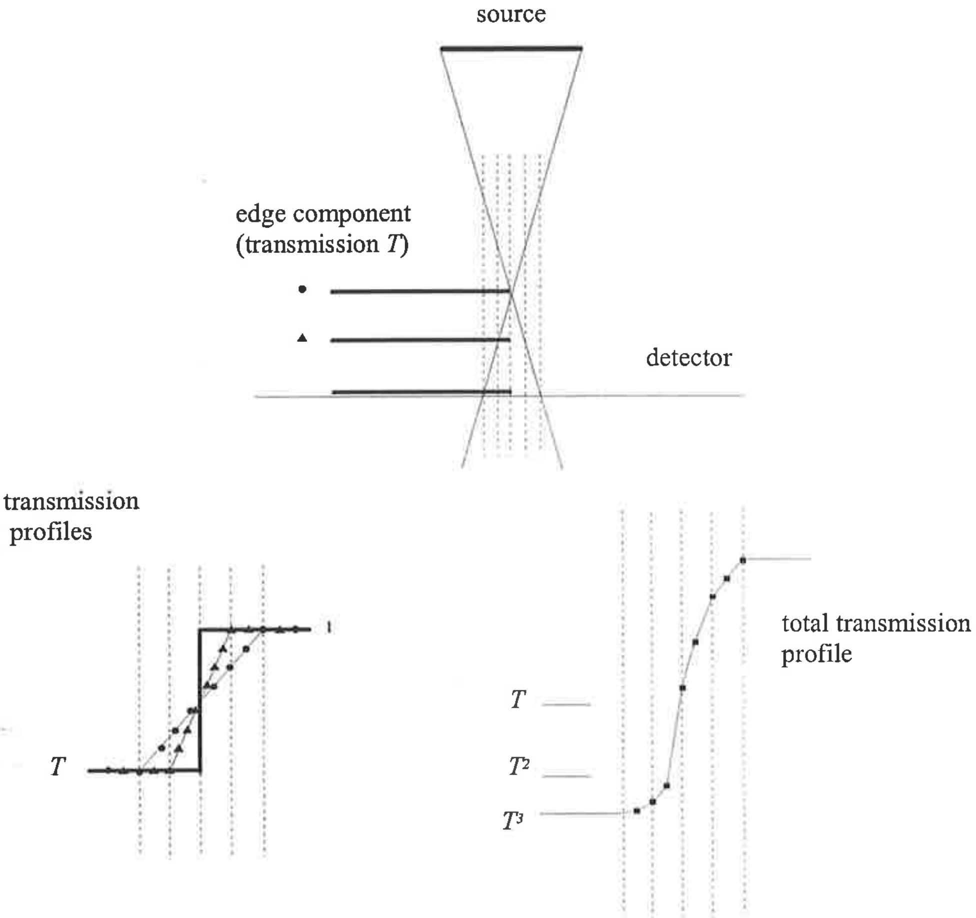

Figure 6-5 Effect of a thick edge on the edge function due to the path length of the rays through the block edge.

Scatter from the block will also influence the measured ESF. The measured profile can be considered as the primary transmission profile plus a broader scattered intensity profile. This scatter profile will depend on the thickness of the edge and will vary with the magnification. The scatter decreases with distance from the centre of the block due to the loss of scatter from adjacent block regions. The scatter will also decrease with increasing air gap between the block and the detector.

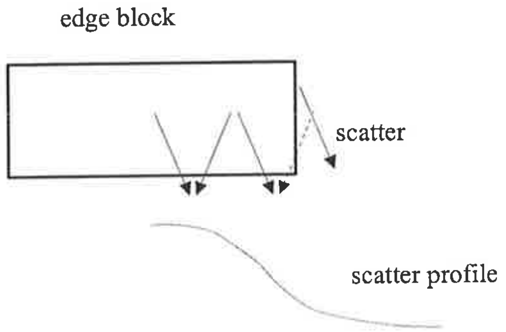

Figure 6-6 Potential scatter contribution to the edge profile.

These effects can be expressed mathematically, giving the measured edge profile at the detector plane as

$$ESF_{tot}(x'') = ESF_{pri}(x'')_{t,M} + ESF_{scat}(x'')_{t,gap} \tag{6.16}$$

where $ESF_{pri}(x'')_{t,M}$ is the primary edge function intensity and $ESF_{scat}(x'')_{t,gap}$ is the scatter profile. These effects will distort the ESF incident at the detector plane with a thick edge object from that resulting from a thin edge or delta object. Therefore the ESFs are not measurements of the system MTF and are used only for comparison of the effect of variation in the source distribution on resolution.

6.4. Methods and Materials

6.4.1. Open field MTF

Modulation transfer function measurements with an open field exposure were initially made to examine the variation in MTF with magnification without the collimated grid present. Two magnifications of 1.0 and 1.77 were employed. A brass edge block of thickness 7.6 cm was placed with its proximal surface at 100 cm from the source of a Siemens KD2 linear accelerator (Siemens Medical Systems Inc., Concord, CA). The block was 7 cm in length along the edge and 5 cm in width. The edge was aligned with the source by closing the collimator jaws to form a narrow slit field parallel to the edge. Radiographs were recorded with the film placed 100 cm below the block and the edge moved until it was aligned in the centre of the slit field. The collimator was then rotated by 180 degrees and the film repeated to ensure that the collimator jaw settings were symmetric about the source. Attenuating pointers were also placed on the proximal and distal surfaces of the edge, and the alignment of these verified on the radiographs to ensure that the edge surface was aligned along the beam direction.

X-omat v film (Kodak Corp., Rochester, NY) was then placed in a Kodak xomatic cassette 1 cm below the brass edge object ($M \approx 1$). The field size was set to 10 × 10 cm and the film exposed to 20 monitor units with 6 MV energy (100 monitor units corresponds to a dose of 1 Gy for a 10 × 10 cm field size at 10 cm depth in water). The film was digitised with a Vidar VXR-12 CCD-camera based film scanner (Vidar Systems Corp., Herndon, VA) at 0.17 mm sampling interval and edge profiles obtained perpendicular to the edge. Conversion of the scanner pixel values to optical density was performed by cubic-spline interpolation of a lookup table. Linearity of the film optical density to dose was earlier confirmed by exposing films to varying dose levels and measuring the resultant optical density levels. The ESF measurement was then repeated at a source to film distance of 190 cm (M = 1.77). The sampling interval was scaled to the object plane to remove the magnification of the object (Equation 6.14).

The MTFs were calculated from the ESF profiles with the algorithm outlined in Chapter 4. Profiles were sampled perpendicularly across the edge as the sampling resolution of the scanner is sufficent to avoid aliasing in the results. Edge profiles were averaged over approximately 3 cm length of the edge and differentiated to obtain the LSF. To further reduce the higher frequency noise, exponential functions were fitted to the tails of the ESFs. MTFs with and without the fitting were compared to ensure that there was no distortion of the MTF introduced by the fitting. The MTF was obtained by Fourier transformation of the LSF.

6.4.2. MTF comparison under open slits and leaves

MTF measurements were made under the centre of an open slit and under the centre of the leaf with the collimated grid simulated by forming multiple slit fields with the collimator jaws. These MTFs were compared to a measurement with an open field exposure. The experimental setup is illustrated in Figure 6-7. The edge block was aligned as for the previous open field measurements. The film cassette was placed 40.0 cm behind the block (M = 1.3). To simulate the collimated grid, a slit field of width 0.5 cm and length 10 cm (at isocentre) was formed with the upper collimator jaws and an exposure recorded on the film. The slit field was then moved 1.0 cm laterally, and a second exposure recorded. The 6 MV nominal energy was employed. To record the open field exposure the collimator jaws were set to 10 × 10 cm.

The geometry was chosen so that the edge was aligned along a central axis of the source perpendicular to the long axis of the slit fields (x-axis). The ESF profiles were then recorded across the edge in the y-direction. These were sampled in the regions of the image under the open slits and under the leaves (Figure 6-8) and reflect the source segment distribution (in the y-direction) that contributes to the image region (Figure 6-7). If the edge was aligned along the long axis of the slits (y-direction) the ESF profiles recorded across the edge would be affected by the intensity variation of the beam profile in the x-direction. Approximately 5 profiles (0.8 mm) were averaged for the region under the leaves and similarly for the image region under the open slits.

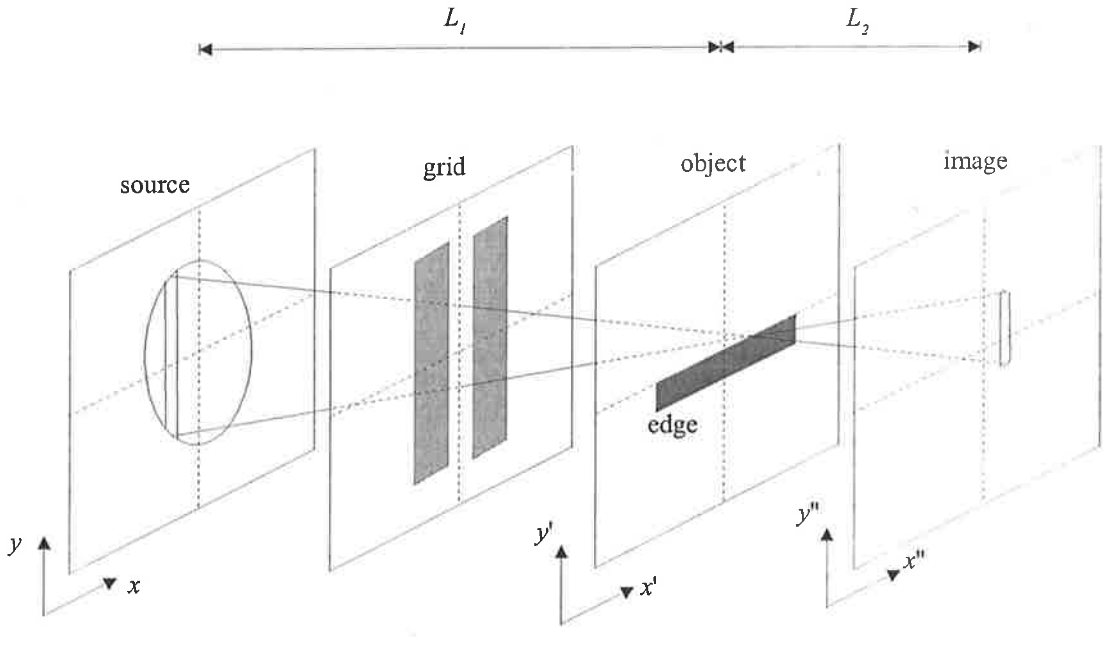

Figure 6-7 Experimental set-up for measurement of the MTFs under the open slits and under the leaves of the collimated grid images.

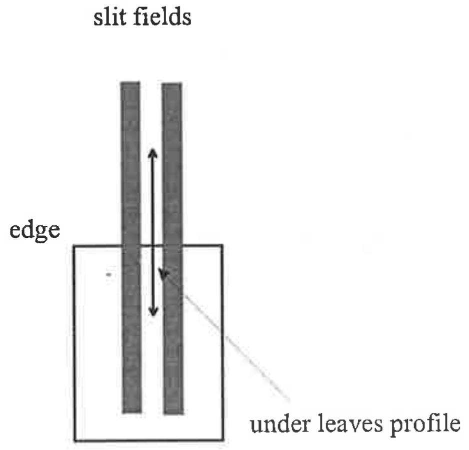

Figure 6-8 Profile sampling in the regions of the image under the leaves and under the open slits.

6.4.3. Scatter

To examine the impact of scatter on the MTFs, an experiment was performed varying the scatter conditions while maintaining the field size and hence effect of the source. The open field MTF was measured with and without 10 cm of solid water present between the edge and the film. The effect of the source is the same for both measurements however the solid water will introduce extra scatter. The edge was aligned as before at 100 cm to the proximal surface. The film was placed 20 cm behind the edge. A 6 MV irradiation was performed with a 10 × 10 cm field size. The 10 cm thickness of solid water was then placed between the edge and the film and a second film exposed. The second exposure was increased to obtain the same transmission and optical density with the solid water present. The MTFs were calculated from edge profiles obtained from the two films.

Measurements were also performed to examine whether there is an MTF difference in the region under the open slits compared to open field imaging due to reduced scatter or to occlusion of peripheral areas of the source. An open field MTF was measured and compared to the same field size formed by multiple contiguous slit irradiations. These two situations should have the same scatter present, but in the latter irradiations the extra-focal source is occluded by the collimated slit. The open field irradiation was performed with the upper collimator jaw forming an 8 cm width field at isocentre, with the orthogonal jaw set to 10 cm. The film cassette was placed at the magnification of 1.3 with 100 cm to the proximal surface of the 7.6 cm edge. To form the segmented field, 8 irradiations of adjacent 1 cm width slit fields were made.

6.4.4. Magnification

The MTFs in the image region under the leaves were measured at three magnifications to examine the variation in MTF with increasing distance of the detector from the object. The edge was aligned as before and the film was placed at three distances below the block of 1.0, 40.0 and 90 cm to give magnifications of approximately 1.0, 1.3 and 1.77. As for Section 6.4.2 two slit fields of 0.5 cm width were exposed at each magnification and the ESF measured in the centre of the region between the two fields. The MTFs were calculated from these profiles to yield the MTF variation under the leaves with increasing magnification.

Images were also acquired to visually compare the resolution at magnification with the resolution at a magnification of 1. The QC-3 phantom discussed in Chapter 5 was placed at 100 cm from the source of the accelerator. The film was placed directly beneath the phantom and two 6 MV slit field irradiations of width 1.0 cm separated by 2.0 cm were performed with the orthogonal field dimension set to 10.0 cm. The phantom was placed so that the 0.25 mm^{-1} bar-pattern of the phantom was directly under the leaves region of the image. The film was then placed at 132.5 cm from the source and the irradiation repeated.

6.4.5. Slit width

The MTFs under the leaves were measured varying the slit width with the leaf width equal to the slit width. As seen in Table 6-1 the segment of the source that contributes to the region under the leaf varies with the slit width and therefore the spatial resolution due to the source may vary. The slit field irradiation images of the edge were formed by setting the upper collimator jaws to slit widths projected to isocentre of 1.0 cm, 0.5 cm, and 0.2 cm. Each slit field was 10 cm long. The film was placed at 40.0 cm below the edge at 100 cm to give a magnification of 1.3. For each slit width two slit fields were exposed with spacing equal to twice the slit width. The 6 MV nominal energy was employed. The exposure was increasd to adjust for the lower transmission through the smaller slit widths to give similar peak optical density values in the images. The MTFs under the leaf regions were calculated for each slit width image.

6.4.6. Source-collimator distance

Increasing distance of the collimation from the source (for the same detector distance) results in more peripheral source segment contributing to the region under the leaves. To determine the effect of this on the spatial resolution, the MTF measurements under the leaves were performed for two source to collimator distances. The upper and the lower collimator jaws were used to form the two 0.5 cm slit field irradiations simulating the collimated grid image. For the upper collimator jaws the distance from the source to the upper surface of the collimation (SCD) was 22.5 cm while for the lower jaws this was 30.0 cm. The film was placed at the magnification of 1.3 for both measurements. For the lower collimator jaw slits the collimator was first rotated by 90 degrees to form the lower collimator jaw grid irradiation in the same direction across the edge as the upper jaw irradiation. The MTFs under the leaves were therefore compared for these two source to collimation distances.

6.4.7. Septal spacing

The source segment that contributes to the image in the region under the leaves also varies with the spacing of adjacent slits. This is referred to as the septal spacing as the centre to centre spacing of the leaves is the same as the centre to centre spacing of the slits. Increasing the septal spacing results in the source segment that contributes to the image under the leaves becomes more peripheral, due to the increased leaf width. The MTF was measured at a septal spacing of 1.25 cm and compared to a 1.0 cm septal spacing measurement. A 0.5 cm width slit was formed with the lower collimator jaws and the film exposed. The centre of the slit was then shifted with the asymmetric jaws laterally by 1.25 cm and the irradiation repeated. The film was placed 40.0 cm below the edge with magnification 1.3. This is equivalent to 0.5 cm slits formed between leaves of 0.75 cm width. This was repeated but with the two slit fields separated by 1.0 cm equivalent to a 0.5 cm leaf width. The MTFs under the leaves for the two septal spacings were compared.

6.4.8. Energy

A comparison was made of the MTF in the image regions under the leaves with two energies of 6 MV and 23 MV to determine whether the energy affects the resolution. The two 0.5 cm slit field irradiations were performed as described earlier. The source to proximal surface of the edge was 100.0 cm and the edge to film distance was 40.0 cm. The

MTF was measured under the leaves for the 6 MV and 23 MV energies.

6.4.9. Contrast-noise ratio

The contrast to noise ratio (CNR) in the image regions under the slits and under the leaves was compared. The low frequency contrast was obtained from the difference in optical density between the high side and low side of the edge profile divided by the average of the two optical densities. The noise level was found from the standard deviation of the low optical density side of the profile under the block. As the optical density of the low side of the profiles was similar for all the profiles, correction for the change in noise level with optical density introduced by the Vidar scanner was not necessary. All measurements were adjusted for the monitor units delivered.

6.5. Results

6.5.1. Open field MTF

The MTFs for the open field irradiation at the two magnifications of 1.0 and 1.77 are shown in Figure 6-9. These show that the MTF decreases at higher spatial frequencies for the increased magnification due to the effect of the source. However an increase in the MTF is evident at lower frequencies below 0.5 mm^{-1}. This low frequency effect is consistent with a reduction in scatter with increasing distance between the block and the detector. This effect is examined further in Section 6.5.3.

6.5.2. MTF comparison under the open slits and under the leaves

An example of a film recorded for the ESF measurements is shown in Figure 6-10. The two slit fields are clearly visible as the dark (high optical density) fields. The optical density reduces markedly under the edge. Figure 6-11 shows the ESF sampled in the region under the leaves compared to the ESF sampled in the region under the open slits between the two slit fields. The profiles have been normalised to the same height for comparison. Much greater blurring of the edge profile under the leaves compared to under the slit aperture is evident. The profiles for the open fields were similar to under the slit aperture and are not shown for clarity, however the MTFs for these were calculated.

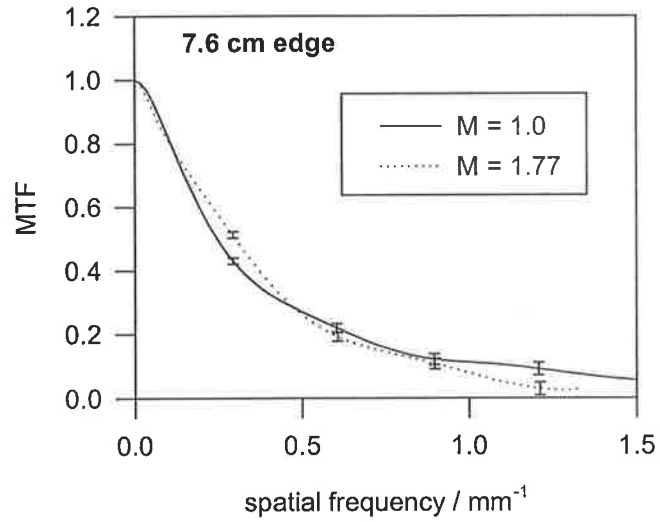

Figure 6-9 MTF for open field irradiation at two magnifications of 1.0 and 1.77. The MTF decreases with increasing magnification at higher spatial frequencies due to the source and increases slightly at lower spatial frequencies due to scatter reduction.

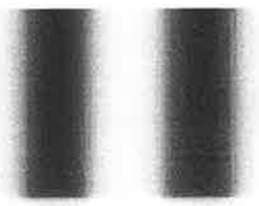

Figure 6-10 Example of film irradiation with two slit fields for measurement of the ESF and MTF under the leaves and under the open slits for the collimated grid irradiation.

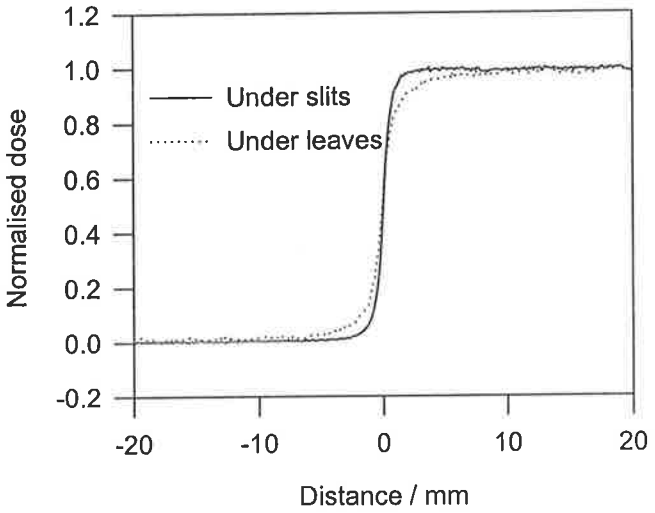

Figure 6-11 ESF under the leaves compared to under the open slits. These show that the blurring of the edge is much greater under the leaves than under the open slits.

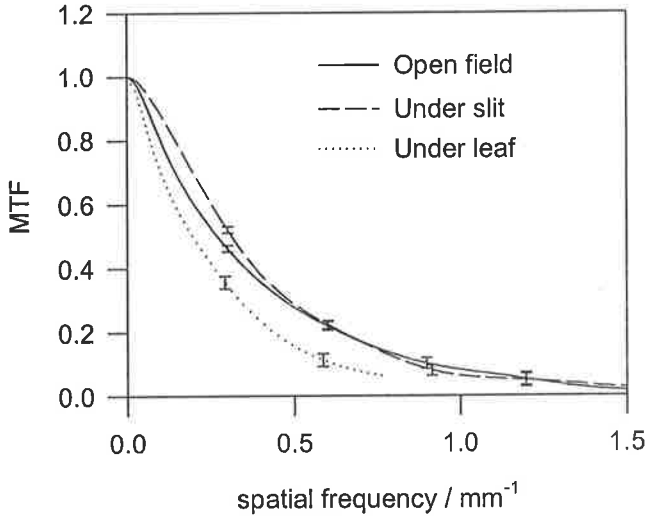

Figure 6-12 MTFs in the image region under the leaves and under the slits compared to an open field. These show a reduction in the MTF under the leaves.

The MTFs calculated from the edge profiles are shown in Figure 6-12. The MTF under the open slits is similar to the open field MTF although slightly higher at frequencies below 0.5 mm^{-1}. This is due to a reduction in scatter (see Section 6.5.3). The scatter will be reduced for the two thin slit fields relative to the wider open field due to a reduced overall field size. There is a marked reduction in MTF under the leaves at all spatial frequencies. Although some low frequency reduction may be due to scatter, the higher frequency reduction suggests that the source segment that irradiates under the leaves is broader. The source segment will be largely extra focal as the central 2 mm of the source is occluded by the collimated grid. The intense narrow focal source would be expected to yield superior spatial resolution than the broader extra-focal source region.

6.5.3. Scatter

The MTFs for the open field with and without the 10 cm of solid water present are shown in Figure 6-13. With the scatter material present the MTF is reduced at lower spatial frequencies (less than 0.5 mm^{-1}). This is a similar frequency range to the increases in the MTF observed with increasing magnification (Figure 6-9) and with reduced field size (Figure 6-12), and suggests that these observed MTF effects are due to scatter. There is no difference in the MTFs at higher spatial frequencies, the scatter is not influencing the MTF values at frequencies greater than approximately 0.5 mm^{-1}.

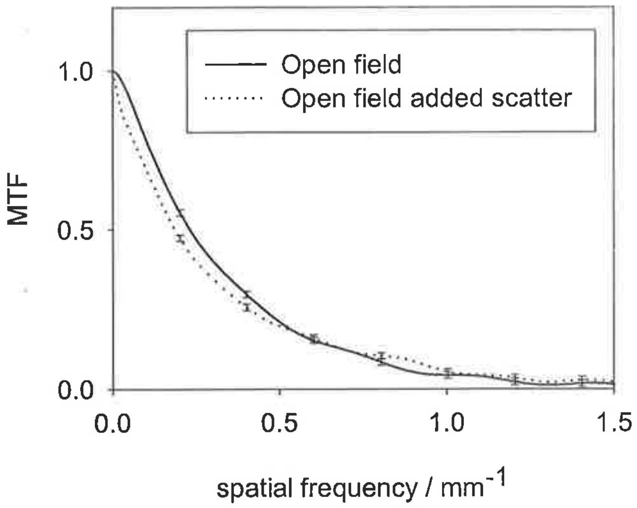

Figure 6-13 Effect of adding 10 cm solid water to increase the scatter on the open field MTF. The increased scatter results in a reduction in the MTF at low spatial frequencies below 0.5 mm^{-1}.

The MTFs measured with the open field and with the multiple slit field irradiations were identical within the experimental uncertainty and are not shown. This suggests that the MTF difference at low frequencies observed between the open field and the slit field is due to reduced scatter in the slit field irradiation (reduced field size), not to occlusion of peripheral regions of the extra focal source. This low frequency difference will reduce when a slit field irradiation is performed with a collimated grid with multiple slit fields rather than the two slit fields employed here. However the overall effective field size will still be less than for an open field irradiation.

6.5.4. Magnification

The MTFs under the leaves for the 0.5 cm slit fields are shown for the three magnifications of 1.0, 1.3 and 1.77. The MTFs decreases with increasing magnification. This is consistent with the increasing effect of the source size with magnification. There is a small increase in the MTF at low frequencies less than 0.5 mm^{-1} apparent for the largest magnification due to reducing scatter with magnification.

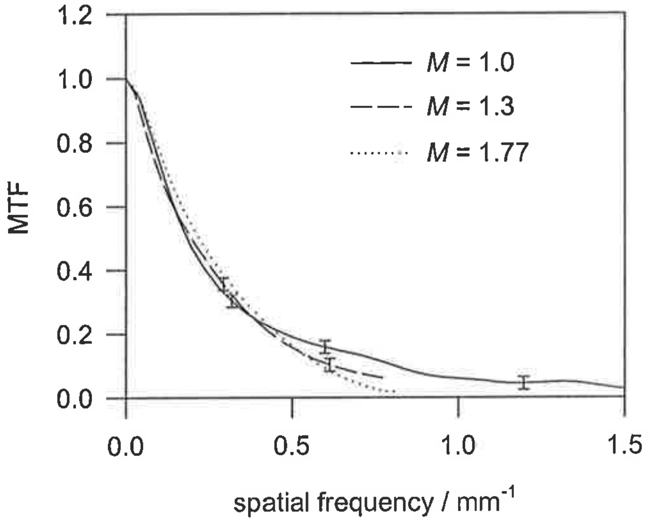

Figure 6-14 Variation of MTF under leaves with magnification. There is a decrease in the MTF with magnification consistent with the effect of source size with magnification.

The reduction in spatial resolution under the leaves with magnification can be seen visually in the images of the phantom shown in Figure 6-15. Only the region under the leaves of the images are shown. The reduction in resolution for the magnification of 1.3 compared to a magnification of 1 can be seen. This reduction is greater for the 1 cm slit width images shown here than for the 0.5 cm slit width.

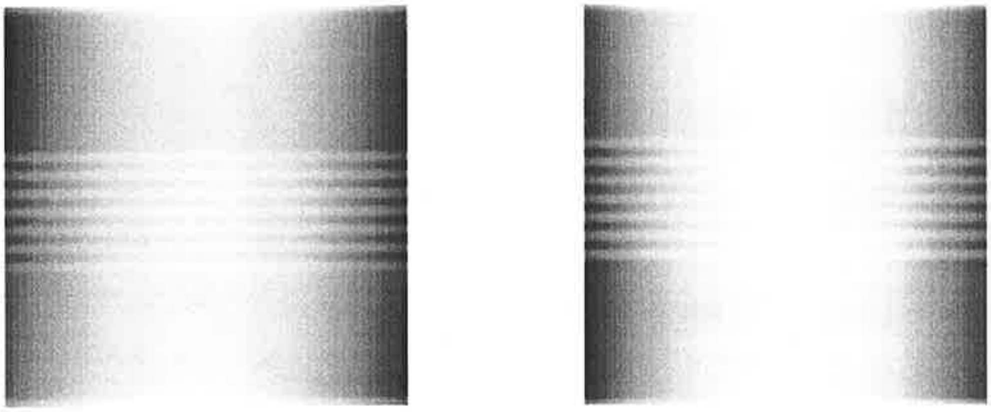

(a) (b)

Figure 6-15 Images of the PIPS phantom in the region under the leaves for (a) $M \approx 1$, and (b) $M = 1.3$. These were acquired by two 1 cm slit width irradiations. The bar-pattern under the leaves for the higher magnification has lower resolution due to the effect of the source.

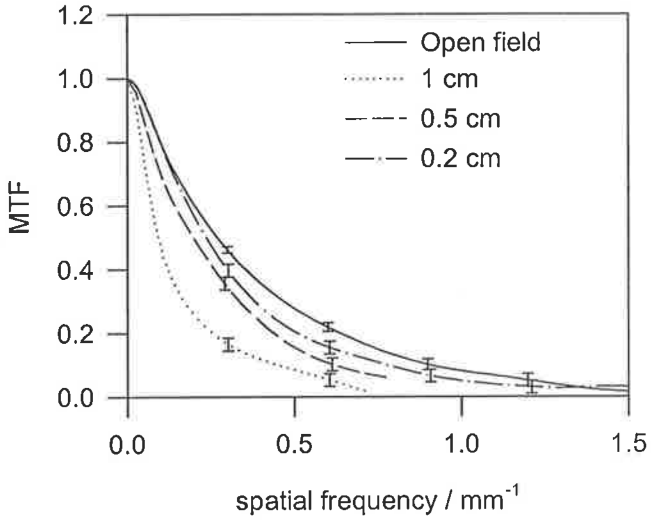

Figure 6-16 MTF under the leaves with slit width. The MTFs increase with decreasing slit width as the contributing source segment becomes more central (focal).

6.5.5. Slit width

The MTFs obtained from profiles under the leaves for slit widths of 1.0, 0.5 and 0.2 cm are shown in Figure 6-16 compared to the open field MTF. All are lower than the open field MTF. The MTFs increase at both lower and higher spatial freqencies with decreasing slit width. The observed trends are consistent with the source segment contributing to the image region becoming more central as the slit width decreases (Table 6-1). As the slit width decreases the focal source begins to irradiate the region under the leaves increasing both the image intensity and the resolution.

6.5.6. Source-collimator distance

The MTFs under the leaves for the 0.5 cm slit width at $M = 1.3$ are shown in Figure 6-17 for the slits formed by the upper (SCD = 22.5 cm) and lower (SCD = 30.0 cm) collimator jaws. The MTFs are similar at higher frequencies with a very small reduction for the greater SCD at low frequencies. For these two source collimator distances the MTF difference is minor.

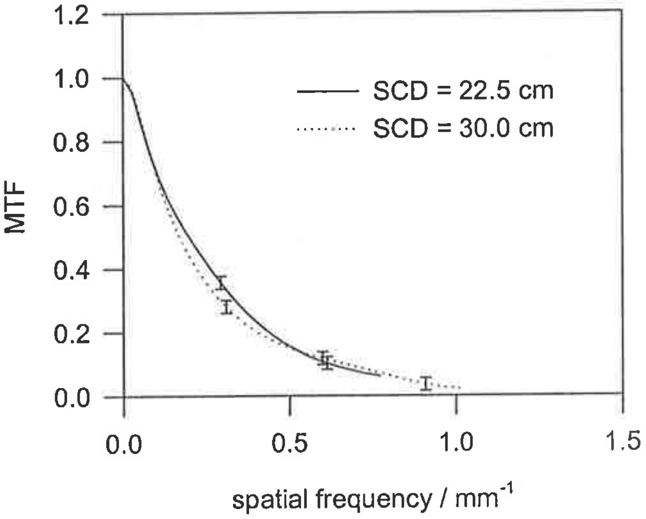

Figure 6-17 MTF under the leaves for two source-collimator distances (SCD) of 22.5 cm and 30.0 cm. The MTFs are similar for these SCD's with a slight reduction for low frequencies at the greater SCD.

6.5.7. Septal spacing

The MTFs under the leaves for the 0.5 cm slit width at $M = 1.3$ are shown in Figure 6-18 for two septal spacings of 1.0 and 1.25 cm. The MTF decreases at lower frequencies slightly for the larger septal spacing. As the intensity is lower for the larger septal spacing, the scatter level from the slit fields may have a greater effect reducing the MTF. The MTFs are similar at the higher frequencies as the change in source segment for these two septal spacings is not sufficient to alter the MTF.

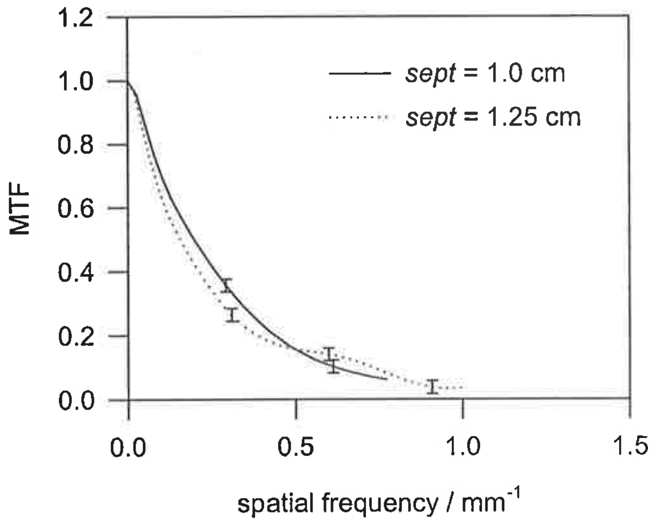

Figure 6-18 MTF under the leaves for the 0.5 cm slit width at $M = 1.3$ for two septal spacings (centre-to-centre slit spacings) of *sept* = 1.0 and *sept* = 1.25 cm. The MTF decreases slightly at low frequencies but is similar at high frequencies.

6.5.8. Energy

The comparison of the MTFs under the leaves for the two energies of 6 and 23 MV is shown in Figure 6-19. The MTFs are similar. The energy of the irradiation does not therefore alter the MTF in the image regions under the leaves and the results for the 6 MV measurements therefore should also represent the 23 MV energy.

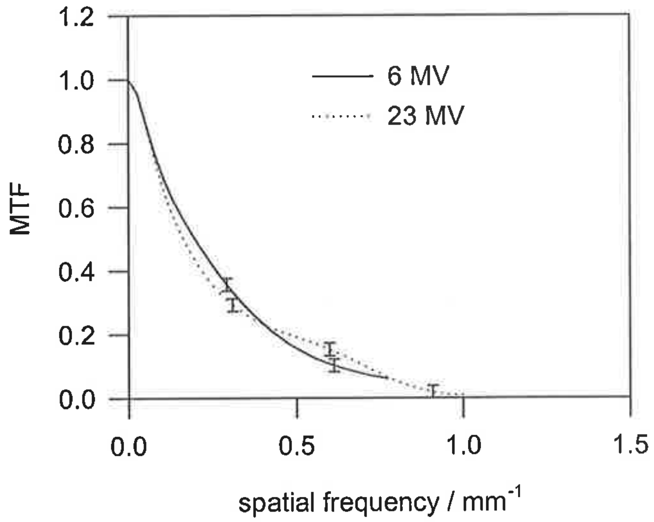

Figure 6-19 MTF under the leaves for the 6 MV and 23 MV energies, and 0.5 cm slit width. The MTFs are similar.

6.5.9. Contrast-to-noise ratio

The noise levels were relatively constant for the images, the variation in the CNR is then determined by the the edge contrast for the regions under the open slits compared to the regions under the leaves.

Table 6-2 Contrast-to-noise ratios under the open slits and under the leaves of the slit field irradiation images.

Slit width / cm	Under slits	Under leaves
10.0 (open)	314	
2.0	321	50
1.0	340	113
0.5	354	148
0.2	532	260

These results show an increase in the low frequency contrast under the open slits with reducing slit width. This was also seen in the MTF results shown in Figure 6-12 and is due to reduced scatter as shown in Section 6.5.3. The overall irradiated area is smaller for the two slit fields used in these measurements as the slit width decreases. This is the basis of slit radiography techniques utilised in diagnostic radiographic imaging. The CNR similarly increases with decreasing slit width under the leaves as seen in Figure 6-16, and approaches the CNR measured for open field imaging for the 0.2 cm slit width. This is again consistent with scatter reduction. The primary intensity increases in the region under the leaves with reducing slit width. This will decrease the scatter fraction and hence improve the contrast.

6.6. Discussion

The edge MTF measurement technique was employed here to examine the spatial resolution under the open slits and under the leaves when an image is formed with a modulated intensity produced by a collimated grid. Due to the low contrast at megavoltage energies a thick edge was necessary to provide sufficient contrast to accurately determine the MTF. The analysis of this technique showed that the thick edge results in broadening of the ESF, an edge penetration effect, and scatter from the edge itself, all of which influence the measured MTF. The measured MTF is also influenced by the response of the detector. However the measured MTFs can be used for comparative measurement of the spatial resolution in these two regions of the image.

The spatial resolution results suggest that forming images of the external anatomy with this collimator design by utilising the modulated intensity pattern formed by alignment of the two levels of grids is feasible. However some loss of spatial resolution will result. The image resolution under the open slits is similar to open field imaging however there is a reduction in spatial resolution under the leaves due to the broad extra-focal source segment distribution that irradiates this region, as well as the effect of scatter at low frequencies. As the leaf width of the grid decreases, the spatial resolution under the leaves improves. Thus smaller leaf widths of the collimator are desirable for this modulated intensity imaging. The MTFs measured for the region directly under the centre of the leaf represent the lowest spatial resolution that would be expected in the image. The spatial resolution will improve for image regions closer to directly under the centre of the slits. This can be seen in Figure 6-15. The effect of varying the SCD and the beam energy on MTF under the leaves was small. The reduction in MTF with increasing septal spacing was also small with a reduction at lower frequencies due to scatter.

The reduction in the MTF under the leaves suggests a larger effective source distribution irradiates this region. The collimated grid results in irradiation by a peripheral extra-focal segment of the source whereas the region under the open slits is irradiated by the focal source. This may increase the effective source size and hence the blurring of the ESF. Table 6-1 shows that the view of the strip of the source from under the 0.5 cm leaves occludes the central 2 mm of the source. Jaffray *et al.* (1993) have measured the focal source size of a KD2 accelerator as 0.5 mm FWHM. This size of source would mean that the intense, narrow focal source would not directly irradiate the region under the leaves, but the broad low intensity extra-focal source would. This would be expected to result in a large blurring of the edge due to the source. The region under the slits is irradiated by the focal source which would dominate the image formation resulting in much less blurring. The MTF results for under the slits show that the MLC can be used for double-movement imaging with no loss of resolution, and possibly slightly improved resolution compared to open field imaging.

The CNR results show that the (low spatial frequency) contrast will be lower in the image regions under the leaves however the CNR increases with reducing slit width. The CNR under the 0.2 cm leaves is similar to open field imaging.

6.7. Conclusion

The spatial resolution of the image regions under the open slits and under the leaves when an image is formed with a collimated grid is present has been compared by MTF measurements to an open field. These measurements were made by imaging an edge object to determine the ESF and MTF. The MTFs for the region under the open slits are similar to open field MTFs while the MTF is reduced for the region under the leaves. The region under the leaves is irradiated by more peripheral (extra-focal) segments of the source through the grid, resulting in lower spatial resolution than the region under the open slits that is irradiated by the intense narrow focal source. The MTF under the leaves improves with reducing slit width as the segment of the source that irradiates the image region becomes more central. The results show that to form images with the aligned dual assembly collimator smaller leaf widths are desirable.

7. Image formation with a dual assembly multileaf collimator design: image processing

7.1. Introduction

Alignment of the leaf assemblies of the dual assembly multileaf collimator design to image the area external to the field results in a modulated radiation intensity distribution incident on the patient. This distribution is due to the addition of the individual slit field beam profiles with high intensity under the open slits of the collimator and low intensity under the leaves. The previous chapter investigated the image quality and therefore utility of these images. The image formed with the assemblies aligned, referred to here as a "single-movement" image contains a pronounced modulation pattern due to the modulated intensity. This chapter investigates and develops image processing methods to reduce the modulation pattern in these images. Both spatial domain and Fourier domain methods are studied.

7.2. Theory

7.2.1. Spatial Domain

In the one-dimensional form of the model of the open field imaging process outlined in Chapter 6, the photon intensity arriving at a point at the image plane can be expressed

$$h(x'') = C \int_{source} f(x) g(ax'' + bx) dx \tag{7.1}$$

where $f(x)$ is the photon intensity emitted toward detector point x'' due to the source point at x, and $g(x') = g(ax'' + bx)$ is the transmittance of the object plane at the point x', with

$$a = L_1 / (L_1 + L_2) \tag{7.2}$$

$$b = L_2 / (L_1 + L_2) = 1 - a \tag{7.3}$$

$$C = 1/(L_1 + L_2)^2 \tag{7.4}$$

This is illustrated in Figure 6.3. For an image point at x'' the photon intensity is formed from the contribution of all source points along ray paths through the planar object with each source point contribution weighted by the transmission of the object along the path. For a magnification of 1 where the detector is placed directly underneath the thin object ($x' = x''$) where $a = 1$ and $b = 0$, Equation 7.1 can be then written

$$h(x'') = C \int_{source} f(x) dx \cdot g(x'') \tag{7.5}$$

The photon intensity at the point is then the integral of the photon intensity emitted to the point from the source multiplied by the transmittance of the object at the point. For open field imaging this total source intensity would be constant over the image, and the image would then solely reflect the transmittance of the object. However when a collimated grid is present, the integrated source intensity varies depending on the segment of the source that contributes to the object point, resulting in the modulated intensity (Chapter 5). Expressing the integrated intensity distribution at the image/object plane as $i(x'')$ gives

$$h(x'') = C \cdot i(x'')g(x'') \tag{7.6}$$

The object transmission is then modulated by the incident intensity. To reduce the modulation in the resulting image, the image could be divided by the incident intensity function to yield the object transmission, equivalent to an image with no grid present. This model can also be modified to include a background scatter level in the image.

$$h(x'') = C \cdot i(x'')g(x'') + S \tag{7.7}$$

where S accounts for the contribution to the image from scatter produced in the object, and the scatter is assumed to be uniformly distributed. The scatter will be a function of the object thickness, field size, beam energy and gap between the detector and the object. If the scatter level is significant then the reconstructed image $h_{rec}(x'')$ would result in the desired image but with a residual modulation present. This occurs because the scatter is not present in the correction image acquired with no object present

$$h_{rec}(x'') = C \cdot g(x'') + S/i(x'') \tag{7.8}$$

To account for the scatter, the reconstruction could be performed by removal of the scatter level from the object image before the division. An alternative to estimating the scatter level would be to measure the correction image through a uniform phantom of the same thickness as the object to be imaged. As the scatter conditions would then be similar, division of the object image by the correction image should then yield the difference in the two images due to the variation in attenuation of the object.

The above is a simplification of the imaging process that applies to a thin object at a magnification of 1. When imaging with magnification greater than 1 the image is a convolution of source distribution and object transmission. The intensity distribution $h(x'')$ incident on the detector is also convolved with the detector response. The thickness of the object is also not considered. Therefore the above formalism is an approximation but provides a framework for spatial domain methods to investigate reducing the modulated intensity in the image.

7.2.2. Frequency Domain

For the imaging situation of magnification equal to 1, the imaging system response in the frequency domain $TF_{tot}(\omega'')$ is found by considering a delta function object, giving

$$TF_{tot}(\omega'') = C \cdot I(\omega'')D(\omega'') * \mathrm{comb}\left(\omega'', \tfrac{1}{\Delta x}\right) \tag{7.9}$$

where $I(\omega'')$ is the Fourier transform of $i(x'')$, $D(\omega'')$ is the transfer function of the detector, and $\mathrm{comb}\left(\omega'', \tfrac{1}{\Delta x}\right)$ is the sampling comb function in the frequency domain for sampling interval Δx. The modulated intensity $i(x'')$ is a periodic function. The Fourier spectrum of a periodic modulated signal is illustrated in Figure 7-1. The periodicity (period = T) of the signal results in a delta function spectrum that repeats periodically in frequency every $1/T$ mm^{-1}. The replicas of the delta functions are weighted by the amplitudes of the Fourier series coefficients of the waveform. This envelope is the Fourier spectrum of the periodic function shape (slit field profile) that repeats with period T. For a 10 mm slit width irradiation pattern, with the slits equally spaced, the period is 20 mm, and hence the delta function frequency is 1/20 mm = 0.05 mm^{-1}. This frequency increases to 0.25 mm^{-1} for a 2 mm slit width irradiation. The modulation could therefore potentially be reduced by zeroing the spectral components of the image at the discrete frequencies of the modulation.

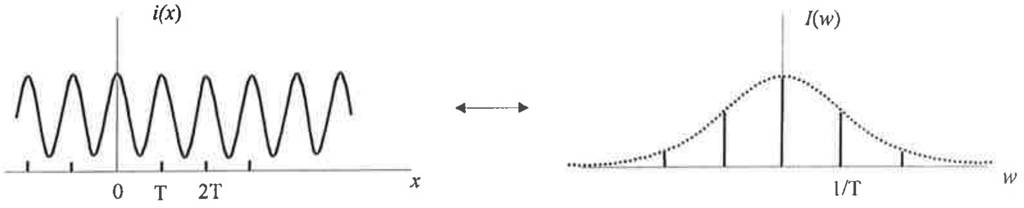

Figure 7-1 Fourier spectrum of a periodic modulated signal. This consists of periodic delta functions weighted by the spectrum of the waveform.

The effect of the detector on the spectrum should also be considered. The detector response will lower or dampen the delta functions due to the modulated intensity. In the case of digitised film, the detector response is the combination of the film/screen response and the Vidar scanner response. The modulation transfer function of the Kodak film/screen combination employed here has been measured by Munro *et al.* (1987). They found that the MTF was ~0.2 at a spatial frequency of 1 mm^{-1}. The MTF of the Vidar scanner was reported in Chapter 4 and has a value of ~0.85 at 1 mm^{-1}. The narrowest slit width employed in this work is 2 mm. Considering a 2 mm width square wave function as the slit field profile, the spectrum of this forms the envelope function and has its first zero crossing at 0.5 mm^{-1}. Therefore the envelope function is likely to be dominant over the detector response and reduce the image spectrum to small values before the detector response has a major effect.

The sampling of the image will result in a periodicity of the spectrum, with the spectrum spaced at $1/\Delta x$ where Δx is the the sampling interval. If this sampling frequency is high then aliasing of the spectrum is avoided. For the sampling period of the Vidar scanner of $\Delta x = 0.17$ mm, the frequency of the replicas of the spectrum due to the sampling is nearly 6 mm^{-1}. The image spectrum would not be expected to be aliased with this sampling frequency. Because of the invariance of the modulation in the y-direction, the two-dimensional spectrum $I(\omega'', v'')$ due to the modulated intensity will consist of delta functions aligned along the ω-axis, corresponding to the x-axis in the spatial domain. If the grid and hence modulation is aligned at some angle to the x-axis, the spectrum due to the modulation will correspondingly be aligned at the same angle.

For the double-movement images formed by movement of both assemblies to the adjacent imaging positions, the junctioning of the fields results in a periodic artifact of lower image values due to penumbral blurring and overlap of the leaf levels. The intensity distribution is then similar to that shown in Figure 7-2. For example a 10 mm slit width will result in a periodic artifact of period 10 mm. The period in this case is equal to the slit width. The frequency spectrum of this type of intensity artifact will be similar to that above, with delta function components at the frequency and multiples of the frequency of the periodic function modified by the envelope of the function. Removal of the periodic pattern is then accomplished by removing these frequency components from the spectrum. The uniform intensity base level or dc level results in a delta function at the zero frequency.

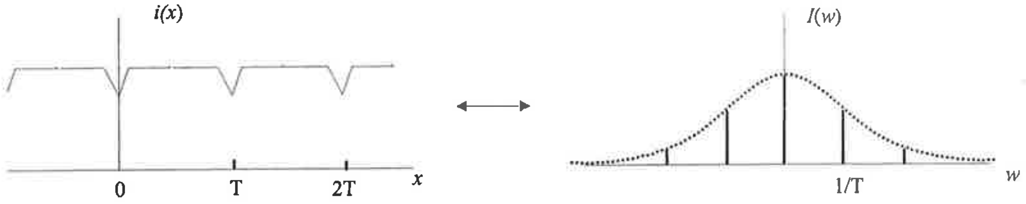

Figure 7-2 Periodic pattern in a double-movement image and subsequent Fourier spectrum.

7.3. Methods

7.3.1. Spatial domain methodology

Initially a spatial domain modulation removal or image reconstruction procedure based on the thin object image formation model (Equation 7.6) was investigated, scatter was not considered. Both film and an electronic portal imaging device were employed. The object employed was the QC-3 phantom (Masthead Imaging, Nanaimo, BC) shown in Figure 7-3. This object is 1.9 cm thick and contains square regions of different density and five regions of bar-patterns of varying frequency. These bar-patterns are comprised of lead of thickness in the beam direction 15 mm, but with different spacings between the bars. The spatial frequencies of the bar-patterns from top to bottom in the figure are 0.15, 0.25, 0.45, 0.20 and 0.10 mm^{-1}. Two brass annular disks of thickness 1.9 cm and diameter 2.2 cm were placed on the phantom left hand side for added detail, as well as a 1 cm thick steel nut on the right side.

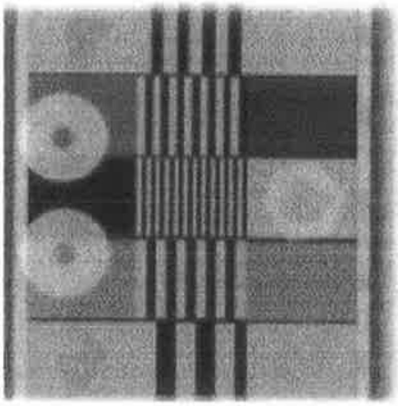

Figure 7-3 Open field image of QC3 phantom for comparison to images reconstructed from multiple slit field irradiation images.

For the film measurements the object was placed at isocentre, 100 cm from the source and the film (Kodax x-omat) placed in a Kodak film cassette at 135 cm from the source. An open field image (no grid present) was acquired with a 10 × 10 cm field size at 6 MV. A modulated image was then formed by multiple slit field exposures each of 0.5 cm width (isocentre) with centre-to-centre spacing of 1.0 cm. Ten exposures were made to form an image of the object simulating an image formed through the MLC design with 0.5 cm leaf width. The slit fields were formed by the upper collimator jaws of a Siemens KD2 accelerator (Siemens Medical Systems Inc., Concord, CA, USA) and moved to each position with the asymmetric jaw capability. The length of the slit fields was defined by the lower collimator jaws which were set to 10 cm.

The object was then removed and the exposures repeated on a separate film to obtain the modulated intensity pattern. This modulation is that incident on the object at 100 cm but magnified to the film and reduced in intensity by the inverse square law. As the transmitted intensity through the object also is reduced by the same inverse square amount and similarly magnified then this is a constant factor in the measurements and should not alter the result. The films were digitised with the Vidar scanner and converted to optical density as described in Chapter 5. The modulated image of the object and the modulated intensity image were then aligned by shifting one image by one pixel and dividing the two until the smallest residual modulation in the result was obtained.

To examine the image reconstruction without alignment considerations, images of the QC-3 object and the modulated intensity without the object were acquired with a Siemens Beamview Plus V1.2 electronic portal imaging device. This EPID consists of a 1 mm thick copper plate backed with a G_2O_2S fluorescent phosphor screen. The light is reflected by a 45° mirror onto a Vidicon camera with a 512 × 480 matrix of detector elements. The object was placed on the EPID surface which is at a fixed distance of 139 cm from the source. An open field image at 6 MV was initially acquired with the field size 15 × 15 cm. The 1 cm lead-alloy grid (Chapter 5) was then placed on the accelerator shadow tray supported on a 1 cm thick perspex plate at 56 cm from the source. This grid produces slit fields of 1.0 cm width separated by 2.0 cm at isocentre. Modulated intensity images were recorded with and without the QC-3 object present. The modulated image with the object present was then divided by the modulated intensity image with no object present and the result compared to the open field image.

To examine the effect of scatter on residual modulation in the reconstructed image, an image was acquired with a thin uniform density object, at a magnification close to 1. A 1.5 mm thick brass plate was placed 1 cm above a BIS-710 imaging device (Wellhofer Dosimetrie, Schwarzenbruck, Germany) positioned at 100 cm from the source of the KD2 accelerator. The BIS-710 consists of a 1.0 mm thick copper metal screen backed with a 0.6 mm thick G_2O_2S fluorescent phosphor screen. The light generated in the phosphor during irradiation is reflected by a 45 degree mylar mirror onto a CCD camera. The camera has a 512 × 512 array of detector elements viewing a maximum area of 30.1 × 30.7 cm. The properties of the BIS-710 for dosimetric measurements have been investigated by Ma *et al.* (1997). They found that the response to incident dose was linear. This was also verified by measurements performed on our detector (Liu *et al.*, 2000). With the lead alloy grid at 56 cm from the source, images were acquired at 6 MV energy with the plate and with the plate removed. A field size of 20 × 20 cm was employed. The image with the plate present was divided by the image without the plate to examine if residual modulation was present in the reconstruction. This experiment was designed so that object thickness, and the source size should have limited effect, any residual modulation should therefore be due to the effect of scatter.

To examine in more detail the effect of scatter level in the object image on the reconstruction when divided by an image with no scatter present, experiments were performed with the BIS-710 device. Solid water slabs were placed above the detector and images recorded with and without the solid water present. The solid water profiles were divided by the no solid water or “in-air” images to examine residual modulation in the reconstruction due to the mismatch of the scatter conditions. The division was also repeated after subtraction of a scatter level from the solid water profiles. The scatter level was varied to obtain the most uniform reconstructed result. The thickness of the solid water, the air-gap to the BIS detector and the field size were varied to determine the change in residual modulation with these parameters. The solid water slabs (Gammex RMI, Middleton, WI, USA) were supported on the tennis racquet section of the treatment couch. The three thicknesses of solid water were 1.0, 4.0 and 10.0 cm. The BIS-710 was positioned at 139 cm from the source of the KD2 accelerator. The slabs were placed at three distances or air-gaps above the BIS detector of 10.2, 39.0 and 52.0 cm to the base of the solid water. The lead-alloy grid was positioned at the accelerator shadow tray level, 56 cm from the source to the base of the grid. Images were recorded with 6 MV energy for each slab thickness and air-gap and a field size of 15 × 15 cm at isocentre. The in-air image with no solid water present was also recorded. Two identical in-air images were recorded and divided to ensure that residual modulation in the reconstruction was not due to noise in the images. Further solid water images were recorded with the air-gap of 39 cm for field sizes of 5 × 5, 10 × 10 and 20 × 20 cm and a solid water thickness of 10 cm. The residual modulation in the images was quantified by examining a central profile from the reconstructed image and calculating the residual modulation in an identical manner to the modulation index defined in Chapter 5.

An alternative to estimating a scatter level is to measure the correction image for the appropriate thickness of phantom, air-gap and field size. These images then contain the correct scatter level if they are applied to patient images taken under similar scatter conditions. Images with the BIS-710 detector were acquired for solid water thicknesses of 0.5 and 10.0 cm to examine this approach. The images were acquired with and without low contrast objects positioned on the surface of the solid water. The detector was placed at 100 cm from the source of the KD2 accelerator with the solid water 1 cm above the detector. The lead-alloy divergent grid was placed at 56 cm from the source. The grid projected slit fields of width 1.0 cm at isocentre, with the centre-to-centre spacing of the slit fields equal to 2.0 cm. Images were acquired with a 20 × 20 cm field size at 6 MV energy. Low contrast objects (2 lead annulli of thickness 0.1 cm) were placed on both the 0.5 and 10 cm of solid water and images acquired with and without these objects present. A pair of scissors was also placed on the 0.5 cm of solid water, i.e. the images were not identical. The images with the solid water and objects present were divided by the images with only the solid water present.

7.3.2. Frequency domain methodology

Two images of the QC-3 phantom were formed with modulated incident intensity by multiple slit field irradiations. The slit widths were 2 mm and 10 mm, with the slits spaced by twice the slit width. The upper collimator jaws of the Siemens KD-2 accelerator were used to form the slits. The field length in the orthogonal direction was 10 cm. The phantom was placed at isocentre (100 cm from the source) and x-omat film at 135 cm from the source in a Kodak cassette. The 6 MV nominal energy was employed. An image of the phantom was acquired with an open field exposure with a 10 × 10 cm field size. The bar patterns of the QC-3 phantom were placed in the same direction as the modulated intensity. As the bar-patterns will produce image detail at discrete spatial frequencies this was done to help elucidate the effect of the image filtering.

Image reconstruction was initially investigated one-dimensionally using a row of the modulated intensity image. The row was taken through the centre of the 0.10 mm^{-1} frequency bar pattern at the bottom of the 2 mm slit width image. The Fourier spectrum of this signal was calculated by the Fast Fourier Transform (FFT) algorithm. The magnitude of this spectrum was then displayed. The components in the spectrum due to the modulation were identified and zeroing filters of a width of 5 spectral values were interactively placed centred on these components. This zeroing or filtering process was applied directly to the Fourier spectrum not the modulus of the spectrum, the modulus identifies the location of the modulation components. Following the filtering, the inverse Fourier transform was applied and the real component of the transform taken to form the reconstructed image profile. This was compared to the same row of the open field image. To determine the change in the resulting signal due to the filtering process alone, the open field profile was Fourier transformed and the same filtering applied to the spectrum. This was then inverse Fourier transformed to obtain the effect of the filtering process.

Two-dimensional Fourier filtering was then investigated for both the 2 mm slit width image and the 10 mm slit width images. The two-dimensional spectra of the modulated intensity images were calculated with the FFT algorithm. For each image the modulus of the spectra was displayed. The Fourier spectrum was then filtered by placing square 5 × 5 zeroing filter matrices, centred at the frequencies of the modulation components. The reconstructed image were formed from the real component of the inverse Fourier transform of the filtered spectrum.

The same filtering method was applied to a double-movement image formed by multiple adjacent slit field irradiations with the slit fields of width 10 mm. The double-movement image contains a periodic pattern or artifact where the dose drops at the junctions of the slit fields due to penumbral blurring. The period of the pattern is 10 mm which results in frequency components at 0.1 mm^{-1} and multiples of 0.1 mm^{-1}. The Fourier transform of the image was calculated and the frequency components for a 5×5 region centred at 0.1 and 0.2 mm^{-1} were zeroed.

7.4. Results

7.4.1. Spatial domain

The film image recorded with the 0.5 cm slit width irradiation is shown in Figure 7-4(a). The reconstructed image formed by dividing this image by an image of the modulated intensity is shown in Figure 7-4(b). The modulation is markedly reduced however some residual modulation remains. The residual modulation in the reconstruction has high image values (peaks) corresponding to the low intensity regions of the irradiation, i.e. the modulation pattern is inverted. This is consistent with the residual modulation being due to a scatter level in the object image that is not present in the image acquired with no object (Equation 7.8). However the possibility exists that the film result may be influenced by misalignment of the two images.

The reconstruction results for the images recorded with the EPID where the images are perfectly aligned is shown in Figure 7-5. Again the modulation is markedly reduced but with some residual modulation. The peaks of the residual modulation correspond as above to the low intensity regions of the irradiation. This effect is therefore not due to misalignment of the two images. To illustrate this further, profiles from the same row of the modulated intensity images with and without the object present are shown in Figure 7-6. A comparison of the reconstructed image row with the same row of the open field image is shown in Figure 7-7. The reconstructed profile clearly shows the peaks in the regions of the low-intensity of the incident irradiation.

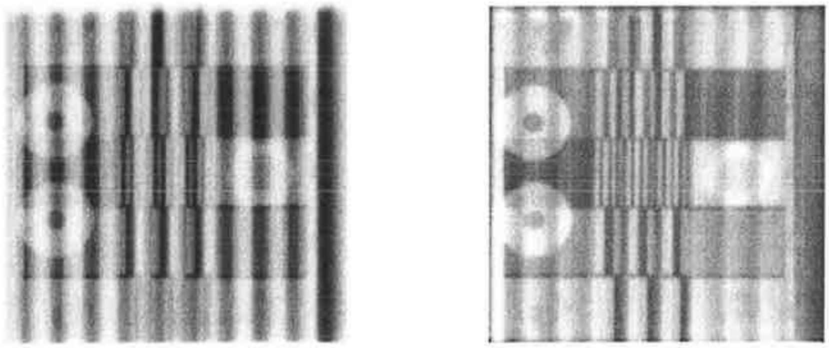
(a) (b)

Figure 7-4 (a) Film image of the QC-3 phantom acquired with the a modulated intensity formed by multiple 0.5 cm width slit fields; (b) Reconstructed image formed by dividing the image by an image acquired of the modulated intensity alone.

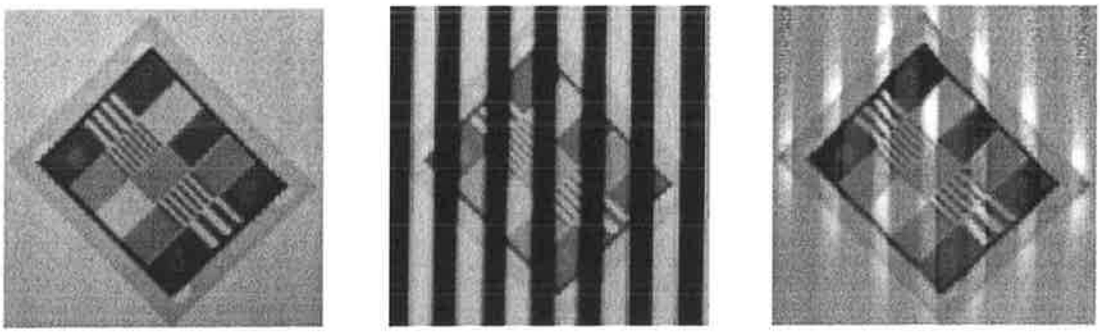
(a) (b) (c)

Figure 7-5 (a) Open field EPID image of the QC-3 phantom, (b) image with the lead alloy grid present, and (b) the reconstructed image formed after division by an image of the modulated intensity distribution.

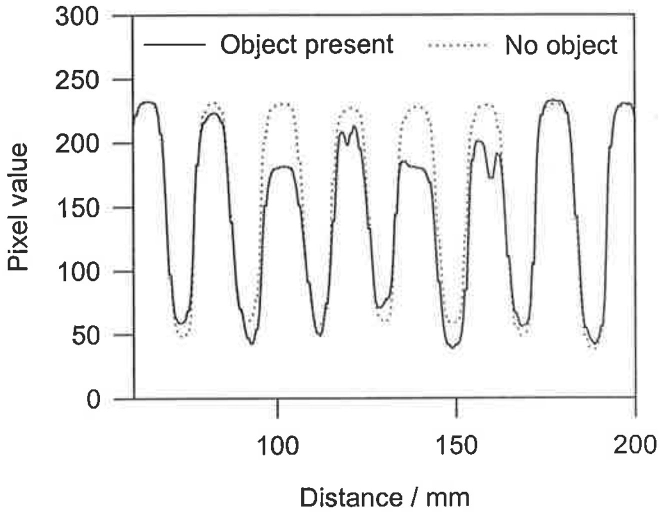

Figure 7-6 EPID row profiles with and without the QC-3 phantom present showing the modification of the signal due to the object.

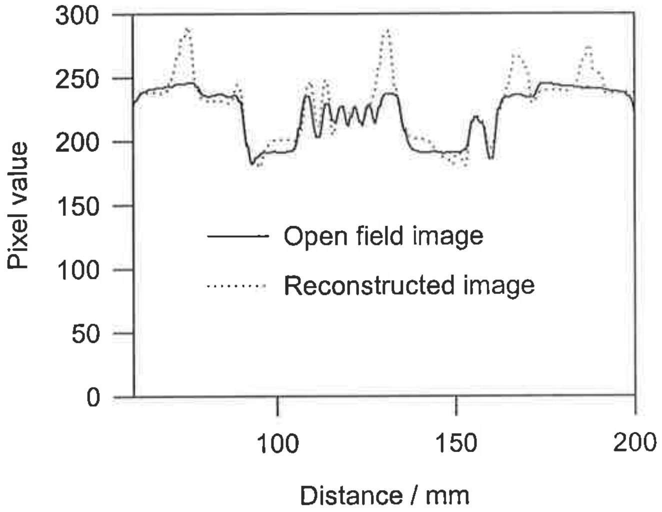

Figure 7-7 EPID row profile comparison of the open field image and the reconstruction from the modulated intensity image.

A row profile from the centre of the BIS-710 image recorded for the uniform plate object, and the same row from the image with the plate object removed is shown in Figure 7-8. The profile with the plate present, as expected, shows a reduction in the values in the high-intensity regions due to the attenuation of the plate. However the low-intensity regions show an increase in the measured intensity with the plate present. This must therefore be due to the presence of the plate resulting in scattered radiation to the detector. The signal measured at the detector is the attenuated primary radiation plus the scattered level. The scatter level will have a greater influence on the low primary intensity regions than the high-intensity regions. This scatter level results in the residual modulation observed in the reconstructed images as it is present for the image with the plate but not the correction image recorded without the plate. When the images are divided a residual modulation will result with the modulation pattern inverted (Equation 7.8).

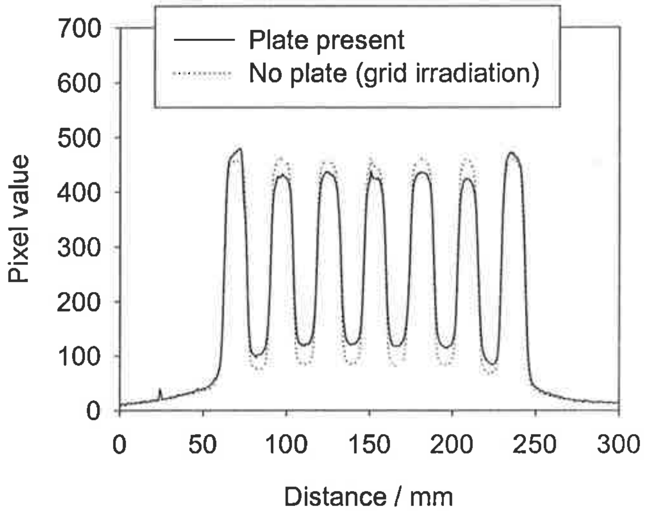

Figure 7-8 Image profiles recorded with and without a uniform plate object present. The recorded values are higher with the plate present in the low-intensity regions due to scatter.

Figure 7-9 shows a central profile from the BIS-710 images recorded with and without 10 cm of solid water present. The result is similar to that seen above where the low-intensity regions show increased level when the solid water is present. Figure 7-10 shows the result of the division of the two images. The residual modulation is due to the scatter contribution to the solid water image. When two images with the same thickness of solid water were divided a uniform result was obtained, so the residual modulation is not due to noise in the images. A scatter level offset was then subtracted from the image formed with the solid water present before the division. This level was varied to attempt to obtain a uniform profile in the reconstructed image. It was found that by appropriate selection of the scatter offset the residual modulation was successfully removed (Figure 7-10). The result then reflects the transmission of the primary intensity due to attenuation in the solid water slab after scatter removal. The profile has slight curvature which is due to the fact that the scatter level is not uniform and decreases toward the edges of the field. As a result of this a profile at the edge of the image has some residual modulation, as the scatter level was chosen to obtain a uniform profile at the field centre (Figure 7-10). The scatter level from the centre of the field over-estimates the scatter level at the edge of the field. The residual modulation is then inverted from the original due to the over-estimation.

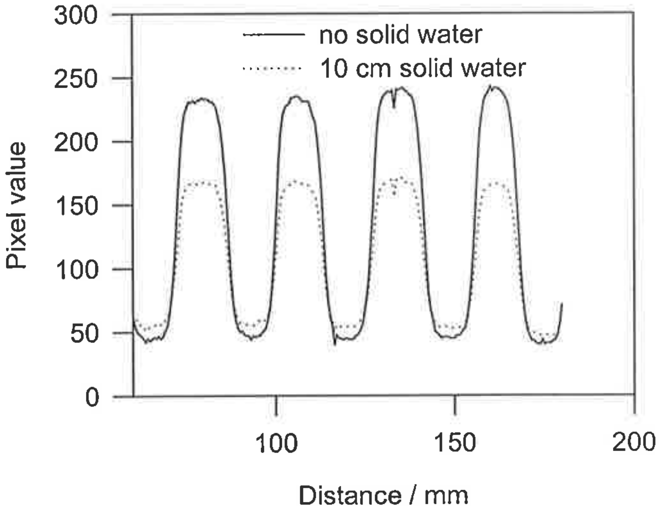

Figure 7-9 Profiles from the images recorded with and without 10 cm of solid water present.

The residual modulation when images with varying thickness of solid water and air-gap were divided by an image acquired with no solid water present are given in Table 7-1. These were calculated from a central row of the reconstructed image. These show an increase in the residual modulation level with increasing slab thickness and a decrease with increasing air-gap. The residual modulation also increased with increasing field size with values of .03, .12 and .23 for the 5 × 5, 10 × 10 and 20 × 20 cm field sizes with a solid water thickness of 10 cm and a 40 cm air gap. Jaffray *et al.* (1994) have determined scatter fractions for megavoltage imaging by Monte Carlo modelling. The scatter fluence was found to increase with increasing field size, slab thickness, and decreasing air gap between the scattering phantom and the detector. The results here for the residual modulation are therefore consistent with the known trends in scatter at these energies. There is very low residual modulation at the largest air-gap.

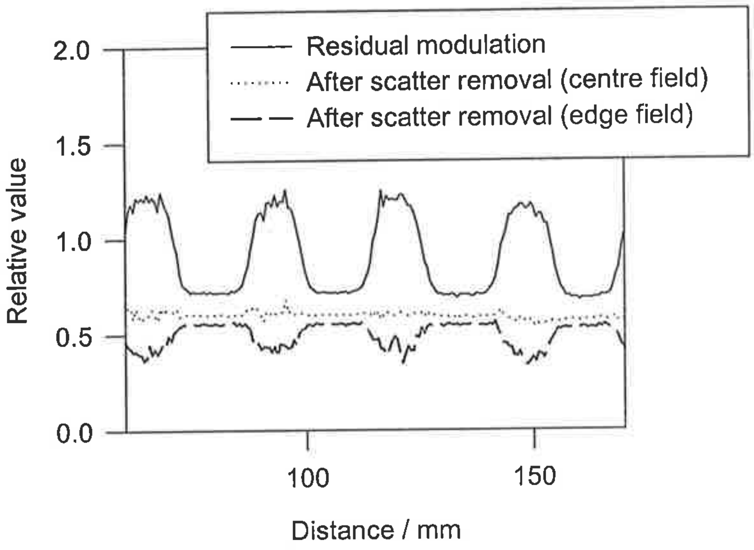

Figure 7-10 Residual modulation resulting from the division of the image with 10 cm of solid water present by the image with no solid water present. Also shown is the when a scatter level was removed from the 10 cm solid water image to yield a flat profile after division.

Table 7-1 Residual modulation after division of an image formed with solid water present by an image with no solid water with the solid water thickness and air gap to detector varied. The results are determined from a central row of the image.

	thickness / cm				
Air gap / cm	1.0	4.0	10.0	15.0	20.0
10	.17	.27	.41		
39	.04	.09	.17	.23	.27
52	.01	.04	.08		

Figure 7-11 (a) and (c) show results for the images formed with the 1.0 cm grid with low contrast objects placed on 0.5 cm and 10 cm thicknesses of solid water respectively. The reconstruction was performed by division of the images by images acquired with the same thicknesses of solid water but with the objects removed. The results of the reconstruction for the two images are shown in Figure 7-11 (b) and (d). The modulated intensity is effectively removed in both cases. The 0.5 cm solid water images show better contrast than the 10 cm thickness for these low contrast objects. These results suggest that when the correction image has similar scatter contribution that the residual modulation in the reconstructed image will be small, and the modulation is successfully removed.

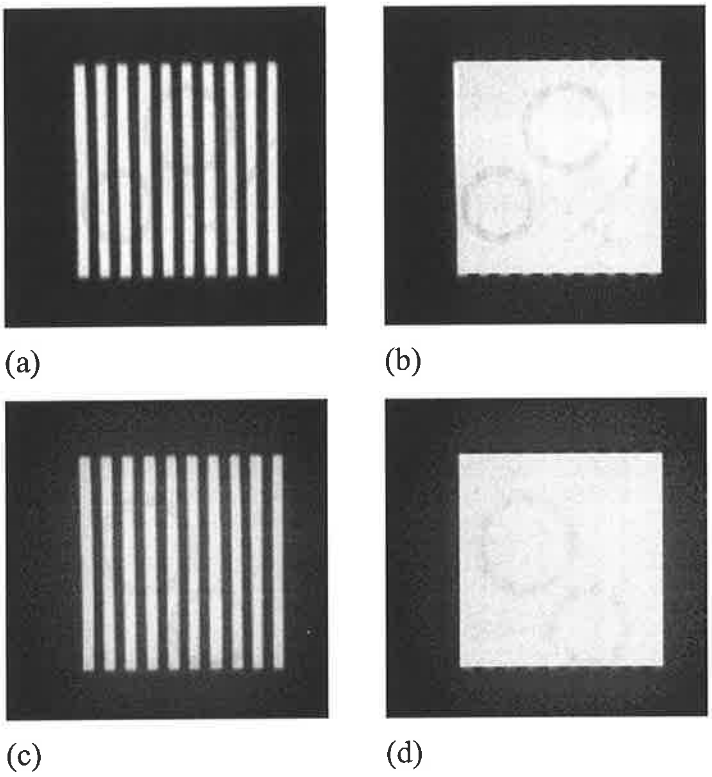

Figure 7-11 Images of low contrast objects and the reconstruction after division by an image without the objects but with the same thickness of scattering material (a) 0.5 cm of solid water irradiation image with grid present, (b) reconstructed image, and (c) 10 cm of solid water irradiation image with grid present, (d) reconstructed image.

7.4.2. Frequency domain

The image of the QC-3 phantom acquired with the multiple 2 mm slit field irradiation is shown in Figure 7-12, compared to the open field image. The row of the open field image through the 0.1 mm^{-1} bar pattern (bottom of image) is shown in Figure 7-13 (a), and the magnitude of the frequency spectrum in Figure 7-13 (b). A strong frequency component at ~ 0.1 mm^{-1} is evident due to the bar-pattern of the object at this frequency.

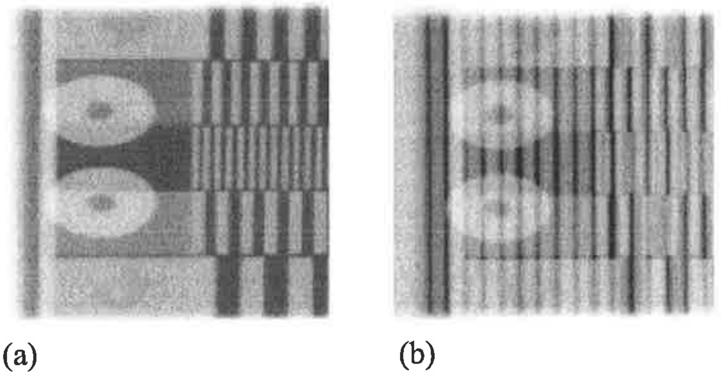
(a) (b)

Figure 7-12 (a) Open field image of the QC3 phantom, and (b) formed with the multiple slit field irradiation.

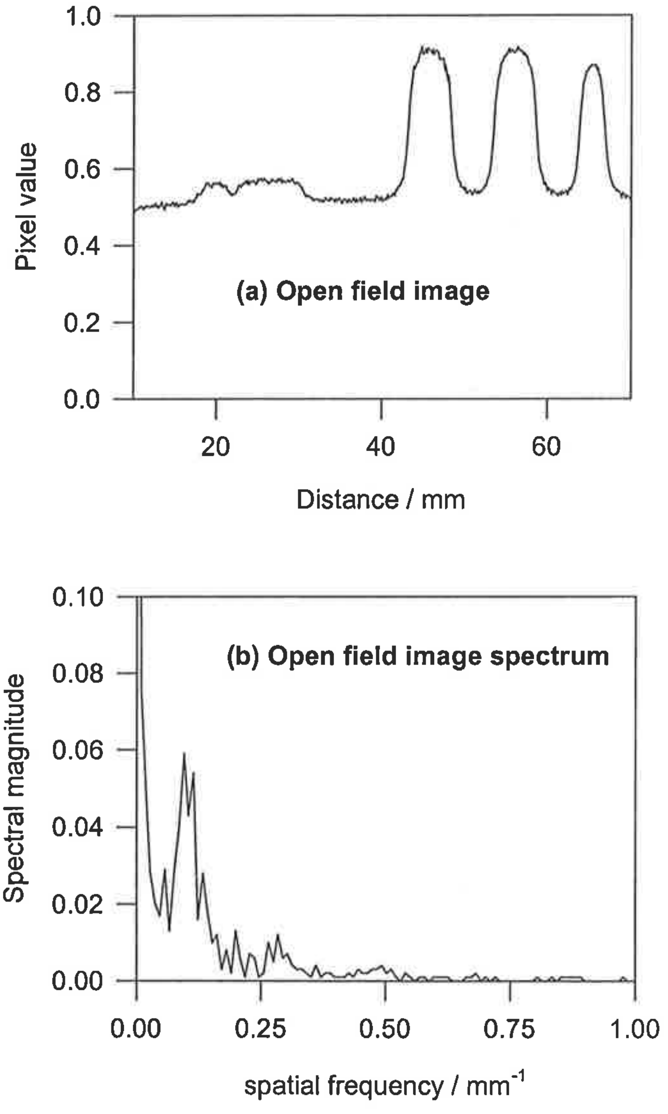

Figure 7-13 (a) Row of the QC3 phantom image acquired with an open field exposure, and (b) the Fourier spectrum of this image row.

The same row of the image of the QC3 phantom formed with the multiple slit irradiation is shown in Figure 7-14(a). The magnitude of the Fourier spectrum of the image row is shown in Figure 7-14(b). The components due to the modulation are apparent. These occur at multiples of 0.25 mm^{-1}, the frequency that corresponds to the period of 4 mm for the 2 mm slit width modulated intensity pattern. These components decrease in height with increasing frequency due to the envelope function as well as the detector response.

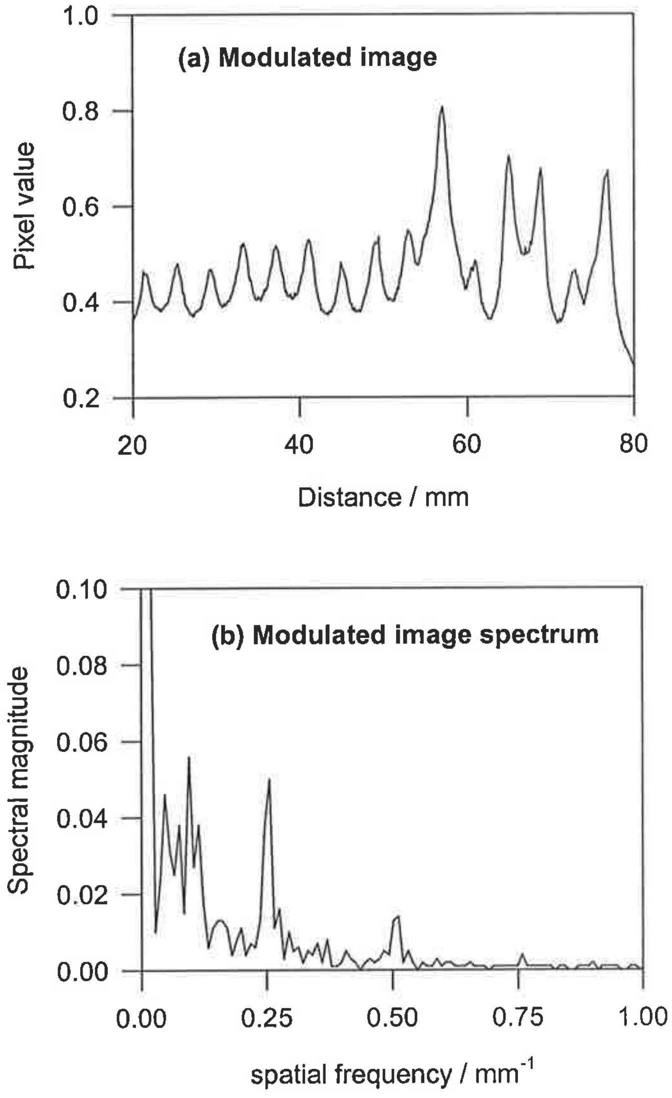

Figure 7-14 (a) Row of the modulated intensity image of the QC3 phantom formed with the 2 mm slit width, and (b) the magnitude of the Fourier spectrum of the image row. This clearly shows the components due to the modulation.

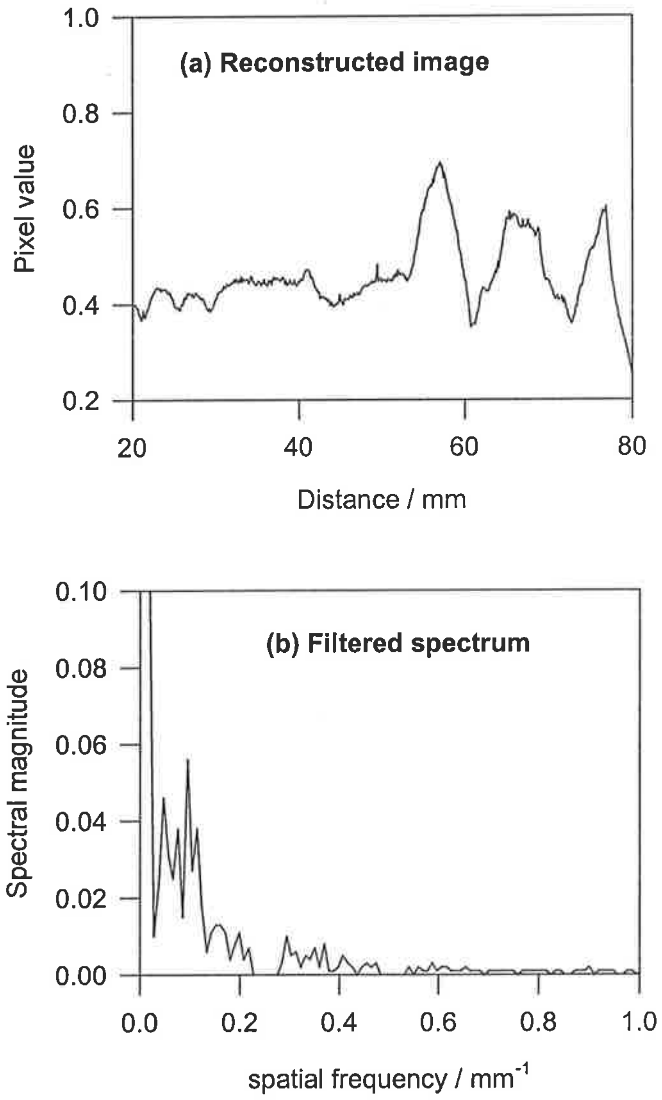

Figure 7-15 (a) Reconstructed row of the image formed by removal of the components in the frequency spectrum, and (b) magnitude of the Fourier spectrum showing the filtering.

The modulated profile was filtered by zeroing the spectral components at the frequency of the modulated intensity and the spectrum inverse Fourier transformed. The result is shown in Figure 7-15(a), and the filtered spectrum in Figure 7-15(b). The modulation has been largely removed from the profile. Distortion of the reconstructed image is evident by comparison to the open field profile. Some distortion would be expected due to the reduction in image quality observed in Chapter 6. This is evident by the Fourier spectrum of the modulated image. The peak at the frequency of the bar-pattern is less well defined showing that distortion has already occurred. However the filtering process will also result in distortion as spatial frequencies are removed from the image spectrum. When the image is reconstructed from this spectrum, these frequencies may be necessary to fully reproduce the image signal. The relative distortion due to the filtering process can be seen in Figure 7-16. The same filtering that was applied to the modulated intensity profile was applied to the open field spectrum and the open field row then reconstructed from this spectrum by inverse Fourier transforming. The distortion in this signal is present but is much less than in the filtered modulated intensity image row. Therefore the distortion was largely already present in the image due to the image formation process rather than introduced by the filtering process.

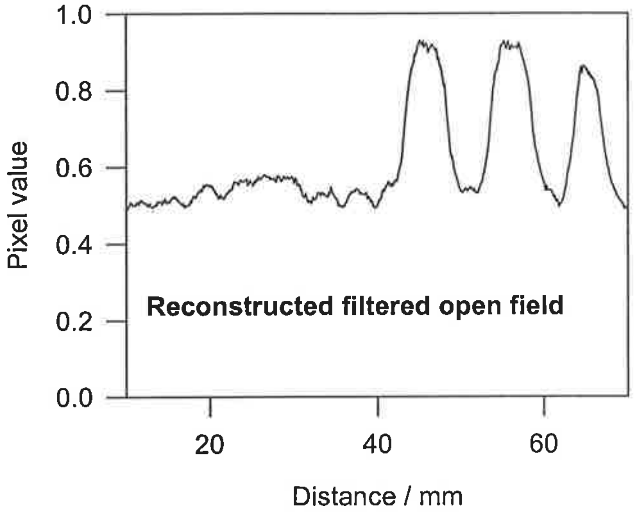

Figure 7-16 Reconstructed row of the open field image after the same filtering was applied as that used for the modulated intensity image row.

The two-dimensional Fourier spectrum of the modulated intensity image of the QC-3 phantom is shown in Figure 7-17. The components at the frequencies due to the grid are prominent. The filtered spectrum is shown in Figure 7-18. Finally the image reconstructed from this filtered spectrum is shown in Figure 7-19. There is much less modulation evident in the reconstruction than in the initial modulated image (Figure 7-12(b)). The 0.25 mm^{-1} frequency bar-pattern is poorly reproduced as this matches the frequency of the modulated intensity that was removed from the spectrum.

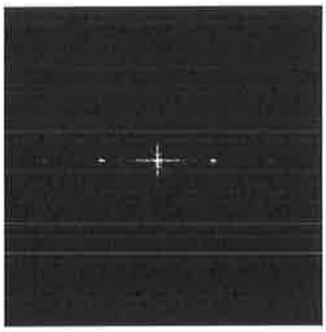

Figure 7-17 Fourier spectrum of the modulated intensity image. The strong frequency components due to the modulation are evident. These are in the direction of the modulation.

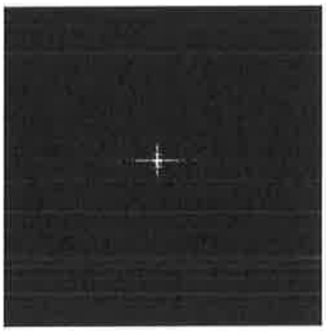

Figure 7-18 Filtered spectrum of the modulated intensity image after zeroing of the frequency components of the modulation.

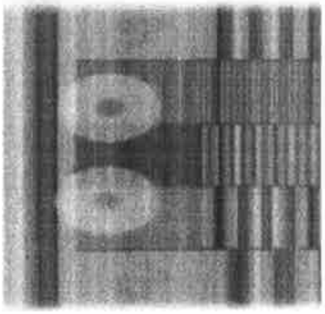

Figure 7-19 Reconstructed image formed from the inverse Fourier transform of the filtered spectrum.

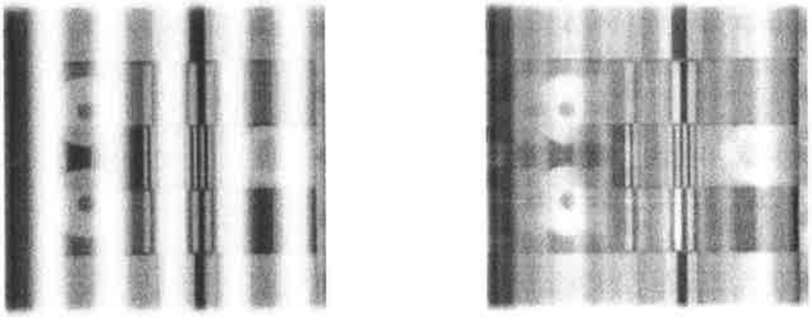
(a) (b)

Figure 7-20 (a) Image formed by multiple 1 cm slit width irradiations, and (b) reconstructed image after filtering of frequency spectrum of the image.

The image formed by multiple 10 mm slit width irradiations is shown in Figure 7-20(a) and the reconstructed image following filtering of the frequency spectrum is shown in Figure 7-20(b). The filtering has distorted the image. This is due to the low frequency of the modulated intensity (0.05 mm^{-1}). Removal of this frequency from the image spectrum results in distortion of the image following inverse Fourier transformation. Therefore this filtering method is more amenable to narrower slit or leaf widths in the collimation design where the frequency of the modulation is then greater.

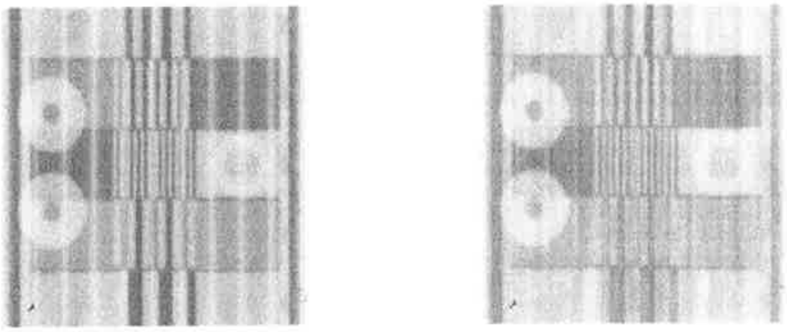
(a) (b)

Figure 7-21 (a) Double-movement image formed by multiple adjacent slit fields of 10 mm width, and (b) the image after the frequency components of the junctioning artifact were zeroed.

The same filtering method was applied to a double-movement image formed by multiple adjacent slit field irradiations with the slit fields of width 10 mm. The double-movement image is shown in Figure 7-21(a). The Fourier transform of the image was calculated and the frequency components for a 5 × 5 region centred at 0.1 and 0.2 mm^{-1} were zeroed. The result is shown in Figure 7-21(b). The artifact is clearly reduced by the filtering process.

7.5. Discussion

The division of an object image by the incident modulated intensity correction image resulted in reduced modulation in the image. However scatter contribution to the image that is not present for the correction image results in residual modulation following the division. This can be reduced by subtraction of a scatter offset level from the object image before the division. However a single scatter level is not present over the entire image and some residual modulation then remains. The scatter level also varies with object thickness, field size and air gap. To minimise the residual modulation in the presence of scatter would involve measurement of a library of correction images measured for various scatter conditions. For a patient image the correction image with similar scatter conditions would be applied. However where the thickness of the patient is non-uniform such as head and neck images this approach would be less successful. When the air-gap is large at 60 cm the residual modulation is small and therefore the division could be performed without consideration for scatter. The advantage of this spatial domain method is that it does not result in a loss of spatial resolution due to the correction method.

The Fourier approach to modulation removal is more generally applied to different imaging situations. The processing would be easy to implement as a single filter could be applied to the Fourier spectrum of all images acquired with the collimator, provided the orientation of the collimator leaves relative to the imager was known. However the filtering results in distortion of the image as frequency components of the object are removed by the filtering process. As the slit width becomes greater the frequencies of the modulation become lower, resulting in greater distortion in the image when the filtering is applied.

7.6. Conclusions

Image processing methods in both spatial and frequency domain have been developed to reduce the modulation pattern in images acquired through the aligned assemblies of the multileaf collimator design. Division of the image by a correction image of the modulated intensity obtained with no object present results in some residual modulation due to scatter contribution to the object image that is not present in the correction image. If the scatter contribution to the correction image is estimated or the correction image acquired under similar scatter conditions then the residual modulation is reduced. Fourier filtering of the spectrum to remove the frequencies of the modulated intensity successfully removes the modulation from the image, however some distortion results from the filtering. The distortion is reduced for images formed with smaller leaf widths as the frequency of the modulation increases.

8. Properties of a prototype dual assembly multileaf collimator

8.1. Introduction

In this chapter the properties of a prototype dual assembly MLC are investigated. The prototype was constructed in the Medical Physics Department of the Royal Adelaide Hospital to examine the properties of a practical dual assembly MLC. The radiation profiles transmitted for imaging the external anatomy are determined and the imaging process with the dual assembly design practically demonstrated. To verify the shielding perfomance of the vertically displaced MLC leaves, measurement of the leakage radiation transmitted through the leaves when shielding is compared to transmission through an alloy block of the same thickness. Measurements were also made of the leaf penumbra to compare the leaf penumbra with that of the secondary jaws and determine whether the penumbra varies for the two leaf levels. The method to reduce dose stair-stepping in angled field edges (Galvin *et al.*, 1996) is investigated utilising MLC lateral movement rather than treatment couch movement to determine whether this is effective.

8.2. Methods and Materials

8.2.1. MLC design and construction

Schematic diagrams of the prototype MLC are shown in Figure 8-1. The MLC is constructed of steel with lead-alloy leaves. It is mounted on a steel base plate that fits into the shadow tray holder of a Siemens KD2 accelerator. A central 15 × 15 cm portion of the base plate is cut out for radiation field transmission and the MLC housing mounted to the surrounding plate. The steel housing supports the MLC leaf assemblies and provides the lateral shifting mechanism. Four separate leaf bank assemblies (two each side) attach to the housing. The leaf assemblies are attached to the housing by screws that can move within slots on the housing to provide the lateral movement capabilty of the leaf banks. The slots are small segments of a circle drawn about the source position, and therefore the leaf assemblies move in an arc about the source.

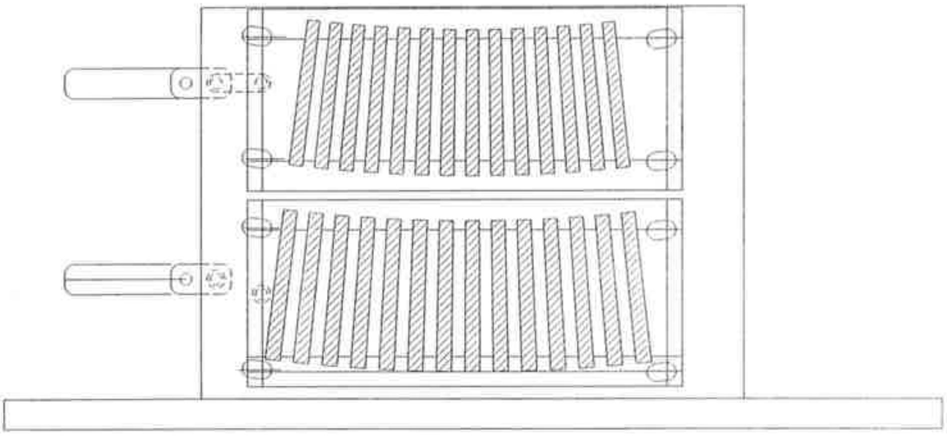

(a)

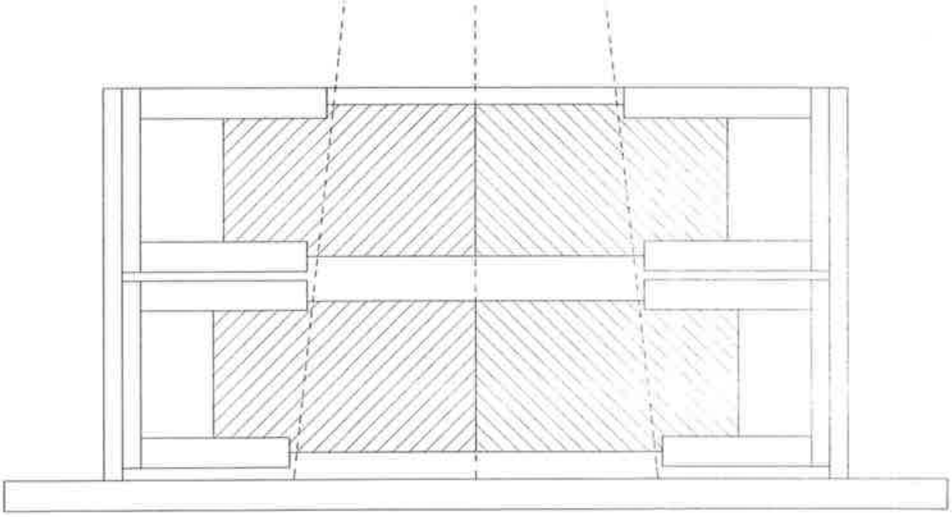

(b)

Figure 8-1 Design diagrams for the prototype dual assembly multileaf collimator, (a) end view, (b) side view showing the base plate, housing, and leaf assemblies that hold the leaves in position.

The leaves were made by first constructing two aluminium moulds, one for the upper leaves and one for the lower leaves. These consisted of two aluminium plates 1.9 cm in width and 5.0 cm in height. The plates were held in position by end sections to form a leaf-shaped gap. The gap between the plates formed the divergent leaf-width mould. The leaf ends were not constructed divergently or the ends curved. The leaves were 50 mm in thickness in the beam direction. Although it was desired to make these thicker this was not possible due to space constraints within the shadow tray region of the accelerator. To construct the leaves lead-alloy was poured into the gap between the plates and left to cool. Once cooled the end-section holding the plates was removed and the plates separated leaving the divergent lead alloy leaf.

The leaves are held in each assembly by slots cut into the top and bottom surfaces of the assembly. These were cut to focus each leaf to the source. In position on the accelerator the distance from the source to the base of the lower leaves was 55.0 cm. The vertical gap between the leaf assemblies is 15 mm. The lower leaves are 5.00 mm in width at the base and 4.55 mm in width at the top. The upper leaves are 4.41 mm in width at the base and 3.96 mm at the top. These dimensions result in alignment of the leaves when the assemblies are moved to the alignment position. The interleaf spacings in the lower level were set to be 4.50 mm at the base of the leaves. For the upper level this was set to be 3.97 mm. This results in a 0.25 mm overlap of the upper and lower leaves when in shielding position. This overlap was designed due to the leaf positioning tolerances to ensure that there was no leakage through the MLC. This means that the leaves project a width of 9.1 mm at isocentre, and a slit width for imaging of 8.2 mm. The leaves are manually retracted. The maximum field size possible to collimate with the MLC is 22 × 8 cm at isocentre, and the maximum overflash image size is 22 × 22 cm. A photograph of the MLC is shown in Figure 8-2 with the one set of the leaf assemblies removed. As each leaf assembly has two separate positions, there are four positions of the collimator, two shielding positions and two imaging positions.

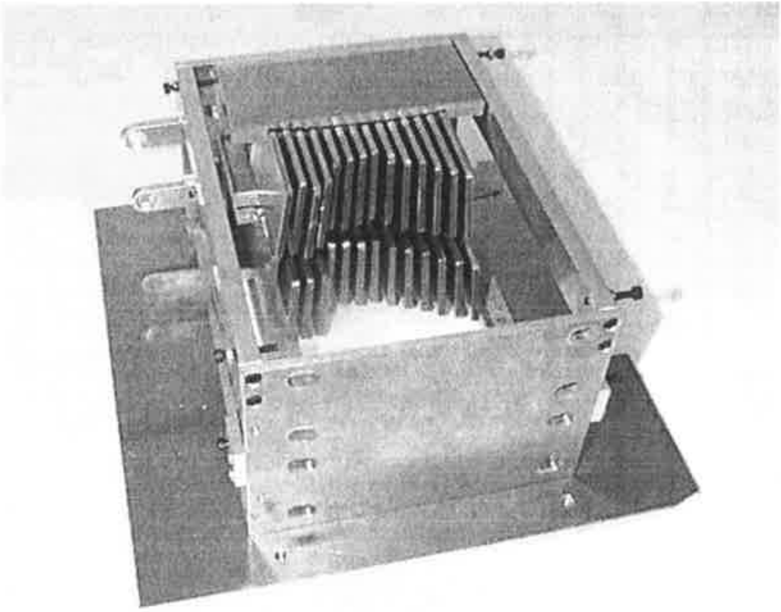

Figure 8-2 Picture taken of the prototype dual assembly MLC. The opposing leaf assemblies have been removed for clarity.

8.2.2. Imaging Performance

The intensity profiles transmitted for imaging with the collimator were measured. A BIS-710 fluoroscopic imaging detector (Wellhofer Dosimetrie, Schwarzenbruck. Germany) was placed at 100 cm from the source, with 1 cm of solid water buildup placed on the surface. The properties of the BIS-710 for dosimetric measurements have been investigated by Ma *et al.* (1997). They found that the response was linear. This was also verified by measurements performed on our detector (Liu *et al.*, 2000).

The collimator was placed in the shadow tray of the Siemens KD2 accelerator. The MLC leaves were initially positioned closed with opposing leaves meeting at the central axis. One level of the leaf assemblies was then laterally shifted to align with the other level and a 6 MV irradiation was recorded as an image by the BIS-710. This was transferred to an analysis package and a profile perpendicular to the long-axis of the leaves obtained half way between the leaf ends and the housing (5.5 cm from the central axis). To record a double-movement image profile, the collimator assemblies were returned to the shielding position and the other level of leaves moved to the aligned position. An irradiation was performed and this image was summed to the first image and the profile obtained as before. This was repeated for the 23 MV nominal beam energy. Open field images of a 10 × 10 cm field were then recorded with the BIS-710 for both energies. The mean pixel value of a central 10 × 10 pixel region was found and the profiles were divided by this value to represent the results as percentage dose of an open 10 × 10 cm irradiation.

To demonstrate the double-exposure image acquisition with the collimator design, images of a Rando anthropomorphic phantom were acquired. The head of the phantom was placed on the treatment couch at 100 cm to the midline distance. A treatment field size of 5 × 5 cm was set on the MLC. The BIS-710 detector was placed at 110 cm from the source below the phantom. An image was acquired with the treatment field. As the field edge is modified by the movement of the leaf levels (Chapter 5), the field edge on the treatment field image was determined by thresholding the image. The thresholded image was then differentiated to obtain a line image of the field edge. Movement of the collimator to the two imaging positions (leaves aligned) was then made with separate images recorded in each position. These images were then summed to obtain the final image with the treatment field area zeroed in one of the images so that the field area did not contain twice the pixel values in the final image. The treatment field was then superimposed on the image.

8.2.3. Leakage

The leakage of the MLC when shielding was compared to that of a lead alloy block of the same thickness. One set of the MLC leaves was fully closed to the central axis while the opposing leaf assemblies were removed. The MLC assemblies were aligned in the shielding position. An asymmetric 10 × 10 cm field size was set on the secondary collimator jaws with the inner edge 2 cm over the central axis so that the entire field was blocked by the MLC leaves. The 1 cm thick perspex shadow tray was then attached underneath the MLC. The BIS-710 was placed at 100 cm from the source, with 2 cm solid water buildup placed on the surface. A 6 MV irradiation was recorded as an image. The MLC was then removed and a lead alloy block with similar dimensions to the area blocked by the leaves of 12 × 8 cm and thickness 5 cm was placed on the shadow tray in the same position as the MLC leaves were previously. The irradiation was repeated and an image recorded. Finally the lead alloy block was removed and an open field irradiation performed. Profiles perpendicular to the long-axis of the leaves were then obtained mid way from the leaf ends to the housing for the MLC image (5.5 cm from central axis) and similarly for the lead alloy block images. These were normalised to the pixel value at the centre of the open field image. The irradiations were then repeated for the 23 MV energy.

8.2.4. Penumbra

The two levels of the MLC leaves are at different distances from the source and therefore may exhibit different penumbra. This would result in a variation of penumbra from leaf to leaf along the field border defined by the MLC. The penumbra of the two levels of the MLC were therefore compared and the penumbra also compared to that of the upper and lower secondary collimators. As the leaf ends are not curved or focussed to the source, the leaf end penumbra was compared to the leaf side penumbra. Also the penumbra of the leaf ends when at the central axis where they are focussed to the source was compared to the leaf end penumbra when the leaves were retracted 5 cm from the central axis where they are no longer focussed.

To obtain the penumbra measurements a 20 × 20 cm field was set on the secondary collimators. One set of the MLC assemblies was removed and the other positioned to form half of a 10 × 10 cm field. A 6 MV image was recorded with the BIS-710 placed at 100 cm from the source of the KD2 accelerator with 2 cm of solid water buildup. The image was transferred to an analysis package and profiles obtained orthogonal to the field borders defined by the upper and lower secondary collimators and the MLC leaf ends and sides. The secondary jaw penumbra was compared to the leaf end penumbra for the leaves positioned to the central axis as these are focussed to the source. Profiles across the leaf ends of both levels of the MLC leaves were obtained for comparison. Profiles across the leaf ends were also obtained for the leaves positioned to the central axis and the leaves positioned 5 cm back from the central axis and compared to a profile across the leaf sides.

8.2.5. Field edge smoothing

Angled field edges defined by MLC's exhibit dose undulation due to the stair-step pattern of the MLC leaves. A method to reduce the undulation has been proposed by Galvin *et al.* (1996). A segment of the field is delivered, the treatment couch (and patient) are then shifted by a fraction of the leaf width in the direction orthogonal to the direction of leaf motion, and the leaves repositioned to the field edge. Another segment of the field dose is delivered with the new position of the leaves.

The lateral shifting capability of the dual-assembly collimator enables this technique to be implemented by movement of the MLC leaves laterally by a fraction of a leaf width rather than movement of the couch. The effectiveness of implementing this method with the MLC was therefore investigated.

A field edge at an angle of 22 degrees was defined by the MLC leaves. The BIS-710 was placed at 100 cm from the source of the KD2 accelerator with 2.0 cm of solid water buildup. An image was acquired to record the isodose distribution resulting from the angled edge. The pixel values were converted to relative dose percentages or isodose lines with these normalised to 100% at the centre of the field. The upper and lower levels of the leaf assemblies were then shifted laterally by half a leaf width and the leaves repositioned to the field border. A second image was acquired in this position. The images were added together to give the net dose distribution for the segmented field. This summed image was then converted to isodose values.

8.3. Results

8.3.1. Imaging Performance

Figure 8-3 shows the results of the beam profiles transmitted by the collimator to form the image of the external anatomy. The dose is represented as percentage of the dose at the centre of a 10 × 10 cm open field. The 6 MV and 23 MV profiles are similar in shape although the 23 MV has higher transmission through the leaves. The profiles for the double-movement of the collimator assemblies for the two energies are shown in Figure 8-4. The profiles show the reduced dose in the junction regions due to the penumbral blurring evident in Figure 8-3 and the overlap of the adjacent leaves resulting in a region that receives no direct irradiation. The peak levels are higher than the single profile due to the addition of the penumbra region dose from the individual profiles. The 23 MV falls off less due to the higher penumbra region level.

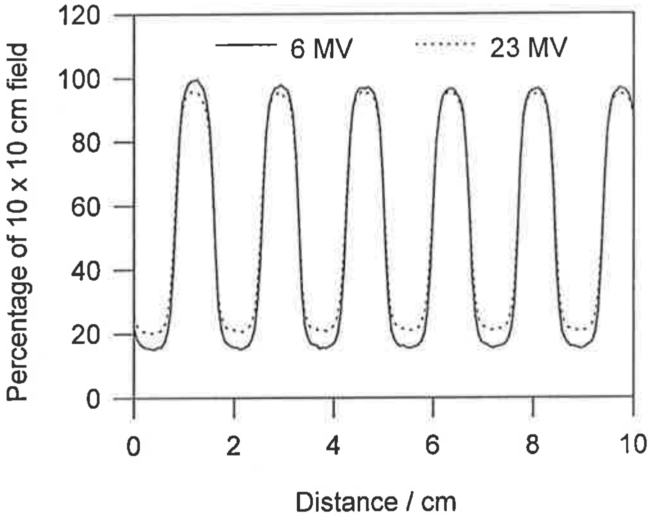

Figure 8-3 Profiles transmitted for imaging by the collimator when in the imaging position with the leaf assemblies aligned.

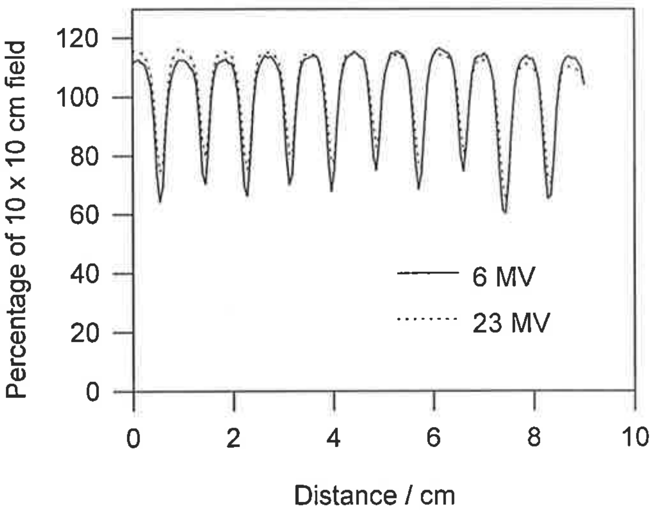

Figure 8-4 Result of the two irradiations with the collimator in the two imaging positions to form a double-movement image.

The image acquisition process with the collimator is illustrated in Figure 8-5. A treatment only image is shown in (a) with the MLC leaves shielding the anatomy external to the field. The two images acquired through the aligned leaves of the MLC are shown in (b) and (c). The composite image formed from these is shown in (d). The composite was formed by first zeroing the field area in one of the aligned MLC leaf images, then adding the two aligned MLC images together. The treatment field border from the treatment only image was then added to the result. The field area in one of the images was zeroed to avoid the treatment field area of the composite image having twice the image values of the surrounding anatomy. The field border detected in the treatment field only image was displayed on the composite as the field shape is distorted by the lateral movement of the leaves.

This double-movement image clearly shows the location of the field relative to the external anatomy which is not visible in the treatment-field only image. The image does contain vertical stripes at the junctions of the slit fields formed by the collimator due to the overlap of the leaves and penumbral blurring, as seen in Figure 8-4. This would be reduced if the overlap of the leaf levels of the collimator was reduced.

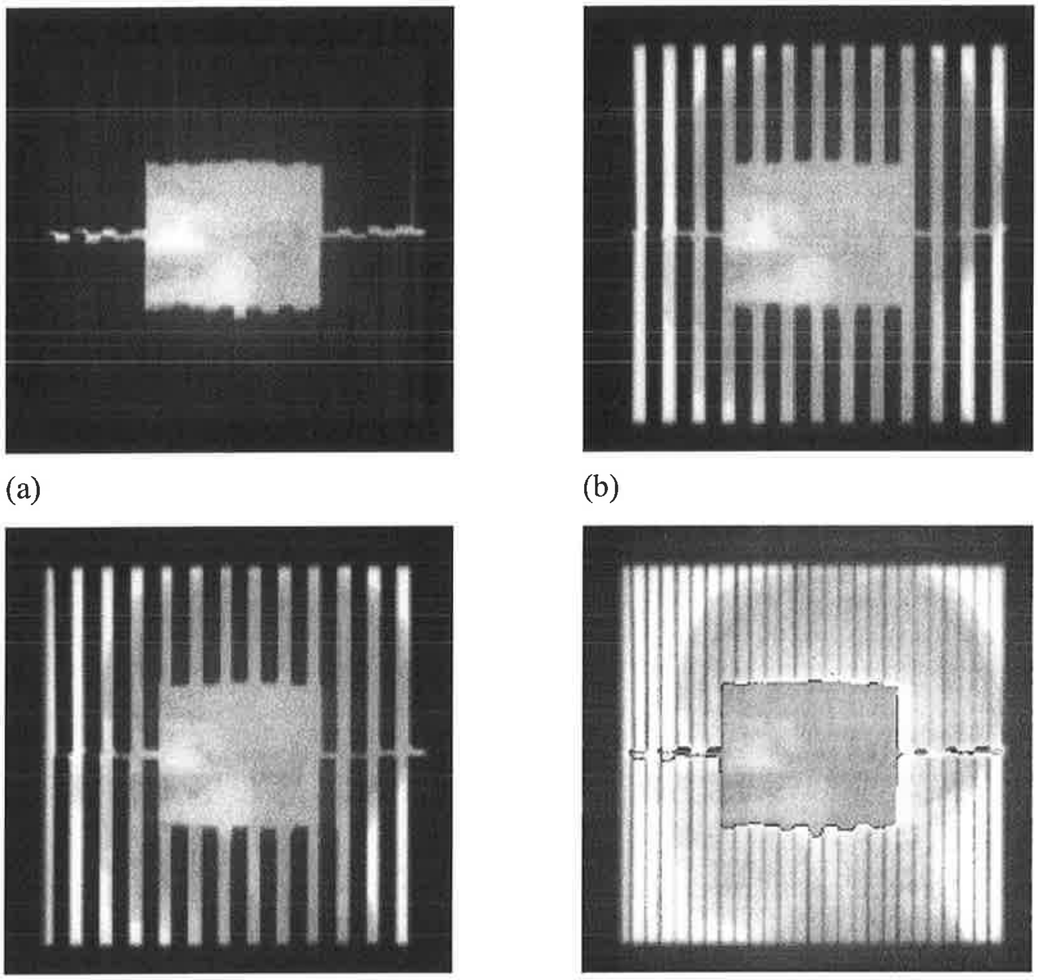

(a) (b)

(c) (d)

Figure 8-5 Double-exposure image acquisition with the MLC, (a) treatment field only image with the MLC in shielding position, (b) leaf levels aligned to image through the collimator, (c) leaf levels aligned in second imaging position to complete the irradiation, and (d) final composite image.

8.3.2. Leakage

The 6 MV radiation profiles transmitted through the MLC leaves and through the lead alloy block are shown in Figure 8-6. The MLC result clearly shows the transmission level under the leaves, and reduced intensity where the two leaf levels are overlapped. The transmission for the MLC leaves is high due to the 5 cm thickness of the lead alloy leaves, however the transmission is similar to a lead alloy block of the same thickness, material and dimensions. The fact that adjacent leaves are vertically displaced in the dual assembly design is not resulting in a higher transmission than a uniform thickness block. This result confirms the findings in Chapter 5 on the shielding performance of the two level design.

The transmission for the 23 MV energy in Figure 8-6(b) is higher than 6 MV however the transmission for the MLC is still similar to that of the uniformly thick alloy block.

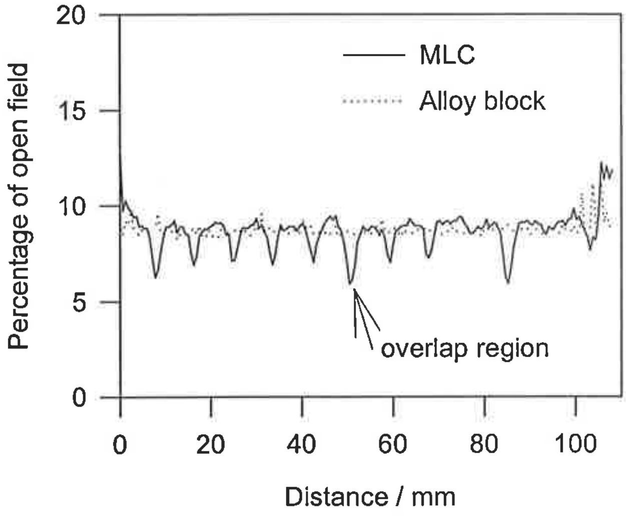

(a)

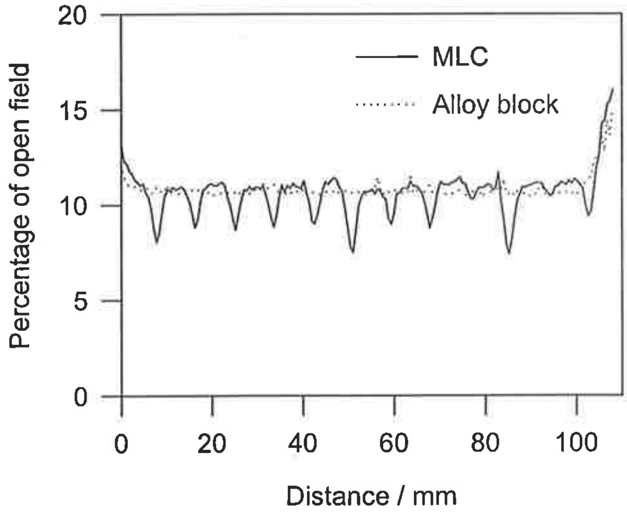

(b)

Figure 8-6 Leakage recorded under the leaves of the collimator when the leaf assemblies were in the shielding position compared to leakage through an alloy block of the same thickness, at (a) 6 MV and (b) 23 MV.

8.3.3. Penumbra

The results for the comparison of the leaf end penumbra with the leaf positioned to the central axis with that of the secondary collimators is shown in Figure 8-7. The dose under the leaf does not fall off as sharply due to the lower thickness and density of the leaf material. The dose is slightly lower in the open field portion of the MLC profile possibly due to the smaller field size defined by the MLC and increased distance of the MLC from the source resulting in occlusion of extra focal radiation. The penumbra measured for the upper level of leaves is similar to the lower level (Figure 8-8), the differences in distances from the source are not sufficient to alter the penumba significantly. The leaf sides have slightly steeper dose falloff than the leaf end as seen in Figure 8-9. The leaf end was recorded with the leaves positioned 5 cm off-axis. The leaf ends are not focussed to the source and hence the penumbra would be expected to be increased relative to the leaf sides that are focussed to the source. The penumbra for the leaves aligned with the central axis and hence focussed to the source, and the leaves positioned 5 cm off-axis are compared in Figure 8-10. The increase in penumbra is apparent, although it is not large at this distance of the leaf ends retracted from the central axis.

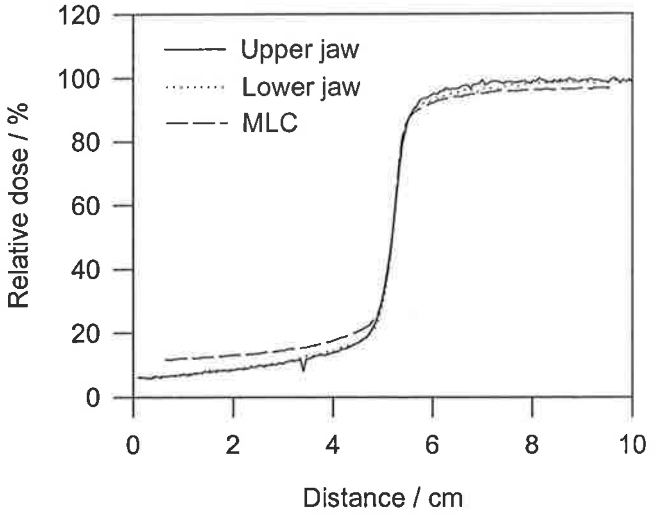

Figure 8-7 Comparison of the leaf end penumbra of the MLC with the upper and lower jaws of the KD2 accelerator.

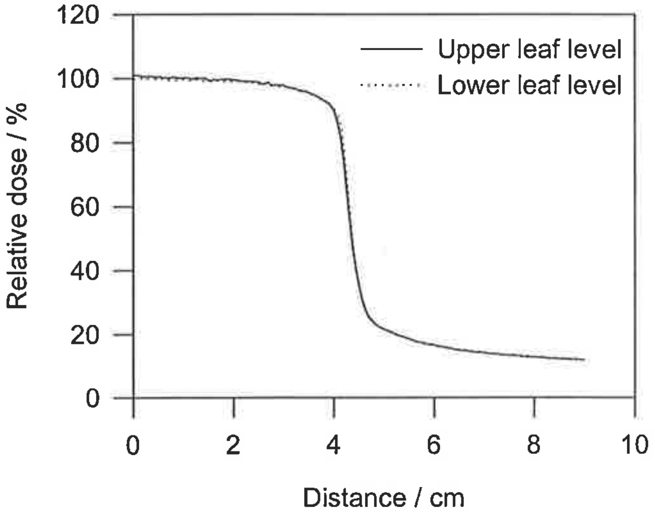

Figure 8-8 Comparison of the leaf end penumbra for the leaves in the upper level and the leaves in the lower level. The penumbra are very similar for the two levels.

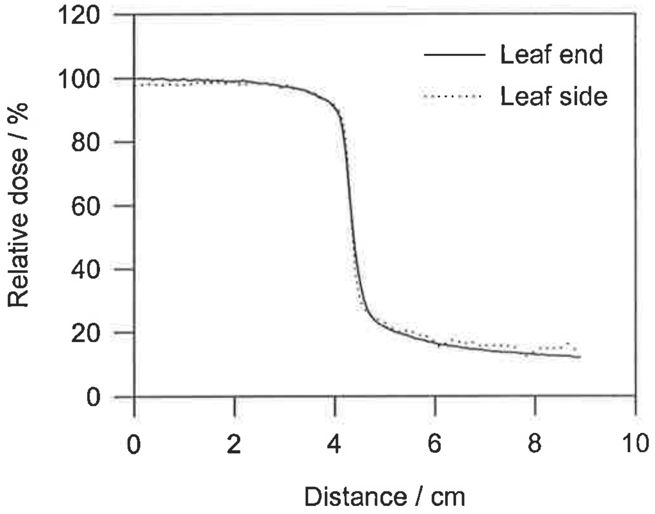

Figure 8-9 Comparison of the penumbra for the leaf end with the leaf side. The leaf side has slightly reduced penumbra as it is focussed to the source.

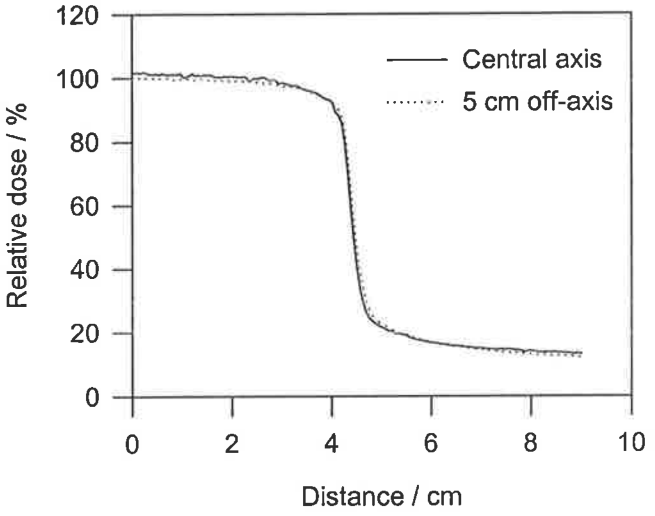

Figure 8-10 Penumba for the MLC leaf ends with the leaves aligned to the central axis and 5 cm off-axis. The penumbra is slightly greater off-axis as the leaves are not then focussed to the source.

8.3.4. Field Edge Smoothing

The image acquired with the angled field edge defined by the MLC leaves is shown in Figure 8-11(a) and converted to isodose levels in (b). The stair stepping is prominent for this angle of field edge. The image resulting from the segmented irradiation with the MLC leaves shifted laterally and repositioned to the border is shown in Figure 8-12(a) with the isodoses shown in (b). The stair-stepping pattern has been largely removed by this technique without increasing the 30%-90% penumbral width (the 30-90% effective penumbra in both cases is 4.5 mm). The lateral movment of MLC leaves is therefore effective at removing the stair-stepping pattern for angled field edges.

8.4. Discussion

The measurements detailed here have characterised properties of the prototype dual assembly collimator developed and constructed at the Royal Adelaide Hospital. The profile transmitted for imaging the external anatomy when the leaf levels are aligned was found to contain only a small overlap between adjacent individual slit field profiles. This is due to the leaf width of nearly 1 cm at isocentre and the fact that the fields are narrower than the leaf width. These profiles are therefore not amenable to single-movement imaging and movement of both assemblies is necessary to form an image of the external anatomy. This imaging process was demonstrated, producing a double-exposure image showing the treatment field location relative to the external anatomy. The final image contains a pronounced stripe artifact due to the slit field apertures being narrower than the leaf width. This artifact could be reduced by image processing however these results suggest that overlap of the two leaf levels as implemented in the prototype is not desirable for image formation. This overlap was necessary in the prototype as precise machining of leaves as well as leaf positioning was not possible. This could be reduced with more precise manufacturing and leaf positioning tolerances.

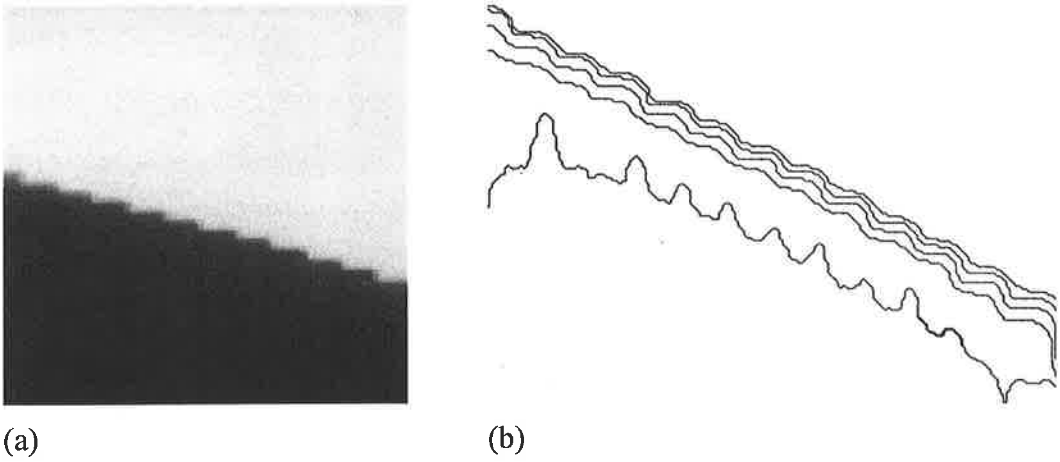

Figure 8-11 (a) Image with the angled field edge defined by the MLC leaves, and (b) the isodose distribution for this angled field edge. The isodose lines from top to bottom of the figure are 90%, 80%, 50%, 30% and 20%. The stair stepping dose pattern is evident.

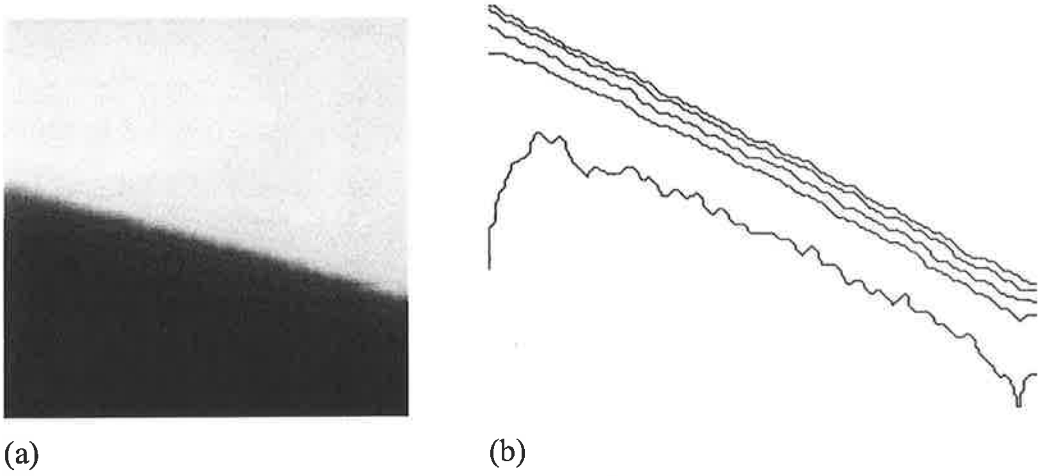

Figure 8-12 (a) Image formed by a two segment irradiation with the MLC leaves shifted laterally by half a leaf width and repositioned to the field border for the second segment, and (b) the isodoses for the field border resulting from this technique (the isodose lines from top to bottom of the figure are 90%, 80%, 50%,30% and 20%). The stair-stepping pattern has been effectively removed from the dose distribution.

The leakage radiation measurements showed that the vertically displaced leaves are shielding as effectively as a solid block of the same material and thickness. Where the leaf levels overlap the transmission is further reduced due to the doubled thickness of the shielding. This confirms the investigations performed in Chapter 5 that determined that off-axis radiation transmission through the MLC is not important.

The leaf end penumbra of the MLC was found to be different from the penumbra of the secondary collimators. However this is mainly due to the 5 cm thickness of the leaves compared to the 7.5 cm thickness of the collimator jaws and the lower density of the lead alloy leaves relative to the tungsten collimators. There was no significant difference in the leaf end penumbra for the two levels of the MLC. This is important in that the field defined by the MLC will not exhibit different penumbra for adjacent leaves defining the border, and prediction of dose distributions in a treatment planning system is therefore simplified.

The field edge smoothing technique implemented with lateral MLC movement rather than couch movement was extremely effective at removing the stair-stepping of the isodoses and did not increase the effective penumbra. This was achieved with the field segmented into two sub fields. Lateral movement of the MLC leaves rather than the treatment couch would mean sophisticated modifications to accurately translate the treatment couch would not be required.

Percentage depth dose and output factor measurements were not made for the prototype MLC. The properties of MLC for these parameters have been widely studied and it is unlikely that the dual assembly design will differ from the traditional design.

8.5. Conclusions

The imaging, shielding, penumbra and field edge smoothing properties of a prototype dual assembly multileaf collimator have been investigated. The radiation profiles transmitted for imaging the external anatomy showed that the collimator is suitable for imaging provided both leaf assemblies are translated to irradiate the external anatomy. The leakage transmission through the vertically displaced MLC leaves when shielding was found to be similar to the transmission through a solid block of the same material and thickness. The penumbra for the two levels of leaves was found to be similar. Utilising MLC lateral movement rather than treatment couch movement to reduce stair-stepping of angled field edges was found to be effective.

9. Conclusions

9.1. Main findings

A dual assembly multileaf collimator design has been investigated. The design, consisting of two levels of alternate leaves and leaf width spaces facilitates rapid acquisition of double-exposure treatment verification images. This is achieved by lateral motion of one level of leaves to align with the other level, resulting in radiation transmission through the MLC in the form of a grid of multiple slit fields. This produces a transmitted intensity distribution with characteristics dependent on the design features of the collimator. In Chapter 5 these characteristics were investigated and the leaf width (slit width) was found to have the major effect on the transmitted distribution. For small leaf widths the individual slit field profiles become broader and overlap to produce a modulated transmission profile and hence image. This is due to the greater effect of the source size for smaller leaf widths. The adequacy of shielding with this design where adjacent leaves are vertically displaced was also investigated. It was found that the shielding is adequate with alignment or very small overlap of the adjacent leaf sides. Therefore provided the leaves can be accurately positioned then the conventional tongue and groove should not be necessary. This would reduce underdose in intensity modulated treatments for sequentially irradiated contiguous areas.

In Chapter 6 the spatial resolution of the image regions under the open slits and under the leaves when an image is formed with the multiple slit field irradiation was examined. The spatial resolution for the region under the leaves was found to be poorer than under the slits. This is due to the more peripheral broader extra-focal segment of the source that contributes to the image under the leaves compared to the intense narrow focal source that contributes to the image under the open slits. The MTF under the leaves improves with reducing leaf widths again suggesting that smaller leaf widths are desirable. To remove the modulation from the image, processing methods in both spatial and frequency domain were investigated in Chapter 7. Division of the image by a correction image of the intensity modulation with no object present resulted in residual modulation due to scatter contribution to the object image that is not present in the correction image. Fourier filtering of the spectrum to remove the frequencies of the modulated intensity successfully removed the modulation from the image for smaller leaf widths, however some distortion results from the filtering.

Chapter 8 examined the imaging, shielding, penumbra and field edge smoothing properties of a prototype dual assembly multileaf collimator. The radiation profiles transmitted for imaging the external anatomy showed that the collimator is suitable for imaging provided both leaf assemblies are translated to irradiate the external anatomy. The leakage transmission through the vertically displaced MLC leaves when shielding was found to be similar to the transmission through a solid block of the same material and thickness. The penumbra for the two levels of leaves was found to be similar. Utilising MLC lateral movement rather than treatment couch movement to reduce stair-stepping of angled field edges was found to be effective.

9.2. Future research

A natural extension of this design would be the acquisition of cone-beam tomographic images formed from images acquired at several linear accelerator gantry angles around the patient. The image at each gantry location would contain the treatment field location information and the larger area exposure. A CT image could then be constructed that would show a slice of the patient anatomy with the treated field location superimposed. The feasibility of cone-beam CT with the collimator design could therefore be investigated.

Another possibility would be an investigation into the scatter reduction in the images formed with the multiple slit field irradiation. Potentially improved contrast could be obtained with this type of irradiation compared to open field imaging. This is suggested by the increased MTF results for the region under the slits compared to open field imaging.

References

Althof V.G.M., de Boer J.C.J, Huizenga H., Stroom J.C., Visser A.G., and Swanenberg B.N. (1996) Physical characteristics of a commercial electronic portal imaging device, Med. Phys., 23, 1845-1855

Antonuk L.E., Boudry J., Yorkston J., Wild C.F., Longo M.J. and Street R.A. (1990) Radiation-damage studies of amorphous-silicon photodiode sensors for applications in radiotherapy x-ray imaging, Nucl. Inst. Meth., A299, 143-146

Antonuk L.E., Boudry J., Huang W., McShan D.L., Morton E.J., Yorkston J., Longo M.J. and Street R.A. (1992) Demonstration of megavoltage and diagnostic x-ray imaging with hydrogenated amorphous silicon arrays, Med. Phys., 19, 1455-1466

Baily N.A., Horn R.A., Kampp T.D. (1980) Fluoroscopic visualization of megavoltage therapeutic x ray beams, Int. J. Radiat. Oncol. Biol. Phys., 6, 935-939

Balog J.P., Mackie T.R., Wenman D.L., Glass M., Fang G. and Pearson D. (1999) Multileaf collimator interleaf transmission, Med. Phys., 26, 176-186

Balter J.M., Pelizzari C.A. and Chen G.T. (1992) Correlation of projection radiographs in radiation therapy using open curve segments and points, Med. Phys., 19, 329-334

Barakat R. (1965) Determination of the optical transfer function directly from the edge spread function, J. Opt. Soc. Am. 55, 1217-1221

Barrett H.H and Swindell W. (1981) Radiological Imaging, Vol. I and Vol II, Academic Press, New York, USA

Bel A., van Herk M., Bartelink H. and Lebesque J.V. (1993) A verification procedure to improve patient set-up accuracy using portal images, Radiother.Oncol., 29, 253-260

Bentzen S. M. (1983) Evaluation of the spatial resolution of a CT scanner by direct analysis of the edge response function, Med. Phys. 10, 579-581

Bevington P. and Robinson K. (1992) Data reduction and error analysis for the physical sciences 2nd ed. McGraw-Hill Inc., New York

Biggs P., Goitein M. and Russell M. (1985) A diagnostic x-ray field verification device for a 10 MV linear accelerator, Int. J. Radiat. Oncol. Biol. Phys., 11, 635-643

Bijhold J., Gilhuijs K.G.A., van Herk M. and Meertens H. (1991a) Radiation field edge detection in portal images, Phys. Med. Biol., 36, 1705-1710

Bijhold J., van Herk M., Vijlbrief R. and Lebesque J.V. (1991b) Fast evaluation of patient set-up during radiotherapy by aligning features in portal and simulator images, Phys. Med. Biol., 36, 1665-1679

Bijhold J., Lebesque J.V., Hart A.A. and Vijlbrief R.E. (1992) Maximizing setup accuracy using portal images as applied to a conformal boost technique for prostatic cancer, Radiother. Oncol., 24, 261-271

Bissonnette J.-P., Jaffray D., Fenster A. and Munro P. (1994) Optimal radiographic magnification for portal imaging, Med. Phys. 21, 1435-1445

Bissonnette J.P. and Munro P. (1996) Evaluation of a high-density scintillating glass for portal imaging Med. Phys., 23, 401-406

Bissonnette J.P., Cunningham I.A. and Munro P. (1997) Optimal phosphor thickness for portal imaging, Med. Phys., 24, 803-814

Blackman R. B. and Tukey J. W. (1958) The measurement of power spectra, Dover, New York, USA

Bortfeld T., Kahler D.L., Waldron T.J. and Boyer A. (1994) X-ray field compensation with multileaf collimators, Int. J. Radiat. Oncol. Biol. Phys., 28, 723-730

Boyer A.L., Ochran T.G., Nyerick C.E. and Waldron T.J. (1992a) Clinical dosimetry for implementation of a multileaf collimator, Med. Phys., 19, 1255-1261

Boyer A.L., Antonuk L., Fenster A., van Herk M., Meertens H., Munro P., Reinstein L.E. and Wong J. (1992b) A review of electronic portal imaging devices (EPIDs), Med. Phys., 19, 1-16

Brahme A. (1987) Design principles, beam properties, and clinical possibilities of a new generation of radiotherapy equipment, Acta Oncol., 26, 403-412

Brahme A. (1998) Optimal setting of multileaf collimators in stationary beam radiation therapy, Strahlenther. Onkol. 164: 343-50

Brahme A. (1993) Optimisation of radiation therapy and the development of multileaf collimation, Int. J. Radiat. Oncol. Biol. Phys., 25, 373-375

Convery D.J. and Rosenbloom M.E. (1992) The generation of intensity-modulated fields for conformal radiotherapy by dynamic collimation, Phys. Med. Biol., 37, 1359-1374

Cunningham I. A. and Fenster A. (1987) A method for modulation transfer function determination from edge profiles with correction for finite-element differentiation, Med. Phys. 14, 533-537

Cunningham I.A. and Reid B.K. (1992) Signal and noise in modulation transfer function determinations using the slit, wire, and edge techniques, Med. Phys. 19, 1037-1044

Das I.J., Desobry G.E., McNeeley S.W., Cheng E.C. and Shultheiss T.E. (1998) Beam characteristics of a retrofitted double-focussed multileaf collimator, Med. Phys., 25, 1676-1684

De Neve W., van den Heuvel F., Coghe M., Verellen D., de Beukeleer M., Roelstraete A., de Roover P., Thon L. and Storme G. (1993) Interactive use of on-line portal imaging in pelvic radiotherapy, Int. J. Radiat. Oncol. Biol. Phys., 25, 517-524

Denham J.W., Daily M.J., Hunter K., Wheat J., Fahey P.P. and Hamilton C.S. (1993) Objective decision-making following a portal film. The results of a pilot study, Int. J. Radiat. Oncol. Biol. Phys., 26, 869-876

Dobbins III J. T. (1995) Effects of undersampling on the proper interpretation of modulation transfer function, noise power spectra, and noise equivalent quanta of digital imaging systems, Med. Phys. 22, 171-181

Droege, R.T. (1979a) A megavoltage MTF measurement technique for metal screen-film detectors, Med. Phys., 6, 272-279

Droege R.T. and Bjarngard B. (1979b) Metal screen-film detector MTF at megavoltage x-ray energies, Med. Phys., 6, 515-518

Evans P.M., Gildersleve J.Q., Morton E.J., Swindell W., Coles R., Ferraro M., Rawlings C., Xiao Z.R. and Dyer J. (1992) Image comparison techniques for use with megavoltage imaging systems, Br. J. Radiol., 65, 701-709

Ezz A., Munro P., Porter A.T., Battista J., Jaffray D.A., Fenster A. and Osborne S. (1992) Daily monitoring and correction of radiation field placement using a video-based portal imaging system: a pilot study, Int. J. Radiat. Oncol. Biol. Phys., 22, 159-165

Frazier A., Yan D., Du M., Wong J., Vicini F., Matter R., Joyce M. and Martinez A. (1993) Effects of treatment setup variation on beam's eye view dosimetry for radiation therapy using the multileaf collimator vs. the cerrobend block, Int. J. Radiat. Oncol. Biol. Phys., 33, 1247-1256

Fritsch D.S., Chaney E.L., Boxwala A., McAuliffe M.J., Raghavan S., Thall A. and Earnhart J.R. (1995) Core-based image registration for automatic radiotherapy treatment verification, Int. J. Radiat. Oncol. Biol. Phys., 33, 1287-3000

Fujita H., Tsai D.-Y., Itoh T., Doi K., Morishita J., Ueda K. and Ohtsuka A. (1992) A simple method for determining the modulation transfer function in digital radiology, IEEE Trans. Med. Imag. 11, 34-39

Galbraith G. (1989) Low-energy imaging with high-energy bremsstrahlung beams, Med. Phys., 16, 734-746

Galvin J.M., Smith A.R., Moeller R.D., Goodman R.L., Powlis W.D., Rubenstein J., Solin L.J., Michael B., Needham M., Huntzinger C.J. and Kligerman M.M. (1992) Evaluation of a multileaf collimator design for a photon beam, Int. J. Radiat. Oncol. Biol. Phys., 23, 789-801

Galvin J.M., Smith A.R. and Lally B. (1993a) Characterization of a multileaf collimator system, Int. J. Radiat. Oncol. Biol. Phys., 25, 181-192

Galvin J.M., Chen X.-G. and Smith R.M. (1993b) Combining multileaf fields to modulate fluence distributions, Int. J. Radiat. Oncol. Biol. Phys., 27, 697-705

Galvin J.M., Leavitt D.D. and Smith A.A. (1996) Field edge smoothing for multileaf collimators, Int. J. Radiat. Oncol. Biol. Phys., 35, 89-94

Galvin J.M., Han K. and Cohen R. (1998) A comparison of multileaf collimator and alloy block field shaping, Int. J. Radiat. Oncol. Biol. Phys., 40, 721-731

Galvin J.M. (1999) The Multileaf Collimator - A complete guide, AAPM Refresher Course, Nashville, USA.

Giger M.L. and Doi K. (1984) Investigation of basic imaging properties in digital radiography. I. Modulation transfer function, Med. Phys., 11, 287-295

Gildersleve J., Dearnaley D.P., Evans P.M., Law M., Rawlings C., Swindell W. (1994) A randomised trial of patient repositioning during radiotherapy using a megavoltage imaging system, Radiother. Oncol., 31, 161-168

Gilhuijs K.G.A. and van Herk M. (1993a) Automatic on-line inspection of patient setup in radiation therapy using digital portal images, Med. Phys., 20, 667-677

Gilhuijs K.G.A., El-Gayed A.A.H., van Herk M. and Vijlbrief R.E. (1993b) An algorithm for automatic analysis of portal images: clinical evaluation for prostate treatments, Radiother. Oncol., 29, 261-268

Gilhuijs K.G.A., van de Ven P.J.H., and van Herk M. (1995) Automatic three-dimensional inspection of patient setup in radiation therapy using portal images, simulator images, and computed tomography data, Med. Phys., 23, 389-399

Gilhuijs K.G.A., Drukker K., Touw A., van de Ven P.J.H. and van Herk M. (1996) Interactive three dimensional inspection of patient setup in radiation therapy using digital portal images and computed tomography data, Int. J. Radiat. Oncol. Biol. Phys., 34, 873-885

Gluhchev G. and Shalev S. (1993) Robust registration in case of different scaling, SPIE, 1898, 126-133

Gluhchev G. and Shalev S. (1995) Contrast enhancement of portal images with adaptive histogram clip, 37th Annual Meeting of the AAPM, Boston, USA

Gonzalez R.C. and Woods R.E. (1992) Digital Image Processing, Addison-Wesley Inc., Reading, MA, USA

Hanley J., Mageras G.S., Sun J., Kutcher G.J. (1995) The effects of out-of-plane rotations on two-dimensional portal image registration in conformal radiotherapy of the prostate, Int. J. Radiat. Oncol. Biol. Phys., 33, 1331-1343

Haus A.G., Dickerson R.E., Huff, K.E., Monte S., Schlager A., Atanas M. and Matloubieh A. (1997) Evaluation of a cassette-screen-film combination for radiation therapy portal localization imaging with improved contrast, Med. Phys., 24, 1605-1608

Herman M.G., Abrams R.A. and Mayer R.R. (1994) Clinical use of on-line portal imaging for daily treatment verification, Int. J. Radiat. Oncol. Biol. Phys., 28, 1017-23

Huq M.S., Yu Y., Chen, Z.-P. and Suntharalingam N. (1995) Dosimetric characteristics of a commercial multileaf collimator, Med. Phys., 22, 241-247

Heiny L. (1994) Windows graphics programming with Borland C++, 2nd ed, John Wiley & Sons, Inc., New York, USA

Hummel, R. (1977) Image enhancement by histogram transformation, Comput. Graph. Imag. Proc., 6, 184-195

Jaffe C. and Webster E.W. (1975) Radiographic contrast improvement by means of slit radiography, Radiology, 116, 631-635

Jaffray D.A., Battista J.J., Fenster A. and Munro P. (1993) X-ray sources of medical linear accelerators: Focal and extra-focal radiation, Med. Phys., 20, 1417-1427

Jaffray D.A., Battista J.J., Fenster A. and Munro P. (1994) X-ray scatter in megavoltage transmission radiography: Physical characteristics and influence on image quality, Med. Phys., 21, 45-60

Jaffray D.A., Chawla K., Yu C. and Wong J.W. (1995) Dual-beam imaging for online verification of radiotherapy field placement, Int. J. Radiat. Oncol. Biol. Phys., 33, 1273-1280

Jaffray D.A., Drake D.G., Chawla K. and Wong J.W. (1996) Characterization of a clinical fluoroscopic portal imager, Proceedings of the 4th International Workshop on electronic portal imaging, Amsterdam, The Netherlands.

Jaffray D.A., Drake D.G., Moreau M., Martinez A.A. and Wong J.W. (1999) A radiographic and tomographic imaging system integrated into a medical linear accelerator for localization of bone and soft-tissue targets, Int. J. Radiat. Oncol. Biol. Phys., 45, 773-789

Johns H.E. and Cunningham J.R. (1983) The Physics of Radiology (4th edition), Charles C Thomas, Springfield, Illinois.

Jones R.A. (1967) An automated technique for deriving MTFs from edge traces, Photog. Sci. Eng. 11, 102-106

Jordan T.J. and Williams P.C. (1994) The design and performance characteristics of a multileaf collimator, Phys. Med. Biol., 39, 231-251

Judy P. F. (1976) The line spread function and modulation transfer function of a computed tomographic scanner, Med. Phys. 3, 233-236

Källman P., Lind B., Eklöff A. and Brahme A. (1988) Shaping of arbitrary dose distributions by dynamic multileaf collimation, Phys. Med. Biol., 33, 1291-1300

Khan F. (1994) The physics of radiation therapy, 2nd ed., Williams and Wilkins, Baltimore, USA.

Klein E.E., Harms B.S., Low D.A., Willcut V. and Purdy J.A. (1995) Clinical implementation of a commercial multileaf collimator: dosimetry, networking, simulation, and quality assurance, Int. J. Radiat. Oncol. Biol. Phys., 33, 1195-1208

Lam K.S., Partowmah M. and Lam W.C. (1986) An on-line electronic portal imaging system for external beam radiotherapy, Br. J. Radiol., 59, 1007-1013

Le Heron J. C. and Poletti J. L. (1988) Measurement of x-ray image intensifier sharpness in the x-ray department, Phys. Med. Biol. 33, 93-104

Leong J. (1986) Use of digital fluoroscopy as an on-line verification device in radiation therapy, Phys. Med. Biol., 31, 985-992

Ling C.C., Burman C., Chui C.S., Kutcher G.J., Leibel S.A., LoSasso T., Mohan R., Bortfeld T., Reinstein L., Spirou S., Wang X.H., Wu Q., Zelefsky M. and Fuks Z. (1996) Conformal radiation treatment of prostate cancer using inversely-planned intensity-modulated photon beams produced with dynamic multileaf collimation, Int. J. Radiat. Oncol. Biol. Phys., 35, 721-730

Liu G., van Doorn T. and Bezak E. (2000) Assessment of flatness and symmetry with an EPID, 6th International Worshop on electronic portal imaging, Brussels

LoSasso T., Chui C.S., Kutcher G.J., Leibel S.A., Fuks Z. and Ling CC. (1993) The use of a multi-leaf collimator for conformal therapy of the prostate and nasopharynx, Int. J. Radiat. Oncol. Biol. Phys., 25, 161-170

Luchka K. and Shalev S. (1996) Pelvic irradiation of the obese patient: A treatment strategy involving megavoltage simulation and intratreatment setup corrections, Med. Phys., 23, 1897-1902

Ma L., Geis P.B. and Boyer A.L. (1997) Quality assurance for dynamic multileaf collimator modulated fields using a fast beam imaging system, Med. Phys., 24, 1213-1220

Mersseman B. and De Wagter C. (1998) Characteristics of a commercially available film digitizer and their significance for film dosimetry, Phys. Med. Biol., 43, 1803-1812

McParland B.J. (1993) Uncertainty analysis of field placement error measurements using digital portal and simulation image correlations, Med. Phys., 20, 679-685

Meertens H., van Herk M. and Weeda J. (1985) A liquid ionisation detector for digital radiography of therapeutic megavoltage photon beams, Phys. Med. Biol., 30, 313-321

Meertens H., Bijhold J. and Strackee J. (1990) A method for the measurement of field placement errors in digital portal images, Phys. Med. Biol., 35, 299-323

Metz C. and Doi K. (1979) Transfer function analysis of radiographic imaging systems, Phys. Med. Biol. 24, 1079-1106

Mohan R., Chui C. and Lidofsky L. (1985) Energy and angular distribution of photons from medical linear accelerators, Med. Phys., 12, 592-597

Mohan R. (1995) Field shaping for three-dimensional conformal radiation therapy and multileaf collimation, Semin. Radiat. Oncol. 5, 86-99

Morton E.J., Swindell W., Lewis D.G. and Evans P.M. (1991) A linear array, scintillation crystal-photodiode detector for megavoltage imaging, Med. Phys., 18, 681-691

Motz J.W. and Danos M (1978) Image information content and patient exposure, Med. Phys., 5, 8-22

Munro P., Rawlinson J.A. and Fenster A. (1987a) Therapy imaging: A signal-to-noise analysis of metal plate/film detectors, Med. Phys. 14, 975-984

Munro P., Rawlinson J.A. and Fenster A. (1987b) Therapy imaging: Limitations of imaging with high energy x-ray beams, Proc. SPIE 767, 178-184

Munro P., Rawlinson J.A. and Fenster A. (1990) A digital fluoroscopic imaging device for radiotherapy localization, Int. J. Radiat. Oncol. Biol. Phys., 18, 641-649

Munro P. and Bouius D.C. (1998) X-ray quantum limited portal imaging using amorphous silicon flat-panel arrays, Med. Phys., 25, 689-702

Palta J.R., Yeung D.K. and Frouhar V. (1996) Dosimetric considerations for a multileaf collimator system, Med. Phys. 23, 1219-1224

Pasche O. (1903) Uber eine neue Blendenvorrichtung in der Rontgentechnik, Deutsche Med. Wochenschr, 29, 266-267

Perera T., Moseley J. and Munro P. (1999) Subjectivity in interpretation of portal films. Int. J. Radiat. Oncol. Biol. Phys., 45, 529-534

Pizer S.M., Austin J.D., Perry J.R., Safrit H.D. and Zimmerman J.B. (1986) Adaptive histogram equalization for automatic contrast enhancement of medical images, SPIE, 626, 242-250

Pouliot J. and Lirette A. (1996) Verification and correction of setup deviations in tangential breast irradiation using EPID: Gain versus workload, Med. Phys., 23, 1393-1398

Press W.H., Teukolsky S.A., Vetterling W.T. and Flannery B.P. (1995) Numerical Recipes in C, 2nd ed., Cambridge University Press, Cambridge, UK

Que W. and Rowlands J.A. (1995) X-ray imaging using amorphous selenium: inherent spatial resolution, Med.Phys., 22, 365-374

Reichenbach S. E., Park S. K. and Narayanswamy R. (1991) Characterising digital image acquisition devices, Opt. Eng. 30, 170-177

Samei E. and Flynn M. J. (1998) A method for measuring the presampling MTF of digital radiographic systems using an edge test device, Med. Phys. 25, 102-113

Sephton R., Green M. and Fitzpatrick C. (1989) A new system for port films, Int. J. Radiat. Oncol. Biol. Phys., 16, 251-258

Sephton R. and Hagekyriakou J. (1995) A diagnostic-quality electronic portal imaging system, Radiother. Oncol., 35, 240-247

Shalev S., Lee T., Leszczynski K., Cosby S., Chu T., Reinstein L and Meek A. (1989) Video techniques for on-line portal imaging, Comput. Med. Imaging. Graph., 13, 217-226

Spirou S.V. and Chui C.S. (1994) Generation of arbitrary fluence profiles by dynamic jaws or multileaf collimators, Med. Phys. 21, 1031-1041

Steckner M. C., Drost D. J. and Prato F. S. (1993) A cosine modulation artifact in modulation transfer function computations caused by the misregistration of line spread profiles, Med. Phys. 20, 469-473

Stremler F. (1990) Introduction to communication systems, Addison-Wesley Inc., Reading, MA, USA

Steinberg T. (1999) Improved beam edge conformity using an MLC shift technique, Med. Phys., 26, 1098, (abstract)

Svatos M., Verhey L. and Steinberg T. (1999) The use of multiple static fields to smooth MLC field edges (abstract), Med. Phys. 26, 1152

Swerdloff S., Mackie T.R. and Holmes T. (1994) Multi-leaf attenuator for radiation therapy, US Patent 5,351,280

Swindell W., Morton E.J., Evans P.M. and Lewis D.G. (1991) The design of megavoltage projection imaging systems: Some theoretical aspects, Med. Phys., 18, 855-866

Taborsky S.C., Lam W.C., Sterner R.E. and Skarda G.M. (1982) Digital imaging for radiation therapy verification, Opt. Eng., 21, 888-893

Tatian B. (1965) Method of obtaining the transfer function from the edge response function, J. Opt. Soc. Am. 55, 1014-1019

van den Heuvel F., de Neve W., Verellen D., Coghe M., Coen V. and Storme G. (1995) Clinical implementation of an objective computer-aided protocol for intervention in intra-treatment correction using electronic portal imaging, Radiother. Oncol., 35, 232-239

van Herk M. and Meertens M. (1988) A matrix ionisation chamber imaging device for on-line patient setup verification during radiotherapy, Radiother. Oncol., 11, 369-378

van Herk M. (1991) Physical aspects of a liquid-filled ionization chamber with pulsed polarizing voltage, Med. Phys., 18, 692-702

van Herk M., Fenci W. and van Dalen A., (1995) Design and implementation of a high speed matrix ionisation chamber system, Med. Phys., 22, 991 (abstract)

Villafana T. (1975a) Effect of microdensitometer scan slit misalignment in MTF determinations, Med. Phys. 2, 255-258

Villafana T. (1975b) Modulation transfer function of a finite scanning microdensitometer slit, Med. Phys. 2, 251-254

Visser A.G., Huizenga H., Althof V.G. and Swanenburg B.N. (1990) Performance of a prototype fluoroscopic radiotherapy imaging system, Int. J. Radiat. Oncol. Biol. Phys., 18, 43-50

Webb S. ed. (1988) The physics of medical imaging, Institute of Physics Publishing, Bristol, UK

Webb S. (1993a) The effect on tumour control probability of varying the setting of a multileaf collimator with respect to the planning target volume, Phys. Med. Biol., 38, 1923-36

Webb S. (1993b) The physics of three-dimensional radiation therapy, Institute of Physics Publishing, Bristol, UK

Webb S. (1997) The physics of conformal therapy – advances in technology, Institute of Physics Publishing, Bristol, UK

Wong J.W., Binns W.R.., Cheng A.Y., Gear L.Y., Epstein J.W., Klarmann J. and Purdy J.A. (1990) On-line radiotherapy imaging with an array of fiber-optic reducers, Int. J. Radiat. Oncol. Biol. Phys., 18, 1477-1484

Wowk B. and Shalev S. (1993) Grooved phosphor screens for on-line portal imaging, Med. Phys., 20, 1641-1651

Wowk B., Radcliffe T., Leszczynski K. W., Shalev S. and Rajapakshe R. (1994a) Optimisation of metal/phosphor screens for on-line portal imaging, Med. Phys., 21, 227-235

Yin F-F, Giger M. L. and Doi K. (1990) Measurement of the presampling modulation transfer function of film digitisers using a curve fitting technique, Med. Phys. **17**, 962-966

Yorkston J., Antonuk L.E., Seraji N., Huang W., Siewerdsen J. and El-Mohri Y. (1994) Evaluation of the MTF for a-Si:H imaging arrays, Proc. SPIE, 2163, 141-149

Zhao W. and Rowlands J.A. (1992) Large-area solid state detector for radiology using amorphous selenium, Proc. SPIE 1651, 134-143

Zhao W. and Rowlands J.A. (1993) Digital radiology using self-scanned readout of amorphous selenium, Proc. SPIE 1896, 114-120

Zhu Y., Boyer A.L. and Desobry G.E. (1992) Dose distributions of x-ray fields as shaped with multileaf collimators, Phys. Med. Biol., 37, 163-173